

Density functional theory and dynamical mean-field theory: A way to model strongly correlated systems

DISSERTATION
zur Erlangung des Doktorgrades
der Naturwissenschaften

vorgelegt beim Fachbereich Physik
der Goethe-Universität Frankfurt
in Frankfurt am Main

von
Steffen Backes
aus Frankfurt-Höchst

Frankfurt am Main, April 2017

D 30

vom Fachbereich Physik der
Goethe Universität Frankfurt
als Dissertation angenommen.

Dekan: Prof. Dr. Owe Philipsen

Gutachter: Prof. Dr. Roser Valentí
apl. Prof. Dr. Eberhard Engel
Prof. Dr. Silke Biermann

Datum der Disputation: 13. Februar 2017

Zusammenfassung

Diese Arbeit ist der sogenannten LDA+DMFT Methode und ihrer Anwendung in der theoretischen Beschreibung und Modellierung von unkonventionellen Supraleitern gewidmet. Diese Methode ist besonders dazu geeignet, Elektronen in Festkörpern zu untersuchen, die sehr stark miteinander wechselwirken und sich nicht mehr angemessen durch andere konventionelle Theorien beschreiben lassen.

Die meisten Materialien, die in der theoretischen Festkörperphysik untersucht werden, bestehen aus einem regelmäßigen Gitter von Atomrümpfen, die das sogenannte Kristallgitter aufbauen, und ihren Elektronen, die sich im Kristallgitter bewegen können. Die mathematische Beschreibung der elektronischen Dynamik eines Festkörpers ist das Feld der theoretischen Festkörperphysik. Sie beschäftigt sich mit dem Aufstellen von physikalischen Modellen zur Beschreibung eines Festkörpers und seiner Elektronen, mit dem Lösen der daraus folgenden mathematischen Gleichungen und der Interpretation derselben im Bezug auf experimentell beobachtbare Größen.

Aus der Kenntnis der Dynamik der Elektronen lassen sich nicht nur vielzahlige beobachtbare Eigenschaften ableiten, die etwa mit experimentellen Untersuchungen verglichen werden können, sondern auch Vorhersagen gewinnen, die wiederum zu neuen Einsichten, Ansätzen oder Materialien in der experimentellen Festkörperphysik führen können. Insbesondere lassen sich mit theoretischen Modellen materialspezifische Eigenschaften untersuchen und vorhersagen, zu denen beispielsweise die elektrische Leitfähigkeit, die optischen, magnetischen und thermischen Eigenschaften, strukturelle Parameter und auch mögliche Supraleitung, bei der der elektrische Widerstand des Materials praktisch auf Null absinkt, gehören.

Der typische Abstand von den Atomkernen in Festkörpern beträgt etwa 10^{-9} Meter. Dies hat zur Folge, dass die elektrostatische Wechselwirkung, die sogenannte Coulombkraft, die wichtigste Wechselwirkung zwischen den Atomen und Elektronen in diesen Systemen ist. Zwischen zwei Ladungen steigt die Coulombkraft proportional zum Inversen des Abstandes an, was im Festkörper dazu führt, dass alle anderen Kräfte wie die Schwerkraft um Größenordnungen kleiner sind und daher vernachlässigt werden können. Damit lässt sich eine äußerst präzise Beschreibung der Dynamik von Elektronen in einem Festkörper ausschließlich über Berücksichtigung der Coulombkraft erreichen.

In der theoretischen Physik können wir im Rahmen der Quantenmechanik Differentialgleichungen aufstellen, die die zeitliche Entwicklung der quantenmechanischen Wellenfunktionen der Elektronen beschreiben. Diese bestehen aus der sogenannten Schrödingergleichung, die das zeitliche Verhalten der Wellenfunktion der Elektronen in Bezug zu ihrer kinetischen und potentiellen Energie setzt. Da im Festkörper die Coulombkraft die dominierende ist, ist die potentielle Energie rein durch das Coulombgesetz gegeben.

Diese potentielle Energie eines einzelnen Elektrons setzt sich zusammen aus der Wechselwirkung mit allen anderen im Festkörper vorhandenen Elektronen, sowie der Wechselwirkung mit den Atomrümpfen des Gitters. Die erstere Wechselwirkung ist eine abstoßende, das heißt, aufgrund der gleichen negativen Ladung der Elektronen erfahren diese eine repulsive Kraft, je näher sich zwei Elektronen einander annähern. Andererseits ist die zweite Wechselwirkung zwischen den Elektronen und Atomrümpfen eine anziehende, da die Atomkerne aufgrund ihrer Bausteine, der positiven geladenen Protonen und neutralen Neutronen, eine entgegengesetzte Ladung zu den Elektronen besitzen.

Diese beiden sehr verschiedenen Wechselwirkungen, die sich im Festkörper auf kleinstem Raum abspielen, erzeugen eine komplizierte zeitliche Entwicklung der elektronischen Dynamik. Die Elektronen sind daher nicht frei, sondern eingeschränkt in ihrer Bewegung durch die unterschiedlichen abstoßenden und anziehenden Kräfte im Festkörper.

Das Lösen der resultierenden Schrödingergleichung gestaltet sich damit als sehr schwierig. Das Gewinnen einer exakten Lösung ist in der Praxis nicht möglich, da allein die schiere Menge gekoppelter Gleichungen nicht im Computer gespeichert werden kann. Daher bemüht man sich in der

theoretischen Festkörperphysik, möglichst effektive Näherungen zu der exakten Lösung zu finden, die das Verhalten des Materials qualitativ noch korrekt wiedergeben, aber eine ausreichende Vereinfachung der Gleichungen ergeben, so dass diese sich analytisch oder numerisch lösen lassen.

Eine der häufigsten Näherungen ist die sogenannte Born-Oppenheimer Näherung, welche bereits eine signifikante Vereinfachung des Problems erreicht. In den Differentialgleichungen, die den Festkörper beschreiben, geht die Dynamik der Atomkerne gleichberechtigt mit der der Elektronen ein. Dabei muss berücksichtigt werden, dass die Atomkerne aufgrund ihrer immens höheren Masse, die etwa das zweitausend- bis zwanzig tausendfache eines Elektrons beträgt, eine viel langsamere Dynamik als die der Elektronen besitzen. Aus dem Gesichtspunkt der Elektronen stehen die Atomkerne daher quasi "still", da ihre Bewegung signifikant langsamer als die der Elektronen abläuft. Daher approximiert man die Atomkerne in der Born-Oppenheimer Näherung als fixiert und unbeweglich, woraus sich wiederum ableiten lässt, dass in den Differentialgleichungen des Systems der kinetische Anteil der Atomkerne und deren Wechselwirkungen untereinander nicht berücksichtigt werden müssen.

Damit reduziert sich das Lösen der Schrödingergleichung rein auf das elektronische Problem. Die Atomkerne an den fixen Gitterpositionen erzeugen ein statisches Hintergrundpotential, in dem sich die Elektronen bewegen und wechselwirken. Auf der Basis dieser Form von Differentialgleichungen bauen zahlreiche erfolgreiche Theorien und Methoden auf.

Obwohl diese Form der Schrödingergleichung nun eine deutliche Vereinfachung erfahren hat, ist sie immer noch zu komplex um im allgemeinen Fall analytisch gelöst werden zu können. Einen wertvollen Einblick liefern dabei Näherungen der sogenannten Molekularfeldtheorien. Diese bilden das System von wechselwirkenden Elektronen auf ein effektives ein-Teilchen Problem ab, bei dem ein einzelnes Elektron nicht direkt mit den anderen Elektronen interagiert, sondern über ein effektives umgebendes Potential beeinflusst wird. Dazu vernachlässigt man zeitliche und räumliche Fluktuationen der Elektronenverteilung im Raum und approximiert diese durch eine zeitlich konstante Dichte, mit der das jeweilige Elektron wechselwirkt. Da diese Dichte aus der Mittelung über alle Elektronen gebildet wird, beeinflusst sich die Elektronenverteilung dadurch effektiv selbst, wodurch eine Selbstkonsistenzrelation für die endgültige Elektronendichte entsteht. Dieses Problem kann dann iterativ gelöst werden, so dass man eine der Molekularfeldtheorie entsprechend konsistente Dichte erhält, die die gesamte Elektron-Elektron-Wechselwirkung effektiv beschreiben kann.

Als Nachteil dieser Methode stellt sich heraus, dass die Vernachlässigung jeglicher zeitlicher und räumlicher Fluktuationen in der Dichte nicht korrekt Phasenübergänge beschreiben kann, in denen die Korrelationslänge, also der mittlere Abstand über den sich Elektronen effektiv spüren können, sehr groß wird. Damit werden etwa bestimmte Phasen als zu stabil eingeschätzt, die in Wahrheit durch Quantenfluktuationen destabilisiert werden. Auch können Systeme mit vermehrt inhomogener Elektronenverteilung nicht akkurat beschrieben werden.

Einer der heutzutage am weitesten verbreiteten Methoden, die sich als eine verbesserte Variante der Molekularfeldtheorie verstehen lässt, ist die sogenannte Dichtefunktionaltheorie (DFT). Diese Theorie baut auf den Theoremen von Walter Kohn und Pierre Hohenberg auf, welche besagen, dass anstatt der quantenmechanischen Wellenfunktionen der Elektronen nur die Dichte der Elektronen ausreicht, um das System im Grundzustand vollständig zu beschreiben. Dieser Formalismus führt zu einer deutlichen methodischen Vereinfachung, da nun anstatt der sehr hohen Anzahl an Wellenfunktionen nur eine einzige Funktion, die der Dichte, gespeichert werden muss. Diese Formulierung ist an sich exakt und kann prinzipiell eingesetzt werden, um Grundzustandseigenschaften zu untersuchen.

Auf diesen Theoremen aufbauend, entwickelten Walter Kohn und Lu Jeu Sham einen Formalismus, der das wechselwirkende Elektronensystem exakt abbildet auf ein effektives nicht-wechselwirkendes System. Sie leiteten Gleichungen her, die es ermöglichen, das reelle System über das effektive nicht-wechselwirkende System zu beschreiben und die exakte Grundzustandsdichte zu berechnen. Dies führt ähnlich in der besprochenen Molekularfeldtheorie zu einer deutlichen Vereinfachung, da nicht mehr die komplizierte Form der direkten Elektron-Elektron-Wechselwirkung

behandelt werden muss, sondern die Elektronen über ein effektives Feld, was selbstkonsistent gefunden werden muss, wechselwirken. Diese Abbildung ist prinzipiell exakt, in der Praxis müssen aber weiterhin bestimmte Näherungen angewendet werden.

Diese Näherungen in praktischen Implementationen von DFT beziehen sich auf den sogenannten Austausch-Korrelations-Term, der die effektive Elektron-Elektron-Wechselwirkung enthält, die über die Wechselwirkung mit der Elektronendichte hinausgehen. Dieser Term wird meist approximiert durch den Beitrag, den man für ein homogenes Elektronengas mit der vorgegebenen Dichte erhalten würde. Diese Näherung bezeichnet man als lokale-Dichte Approximation (LDA). Als Folge dessen eignet sich diese Approximation sehr gut für Systeme, in denen die Elektronen eine sich im Raum nur langsam und stetig ändernde Dichte erzeugen. Dies trifft auf viele Materialien und insbesondere Metalle zu, so dass damit der DFT als sogenannte *ab initio* Methode, welche ohne Wahl freier Parameter auskommt, große Popularität und Erfolg zu Teil wurde. Über die Zeit konnte sich die DFT somit als die Standardmethode zur theoretischen Untersuchung von Festkörpern etablieren.

Für Systeme, in denen die Elektronendichte dagegen nicht als homogen genähert werden kann, sorgt die LDA dafür, dass teilweise quantitativ und qualitativ keine Übereinstimmung mit experimentellen Beobachtungen erzielt werden kann. Insbesondere sagt die DFT für gewisse Systeme metallische Eigenschaften vorher, wohingegen diese in der Praxis Isolatoren sind, was zum Beispiel in Übergangsmetalloxiden beobachtet wurde. Auch die Tatsache, dass in der DFT nur Eigenschaften des Grundzustandes zugänglich sind, erlaubt es nicht, physikalisch gerechtfertigte Aussagen über angeregte Zustände zu treffen.

Um diese Defizite zu beseitigen, wurden unter anderem die Approximation des Austausch-Korrelations-Term verbessert, was zur Entwicklung der sogenannten generalisierten Gradienten-Methode, die auch die lokale Änderung der Elektronendichte berücksichtigt, sowie von Hybridfunktionalen führte. Ein anderer Ansatz verfolgt die Idee, starke elektronische Wechselwirkungen, die nicht ausreichend in der DFT beschrieben werden, in erster Näherung auf einem effektiven Gittermodell zu berechnen und dann der DFT wieder zuzuführen, wie es zum Beispiel in der sogenannten LDA+U Methode angewandt wird. Diese Erweiterungen haben zu einer verbesserten Beschreibung von Materialien geführt, konnten aber insbesondere nicht das isolierende Verhalten von vielen Materialien physikalisch korrekt beschreiben.

Zunächst separat von der DFT wurden effektive minimale Modelle zur Beschreibung von Festkörpern entwickelt, die neue und andere Lösungsansätze hervorbrachten. Das bekannteste Modell ist das Hubbardmodell, bei dem der Festkörper durch ein periodisches Gitter von Atomrümpfen approximiert wird, in dem die Elektronen mit einer gewissen Amplitude von Atom zu Atom hüpfen können, und nur wechselwirken, wenn sie sich auf dem gleichen Gitterplatz befinden. Dieses Modell ist eine Vereinfachung des kinetischen und des Coulombterms der Schrödingergleichung, beinhaltet aber weiterhin das volle Spektrum der Wechselwirkungsstärke vom nicht wechselwirkenden metallischen System bis hin zu einem stark wechselwirkenden System mit inhomogener Dichte, wo die Coulombwechselwirkung dominiert.

Auch das Hubbardmodell ist in dieser Form außer in speziellen Grenzfällen nicht analytisch lösbar und bedarf daher besonderer approximativer oder numerischer Methoden zur Lösung. Eine sehr erfolgreiche Methode, die 1989 von Walter Metzner und Dieter Vollhardt vorgeschlagen wurde, ist die dynamische Molekularfeldtheorie (DMFT). Sie ist ähnlich zur klassischen, statischen Molekularfeldtheorie, behält aber dem Namen entsprechend die volle zeitabhängige Dynamik des Systems.

In der DMFT wird der Grenzfall von unendlicher Dimensionalität betrachtet, oder auch äquivalent der Grenzfall in dem die Konnektivität des Gitters, also die Anzahl an Gitternachbarn jedes Gitterplatzes, gegen unendlich geht. Im Falle eines kubischen Gitters in zwei Dimensionen beträgt die Anzahl an nächsten Nachbarn eines Platzes bereits vier, in drei Dimensionen bereits 6. Metzner und Vollhardt konnten zeigen, dass im Fall unendlicher Dimensionalität sich die Lösung des Hubbardmodells grundlegend vereinfacht und sich in die Lösung eines effektiven Störstellenproblems umformulieren lässt. Das bedeutet, dass jeder Gitterpunkt seine Umgebung nicht als diskrete umgebende Gitterplätze erfährt, sondern als ein effektives homogenes aber zeitabhängiges Feld wahrnimmt.

Ähnlich der klassischen Molekularfeldtheorie muss auch in der dynamischen Molekularfeldtheorie dieses effektive Feld selbstkonsistent bestimmt werden.

Diese Abbildung im Grenzwert unendlicher Dimensionalität hat den Vorteil, dass effiziente numerische Verfahren angewendet werden können, um das Störstellenproblem sehr akkurat zu lösen. Aufgrund der Tatsache, dass dieser Grenzfall keine weiteren Näherungen am kinetischen Term oder dem Coulombterms vornimmt, bleibt die volle Konkurrenz zwischen diesen beiden Termen erhalten. Dies erlaubt es, auch für stark wechselwirkende Systeme sehr genaue Lösungen zu erhalten, solange die Anzahl an nächsten Nachbarplätzen groß ist. Mit der DMFT wurde es somit möglich, bedeutsamen Einblick in die Physik des Hubbardmodells zu gewinnen. Insbesondere konnte damit der Metall-Isolatorübergang als Funktion der Stärke der Coulombwechselwirkung beschrieben werden.

Da das Hubbardmodell ein effektives Modell mit frei wählbaren Parametern wie der Hüpfamplitude ist, blieb der DMFT zunächst die erfolgreiche Anwendung auf realistische Systeme verwehrt. Schnell wurden jedoch Versuche unternommen, die DMFT auf reale Systeme zu erweitern. Dies führte zur Entwicklung der sogenannten LDA+DMFT Methode. Sie kombiniert dabei die Vorteile der *ab initio* DFT mit den Fähigkeiten der DMFT, so dass die Defizite der DFT, stark wechselwirkende Systeme zu beschreiben, durch DMFT ausgeglichen werden. Diese Kombination erlaubt es prinzipiell, stark korrelierte *ab initio* Rechnungen für realistische Festkörper durchzuführen.

Die LDA+DMFT Methode wurde fortan erfolgreich zur Untersuchung von einer Vielzahl von Materialien eingesetzt, die sich vorher nur unzureichend von der DFT beschreiben ließen. Zusätzlich zur Fähigkeit, stark wechselwirkende Systeme untersuchen zu können, erweisen sich als Vorteile der LDA+DMFT unter anderem die korrekte Behandlung von Elektronenanregungen, was zu einer deutlichen Verbesserung der Vergleichbarkeit von Theorie und Experiment führte, sowie die Berücksichtigung von endlicher Temperatur, so dass nicht nur Grundzustandseigenschaften zugänglich sind.

In dieser Arbeit werden wir die LDA+DMFT Methode verwenden, um die Familie der unkonventionellen eisenbasierten Supraleiter zu untersuchen. Der Grundbaustein dieser Systeme besteht aus einer Eisen-Pniktid- oder Eisen-Chalkogen-Schicht, in der die Eisenatome ein regelmäßiges rechteckiges Gitter bilden. Oberhalb und unterhalb dieser Ebene befinden sich die Pniktid- oder Chalkogenatome, welche tetraederförmig um die Eisenatome angeordnet sind. Diese atomaren Schichten können nun kombiniert mit anderen Atomen in verschiedener Form auftreten.

Die strukturell einfachste Form der eisenbasierten Supraleiter besteht aus übereinander angeordneten Eisen-Pniktid- oder Eisen-Chalkogen-Schichten, wie sie zum Beispiel in der Verbindung FeSe auftreten. Diese Gruppe wird aufgrund der Stöchiometrie 11-Familie genannt. Bei den 111-Systemen befinden sich weitere Atome, zum Beispiel aus der Alkalireihe, zwischen den Eisenschichten, wie im System LiFeAs der Fall. Desweiteren gibt es die sogenannte 122-Familie, bei der nach jeder Zwischenschicht von Fremdatomen die Eisenschicht in Schichtrichtung gespiegelt ist. Das bekannteste System dieser Familie ist BaFe₂As₂. In der 1111-Familie befinden sich zwischen den Eisenschichten weitere komplex angeordnete Schichten von Atomen, wobei als bekanntes Beispiel LaFeAsO zu nennen wäre.

Entdeckt wurden die supraleitenden Eigenschaften von eisenbasierten Supraleitern das erste Mal 2006 in LaFePO, welches eine Sprungtemperatur von etwa 4 K aufwies. Bald danach konnte bereits in dem System LaFeAsO_{1-x}F_x eine Sprungtemperatur von 26 K erreicht werden. Die Entdeckung der Supraleitung in diesen Materialien kam zunächst überraschend, da in bekannten Kuprat-Supraleitern die Dotierung mit Eisen generell eine Absenkung der Sprungtemperatur zur Folge hatte. Die höchsten Sprungtemperaturen reichen heute bis an 56 K heran, wobei vereinzelt auch von möglichen Werten über 100 K in dünnen Schichtsystemen berichtet wird.

Die Physik der eisenbasierten Supraleiter wird im wesentlichen von den *3d* Orbitalen der Eisenatome bestimmt, die den dominanten Beitrag zur Zustandsdichte an der Fermikante bilden. Damit sind diese Materialien unter Normalbedingungen Metalle. Aufgrund der starken räumlichen Lokalisierung der Eisen *3d* Orbitale beobachtet man aber auch Effekte von elektronischen Korrelationen in diesen Materialien, die zum großen Teil nicht von der DFT korrekt beschrieben werden können. Je nach System können dabei die Abweichungen im Vergleich zum Beispiel zu

spektroskopischen Experimenten sehr gering sein, oder sich auch signifikant und qualitativ unterscheiden. Insbesondere im Bereich der Loch-dotierten Supraleiter wie KFe_2As_2 wird der Einfluss der elektronischen Korrelationen auf die Eigenschaften der Systeme immer wichtiger, welche sich dadurch nur unzureichend im Rahmen der DFT beschreiben lassen.

Speziell um ein besseres Verständnis zum Mechanismus der Supraleitung in diesen Systemen zu gewinnen, bedarf es hochentwickelter theoretischer Methoden, die auf eine akkurate Beschreibung der elektronischen Struktur angewiesen sind. Deswegen ist es insbesondere in diesen Systemen wichtig, elektronische Korrelationen ausreichend genau zu behandeln, so dass oftmals eine Beschreibung innerhalb der DFT nicht ausreichend ist. Im Rahmen dieser Arbeit motiviert diese Tatsache die Anwendung der LDA+DMFT Methode auf eisenbasierte Supraleiter.

Im ersten Kapitel dieser Arbeit werden wir eine Einleitung zur theoretischen Beschreibung von Festkörpern geben. Dabei gehen wir auf die grundlegenden Methoden ein, wie ein wechselwirkendes Elektronensystem quantenmechanisch beschrieben werden kann. Im Anschluss werden wir eine Einführung zu eisenbasierten Supraleitern geben und auf ihre strukturellen wie elektronischen Eigenschaften eingehen.

Im zweiten Kapitel werden wir zuerst die Grundlagen der DFT einführen und zeigen, an welcher Stelle Approximationen notwendig sind und welche zur Unterschätzung von elektronischen Korrelationen führen. Dabei werden wir auch mögliche Erweiterungen wie LDA+U oder Hybridfunktionale ansprechen.

Im dritten Kapitel werden wir dann den Formalismus Greenscher Funktionen einführen, welche die Grundlage für die DMFT legen. Insbesondere besprechen wir die Formulierung in imaginärer Zeit und Frequenz, welche eine sehr elegante Handhabung der entstehenden Gleichungen zur Folge haben.

Das daraus ergebende Problem der analytischen Fortsetzung werden wir im vierten Kapitel diskutieren. Zur Extrahierung von physikalischen Observablen ist eine Rücktransformation von der imaginären zur reellen Zeitachse vonnöten, welche aufgrund der schlechten Konditionierung des Problems nicht einfach zu lösen ist. Dabei werden wir verschiedene Methoden vorstellen und vergleichen.

Im fünften Kapitel führen wir dann das Konzept der DMFT ein und beschreiben die Herleitung der wichtigsten Formeln zur effektiven Lösung des Hubbardmodells.

Im darauf folgenden sechsten Kapitel widmen wir uns der Kombination der DFT und der DMFT, um den LDA+DMFT Formalismus zu entwickeln. Dabei beschreiben wir, wie mit Hilfe einer Projektionsmethode eine lokale Basis aus den DFT Blochfunktionen gewonnen werden kann, mit deren Hilfe das effektive Hubbardmodell aufgestellt wird. An dieser Stelle gehen wir außerdem darauf ein, welche Folgen das sogenannte Energiefenster hat, welches man für die Projektion wählen muss. Abhängig davon, wie viele Blochzustände für die Projektion verwendet werden, erzeugt dies eine unterschiedliche Lokalisierung der lokalen Orbitalzustände, welche bedeutsame Folgen für die Wahl der effektiven Coulombwechselwirkung und damit dem Grad der Korrelationen hat.

Daran schließt sich eine Diskussion des Doublecounting-Problems an, welches innerhalb der LDA+DMFT Methode von enormer Wichtigkeit ist. Es tritt auf, da bereits in DFT bestimmte Korrelationen behandelt werden, die wiederum in DMFT auch berücksichtigt werden. Daraus ergibt sich eine doppelte Berücksichtigung dieser Beiträge, die abgezogen werden muss. Da die DFT und DMFT fundamental unterschiedlich formuliert sind, lässt sich dieses Problem nicht exakt lösen und bedarf approximativer Ansätze. Wir untersuchen dabei die Auswirkungen verschiedener Varianten und zeigen auf, in welchen Systemen Unterschiede in den Methoden relevant werden.

Je nach Wahl des Projektionsfensters ergibt sich ein anderer Wert der effektiven Coulombwechselwirkung, denn alle Zustände, die bei der Projektion nicht berücksichtigt werden, tragen zu einer Abschirmung bei, die den Wert der effektiven Wechselwirkung reduziert. Dabei besprechen wir die Konstruktion der Coulombmatrix für verschiedene Orbitaltypen sowie übliche Approximationsmöglichkeiten.

Im siebten Kapitel wenden wir dann die LDA+DMFT Methode auf das lochdotierte System KFe_2As_2 an und untersuchen die Einflüsse elektronischer Korrelationen auf die elektronische Struktur. Dabei stellen wir fest, dass dieses System starke Korrelationseffekte zeigt, welche für eine

deutliche Bandbreitenrenormierung und Änderungen in der Fermifläche im Vergleich zu der DFT sorgen. Damit zeigen wir, dass eine Übereinstimmung mit experimentellen Beobachtungen nur unter korrekter Berücksichtigung von Korrelationen möglich ist.

Im achten Kapitel erweitern wir dann unsere Untersuchungen, ausgehend vom lochdotierten KFe_2As_2 , auf die isovalenten Systeme RbFe_2As_2 und CsFe_2As_2 , welche bisher noch nicht im Rahmen von LDA+DMFT untersucht wurden. Diese zeichnen sich durch einen vergrößerten interatomaren Abstand aus, da der atomare Radius von Kalium nach Rubidium zu Cäsium anwächst. Dies hat zur Folge, dass die Hybridisierung der Eisenorbitale sinkt und damit deren Lokalisierung zunimmt. Wir werden dabei zeigen, dass entlang dieser Reihe die Korrelationen zunehmen in Übereinstimmung mit experimentellen Beobachtungen. Insbesondere sind die elektronischen Zustände in diesen Systemen von äußerst inkohärenter Natur, welche sich nicht mehr als Fermiflüssigkeit beschreiben lassen. Die Ursache dafür identifizieren wir in der Hundskopplung, welche Orbitalfluktuationen unterdrückt und das System stark korreliert erscheinen lässt. Unsere Untersuchungen für verschiedene Wechselwirkungsstärken zeigen aber, dass diese Systeme nicht in direkter Nähe zu einem Mottübergang liegen, wie zuerst in anderen Veröffentlichungen postuliert wurde.

Im neunten Kapitel stellen wir dann Ergebnisse zu dem wohluntersuchten System SrVO_3 vor, welche in Kollaboration mit einer Experimentalgruppe erzielt wurden. SrVO_3 ist als System besonders interessant, weil es eine vergleichsweise einfache Struktur, aber gleichzeitig starke Korrelationseffekte aufweist. In der Literatur wurde ein experimentell beobachteter Zustand unterhalb der Fermikante als Hubbardband identifiziert und mit LDA+DMFT Rechnungen bestätigt. Wir gingen dabei der Frage nach, in wie weit diese Interpretation wirklich korrekt ist. Aus anderen Verbindungen wie SrTiO_3 ist nämlich bekannt, dass Sauerstoff-Fehlstellen sehr ähnliche Zustände bei derselben Energie erzeugen können, was aber in SrVO_3 noch nicht berücksichtigt wurde. Daher führten wir umfassende LDA+DMFT Untersuchungen des Systems unter Berücksichtigung dieser Fehlstellen durch, die tatsächlich zeigen, dass der beobachtete Zustand unterhalb der Fermikante aus zwei Komponenten besteht: Einmal aus dem bisher bekannten Hubbardband, aber zusätzlich auch aus einem Beitrag der Sauerstoff-Fehlstellen. Dieses Ergebnis liefert nicht nur wichtige Hilfestellung bei der experimentellen Untersuchung zukünftiger verwandter Systeme, sondern bestätigt auch die Gültigkeit bestehender LDA+DMFT Untersuchungen.

Im letzten Teil dieser Arbeit fassen wir noch einmal die wichtigsten Punkte und Ergebnisse zusammen und geben einen Ausblick auf mögliche Erweiterungen von LDA+DMFT, wie beispielsweise die schrittweise Berücksichtigung von nichtlokalen Korrelationen, einer dynamischen Coulombwechselwirkung oder Möglichkeiten zur Behandlung des Doublecounting Problems.

Abstract

The study of the electronic properties of correlated systems is a very diverse field and has led to valuable insight into the physics of real materials. In these systems, the decisive factor that governs the physical properties is the ratio between the electronic kinetic energy, which promotes delocalization over the lattice, and the Coulomb interaction, which instead favours localized electronic states. Due to this competition, correlated electronic systems can show unique and interesting properties like the Metal-Insulator transition, diverse phase diagrams, strong temperature dependence and in general a high sensitivity to the environmental conditions.

A theoretical description of these systems is not an easy task, since perturbative approaches that do not preserve the competition between the kinetic and interaction terms can only be applied in special limiting cases. One of the most famous approaches to obtain the electronic properties of a real material is the *ab initio* density functional theory (DFT) method. It allows one to obtain the ground state density of the system under investigation by mapping onto an effective non-interacting system that has to be found self-consistently. While being an exact theory, in practical implementations certain approximations have to be made to the exchange-correlation potential.

The local density approximation (LDA), which approximates the exchange-correlation contribution to the total energy by that of a homogeneous electron gas with the corresponding density, has proven quite successful in many cases. Though, this approximation in general leads to an underestimation of electronic correlations and is not able to describe a metal-insulator transition due to electronic localization in the presence of strong Coulomb interaction.

A different approach to the interacting electronic problem is the dynamical mean-field theory (DMFT), which is non-perturbative in the kinetic and interaction term but neglects all non-local fluctuations. It has been successfully used to study the whole range of weakly to strongly correlated lattice models, including the metal-insulator transition, since even in the relevant dimensions of $d = 2$ and $d = 3$ spatial fluctuations are often small.

The extension of DMFT towards realistic system by the use of DFT has been termed LDA+DMFT and has since then allowed for a significant improvement of the understanding of strongly correlated materials.

We dedicate this thesis to the LDA+DMFT method and the study of the recently discovered iron-pnictide superconductors, which are known to show effects of strong electronic correlations. Thus, in many cases these materials cannot be adequately described by a pure DFT approach alone and provide an ideal case for an investigation of their electronic properties within LDA+DMFT.

We will first review the DFT method and point out what kind of approximations have to be made in practical calculations and what deficits they entail. Then we will give an introduction into the Green's function formalism in the real and imaginary time representation and discuss the resulting consequences like analytic continuation to pave the way for the derivation of the DMFT equations. After that, we will discuss the combination of DFT and DMFT into the LDA+DMFT method and how to set up the effective lattice models for practical calculations.

Then we will apply the LDA+DMFT method to the hole-doped iron-pnictide superconductor KFe_2As_2 , which we find to be a rather strongly correlated material that can only be reasonably described when electronic correlations are treated on a proper level beyond the standard DFT approach. Our results show that the LDA+DMFT method is able to significantly improve the agreement of the theoretical calculation with experimental observations.

Then we expand our study towards the isovalent series of KFe_2As_2 , RbFe_2As_2 and CsFe_2As_2 , which we propose to show even stronger effects of electronic correlations due to an increase in localization of the iron $3d$ orbitals. This assumption is indeed confirmed by our calculations and we also find a significant increase in the incoherence properties along the series, which shows that these systems cannot be described within a Fermi-liquid picture even at lower temperatures.

Finally, we close the circle by reinvestigating the probably best studied system within LDA+DMFT, the cubic perovskite SrVO_3 . In the literature there was an overall agreement that

a low-energy feature below the Fermi level in SrVO_3 is to be interpreted as a lower Hubbard band. In contrast to that we show that oxygen vacancies that are well-known in related materials create a similar feature at the same energy, so that an interpretation of this state purely in terms of a lower Hubbard band is not correct.

Contents

1	Introduction	1
1.1	The problem of interacting electrons	1
1.2	The theoretical approach	2
1.3	Iron-based superconductors	4
2	Density functional theory: advantages and shortcomings	7
2.1	The density functional formalism	7
2.2	The Kohn-Sham equations	9
2.3	The local density approximation	10
2.4	GGA and hybrid functionals	10
2.5	LDA+U	11
3	The Green's function formalism	15
3.1	Introduction	15
3.2	Perturbation theory for the time evolution operator and linear response	16
3.3	Zero temperature Green's functions	20
3.3.1	Real time formulation	20
3.3.2	Real frequency formulation	22
3.3.3	Dyson equation and Selfenergy	24
3.4	Finite temperature Green's function	26
3.4.1	Finite-temperature perturbation theory	30
3.5	Imaginary time Green's functions	33
3.6	Matsubara Green's function	38
3.7	Validity of the periodic imaginary time Green's function	40
3.8	Matsubara frequency summations	46
4	Analytic continuation	51
4.1	Introduction	51
4.2	The Padé approximation	55
4.3	The maximum entropy method	56
4.4	Stochastic analytic continuation	59
4.5	Analytic continuation of general Matsubara functions	62
4.6	Practical implementation	63
5	Electronic correlations	65
5.1	The Hubbard model	67
5.2	Dynamical mean-field theory	68
5.2.1	Weiss mean-field theory	68
5.2.2	The Hubbard model in infinite dimensions	70
5.2.3	Simplifications in infinite dimensions - dynamical mean-field theory	72
5.2.4	Derivation of the DMFT equations - effective Anderson impurity model	74

6	The LDA+DMFT approach	81
6.1	Making the transition to realistic systems	81
6.2	Localized basis for the Green's function	82
6.3	The choice of the energy window	85
6.4	The double counting problem	88
6.5	Multiple correlated atoms	93
6.6	Coulomb matrix	95
6.7	Full charge self-consistency	98
6.8	The complete LDA+DMFT cycle	99
6.9	Observables	101
6.9.1	Quasiparticle weight, lifetime and mass enhancement	102
6.9.2	Band structure and Fermi surface	104
6.9.3	Local spectral function $A(\omega)$	105
7	Effects of electronic correlations in KFe_2As_2	107
7.1	Introduction	107
7.2	Computational details	108
7.3	Results	109
7.3.1	Electronic structure	109
7.3.2	De Haas-van Alphen frequencies	112
7.3.3	Sensitivity analysis	114
7.4	Conclusion	116
8	Strong electronic correlations in $A\text{Fe}_2\text{As}_2$ ($A = \text{K, Rb, Cs}$)	117
8.1	Introduction	117
8.2	Computational details	118
8.3	Results	119
8.3.1	Momentum-resolved spectral function $A(\mathbf{k}, \omega)$	119
8.3.2	Spectral weight at the Fermi level and orbital-resolved electronic filling	120
8.3.3	Spectral function $A(\omega)$	121
8.3.4	Effective masses and quasiparticle lifetimes	122
8.3.5	Nature of the Fe $3d$ wave function	124
8.3.6	Dependence on U and J_H	125
8.3.7	Tight binding analysis	127
8.4	Conclusions	128
9	Interplay of electronic correlations and oxygen vacancies in SrVO_3	131
9.1	Introduction	131
9.2	Computational and experimental details	132
9.3	Results	133
9.3.1	Experimental results	133
9.3.2	Theoretical results	135
9.3.3	Standard LDA+DMFT vs. LDA+DMFT including dynamical screening	137
9.3.4	Comparison of DFT results between different oxygen vacancy configurations	138
9.4	Conclusion	138
10	Summary and Outlook	141
	Appendix	145
	References	164

Chapter 1

Introduction

The concept of electronic correlations is one of the hardest, yet most interesting aspects in the field of theoretical as well as experimental solid state physics. This thesis will investigate the realisations of strong electronic correlations due the Coulomb repulsion between electrons in different materials and theoretical concepts of describing and investigating their effects on physical properties.

In this chapter we will give a short overview over the main aspects of this thesis. We will first introduce the very general problem of how an ensemble of electrons in a solid interacts and what problems arise when we want to investigate the system from the viewpoint of a theoretical physicist.

After that, we will review a special type of materials, namely a class of superconductors in which electronic correlations are important to consider for a correct physical description and interpretation of their properties.

1.1 The problem of interacting electrons

One of the most fundamental reasons why solid state physics is such a diverse field and never seems to stop surprising researchers investigating experimentally and theoretically the properties of solid matter is the complicated interplay and interaction of how the electrons “live” and move in-between and around the atoms of a crystal. These electrons originally belonged to the atoms that are the building block of the material, and when we think bringing single atoms close together to assemble the crystal lattice, these electrons start to “feel” the electrons from other atoms and interact with them. How the electrons interact can be described in mathematical terms by the Coulomb interaction, which makes electrons repel each other, but feel attracted to the atoms of the lattice.

This two-sided form of the interaction in general causes electrons to avoid each other, while at the same time they want to cling close to an atom, causing them to accumulate close together around the atoms and feel each other even more! These conflicting interests give rise to a plethora of many-body effects, ranging from nearly-free electronic systems found in metals to highly correlated insulating systems where the Coulomb repulsion between the electrons becomes so dominant that the electrons in the outer atomic shells completely localize on the atomic sites in order to reduce the repulsive interaction from the other electrons on other atoms as much as possible.

Interestingly, these two extreme cases are the easiest to study, since in these limits *approximations* can be made that allow for a significant simplification of the problem without neglecting any other important effects. For example, in a very good metal the Coulomb repulsion only has a negligible contribution to the total energy compared to the kinetic energy of the electrons, which makes it possible to forget about the electron-electron interaction altogether and describe the system as non-interacting electrons without notable loss of accuracy. On the other hand for insulating systems with localized electrons, the kinetic energy contribution can be often be simplified and the system can be described in terms of a Heisenberg model.

Naturally, most systems found in real life fall in-between these two limits and are thus much harder to investigate, since neither the kinetic energy nor the Coulomb interaction dominates over

the other but rather, they compete with each other. As a result, theoretical approaches to these systems need to be able to treat these two contributions on equal footing if we want to be able to describe physical properties with reasonable accuracy. This thesis is dedicated to a method which follows exactly this approach: the dynamical mean-field theory (DMFT).

This method does not resort to severe approximations of neither the kinetic nor the Coulomb interaction part by assuming one of the limits discussed above, and thus retains the competition between these terms even when both are of equal strength. Instead, it makes approximations about the underlying lattice structure which become more accurate the more neighbours surround the atoms in the lattice. In the most simple cubic lattice, one atom has already $Z = 6$ nearest neighbours, and this number can increase quite quickly like in the face-centered cubic (fcc) lattice structure which has $Z = 12$ nearest neighbours for a given site. As Z increases, it can be shown that the special lattice approximation in DMFT becomes exact in the limit of $Z \rightarrow \infty$.

These aspects make DMFT a very valuable approach to study systems that fall in-between the two limits of free and localized electrons, since the lack of approximation on these two parts fully retains their competition allows for an investigation of the whole range from weak to strong interaction strength. In this thesis we will apply the DMFT method in combination with other well-established theoretical methods, called LDA+DMFT, to realistic systems that fall into the category of intermediate to strong electronic interactions. They already show manifestations of strong Coulomb interaction effects but are impossible to describe within methods that drastically approximate the kinetic energy contributions. These systems include the family of the so-called iron-pnictide superconductors, that are a recently discovered and promising type of superconducting materials, as well as well-known transition metal oxides that still pose a substantial challenge to a theoretical description.

In the coming sections we will introduce the fundamentals of the method and the theoretical model we will employ in this thesis in more detail. We will also provide an introduction into the rather new field of iron-pnictide superconductors and their specific properties which makes them well-suited for a study within the LDA+DMFT method.

1.2 The theoretical approach

The main object that describes the interaction of electrons and nuclei in a solid is the many-body Hamiltonian given as

$$\begin{aligned}
 H &= T_{\text{ion}} + T_e + V_{e-e} + V_{e-\text{ion}} + V_{\text{ion-ion}} \tag{1.2.1} \\
 &= - \sum_{i=1}^{N_I} \frac{\hbar^2}{2M_i} \nabla_{\mathbf{R}_i}^2 - \sum_{i=1}^{N_e} \frac{\hbar^2}{2m_i} \nabla_{\mathbf{r}_i}^2 \\
 &\quad - \frac{1}{8\pi\epsilon_0} \sum_{\substack{i,j=1 \\ i \neq j}}^{N_e} \frac{e^2}{|\mathbf{r}_i - \mathbf{r}_j|} - \frac{1}{4\pi\epsilon_0} \sum_{i,j=1}^{N_I, N_e} \frac{e^2 Z_i}{|\mathbf{R}_i - \mathbf{r}_j|} - \frac{1}{8\pi\epsilon_0} \sum_{\substack{i,j=1 \\ i \neq j}}^{N_I} \frac{e^2 Z_i Z_j}{|\mathbf{R}_i - \mathbf{R}_j|}. \tag{1.2.2}
 \end{aligned}$$

It is composed of the kinetic energy contribution of N_I ions T_{ion} and N_e electrons T_e , and the interaction between them. The interacting potential is given by the Coulomb potential, where V_{e-e} is the electron-electron, $V_{e-\text{ion}}$ the electron-ion and $V_{\text{ion-ion}}$ the ion-ion interaction. The Hamiltonian in Eq. (1.2.2) describes the full physics of the system exactly (as far as we know). Though, it cannot be solved due to the sheer number of coupled equations, since $N_I, N_e \sim 10^{23}$. Even for small systems like the hydrogen molecule with two electrons and protons finding the Eigenvalues and Eigenvectors of the Hamiltonian is notoriously difficult due to the fact that the kinetic energy operator and the Coulomb operator cannot be diagonalized by the same set of Eigenstates. Therefore, we will always have to rely on some kind of approximations that simplify the Hamiltonian enough to solve it but retain the most important physical features.

The very first approximation that serves as the starting point for most other further investigations is to neglect the kinetics of the ions, called Born-Oppenheimer approximation (see Chapter 2). Be-

cause the mass of the ions M_i is about three orders of magnitude larger than that of the electrons m_i , the kinetic terms of the ions is neglected, and the ion-ion interaction reduces to a constant, which is usually dropped. With this, one arrives at the simpler Hamiltonian

$$H = T_e + V_{e-e} + V_{e-ion} \quad (1.2.3)$$

$$= - \sum_{i=1}^{N_e} \frac{\hbar}{2m_i} \nabla_{\mathbf{r}_i}^2 - \frac{1}{8\pi\epsilon_0} \sum_{\substack{i,j=1 \\ i \neq j}}^{N_e} \frac{e^2}{|\mathbf{r}_i - \mathbf{r}_j|} - \frac{1}{4\pi\epsilon_0} \sum_{i,j=1}^{N_I, N_e} \frac{e^2 Z_i}{|\mathbf{R}_i - \mathbf{r}_j|}. \quad (1.2.4)$$

One of the most famous and highly successful approaches to obtain a solution of this Hamiltonian is density functional theory (DFT) [1], which we will discuss in more detail in Chapter 2. Instead of calculating the Eigenvectors directly, DFT reformulates the Hamiltonian in terms of the electronic density, which fundamentally reduces the complexity of the problem. While being in principle an exact theory and parameter free (*ab initio*), we have to pay the price of loosing all information about the excited states, since only the ground state properties can be accessed in DFT. In practice, approximations to the electron-electron interactions will be made in DFT, which generally underestimate the localized nature of electrons in correlated materials.

Another approach is to map the interacting Hamiltonian onto an effective lattice model and (usually) to apply approximations to both the kinetic and interaction terms which are supposed to have only little impact on the physical properties. The most well-known lattice model is the so-called Hubbard model [2–4]. Introducing a basis of local orbitals $|\chi_{im\sigma}\rangle$, where i labels the atomic sites of the crystal, m labels the atomic orbitals of the electrons and σ the spin degrees of freedom, we can rewrite the Hamiltonian in Eq. (1.2.4) in second quantization in the following form

$$H = \sum_{ij, mm', \sigma} t_{mm'}^{ij} c_{im\sigma}^\dagger c_{jm'\sigma} + \frac{1}{2} \sum_{\substack{ijkl \\ mm'nn', \sigma\sigma'}} V_{mnm'n'}^{ijkl} c_{im\sigma}^\dagger c_{jn\sigma'}^\dagger c_{ln'\sigma'} c_{km'\sigma}, \quad (1.2.5)$$

where $t_{mm'}^{ij} = \langle \chi_{im\sigma} | T_e + V_{e-ion} | \chi_{jm'\sigma} \rangle$ is the matrix element of the kinetic energy and the background potential generated by the ions, which is also called hopping amplitude, since it corresponds to the annihilation of an electron at site j and recreation at site i , with a possible change of orbitals m' to m . Furthermore, $V_{mnm'n'}^{ijkl} = \langle \chi_{im\sigma} \chi_{jn\sigma'} | V_{e-e} | \chi_{km'\sigma} \chi_{ln'\sigma'} \rangle$ are the matrix elements of the two-particle operator corresponding to the Coulomb interaction.

No simplification has been made so far, and we still face a problem with an infinite number of parameters $t_{mm'}^{ij}$, $V_{mnm'n'}^{ijkl}$. To reduce the complexity of the Hamiltonian, the Coulomb interaction can be assumed to be a short-range local interaction

$$V_{mnm'n'}^{ijkl} = U_{mnm'n'} \delta_{ij} \delta_{jk} \delta_{kl}. \quad (1.2.6)$$

This approximation is often not a severe one, since the site-offdiagonal matrix elements $V_{mnm'n'}^{ijkl}$ are usually small, because the product of the local orbitals $\chi(r) \sim e^{-r}$ with the Coulomb term $V(r) \sim 1/r$ falls off very quickly as a function of distance (see also discussion in Chapter 5). Depending on the specific type of orbitals, many other orbital-offdiagonal terms can be shown to either vanish by symmetry or be very small. One of the most widely used approximations is to keep only the density-density terms of the interaction, *i.e.* $U_{mnm'n'} = U_{mn} \delta_{mm'} \delta_{nn'}$. With this approximation, one arrives at the simplified Hubbard model

$$H = \sum_{ij, mm', \sigma} t_{mm'}^{ij} c_{im\sigma}^\dagger c_{jm'\sigma} + \frac{1}{2} \sum_{\substack{i \\ mn, \sigma\sigma'}} U_{mn} n_{im\sigma} n_{in\sigma'}, \quad (1.2.7)$$

where $n_{im\sigma} = c_{im\sigma}^\dagger c_{im\sigma}$ is the particle number operator. This is the final form of the Hamiltonian that will be used to investigate real materials in this thesis. By appropriately choosing the parameters $t_{mm'}^{ij}$ and U_{mn} of the model, a good representation of the real system can be usually achieved. In

this thesis we will use the so-called LDA+DMFT method to obtain the necessary input parameters and solve the effective Hamiltonian in Eq. (1.2.7).

Even though we already simplified the original Hamiltonian in Eq. (1.2.2) quite extensively, Eq. (1.2.7) still cannot be solved analytically except in one dimension [5]. For that reason we have to resort to further approximations and numerical methods. As already mentioned, in this thesis we will be interested in materials that can neither be described in terms of almost free electrons, where the kinetic energy dominates $t_{mm'}^{ij}/U_{mn} \rightarrow \infty$, nor as localized systems, where the Coulomb energy dominates $t_{mm'}^{ij}/U_{mn} \rightarrow 0$. Therefore, perturbative theories on the kinetic or interacting term are ruled out. Instead, we will employ the dynamical mean-field theory, which is non-perturbative in both $t_{mm'}^{ij}$ and U_{mn} . It relies on the observation by Metzner and Vollhardt [6], that in the limit of infinite dimensions, or infinite number of nearest-neighbours, the Selfenergy of the interacting electronic system becomes a purely local quantity where all site-offdiagonal terms vanish.

This finding leads to a significant simplification of the original Hubbard model, which in this limit can be exactly mapped onto a single impurity problem embedded in a non-interacting bath, as shown by Georges and Kotliar [7]. All spatial degrees of freedom can be integrated out and only temporal fluctuations remain, which makes it possible to use efficient numerical methods like continuous-time quantum Monte Carlo [8, 9], that can obtain an exact solution of the $d \rightarrow \infty$ impurity model (within numerical accuracy). This method will allow us to study the whole range of the competition between the kinetic energy and interaction strength, since no further approximation is made on these terms. For real systems we loose the momentum-dependence of the Selfenergy, which is supposed not to be a severe approximation in the relevant case of three dimensions. All the systems we are going to study either show a cubic perovskite crystal structure with $Z = 6$ nearest-neighbours or the face-centered cubic lattice structure with $Z = 12$, where the local approximation is known to hold quite well [10].

In addition to DMFT, which is used to solve the Hamiltonian, we will employ DFT to obtain an *ab initio* effective Hubbard model by a projection technique as explained in Chapter 6.2. This combination of DFT for setting up a realistic Hubbard model and DMFT for solving it, is termed LDA+DMFT (local density approximation + dynamical mean-field theory).

First, we will give a brief introduction of DFT in Chapter 2, why it is not able to describe strongly correlated systems adequately and possibilities for improvements by hybrid functionals or LDA+U methods. As the next step we will introduce the formalism of Green's function in Chapter 3 in the real and imaginary time formulation, and the resulting peculiarities like Matsubara frequency summations or the problem of analytic continuation in Chapter 3.8 and 4. Finally, we will discuss the DMFT derivation and the resulting equations in Chapter 5.2, and how they can be combined with DFT to obtain the LDA+DMFT method in Chapter 6.

1.3 Iron-based superconductors

When the first iron-based superconductor $\text{LaFeAsO}_{1-x}\text{F}_x$ with a $T_c = 26$ K [11, 12] was discovered in 2006, it led to the beginning of a new and quickly evolving field of theoretical and experimental research of these materials. The finding of these type of superconductors actually came as a surprise, since at that time it was assumed that iron is in general detrimental to superconductivity since doping it into cuprate superconductors quickly reduces the critical temperature [13]. Though, shortly after the discovery new iron-based materials could be synthesized that reached critical temperatures up to $T_c \approx 56$ K [14] and there are indications that even $T_c > 100$ K might be possible in single-layered materials [15].

All members of the iron-pnictide superconductor family share the same structural element of an iron-pnictide or iron-chalcogenide layer, where the iron atoms form a square lattice are surrounded by a tetrahedron of pnictogen or chalcogen atoms. These layers are then stacked with potentially other atomic species in-between to build up the whole crystal. Possible realizations are for example no ions in-between the layers like in FeSe, called 11 family, or alkali ions between the layers like in LiFeAs, which is called the 111 family. A variation of the latter is the 122 family, where the

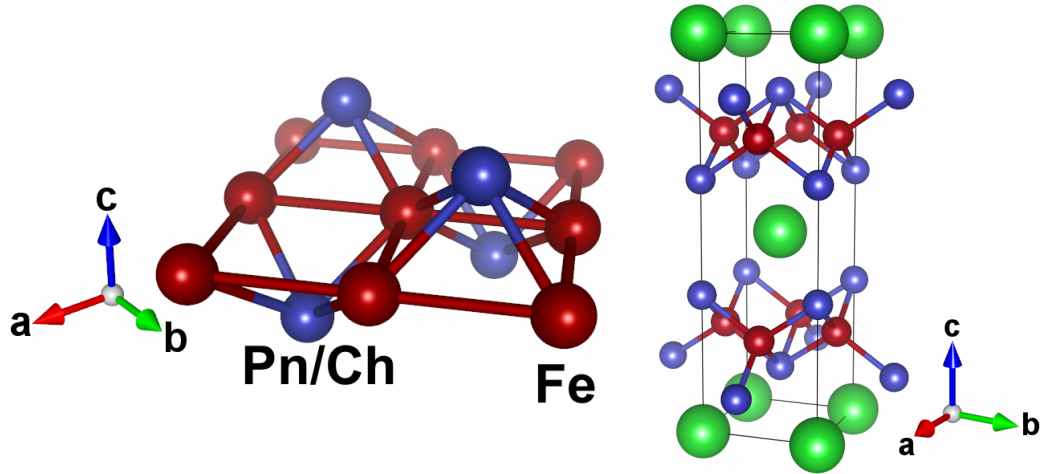


Figure 1.1: The basic structure of iron-based superconductors is a rectangular grid of iron-pnictide or iron-chalcogenide layers (shown on the left side). In this layer, every iron atom is surrounded by a tetrahedron of pnictide or chalcogenide atoms. A typical representative of the 122-family is shown on the right side, where the iron layers are alternatively stacked with other atoms in between the layers. The most prominent examples of the 122-family are BaFe_2As_2 , CaFe_2As_2 or KFe_2As_2 (figure generated with [16]).

unit cell contains two iron-layers with one layer flipped like in BaFe_2As_2 . Furthermore, the 1111 family features more complex layers that are sandwiched between the iron layers like in LaFeAsO . In Fig. 1.1 we show the structure of the 122 member BaFe_2As_2 and the respective iron layer that is characteristic for all the iron based materials.

In this thesis we will put a special focus on the 122 family, specifically the hole-doped compounds that can be obtained from the parent system BaFe_2As_2 by substituting either potassium, rubidium or caesium into the barium site, which show many features of a strongly correlated electronic system.

The iron-based superconductors are three-dimensional metallic systems under ambient conditions with nominally 6 electrons occupying the Fe $3d$ shell. Since the tetrahedral environment of each iron is not a perfect tetrahedron, the iron $3d$ orbitals split only approximately into the two-fold degenerate e_g and three-fold degenerate t_{2g} orbitals. Thus, in the tetragonal phase of the 122 members only the Fe $3d_{xz}$ and $3d_{yz}$ orbitals are exactly degenerate.

In general all Fe $3d$ orbitals have finite weight at the Fermi level, which causes the physics of these systems to be of multi-orbital nature. Due to the partial hybridization with the pnictogen/chalcogen atoms above and below the iron layer, these atoms also contribute to a small degree with $4p$ orbital character around the Fermi level. Though, the most weight at the Fermi level is originating from the Fe $3d_{xy}$, $3d_{xz}$ and $3d_{yz}$ orbitals. In the parent compound up to three bands cross the Fermi level at the Γ point that form Fermi surface pockets of hole-like character, with usually two two additional pockets at the M point of electron-like character.

In the iron-based superconductors the Coulomb repulsion between the electrons occupying the Fe $3d$ orbitals plays an important role for the electronic properties, especially when the system is brought from the nominal $3d^6$ configuration closer to half-filling by hole doping.

While DFT is able to describe the electronic structure of these systems to some extent qualitatively correct [17], strong electronic correlations give rise to certain features that cannot be explained via a DFT approach alone. The most direct comparison of the electronic structure is provided by optical spectroscopy [18], photoemission spectroscopy [19–21] or quantum oscillation experiments [22–26], which can vary from a satisfactory agreement to significant deviations. From these results one generally observes that the neglect of strong correlations in DFT leads to an underesti-

mation of the effective electron mass, bandwidth renormalization, differing sizes of Fermi surface pockets or even qualitatively wrong Fermi surfaces like in LaFePO [27].

Due to this shortcomings of DFT, an improved treatment of the electronic correlations via LDA+DMFT has proven to be quite successful in many materials [27–32]. Promising results and significant improvements of the agreement with experiments have been obtained by the inclusion of aspects that are simply out of the scope of DFT, like possible non-Fermi liquid behaviour [28, 29, 33–35] or the double-faced nature of the Hund’s coupling J_H , which can lead to very different characteristics of correlated systems [33–38]. Especially the latter aspect is still under active discussion [38–41], since the Hund’s coupling J_H can, dependent on the orbital filling, on the one hand render a moderately correlated system even more correlated and bad metal-like, while on the other hand it can reestablish metallic behavior in a highly correlated system [38, 41].

In this thesis we will apply the LDA+DMFT method to the strongly correlated hole-doped 122 series $A\text{Fe}_2\text{As}_2$ ($A=\text{K, Rb, Cs}$) to study especially the effects of electronic correlations that are not captured in DFT, like effective mass enhancements, electronic structure and Fermi surface modifications introduced by correlations, and non-Fermi liquid behavior in combination with the effect of the Hund’s coupling J_H .

The hole doped 122 series is especially interesting for a comparative study, since the isovalent doping by K, Rb and Cs corresponds to an effective negative chemical pressure that leads to an expansion of the unit cell, that in turn increases the localization and thus the correlation of the Fe $3d$ orbitals. Manifestations of correlations were already suggested on the experimental side in form of a coherence-incoherence transition [42, 43] and strongly enhanced Sommerfeld coefficient [42, 44–48], which is proportional to the effective electronic mass. These observations seem to indicate that these hole-doped systems are one of the most strongly correlated 122 iron-pnictide superconductors.

Theoretical investigations seem to confirm the strong electronic correlations in KFe_2As_2 [28, 40, 42, 49]. While there exist LDA+DMFT calculations for KFe_2As_2 [28, 49] that show the effects of correlations on the Fermi surface and susceptibility, the temperature dependence and influence of the Hund’s coupling J_H have not been studied in detail in this system so far.

Therefore, we will devote Chapter 7 solely to the KFe_2As_2 system and our results we obtained within LDA+DMFT for the band structure, Fermi surface and the so-called de Haas-van Alphen frequencies, which give a measure about the extremal cross-sections of the Fermi surface pockets. Chapter 8 will then continue to investigate the hole-doped 122 series $A\text{Fe}_2\text{As}_2$ ($A=\text{K, Rb, Cs}$) with a special focus on correlation induced non-Fermi liquid behavior, where the lifetime of the quasi-particle excitations is significantly reduced, and the influence of the Hund’s coupling J_H , where our LDA+DMFT results for RbFe_2As_2 and CsFe_2As_2 are the first in the literature. In Chapter 9 we will close the cycle and come back to one of the best studied systems within LDA+DMFT, namely SrVO_3 . While basically all experimental and theoretical groups assumed for more than a decade to correctly identify a low-energy spectral feature as a correlation induced Hubbard band [50–57], we will show that the interpretation of this feature solely in terms of incoherent spectral weight is not correct.

Chapter 2

Density functional theory: advantages and shortcomings

One of the most successful methods for theoretical investigation of the properties of solids is the density functional theory (DFT). It is probably one of the most well-known and most often applied approaches, finding wide use in physics, chemistry and material sciences. Its success is not only founded on its accuracy of calculating ground state energies, but also on its versatility, which makes it possible to determine many observable properties of solids, like lattice parameters, elastic constants, magnetization or, to some extent, absorption and excitation spectra, and its generality of being able to be applied to basically any solid material.

2.1 The density functional formalism

We will now give a short overview over the most important equations and approximations that are applied in DFT, and possible weaknesses arising from them. In this section we will follow the ideas of the excellent review on DFT by Cottenier [58].

A solid consists of a collection of electrons that move in a usually, but not necessarily, regular lattice of positively charged ions. The only terms that enter the energetics of the system are given by the kinetic energy of the electrons and ions, and the Coulomb interaction between them. For a usual solid the number of electrons and ions is of the order of $\sim 10^{23}$, making it obviously impossible to be solved exactly right from the start.

Nonetheless, we can exactly write down the physical equations that govern the evolution and energetics of such many-body systems. Assuming that only the Coulomb interaction is the main interaction between all particles involved, the Hamiltonian for any general solid is given by

$$\begin{aligned} H &= T_{\text{ion}} + T_e + V_{e-e} + V_{e-\text{ion}} + V_{\text{ion-ion}} & (2.1.1) \\ &= - \sum_i \frac{\nabla_{\mathbf{R}_i}^2}{2M_i} - \sum_i \frac{\nabla_{\mathbf{r}_i}^2}{2m_i} \\ &\quad - \sum_{ij} \frac{Z_i}{|\mathbf{R}_i - \mathbf{r}_j|} - \frac{1}{2} \sum_{i \neq j} \frac{1}{|\mathbf{r}_i - \mathbf{r}_j|} - \frac{1}{2} \sum_{i \neq j} \frac{Z_i Z_j}{|\mathbf{R}_i - \mathbf{R}_j|}, & (2.1.2) \end{aligned}$$

using atomic units, where $e = m_i = \hbar = \frac{1}{4\pi\epsilon_0} = 1$. m_i , M_i are the electronic and ionic mass, and \mathbf{r}_i , \mathbf{R}_i are the electronic and ionic positions, respectively. The first two terms correspond to the kinetic energies, while the last three terms describe the Coulomb interaction between the particles.

The first approximation that we will apply to the full Hamiltonian in Eq. (2.1.2) is the so-called Born-Oppenheimer approximation. Noticing that the ionic mass is usually three orders of magnitude larger than the electronic mass $M_i \gg m_i$, we know that the dynamics of the ions will much slower

than that of the electrons. Therefore, the ions are basically fixed at their lattice sites on the timescale of the electronic dynamics and we can neglect the kinetic part of the ions without introducing a significant error to the dynamics of the system. Without the kinetic part, $V_{\text{ion-ion}}$ is just a constant since the ionic positions will not change over time and can be dropped.

The resulting Hamiltonian is now much simpler

$$H = T_e + V_{e-e} + V_{e\text{-ion}} \quad (2.1.3)$$

$$= - \sum_i \frac{\nabla_{\mathbf{r}_i}^2}{2m_i} - \frac{1}{2} \sum_{i \neq j} \frac{1}{|\mathbf{r}_i - \mathbf{r}_j|} - \sum_{ij} \frac{Z_i}{|\mathbf{R}_i - \mathbf{r}_j|}, \quad (2.1.4)$$

but still too complicated to be solved exactly. The first two terms T_e, V_{e-e} are completely universal and independent of the particular solid. All information about the material is encoded in $V_{e\text{-ion}}$ and the complicated interaction between a moving electron and moving ion has now been replaced by the much simpler problem of an electron moving in a static background potential.

The big problem of solving the Hamiltonian in Eq. (2.1.4) is that it is completely intractable even if we could devise a numerical procedure to solve it due to its complexity. Its Eigenfunctions $|\psi_n(\mathbf{r})\rangle$ would be given as a linear combination of antisymmetric products of N -electron wave functions, where $N \approx 10^{23}$, which makes any approach that computes $|\psi_n(\mathbf{r})\rangle$ even approximately completely unrealistic.

A possible way out of this dilemma was proposed by Hohenberg and Kohn, who suggested that in the ground state of the system the ground state many-body wave function $|\psi_0(\mathbf{r})\rangle$ is not necessary to describe all properties of the system but only the ground state density $\rho_0(\mathbf{r})$. From this idea they formulated two theorems [1]:

1. There exists a unique mapping between the ground state density $\rho_0(\mathbf{r})$ of a many-body electronic system and the external potential $V_{e\text{-ion}}$. Therefore, the ground state expectation value of any operator is a unique functional of the ground state density

$$\langle \psi_0 | \mathcal{O} | \psi_0 \rangle = O[\rho_0]. \quad (2.1.5)$$

2. The ground state total energy functional $\langle \psi | H | \psi \rangle = E[\rho]$ is given by

$$E[\rho] = \langle \psi | (T_e + V_{e-e}) | \psi \rangle + \langle \psi | V_{e\text{-ion}} | \psi \rangle \quad (2.1.6)$$

$$= F_{\text{HK}}[\rho] + \int \rho(\mathbf{r}) V_{e\text{-ion}}(\mathbf{r}) d\mathbf{r}, \quad (2.1.7)$$

and $E[\rho]$ reaches its minimal value of the ground state energy when $\rho = \rho_0$. The Hohenberg-Kohn functional $F_{\text{HK}}[\rho]$ is universal and contains the kinetic and potential energy contribution of the electrons.

The substitution of the ground state density as the main variable of interest provides a huge simplification, since we now only need to know one single function $\rho(\mathbf{r})$, instead of the much larger and complicated ground state wave function. The Hohenberg-Kohn theorems tell us that the ground state density thus contains exactly as much information as the ground state wave function, so that no information is lost. Though, it is important to point out that this statement is only made for the ground state! For all other states no statement is made about whether they can be substituted by the corresponding density without loss of information. The only information we have is that the density from all other states will have a larger energy $E[\rho]$ than ρ_0 . Since $E[\rho]$ is calculated from the density, we even do not know whether it is equal to $\langle \psi | H | \psi \rangle$ for any other state than the ground state. Therefore, the Hohenberg-Kohn theorems in general do not allow us to draw conclusions about excited states.

2.2 The Kohn-Sham equations

The remaining step to the determination of the ground state density in practice was provided by Kohn and Sham [59], who showed that ρ_0 can be obtained by a related but fictitious non-interacting electron system. For this, one separates the total energy functional in the following way

$$E[\rho] = T_0[\rho] + V_H[\rho] + \underbrace{V_x[\rho] + V_c[\rho]}_{V_{xc}[\rho]} + V_{e-ion}[\rho], \quad (2.2.1)$$

where $T_0[\rho]$ is the functional for the kinetic energy of a non-interacting electron gas, $V_H[\rho]$ is the Hartree contribution given by

$$V_H[\rho] = \frac{1}{2} \int d\mathbf{r} \int d\mathbf{r}' \frac{\rho(\mathbf{r})\rho(\mathbf{r}')}{|\mathbf{r} - \mathbf{r}'|}, \quad (2.2.2)$$

and $V_x[\rho], V_c[\rho]$ are the exchange and correlation contributions that are unknown at this point. They contain all the difficult contributions of exchange and correlation that are not included by the simple Hartree term, which contains only the static Coulomb energy for the electronic density.

Eq. (2.2.1) is nothing but the original total energy functional in Eq. (2.1.7), rewritten in a slightly different way. The important observation is though that it has the same form of a non-interacting electron gas subject to the two effective potentials $V_{xc}[\rho]$ and $V_{e-ion}[\rho]$. The Hamiltonian that would correspond to such energy functional is called the Kohn-Sham Hamiltonian H_{KS} and is given by

$$H_{KS} = - \sum_i \frac{1}{2m} \nabla_i^2 + \int d\mathbf{r}' \frac{\rho(\mathbf{r}')}{|\mathbf{r} - \mathbf{r}'|} + v_{xc} + v_{e-ion}, \quad (2.2.3)$$

where the exchange-correlation and external potential are given by

$$v_{xc} = \frac{\delta V_{xc}[\rho]}{\delta \rho} \quad \text{and} \quad v_{e-ion} = \frac{\delta V_{e-ion}[\rho]}{\delta \rho}. \quad (2.2.4)$$

We can now reformulate the original problem of finding the ground state density by solving the effective Kohn-Sham Hamiltonian: The exact ground state density $\rho_0(\mathbf{r})$ of the original N -electron system is given by

$$\rho_0(\mathbf{r}) = \sum_{i=1}^N \phi_i^*(\mathbf{r})\phi_i(\mathbf{r}), \quad (2.2.5)$$

where the Kohn-Sham wave functions $\phi_i(\mathbf{r})$ are the N lowest-energy Eigenvectors of the effective non-interacting Kohn-Sham Hamiltonian

$$H_{KS}\phi_i = \epsilon_i\phi_i. \quad (2.2.6)$$

This result is now a significant simplification of the original Hamiltonian (2.1.4), which describes interacting electrons moving in a background potential V_{e-ion} . To obtain the same ground state density, we can instead solve Eq. (2.2.6), which describes *non-interacting* electrons moving in an effective potential that depends on the electronic density itself. By this, we have completely avoided the problem of dealing with the complicated electron-electron interaction due to the Coulomb potential.

As a result, the Hamiltonian to diagonalize now depends on the solution, namely the density ρ which defines the Hartree and the exchange-correlation term in Eq. (2.2.3). Therefore, we have obtained a self-consistency relation where we do not know the equation to solve before we have obtained its solution. We first have to guess an initial $\rho_0(\mathbf{r})$, solve the resulting H_{KS} for its Eigenfunctions, obtain the solution $\rho_0(\mathbf{r})$, update the Hartree and the exchange-correlation term and solve the new H_{KS} again until the density is converged. Then we have obtained Kohn-Sham wave function $|\phi_i\rangle$ that generate a density that is consistent with H_{KS} .

It is important to note that the Kohn-Sham wave functions $|\phi_i\rangle$ are not the Eigenfunctions of the original interacting electron problem. Even the $|\phi_i\rangle$ that generate the ground state density ρ_0 are not the ground state, since they correspond to a system of non-interacting electrons. Therefore, also the Eigenenergies ϵ_i are not the Eigenvalues of the true system, though, it is approximately possible to identify certain Kohn-Sham energies to ionization energies, known as the (DFT-)Koopman's theorem [60, 61]. This is very different to the Green's function formalism which we will discuss in Chapter 3, where the concept of excitations of the ground state is properly incorporated from the very beginning.

2.3 The local density approximation

So far, apart from the Born-Oppenheimer approximation the whole scheme we devised for obtaining the ground state density for an interacting electronic system was exact. This is mostly due to the fact that we have put all unknowns about the exchange and correlations arising from the interactions into $V_{xc}[\rho]$. This is where approximations have to be made, since we do not know the form of the exchange-correlation functional.

The most famous approximation to the exchange-correlation functional is the local density approximation (LDA) [62], which postulates that the exchange-correlation functional is given by

$$E_{xc}^{\text{LDA}} = \int \rho(\mathbf{r}) \epsilon_{xc}(\rho(\mathbf{r})) d\mathbf{r}, \quad (2.3.1)$$

where $\epsilon_{xc}(\rho(\mathbf{r}))$ is the exchange-correlation energy of the homogeneous electrons as a function of the density ρ , which is known numerically. E_{xc}^{LDA} is completely local in the sense that the energy contribution of the energy at each point \mathbf{r} only depends on \mathbf{r} via ϵ_{xc} , and not on the neighbouring density. This form assumes that the density of the real system can be locally approximated to be constant and the exchange-correlation energy is therefore given by the homogeneous electron gas with the corresponding density. Thus, by construction we can expect LDA to be a reasonable approximation for systems with a homogeneous or slowly varying density $\rho(\mathbf{r})$. This is fulfilled for systems where the electrons are rather delocalized and weakly correlated (for a more rigorous definition of correlations see Chapter 5).

For systems where the electrons show some degree of localization on the atomic sites like in correlated materials that are close to an insulator transition, the approximation of a slowly varying density is significantly violated. This usually leads to a severe underestimation of the electronic correlation effects, where some insulating materials are actually predicted to be metallic in DFT like in nickel and manganese oxides [63].

Therefore, improvements to the approximations applied to E_{xc}^{LDA} are the defining factor for improving the accuracy and predictive power of DFT. Possible extensions to the LDA have been discussed, which are either based on the improvement of the calculation of the exchange-correlation functional itself, like accounting also for derivatives in the charge density, or by calculating correlation energies by a specialized approach and adding them to the DFT functional. Of these approaches we will now shortly discuss the most popular method, the generalized gradient approximation (GGA) and other hybrid functionals, as well as the LDA+U method. In Chapter 5.2 and 6 we will also discuss the more sophisticated approach of LDA+DMFT, which will be the main focus of this thesis and can be seen as an extension of the LDA+U method.

2.4 GGA and hybrid functionals

The first step of improving the LDA functional, which is only dependent on the value of the density at a specific point \mathbf{r} in space, is to include the next term in the Taylor series of the functional by considering also a dependency on the derivative of the density. This approximation is called generalized gradient approximation (GGA) [64], which respects the linear term of the change of the density at

the given position \mathbf{r} . The exchange-correlation functional is then of the form

$$E_{xc}^{\text{GGA}} = \int \rho(\mathbf{r}) \epsilon_{xc}(\rho(\mathbf{r}), \nabla \rho(\mathbf{r})) d\mathbf{r}. \quad (2.4.1)$$

While GGA in practice usually improves on LDA, it still retains its local nature since its non-locality is restricted only to an infinitesimal area around position \mathbf{r} that defines the derivative of the density.

The next improvements are so-called meta GGA's, which include also the second derivative of the density [65–67]. A famous version is Perdew's TPSS functional [68], but the usage of meta GGA's in practice not very common.

A slightly different approach is taken by the so-called hybrid functionals [69, 70], which include some portion of the exact exchange from Hartree-Fock theory

$$E_x^{\text{HF}} = -\frac{1}{2} \sum_{m,n} f_n f_m \int d\mathbf{r} \int d\mathbf{r}' \frac{\phi_m^*(\mathbf{r}) \phi_n(\mathbf{r}) \phi_n^*(\mathbf{r}') \phi_m(\mathbf{r}')}{|\mathbf{r} - \mathbf{r}'|}, \quad (2.4.2)$$

which is expressed in terms of the Kohn-Sham wave function rather than the density. Therefore, it only implicitly depends on the density. The different hybrid functionals mostly differ in the amount of exact exchange that is mixed into the exchange-correlation energy. The weight can be determined by fitting to experimental data or can also be fixed by so-called adiabatic connection functionals [71, 72].

The PBE0 functional [73] includes the exact exchange with a ratio of 1 : 3, *i.e.* in combination with GGA

$$E_{xc}^{\text{PBE0}} = \frac{1}{4} E_x^{\text{HF}} + \frac{3}{4} E_x^{\text{GGA}} + \frac{1}{4} E_c^{\text{GGA}}. \quad (2.4.3)$$

Another possibility is the B3LYP functional [70, 74], which is obtained from a parameter fit to many simple molecules. It has the form

$$E_{xc}^{\text{B3LYP}} = E_x^{\text{LDA}} + a_0 (E_x^{\text{HF}} - E_x^{\text{LDA}}) + a_x (E_x^{\text{GGA}} - E_x^{\text{LDA}}) + E_c^{\text{LDA}} + a_c (E_c^{\text{GGA}} - E_c^{\text{LDA}}), \quad (2.4.4)$$

where $a_0 = 0.2$, $a_x = 0.72$ and $a_c = 0.81$. The reliance on experimental input and chosen fitting parameters in principle takes away the *ab initio* character of DFT.

In general hybrid functionals are found to perform better than the standard LDA or GGA functionals with respect to binding energies or band gaps. For the description of solids the inclusion of the exact exchange is questionable, since the exact exchange hole in a periodic lattice is much more extended compared to molecules or single atoms but including interactions in a solid, the long-ranged tails of the exchange hole are efficiently screened. Therefore, the long-range part of the exact exchange should be mixed into the exchange-correlation functional with a smaller ratio than the short-range part, which is taken into account for example in the HSE functionals [75, 76]. As a result, hybrid functionals are not always more accurate than standard LDA, since in LDA parts of the underestimated long-ranged contribution of the exchange already cancel with similar overestimated contributions from correlations that are taken into account in LDA [77].

2.5 LDA+U

The most prominent deficiency of DFT and the local density approximation is the failure to describe strongly correlated systems and their the famous hallmark of the Mott-insulator transition. In contrast to band insulators that originate from closed electronic shells, the insulating ground state in Mott insulators arises from the strong Coulomb repulsion between the electrons, which forces them to localize on the atomic sites in atomic-like local orbitals [78]. This state is a true many-body phenomena, which cannot be described by a Slater-determinant of single-particle states, which is the reason why also standard Hartree-Fock fails to describe the Mott-insulator transition.

The LDA and GGA functionals are also unable to capture these insulating states by construction, being based on the exchange-correlation energy of a homogeneous electron gas. In the Mott-insulator, the electrons are localized on the atomic sites, which renders the electronic density $\rho(\mathbf{r})$ highly inhomogeneous and almost as Delta function-like, centered on the atomic sites. Similarly, also the intermediate regime where the electrons show some degree of localizations and a higher “effective mass” due to the electronic correlations cannot be sufficiently described in a local density approximation.

Instead of directly improving the DFT functionals, the idea of the LDA+U method utilizes a completely different approach to include strong electronic correlations. This is done by considering the so-called Hubbard model [2–4] that explicitly takes into account the competition between the kinetic and Coulomb energy (the Hubbard model will be discussed in more detail in Chapter 5.2). In its simplest form, the Hubbard Hamiltonian describes electrons in a single local atomic orbital on a lattice and is given by

$$H = \sum_{\langle i,j \rangle, \sigma} t_{ij} c_{i\sigma}^\dagger c_{j\sigma} + U \sum_i n_{i\uparrow} n_{i\downarrow}, \quad (2.5.1)$$

where $c_{i\sigma}^\dagger, c_{i\sigma}$ are the creation/annihilation operators of an electron on site i with spin σ . t_{ij} is the hopping amplitude to the nearest neighbouring sites, indicated by the summation over $\langle i, j \rangle$ and U is the effective Coulomb interaction that raises the energy if two electrons of opposite spin occupy the same site.

This model is able to describe the metal-insulator transition [79–81] for large values of U/t_{ij} , *i.e.* when the Coulomb interaction is much larger than the kinetic contribution. For $U/t_{ij} \ll 1$, the ground state corresponds to that of free electrons with the dispersion given by the Fourier transform of the hopping amplitudes t_{ij} . On the other hand, for $U/t_{ij} \gg 1$ the ground state at half filling corresponds to each atomic site being occupied by exactly one electron since it minimizes the total energy. In this case the system is insulating because electrons cannot hop to neighbouring sites due to the energy barrier U . Such insulating state at half filling is usually impossible to obtain within the local density approximation and instead would predict the system to be metallic.

Therefore, the case of weak Coulomb interactions $U/t_{ij} \ll 1$ is usually well described within the usual approximations to the DFT exchange-correlation potentials, since the electronic wave functions are close to that of free particles and thus create a very homogeneous electronic density. The opposite case $U/t_{ij} \gg 1$, leading to a very inhomogeneous density, is the problematic one.

LDA+U is one of the simplest approaches of combining standard DFT with a more sophisticated treatment of the correlation part of the exchange-correlation potential [63, 82–84]. It is based on the mapping of the system under consideration onto an effective Hubbard model, solving the model and adding the correlation terms back into the DFT functional.

Within LDA+U the total energy functional is given as

$$E^{\text{LDA+U}}[\rho] = E^{\text{LDA}}[\rho] + E^{\text{Hub}}[n_{mm'}^{i\sigma}] - E^{\text{DC}}[n^{i\sigma}], \quad (2.5.2)$$

where E^{Hub} includes the correlation effects from the electron-electron interactions in the Hubbard model. E^{DC} is a so-called Hubbard term, that is needed to subtract the contributions that are both accounted for in DFT and the solution of the Hubbard model (for a more detailed discussion see Chapter 6.4). The Hubbard correction is only applied to a set of localized orbitals like d - or f -shells, which are the most affected by electronic correlations due to the short electron-electron distance in these narrow orbitals. The Hubbard term E^{Hub} is a functional of the occupation numbers of these orbitals that are given by a projection from the occupied Kohn-Sham wave function onto the set of localized orbitals $|\chi_m^i\rangle$

$$n_{mm'}^{i\sigma} = \sum_{kv} f_{kv}^\sigma \langle \phi_{kv}^\sigma | \chi_m^i \rangle \langle \chi_m^i | \phi_{kv}^\sigma \rangle, \quad (2.5.3)$$

where f_{kv}^σ is the Fermi-Dirac occupation of the Kohn-Sham states and i labels the atomic sites. In the basis-set independent generalization of LDA+U [85], the contribution to the DFT energy functional

was shown to be in first order (we focus only on a single site for simplicity)

$$E^{\text{Hub}}[n_{mm'}^\sigma] = \frac{1}{2} \sum_{mm'\sigma} U_{mm'} n_{m\sigma} n_{m'\bar{\sigma}} + \sum_{m>m'\sigma} (U_{mm'} - J_{mm'}) n_{m\sigma} n_{m'\sigma}, \quad (2.5.4)$$

where $U_{mm'} = \langle mm' | V_{\text{Coulomb}} | mm' \rangle$ and $J_{mm'} = \langle mm' | V_{\text{Coulomb}} | m'm \rangle$ are the matrix elements of the screened Coulomb interaction in the local orbital basis (see Chapter 6.6). The second term is a result of the Hund's coupling which energetically favours parallel spin orientations.

In this form the LDA+U correction consists basically of the Hartree term only applied to the correlated orbitals, with the Coulomb interaction approximated by a screened constant value $U_{mm'}, J_{mm'}$. Though, the difference to static mean-field theory is that it is determined self-consistently within the DFT calculation. The correction penalizes the double occupation of the local orbitals and will thus modify the occupations of the correlated sector with respect to standard LDA. The (assumed to be) uncorrelated sector is reasonably well described within LDA, so the total charge ρ that minimizes the energy is found self-consistently within the Kohn-Sham Hamiltonian under the constraint of the energy penalty given by Eq. (2.5.4).

LDA+U is capable of describing the magnetic ground state of Mott-insulators, since it can open a gap by forming long-range magnetic or orbital order. As an example let us consider the most simple case of a system with only one correlated orbital at half filling. Since the second term in Eq. (2.5.4) vanishes for one orbital and using $n_\uparrow + n_\downarrow = 1$, we can write the Hubbard correction as

$$E^{\text{Hub}}[n^\sigma] = \frac{U}{2} \sum_{\sigma} n_{\sigma} n_{\bar{\sigma}} \quad (2.5.5)$$

$$= U n_\uparrow (1 - n_\uparrow). \quad (2.5.6)$$

The resulting E^{Hub} as a function of n_\uparrow has a maximum of $\frac{1}{4}U$ at $n_\uparrow = 0.5$ and two minima of $E^{\text{Hub}} = 0$ for $n_\uparrow = 0, 1$. This means that LDA+U favours the magnetic polarization of the system, where the spin occupations are as different as possible to minimize the energy. From the potential difference of the two spin species we see that

$$\frac{\delta E^{\text{Hub}}[n^\sigma]}{\delta n_\uparrow} - \frac{\delta E^{\text{Hub}}[n^\sigma]}{\delta n_\downarrow} = U(n_\downarrow - n_\uparrow), \quad (2.5.7)$$

which shows that the two states are separated by U in the polarized case, which gives a measurement of the energy gap between them. Thus, in agreement with the metal-insulator transition in the Hubbard model, LDA+U is able to open a gap of the order of U in the Kohn-Sham spectrum of the system.

Although this result is a huge improvement upon standard LDA, we have to keep in mind that the opening of the gap is only possible if degeneracies between the orbital and spin occupations are lifted already in LDA. If there were no spin differentiation in our example of the one-orbital system, the potentials for the two spin species would be exactly identical and no gap would open for any value of U . Therefore, LDA+U cannot describe a gap opening in a paramagnetic one-band system and one often artificially imposes or breaks certain symmetries within a crystal in order to push the system in the right direction of possible insulating instabilities.

In the language of Green's functions, which will be discussed in Chapter 3, the LDA+U formalism corresponds to a zeroth-order approximation of the Selfenergy which has no frequency dependence and no imaginary part. As a result the modified Kohn-Sham energies are shifted by a constant regardless of their distance to the Fermi level, which excludes effects like bandwidth renormalization and increase of the effective electron masses. Due to the absent imaginary part of the Selfenergy, the new Kohn-Sham energies are still real, which means excitations have infinite lifetime even in the presence of interactions.

This is in stark contrast to the "true" metal-insulator transition induced by electronic interactions, which is related to the divergence of the imaginary part of the Selfenergy at the Fermi level [80, 81]. Here, the gap opens because quasiparticle excitations of the ground state are immediately suppressed

and have zero lifetime due to the strong electronic interactions. Especially in the paramagnetic half-filled case electrons can localize on the atomic sites and open a gap due to electronic correlations without any spin polarization of the system. Therefore, the gap in LDA+U is usually of a completely different nature than the one found in more sophisticated treatments.

To capture these effects one has to go beyond the zeroth-order approximation of LDA+U and include the full frequency dependence and imaginary parts of the Selfenergy. One option is the dynamical mean-field theory (DMFT), which is the main tool we are going to use in this thesis to study correlation effects in systems where the local Coulomb interactions become significant and cannot be adequately described by DFT and its extensions like hybrid functionals or LDA+U.

Chapter 3

The Green's function formalism

3.1 Introduction

In order to introduce the dynamical mean-field theory (DMFT) to improve existing density functional theory calculations, we will first take an excursion and introduce the language in which DMFT is formulated: The language of Green's functions. In this review we will follow the outline of the beautiful script by Tremblay [86] on this subject, and use atomic units ($\hbar = k_B = 1$).

We will see that Green's functions themselves possess useful mathematical properties and are a very natural tool for comparing theoretical results to experiment. They are versatile in describing properties of a quantum system in the sense that they separate the contribution of the non-interacting system, given by the solution of the non-interacting Hamiltonian

$$H_0,$$

and the contribution of the interacting system

$$H_0 + H_{\text{int}}.$$

In this context H_{int} is the Coulomb interaction, but can in general be any arbitrary Operator, which is not a one-particle Operator. This allows for a plethora of methods and approximations to treat these two contributions separately: First, the usually simpler, but not necessarily simple task of solving the non-interacting part H_0 is performed, and then the interaction can be "switched on", in the sense that in practice different kinds of approximations are employed to perturbatively or non-perturbatively add the contribution of H_{int} to the Hamiltonian.

This property of a Green's function can be put more clearly mathematically: For a given linear differential operator L the Green's function $G : \mathbb{R}^N \times \mathbb{R}^N \mapsto \mathbb{C}, (x, x') \mapsto G(x, x')$ is the so-called "fundamental solution", *i.e.* it has the property

$$LG = \delta_0, \tag{3.1.1}$$

where δ_0 is defined as the Dirac function $\delta(x - 0)$. This can be also seen as G being the solution to a homogeneous initial value problem

$$\begin{cases} Lu(x) &= 0 \\ u(0) &= \delta_0 \end{cases}. \tag{3.1.2}$$

Having obtained the solution G for the homogeneous differential equation, it can be used to obtain the solution for the inhomogeneous differential equation

$$Lu(x) = f(x), \tag{3.1.3}$$

by convolution of the Green's function and $f(x)$ via

$$u(x) = \int G(x-s)f(s) ds. \quad (3.1.4)$$

The proof is straightforward: We want to show that $Lu(x) = f(x) \forall x$ for $u(x)$ given by Eq. (3.1.4). Applying $L(x)$ to $u(x)$ we obtain

$$Lu(x) = L \int G(x-s)f(s) ds \quad (3.1.5)$$

$$= \int [LG(x-s)]f(s) ds \quad (3.1.6)$$

$$= \int \delta(x-s)f(s) ds \quad (3.1.7)$$

$$= f(x). \quad (3.1.8)$$

Therefore, in the mathematical sense the Green's function is considered as a fundamental solution, because it allows one to obtain the solution to the inhomogeneous differential equation from solving an initial value problem of the homogeneous differential equation.

For a physical example we can consider the problem of solving the Poisson equation in electrostatics

$$\Delta\phi = -\rho/\epsilon. \quad (3.1.9)$$

If we want to find the Green's function for the linear differential Operator Δ , we have to solve

$$LG(x, x') = \Delta G(x, x') = \delta(x - x'), \quad (3.1.10)$$

which corresponds to finding the solution for the electric potential for a point charge located at x . The solution is given by

$$G(x, x') = -\frac{1}{4\pi|x-x'|}, \quad (3.1.11)$$

since

$$\Delta G(x, x') = -\frac{1}{4\pi} \Delta \left(\frac{1}{|x-x'|} \right) \quad (3.1.12)$$

$$= \delta(x-x'). \quad (3.1.13)$$

With the Green's function we can now solve the general Poisson equation of electrostatics, resulting in the well known formula

$$\phi(x) = - \int G(x, x') \frac{\rho(x')}{\epsilon} dx' \quad (3.1.14)$$

$$= \int \frac{\rho(x')}{4\pi\epsilon|x-x'|} dx'. \quad (3.1.15)$$

The Green's function in many-body physics shares similar features as the Green's function we introduced so far, but it is used in a slightly different fashion.

3.2 Perturbation theory for the time evolution operator and linear response

The main motivation in many-body physics for the introduction of Green's functions is its application in linear-response theory. Starting from a system in thermal equilibrium, we are interested in the

response to a weak perturbation by some external field $f(r, t)$. This can be for example the electrical conductivity as a response to a small electric field, or the thermal conductivity as a response to a temperature gradient, the magnetic susceptibility, etc. The procedure is very similar to the one we used above: We first consider the full Hamiltonian as the unperturbed and time-independent Hamiltonian H_0 , and then add a small perturbation $V(t)$, which is switched on at some point in time. So in total we have the time-dependent Hamiltonian

$$H(t) = H_0 + V(t), \quad (3.2.1)$$

where the perturbation is given by

$$V(t) = \int O(r, t) f(r, t) dr. \quad (3.2.2)$$

In Eq. (3.2.2), $O(r, t)$ corresponds to the Operator of some local observable of the system, excluding the perturbation, and $f(r, t)$ is as already mentioned the external field which couples to the observable $O(r)$. For example, an external magnetic field in z -direction $f(r, t) = h_z(r, t)$ can couple to the magnetization $O(r) = M_z(r)$.

Since we now have introduced a perturbation that will modify very likely the observables of the system, we are interested how the expectation value of operators

$$\langle A(r, t) \rangle, \quad (3.2.3)$$

changes over time as the perturbation is switched on. This we will do now in the interaction or Dirac picture instead of the usual Schrödinger picture, which especially helpful when the Hamiltonian can be separated into a form like $H(t) = H_0 + V(t)$. In this picture, both the operators and wave functions acquire a time dependence, but the time evolution is split between the unperturbed part and the perturbation. This means we define the operators and wave functions in the interacting picture as

$$|\psi_I(t)\rangle = e^{iH_0 t} |\psi_S(t)\rangle \quad (3.2.4)$$

$$A_I(t) = e^{iH_0 t} A_S e^{-iH_0 t}, \quad (3.2.5)$$

where the subscript S indicates the definition in terms of the Schrödinger picture, where H_0 is time-independent. As a result, the unperturbed H_0 in the Dirac picture stays also time-independent

$$H_{0,I}(t) = e^{iH_0 t} H_{0,S} e^{-iH_0 t} = H_{0,S}. \quad (3.2.6)$$

With the perturbation in the Dirac picture $V_I(t)$, it can be shown right away that this results in the time evolution for the wave function being governed by $V_I(t)$, while for operators A it is governed by H_0

$$i \frac{d}{dt} |\psi_I(t)\rangle = V_I(t) |\psi_I(t)\rangle \quad (3.2.7)$$

$$i \frac{d}{dt} A_I(t) = [A_I(t), H_0], \quad (3.2.8)$$

where we considered no explicit time dependence of the operators in the Schrödinger picture. We will use this framework to develop a perturbation expansion of the time evolution operator $U_I(t, t_0)$ in the Dirac picture in powers of the perturbation $V_I(t)$. The very foundation is the important observation that the time evolution of U in the interaction picture can be obtained in another way. The explicit form of $U_I(t, t_0)$ can be deduced via

$$|\psi_I(t)\rangle = U_I(t, t_0) |\psi_I(t_0)\rangle \quad (3.2.9)$$

$$= U_I(t, t_0) e^{iH_0 t_0} |\psi_S(t_0)\rangle, \quad (3.2.10)$$

while the left side is given as

$$|\psi_I(t)\rangle = e^{iH_0 t} |\psi_S(t)\rangle \quad (3.2.11)$$

$$= e^{iH_0 t} U_S(t, t_0) |\psi_S(t_0)\rangle, \quad (3.2.12)$$

where $t > t_0$. So we have

$$(U_I(t, t_0)e^{iH_0t} - e^{iH_0t}U_S(t, t_0))|\psi_S(t_0)\rangle = 0 \quad \forall |\psi_S(t_0)\rangle \quad (3.2.13)$$

$$\Rightarrow U_I(t, t_0) = e^{iH_0t}U_S(t, t_0)e^{-iH_0t_0}. \quad (3.2.14)$$

This leads to a time evolution which is different from the standard operators in the interaction picture and actually has the same form as the wave function

$$i\frac{d}{dt}U_I(t, t_0) = i\frac{d}{dt}(e^{iH_0t}U_S(t, t_0)e^{-iH_0t_0}) \quad (3.2.15)$$

$$= i(iH_0U_I(t, t_0) + e^{iH_0t}(-iH)U_S(t, t_0)e^{-iH_0t_0}) \quad (3.2.16)$$

$$= i(iH_0U_I(t, t_0) - iH_I(t)U_I(t, t_0)) \quad (3.2.17)$$

$$= V_I(t)U_I(t, t_0), \quad (3.2.18)$$

where we have used that

$$\frac{d}{dt}U_S(t, t_0) = \frac{d}{dt}e^{-i\int_{t_0}^t H(t')dt'} \quad (3.2.19)$$

$$= -iH(t)e^{-i\int_{t_0}^t H(t')dt'}. \quad (3.2.20)$$

Please note that this relation only applies to the time evolution operator and only in the interaction picture, which is not generally the case for normal operators $A_I(t)$. Using the fact that $U(t_0, t_0) = \mathbb{1}$ in any picture, we can integrate Eq. (3.2.18) to obtain

$$\int_{t_0}^t \frac{d}{dt'}U_I(t', t_0) dt' = -i \int_{t_0}^t V_I(t')U_I(t', t_0) dt' \quad (3.2.21)$$

$$\Rightarrow U_I(t, t_0) = \mathbb{1} - i \int_{t_0}^t V_I(t')U_I(t', t_0) dt', \quad (3.2.22)$$

which defines a recurrence relation, that can for instance be solved by iteration. Inserting $U_I(t, t_0)$ into the right side of Eq. (3.2.22) again, we get

$$U_I(t, t_0) = \mathbb{1} - i \int_{t_0}^t V_I(t') \left(\mathbb{1} - i \int_{t_0}^{t'} V_I(t'')U_I(t'', t_0) dt'' \right) dt' \quad (3.2.23)$$

$$= \mathbb{1} - i \int_{t_0}^t V_I(t') dt' + (-i)^2 \int_{t_0}^t V_I(t') \int_{t_0}^{t'} V_I(t'')U_I(t'', t_0) dt'' dt' \quad (3.2.24)$$

$$= \mathbb{1} - i \int_{t_0}^t V_I(t') dt' + (-i)^2 \int_{t_0}^t V_I(t') \int_{t_0}^{t'} V_I(t'') dt'' dt' + \dots, \quad (3.2.25)$$

which creates an infinite sum of nested integrals. Consider for example the second order term and let us approximate the integrals by a sum, where we chop the interval $[t_0, t]$ into N pieces with a separation $\Delta t = (t - t_0)/N$

$$\int_{t_0}^t V_I(t') \int_{t_0}^{t'} V_I(t'') dt'' dt' = \lim_{N \rightarrow \infty} \Delta t \sum_{n=0}^N V_I(t_0 + n\Delta t) \left(\Delta t \sum_{m=0}^n V_I(t_0 + m\Delta t) \right). \quad (3.2.26)$$

So we get sums of terms of the form $V_I(t_0 + n\Delta t)V_I(t_0 + m\Delta t)$, where always $n \geq m$, which means we have a *time-ordered* product of the operators. In order to simplify the calculation, we are tempted to increase the upper limit of the sum over m in Eq. (3.2.26) also to N and divide by a factor of two in order not to count any term twice. But this in turn of course destroys the time order of the

operators. For this, we introduce the *time-ordering operator* T_+ , which acts on any time-dependent operators $A(t), B(t)$ in the following way

$$T_+ [A(t)B(t')] = \begin{cases} A(t)B(t') & \text{for } t \geq t' \\ B(t')A(t) & \text{for } t < t' \end{cases} \quad (3.2.27)$$

$$\text{and } T_+ [A(t_1)B(t_2) + A(t_3)B(t_4)] = T_+ [A(t_1)B(t_2)] + T_+ [A(t_3)B(t_4)]. \quad (3.2.28)$$

With the index “+” we indicate that there is no additional sign involved when commuting the operators $A(t)$ and $B(t)$ (later on we will encounter cases where this is necessary in fermionic systems). With this, we can rewrite the sum in Eq. (3.2.26) as

$$\int_{t_0}^t V_I(t') \int_{t_0}^{t'} V_I(t'') dt'' dt' = \lim_{N \rightarrow \infty} \Delta t \sum_{n=0}^N V_I(t_0 + n\Delta t) \left(\Delta t \sum_{m=0}^N V_I(t_0 + m\Delta t) \right) \quad (3.2.29)$$

$$= \lim_{N \rightarrow \infty} \frac{(\Delta t)^2}{2!} T_+ \left[\sum_{n,m=0}^N V_I(t_0 + n\Delta t) V_I(t_0 + m\Delta t) \right] \quad (3.2.30)$$

$$= \frac{1}{2!} T_+ \left[\int_{t_0}^t V_I(t') dt' \int_{t_0}^t V_I(t'') dt'' \right] \quad (3.2.31)$$

$$= \frac{1}{2!} T_+ \left[\left(\int_{t_0}^t V_I(t') dt' \right)^2 \right], \quad (3.2.32)$$

where the factor $1/2!$ ensures that we do not count any term $V(t)V(t')$ twice since $T_+ [V(t')V(t)]$ gives the same contribution. This result now allows us to rewrite each term in the integral series in Eq. (3.2.25) in the following way

$$U_I(t, t_0) = \mathbb{1} - i \int_{t_0}^t V_I(t') dt' + (-i)^2 \int_{t_0}^t V_I(t') \int_{t_0}^{t'} V_I(t'') dt'' dt' + \dots \quad (3.2.33)$$

$$= \mathbb{1} + T_+ \left[\sum_{n=1}^{\infty} \frac{(-i)^n}{n!} \left(\int_{t_0}^t V_I(t') dt' \right)^n \right] \quad (3.2.34)$$

$$= T_+ \exp \left\{ -i \int_{t_0}^t V_I(t') dt' \right\} \quad (3.2.35)$$

With this form of the time evolution operator we now come back to our original task of obtaining the expectation value of some operator A under the influence of the perturbation V . The perturbation in the interaction picture was given by

$$V_I(t) = \int O_I^0(r, t) f(r, t) dr, \quad (3.2.36)$$

where $O_I^0(r, t)$ denotes the unperturbed observable the perturbation couples to

$$O_I^0(r, t) = e^{iH_0 t} A(r) e^{-iH_0 t}. \quad (3.2.37)$$

We now would like to calculate the expectation value of some operator $A(r)$ in the presence of the perturbation at time t

$$\langle A(r, t) \rangle. \quad (3.2.38)$$

If we switch on the perturbation at time t_0 , we start in some equilibrium state and evolve the system with the full time evolution operator including the perturbation up to time t

$$\langle A(r, t) \rangle = \langle U^\dagger(t, t_0) A(r) U(t, t_0) \rangle, \quad (3.2.39)$$

or in the interaction picture

$$\langle A(r, t) \rangle = \langle U_I^\dagger(t, t_0) A_I^0(r, t) U_I(t, t_0) \rangle, \quad (3.2.40)$$

where $A_I^0(r, t)$ corresponds to the unperturbed operator evolution. We now make use of the perturbation series for $U_I(t, t_0)$ we have just developed. Using the expansion up to *linear* order in the perturbation

$$U_I(t, t_0) \approx \mathbb{1} - i \int_{t_0}^t V_I(t') dt' + \dots, \quad (3.2.41)$$

we obtain for the modified expectation value

$$\langle A(r, t) \rangle = \langle U_I^\dagger(t, t_0) A_I^0(r, t) U_I(t, t_0) \rangle \quad (3.2.42)$$

$$\approx \left\langle A_I^0(r, t) + i \int_{t_0}^t V_I(t') A_I^0(r, t) dt' - i \int_{t_0}^t A_I^0(r, t) V_I(t') dt' \right\rangle \quad (3.2.43)$$

$$= \langle A_I^0(r, t) \rangle + i \int_{t_0}^t \langle [V_I(t'), A_I^0(r, t)] \rangle dt'. \quad (3.2.44)$$

So we obtain for the change of the expectation value up to first order

$$\delta \langle A(r, t) \rangle = i \int_{t_0}^t \langle [V_I(t'), A_I^0(r, t)] \rangle dt' \quad (3.2.45)$$

$$= i \int_{t_0}^t \int \langle [O_I^0(r', t'), A_I^0(r, t)] \rangle f(r', t') dr' dt'. \quad (3.2.46)$$

To make this result more general, we extend the integration to $t' = \pm\infty$ and consider the perturbation to be “switched on” adiabatically slowly. Via the Heaviside function we then cut off the integration at t . In this way we can obtain the following form

$$\delta \langle A(r, t) \rangle = \int_{-\infty}^{\infty} \chi_{OA}^R(r, t, r', t') f(r', t') dr' dt', \quad (3.2.47)$$

where we defined the “retarded” response function $\chi_{OA}^R(r, t, r', t')$ as

$$\chi_{OA}^R(r, t, r', t') = i\theta(t - t') \langle [O_I^0(r', t'), A_I^0(r, t)] \rangle. \quad (3.2.48)$$

We call this response function retarded, because the response, *i.e.* the change we measure in the expectation value $\langle A(r, t) \rangle$ comes after the perturbation via $\theta(t - t')$, which ensures physical time causality. It is important to note that both operators in $\langle [O_I^0(r', t'), A_I^0(r, t)] \rangle$ are defined as the unperturbed operators, *i.e.* their time evolution up to time t is defined via the unperturbed system H_0 . From this result we see that in linear response the correlation function $\chi_{OA}^R(r, t, r', t')$ of the *unperturbed* system provides the information of how strongly the system reacts to an external perturbation. The perturbation $f(r, t)$ itself then acts as a proper weighting factor when calculating expectation values of observables.

Please note that the correlation function $\chi_{OA}^R(r, t, r', t')$ is formally identical to the Green's function introduced in the previous chapter as a fundamental solution. Therefore, $\chi_{OA}^R(r, t, r', t')$ can be interpreted as the fundamental solution or the Green's function of the unperturbed system. This notion will be made more rigorous in the next chapters.

3.3 Zero temperature Green's functions

3.3.1 Real time formulation

The main idea of the last section was to prepare a system in some equilibrium state corresponding to the Hamiltonian H and then perturb the system to see how the observables of the system change

over time. In the same manner we will now use this formalism to prepare an initial state $\psi(r)$ and see that the evolution of a state $\psi(r, t)$ is given by a similar form as an integration over a correlation function times the unperturbed state. This correlation function we will then identify with a Green's function.

To start with an introduction to Green's functions we first will discuss the formalism in the context of the one-body Schrödinger equation. Let us assume we prepare a state $|\psi_0\rangle$ at a given time t' . The evolution of this state to a later time $t > t'$ is given as

$$|\psi(t)\rangle = e^{-iH(t-t')} |\psi_0(t')\rangle, \quad (3.3.1)$$

where we consider the one-body Hamiltonian H to be time-independent. In terms of the position representation we have

$$\psi(\mathbf{r}, t) = \langle \mathbf{r} | e^{-iH(t-t')} | \psi_0(t') \rangle \quad (3.3.2)$$

$$= \int \langle \mathbf{r} | e^{-iH(t-t')} | \mathbf{r}' \rangle \langle \mathbf{r}' | \psi_0(t') \rangle d\mathbf{r}' \quad (3.3.3)$$

$$= \int \langle \mathbf{r} | e^{-iH(t-t')} | \mathbf{r}' \rangle \psi_0(t', r') d\mathbf{r}' \quad (3.3.4)$$

In order to implicitly enforce causality where $t > t'$, we multiply on both sides with the Heaviside function $\theta(t - t')$

$$\psi(\mathbf{r}, t)\theta(t - t') = \int \theta(t - t') \langle \mathbf{r} | e^{-iH(t-t')} | \mathbf{r}' \rangle \psi_0(t', r') d\mathbf{r}' \quad (3.3.5)$$

$$= i \int G^R(\mathbf{r}, t, \mathbf{r}', t') \psi_0(t', r') d\mathbf{r}', \quad (3.3.6)$$

and we introduce the definition of the so-called *retarded Green's function*

$$G^R(\mathbf{r}, t, \mathbf{r}', t') = -i\theta(t - t') \langle \mathbf{r} | e^{-iH(t-t')} | \mathbf{r}' \rangle. \quad (3.3.7)$$

In the same way we also can define the *advanced Green's function*, which describes the evolution to a state at time $t < t'$

$$G^A(\mathbf{r}, t, \mathbf{r}', t') = i\theta(t' - t) \langle \mathbf{r} | e^{-iH(t-t')} | \mathbf{r}' \rangle. \quad (3.3.8)$$

Since we assumed H to be time-independent in the beginning, we can also write the Green's function in terms of the time difference $s = t - t' > 0$

$$G^R(\mathbf{r}, s, \mathbf{r}', 0) = -i\theta(s) \langle \mathbf{r} | e^{-iHs} | \mathbf{r}' \rangle. \quad (3.3.9)$$

So the time invariance of the system, namely H , makes the Green's function time translationally invariant, as expected. If the Hamiltonian is time-dependent, H cannot be pulled out of the integration over time, so we have the more general form

$$G^R(\mathbf{r}, t, \mathbf{r}', t') = -i\theta(t - t') \langle \mathbf{r} | e^{-i \int_{t'}^t H(s) ds} | \mathbf{r}' \rangle, \quad (3.3.10)$$

which in general is not time translationally invariant due to the explicit dependence on t and t' . At first glance we have not gained anything, but this representation will turn out very useful. For the time evolution of the wave functions it has exactly the same form that we have seen in the discussion of the Green's function in the examples about electrostatics and the correlation function in linear response theory. In this picture, the initial wave function couples to the Green's function, which itself does not depend on the wave function but only on H , namely the properties of the system. The perturbation, *i.e.* time evolution sets in at t' and the response at some time $t > t'$ is given by the time-evolved wave function $\psi(\mathbf{r}, t)$. Therefore, the Green's function $G^R(\mathbf{r}, t, \mathbf{r}', t')$ is also called a *propagator*, since it propagates the initial wave function $\psi(\mathbf{r}, t')$ at time t' to the final wave function $\psi(\mathbf{r}, t)$ at time $t > t'$.

3.3.2 Real frequency formulation

We will see later that the Green's function as a function of frequency ω , resp. energy $\hbar\omega$ is a very useful quantity. The time translational invariant Green's function defined in Eq. (3.3.9) allows us to define the Fourier transform of $G^R : \mathbb{R}^3 \otimes \mathbb{R}^3 \otimes \mathbb{R} \rightarrow \mathbb{C}$, with $s \in \mathbb{R}$ being a continuous parameter for the time, as follows

$$G^R(\mathbf{r}, \mathbf{r}', w) = \int_{-\infty}^{\infty} e^{i\omega s} G^R(\mathbf{r}, s, \mathbf{r}', 0) ds \quad (3.3.11)$$

$$= -i \int_0^{\infty} e^{i\omega s} \langle \mathbf{r} | e^{-iHs} | \mathbf{r}' \rangle ds. \quad (3.3.12)$$

To evaluate this equation, we insert the Eigenstates $\{|n\rangle\}$ of the Hamiltonian H , i.e. $H|n\rangle = E_n|n\rangle \forall n$ as a complete set of basis states, where

$$\langle \mathbf{r} | e^{-iHs} | \mathbf{r}' \rangle = \sum_{n,m} \langle \mathbf{r} | m \rangle \langle m | e^{-iHs} | n \rangle \langle n | \mathbf{r}' \rangle \quad (3.3.13)$$

$$= \sum_n \langle \mathbf{r} | n \rangle e^{-iE_n s} \langle n | \mathbf{r}' \rangle, \quad (3.3.14)$$

so we get

$$G^R(\mathbf{r}, \mathbf{r}', w) = -i \int_0^{\infty} e^{i\omega s} \left(\sum_n \langle \mathbf{r} | n \rangle e^{-iE_n s} \langle n | \mathbf{r}' \rangle \right) ds. \quad (3.3.15)$$

In general we would like to exchange the sum and integral in Eq. (3.3.15) and perform the integration over s , but this is not allowed since $\int_0^{\infty} e^{i\omega s} e^{-iE_n s} ds$ does not converge, which can be easily seen from

$$\int_0^{\infty} e^{i(\omega - E_n)s} ds = \frac{1}{i(\omega - E_n)} \left[e^{i(\omega - E_n)s} \right]_0^{\infty}. \quad (3.3.16)$$

To define a meaningful Fourier transform, we have to lift the restriction of $\omega \in \mathbb{R}$ and relax it to $\omega \in \mathbb{R} \otimes \{i\eta\}$, with $\eta > 0$ small, i.e. we shift the domain of the real frequencies slightly upwards into the complex plane by the imaginary part η . We will later more rigorously show that expanding the domain of general Green's functions to the complex plane is reasonable and that $G^R(\mathbf{r}, \mathbf{r}', w)$ is actually well defined in the whole complex plane except for the real axis $\omega \in \mathbb{C} \setminus (\mathbb{R} \otimes \{i0\})$. Note the important requirement of $\eta > 0$, which allows us to evaluate the Fourier transform

$$G^R(\mathbf{r}, \mathbf{r}', w) = -i \int_0^{\infty} \sum_n \langle \mathbf{r} | n \rangle e^{i(\omega + i\eta - E_n)s} \langle n | \mathbf{r}' \rangle ds \quad (3.3.17)$$

$$= -i \sum_n \langle \mathbf{r} | n \rangle \left(\int_0^{\infty} e^{i(\omega + i\eta - E_n)s} ds \right) \langle n | \mathbf{r}' \rangle \quad (3.3.18)$$

$$= -i \sum_n \langle \mathbf{r} | n \rangle \left[\frac{e^{i(\omega + i\eta - E_n)s}}{i(\omega + i\eta - E_n)} \right]_0^{\infty} \langle n | \mathbf{r}' \rangle \quad (3.3.19)$$

$$= \sum_n \frac{\langle \mathbf{r} | n \rangle \langle n | \mathbf{r}' \rangle}{\omega + i\eta - E_n} \quad (3.3.20)$$

$$= \langle \mathbf{r} | \frac{1}{(\omega + i\eta)\mathbb{1} - H} | \mathbf{r}' \rangle. \quad (3.3.21)$$

The physical Green's function is then set as the limit when η goes to zero

$$G^R(\mathbf{r}, \mathbf{r}', w) := \lim_{\eta \rightarrow 0^+} G^R(\mathbf{r}, \mathbf{r}', w + i\eta). \quad (3.3.22)$$

In the following we will always regard the Green's function as the limit of $\eta \rightarrow 0^+$, unless noted otherwise. In most cases when writing the form of the Green's function explicitly, we will also include the $i\eta$ term, but η is considered to be very small and positive.

From this we see that the Green's function in frequency representation has poles at the Eigenenergies E_n of H , which are responsible for the non-convergence of Eq. (3.3.15). Everywhere else the function is indeed well defined for $\omega \in \mathbb{C} \setminus \{E_n\}$. In the same way we can obtain the Fourier transform of the advanced Green's function defined in Eq. (3.3.8), where we have to choose $\omega - i\eta$, $\eta > 0$ for the integral to converge, which leads to

$$G^A(\mathbf{r}, \mathbf{r}', \omega) = \sum_n \frac{\langle \mathbf{r}|n\rangle \langle n|\mathbf{r}'\rangle}{\omega - i\eta - E_n} \quad (3.3.23)$$

$$= \langle \mathbf{r} | \frac{1}{(\omega - i\eta)\mathbb{1} - H} | \mathbf{r}' \rangle. \quad (3.3.24)$$

So far we have defined the Green's function in terms of the position representation but of course any complete basis suffices. We have already written down the operator representation of the Green's function in Eq. (3.3.21), which is also called *resolved* operator. For the sake of completeness we list the real time and real frequency Green's function operators we have encountered so far

$$G^R(t) = -i\theta(t)e^{-iHt}, \quad (3.3.25)$$

$$G^A(t) = i\theta(-t)e^{-iHt}, \quad (3.3.26)$$

$$G^R(\omega) = \frac{1}{(\omega + i\eta)\mathbb{1} - H}, \quad (3.3.27)$$

$$G^A(\omega) = \frac{1}{(\omega - i\eta)\mathbb{1} - H}. \quad (3.3.28)$$

In frequency space we see that the advanced Green's function is actually the retarded Green's function evaluated in the lower half of the complex plane instead of the upper. The two limits of $G^R(\omega)$ and $G^A(\omega)$ for $\eta \rightarrow 0$ do not coincide, so the operator $G(z) = \frac{1}{z\mathbb{1} - H}$ is discontinuous at the real frequency axis

$$\lim_{\eta \rightarrow 0^+} (G^R(\omega) - G^A(\omega)) = \lim_{\eta \rightarrow 0^+} (G(\omega + i\eta) - G(\omega - i\eta)) \quad (3.3.29)$$

$$= \lim_{\eta \rightarrow 0^+} \left(\frac{(\omega - i\eta)\mathbb{1} - H - (\omega + i\eta)\mathbb{1} + H}{(\omega\mathbb{1} - H)^2 + \eta^2\mathbb{1}} \right) \quad (3.3.30)$$

$$= \lim_{\eta \rightarrow 0^+} 2i \left(\frac{-\eta\mathbb{1}}{(\omega\mathbb{1} - H)^2 + \eta^2\mathbb{1}} \right) \quad (3.3.31)$$

$$= -2\pi i \delta(\omega\mathbb{1} - H), \quad (3.3.32)$$

where δ is the Dirac delta function. In the last step we have used the representation of δ in terms of a Lorentzian

$$\lim_{\eta \rightarrow 0^+} \frac{1}{\pi} \frac{\eta}{(x - x_0)^2 + \eta^2} = \delta(x - x_0). \quad (3.3.33)$$

This result we have already seen; the Green's function is basically a sum of poles at the Eigenenergies of H . This already indicates a close relation to the density of states (DOS), which we can formulate in a more rigorous way since we now know the exact functional dependence. We first note

that

$$\lim_{\eta \rightarrow 0^+} G(\mathbf{r}, \mathbf{r}, \omega \pm i\eta) = \lim_{\eta \rightarrow 0^+} \sum_n \frac{\langle \mathbf{r}|n\rangle \langle n|\mathbf{r}\rangle}{\omega \pm i\eta - E_n} \quad (3.3.34)$$

$$= \lim_{\eta \rightarrow 0^+} \sum_n |\langle \mathbf{r}|n\rangle|^2 \frac{\omega - E_n \mp i\eta}{(\omega - E_n)^2 + \eta^2} \quad (3.3.35)$$

$$= \lim_{\eta \rightarrow 0^+} \sum_n \frac{(\omega - E_n) |\langle \mathbf{r}|n\rangle|^2}{(\omega - E_n)^2 + \eta^2} + \lim_{\eta \rightarrow 0^+} \sum_n \frac{\mp i\eta |\langle \mathbf{r}|n\rangle|^2}{(\omega - E_n)^2 + \eta^2} \quad (3.3.36)$$

$$= \sum_n \frac{|\langle \mathbf{r}|n\rangle|^2}{\omega - E_n} \mp i\pi \sum_n \delta(\omega - E_n) |\langle \mathbf{r}|n\rangle|^2 \quad (3.3.37)$$

If we compare this to the DOS, given by $\rho(E) = \sum_n \delta(E - E_n)$, then we see that

$$\rho(E) = \sum_n \delta(E - E_n) \quad (3.3.38)$$

$$= \int \sum_n \langle \mathbf{r}|n\rangle \delta(E - E_n) \langle n|\mathbf{r}\rangle d\mathbf{r} \quad (3.3.39)$$

$$= \mp \frac{1}{\pi} \lim_{\eta \rightarrow 0^+} \int \text{Im} G(\mathbf{r}, \mathbf{r}, \omega \pm i\eta) d\mathbf{r} \quad (3.3.40)$$

$$= \mp \frac{1}{\pi} \lim_{\eta \rightarrow 0^+} \text{Tr} [\text{Im} G(\omega \pm i\eta)]. \quad (3.3.41)$$

Eq. (3.3.41) basically proves our intuitive picture of the Green's function encoding the spectral information for a system described by the Hamiltonian H . It is very important since it will allow us later to relate our results obtained in the language of Green's functions to experimental observables. We will also see that this relation is still valid when we introduce finite temperature Green's function, but has a slightly different interpretation.

3.3.3 Dyson equation and Selfenergy

So far we have only considered a general one-body Hamiltonian H that builds up the Green's function. For example, the retarded Green's function in frequency space was given by

$$G^R(\omega) = [(\omega + i\eta)\mathbb{1} - H]^{-1}. \quad (3.3.42)$$

In practice we often face problems where the Hamiltonian can be separated in the following form

$$H = H_0 + V, \quad (3.3.43)$$

where H_0 usually corresponds to a simple time-independent one-body part, *e.g.* a free particle, and V is a time-independent one-body potential. In general H_0 is easier to diagonalize, while V does not commute with H_0 , so it is not diagonal in the basis of H_0 . We now want to develop a perturbative expression that allows us to obtain the full Green's function given by $H_0 + V$ starting from the Green's function given by H_0 . This will lead us to objects like the Selfenergy and the Dyson equation.

Let us assume we can diagonalize H_0 , then we know the expression of the Green's function given by H_0 , labeled by G_0^R

$$G_0^R(\omega) = [(\omega + i\eta)\mathbb{1} - H_0]^{-1} \quad (3.3.44)$$

$$= \sum_n \frac{|n\rangle \langle n|}{\omega + i\eta - \epsilon_n}, \quad (3.3.45)$$

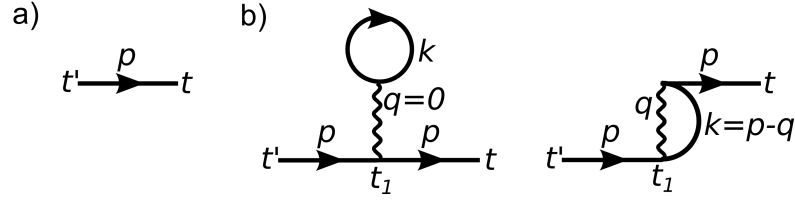


Figure 3.1: Illustration of the diagrammatic evaluation of the full Green's function $G^R(\omega) = [(\omega + i\eta)\mathbb{1} - H_0 - V]^{-1}$ in terms of a perturbative expansion in orders of V in momentum space. The full Green's function is expanded in a sum of Green's functions $G_0^R(\omega) = [(\omega + i\eta)\mathbb{1} - H_0]^{-1}$, indicated by the arrows, and multiple powers of V , indicated by the wiggly line. All internal degrees of freedom are integrated out. a) shows the zeroth order contribution, which equals to the unperturbed result $G_0^R(\omega)$. b) shows all contributions of the first order in V .

where $|n\rangle$ are the Eigenstates of H_0 with the Eigenenergies $H_0 |n\rangle = \epsilon_n |n\rangle$. Including the one-body potential V we can write the full Green's function as follows

$$G^R(\omega) = [(\omega + i\eta)\mathbb{1} - H_0 - V]^{-1} \quad (3.3.46)$$

$$= \left[(G_0^R)^{-1}(\omega) - V \right]^{-1}. \quad (3.3.47)$$

Multiplication by the term on the right and rearranging the resulting terms we get

$$G^R(\omega) = G_0^R(\omega) + G_0^R(\omega)V G^R(\omega). \quad (3.3.48)$$

This equation is also called the Lippman-Schwinger equation in scattering theory. Since this is a recursive relation similar to the perturbation series we obtained for the time evolution operator in Chapter 3.2, we can also iterate this equation to obtain a perturbation series for $G^R(\omega)$ in powers of V . Inserting $G^R(\omega)$ into the right hand side of Eq. 3.3.48 we obtain the series

$$G^R(\omega) = G_0^R(\omega) + G_0^R(\omega)V G_0^R(\omega) + G_0^R(\omega)V G_0^R(\omega)V G_0^R(\omega) + \dots \quad (3.3.49)$$

The infinite can be diagrammatically represented in terms of Feynman diagrams [87]. The n -th term in the sum corresponds to the n -th order in the perturbation series and includes V to the power n . The first two terms evaluated diagrammatically are shown in Fig. 3.1.

Choosing the Eigenbasis of the Hamiltonian H_0 in which the unperturbed Green's function $G_0^R(\omega)$ is diagonal, the series for the full Green's function takes the form

$$\langle n|G^R(\omega)|n'\rangle = G_0^R(n, \omega) + G_0^R(n, \omega) \langle n|V|n'\rangle G_0^R(n', \omega) \quad (3.3.50)$$

$$+ \int dm G_0^R(n, \omega) \langle n|V|m\rangle G_0^R(m, \omega) \langle m|V|n'\rangle G_0^R(n', \omega) + \dots \quad (3.3.51)$$

We now define the *irreducible Selfenergy* $\Sigma^R(\omega)$ that contains all the contribution of V and terms arising from the integration over internal indices via

$$\langle n|G^R(\omega)|n'\rangle = G_0^R(n, \omega) + G_0^R(n, \omega) \langle n|\Sigma^R(\omega)|n'\rangle \langle n|G^R(\omega)|n'\rangle. \quad (3.3.52)$$

Solving this equation for $G^R(\omega)$ we obtain the so-called Dyson equation

$$\langle n|(G^R(\omega))^{-1}|n'\rangle = (G_0^R(n, \omega))^{-1} - \langle n|\Sigma^R(\omega)|n'\rangle. \quad (3.3.53)$$

In the diagrammatic form the Selfenergy $\Sigma^R(\omega)$ now corresponds to the same diagrams generated by Eq. 3.3.49 that are shown in Fig. 3.1 just with the outer "legs" of the unperturbed Green's function

$G_0^R(\omega)$ removed. This equation is very helpful since it allows us to relate the unperturbed Green's function, which is usually much more simple to obtain, with the full Green's function via the Self-energy, that can be calculated by perturbative methods. Since this still results to solving the full problem including the potential V , in practice either truncations of the infinite series or other approximative schemes have to be applied. In Chapter 5.2 we will discuss the dynamical mean-field theory as powerful tool to obtain the Selfenergy in an approximative but controlled way.

3.4 Finite temperature Green's function

It is important to note that the previously defined Green's function do not incorporate any effects of temperature. They are defined in terms of the Eigenstates of the Hamiltonian and do not consider any temperature-induced finite lifetime or broadening effects. The main observable that can be extracted from the Green's function is the density of states, which is just a sum of Dirac Delta functions at the Eigenenergies of the Hamiltonian.

In this section we will deal with the subject of how to include finite temperature effects directly in the propagator, namely the Green's function, by defining it as the average within the grand canonical ensemble, where all energy states contribute with a weight given by the Boltzmann factor $e^{-\beta E}$.

Reminder from second quantization:

Since we want to describe many particle systems at finite temperature, we will use the second quantization representation. For this, let us restate the most important aspects of second quantization, that will be relevant further on.

We define the Fock states as a basis of our Hilbert space in the usual way, where a quantum wave function is represented by the occupation numbers n_i of single particle states $|i\rangle$

$$|\psi\rangle = |n_0, n_1, n_2, \dots\rangle, \quad (3.4.1)$$

with the vacuum state

$$|0\rangle = |0, 0, 0, \dots\rangle. \quad (3.4.2)$$

The creation and annihilation operators

$$\begin{array}{ll} \text{Fermionic:} & \text{Bosonic:} \\ \{c_i, c_j\} = \{c_i^\dagger, c_j^\dagger\} = 0 & [b_i, b_j] = [b_i^\dagger, b_j^\dagger] = 0 \end{array} \quad (3.4.3)$$

$$\{c_i, c_j^\dagger\} = \delta_{ij} \quad [b_i, b_j^\dagger] = \delta_{ij}, \quad (3.4.4)$$

which can raise or lower the occupation of a given state

$$\begin{array}{ll} \text{Fermionic:} & \text{Bosonic:} \\ c_i^\dagger |\dots, n_i, \dots\rangle = (1 - n_i) |\dots, n_i + 1, \dots\rangle & b_i^\dagger |\dots, n_i, \dots\rangle = \sqrt{n_i + 1} |\dots, n_i + 1, \dots\rangle \end{array} \quad (3.4.5)$$

$$c_i |\dots, n_i, \dots\rangle = n_i |\dots, n_i - 1, \dots\rangle \quad b_i |\dots, n_i, \dots\rangle = \sqrt{n_i} |\dots, n_i - 1, \dots\rangle. \quad (3.4.6)$$

We defined the many particle states in terms of the basis states $\{|i\rangle\}$, but we can change into any other appropriate basis $\{|\alpha\rangle\}$ by

$$c_\alpha^\dagger = \sum_i \langle i|\alpha\rangle c_i^\dagger, \quad (3.4.7)$$

$$c_\alpha = \sum_i \langle \alpha|i\rangle c_i. \quad (3.4.8)$$

For the special case of the position states $\{|\mathbf{r}\rangle\}$, the new operators are called *quantum field operators*, and create or annihilate a particle at position \mathbf{r}

$$\Psi^\dagger(\mathbf{r}) = \sum_i \langle i|\mathbf{r}\rangle c_i^\dagger = \sum_i \phi_i^*(\mathbf{r}) c_i^\dagger \quad (3.4.9)$$

$$\Psi(\mathbf{r}) = \sum_i \langle \mathbf{r}|i\rangle c_i = \sum_i \phi_i(\mathbf{r}) c_i. \quad (3.4.10)$$

One particle operators in second quantization have the form

$$A = \sum_{ij} a_{ij} c_i^\dagger c_j, \quad \text{with } a_{ij} = \langle i|A|j\rangle, \quad (3.4.11)$$

and for two particle operators we have the form

$$V = \frac{1}{2} \sum_{ijkl} v_{ijkl} c_i^\dagger c_j^\dagger c_l c_k, \quad \text{with } v_{ijkl} = \langle ij|V|kl\rangle. \quad (3.4.12)$$

Since we will make further use of it, we also revisit the definition of the Heisenberg picture, where the wave functions are constant in time but the operators evolve

$$A(t) := e^{iHt} A e^{-iHt} \quad (3.4.13)$$

$$|\psi(t)\rangle := |\psi(0)\rangle \quad (3.4.14)$$

$$\frac{d}{dt} A(t) = i[H, A(t)] + \frac{\partial A}{\partial t}, \quad (3.4.15)$$

where the Hamiltonian H has no explicit time-dependence in the Schrödinger picture. For the moment, this short listing of the most important points of second quantization will suffice for introducing the finite temperature many particle Green's function.

Recall the definition of the retarded Green's function given in Eq. (3.3.7)

$$G^R(\mathbf{r}, t, \mathbf{r}', t') = -i\theta(t - t') \langle \mathbf{r}|e^{-iH(t-t')}|\mathbf{r}'\rangle, \quad (3.4.16)$$

but what role do we assign to $|\mathbf{r}\rangle$ in second quantization? In the single-particle case this state represents a particle located at position \mathbf{r} . In second quantization we can create an additional particle at point \mathbf{r} by acting the field operator from Eq. (3.4.9) on a given state. Let us assume we are given a many-body ground state wave function $|\psi_0\rangle$, which for a fermionic system we consider here is in general a linear combination of Slater determinants. In this case, the symbolic replacement of $|\mathbf{r}\rangle$ by $\Psi^\dagger(\mathbf{r})|\psi_0\rangle$, which creates an additional particle at point \mathbf{r} , seems natural, so we *define* the retarded Green's function in second quantization by

$$G^R(\mathbf{r}, t, \mathbf{r}', t') = -i\theta(t - t') \langle \psi_0|\Psi(\mathbf{r})e^{-iH(t-t')}\Psi^\dagger(\mathbf{r}')|\psi_0\rangle \quad (3.4.17)$$

$$= -i\theta(t - t') \langle \psi_0|e^{-iHt} e^{iHt} \Psi(\mathbf{r}) e^{-iHt} e^{iHt'} \Psi^\dagger(\mathbf{r}') e^{-iHt'} e^{iHt'} |\psi_0\rangle \quad (3.4.18)$$

$$= -i\theta(t - t') \langle \psi_0|e^{-iHt} \Psi(\mathbf{r}, t) \Psi^\dagger(\mathbf{r}', t') e^{iHt'} |\psi_0\rangle. \quad (3.4.19)$$

If we set the energy of the ground state to zero, which can always be done since we are free to specify a reference energy, we obtain the form

$$G^R(\mathbf{r}, t, \mathbf{r}', t') = -i\theta(t - t') \langle \psi_0|\Psi(\mathbf{r}, t) \Psi^\dagger(\mathbf{r}', t')|\psi_0\rangle. \quad (3.4.20)$$

This form of the Green's function now allows for another interpretation of its properties, with the nuance more focussed on the "propagating" properties: Starting from the ground state $|\psi_0\rangle$, we first create a particle at position \mathbf{r}' at time t' , then annihilate a particle at \mathbf{r} at time t and compare the resulting state with the initial ground state. A more illustrative interpretation is, that the Green's function in Eq. (3.4.20) prepares a state where a particle has been created at \mathbf{r}' at time t' above the

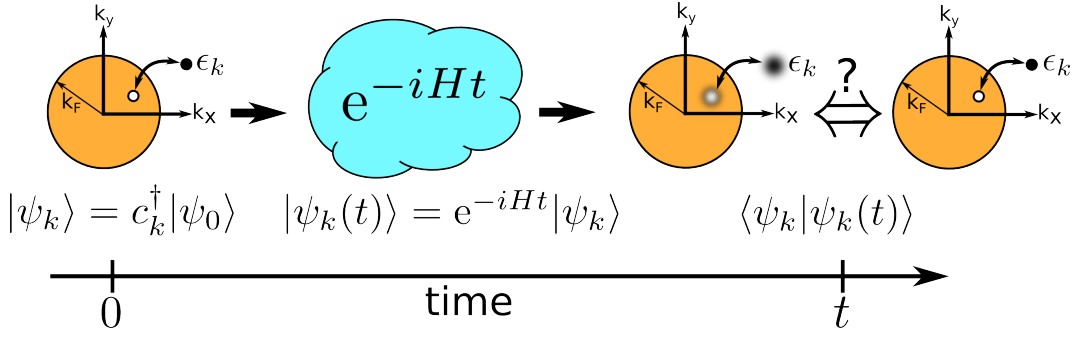


Figure 3.2: Illustration of the Green's function as its role as a propagator. First we create an excitation of the ground state $|\psi_k\rangle = c_k^\dagger |\psi_0\rangle$ at time $t = 0$. Then we let the state propagate in time up to $t > 0$, which is done by the multiplication of the operator e^{-iHt} . This yields the state $|\psi_k(t)\rangle = e^{-iHt} |\psi_k\rangle$.

After that, we measure how much of the original state $|\psi_k\rangle$ is left in the final state by taking the overlap $\langle \psi_k | \psi_k(t) \rangle$. This is (up to a phase factor) exactly the property that defines the Green's function $G_{k,k}^R(t, 0) = -i\theta(t) \langle \psi_0 | \Psi(k, t) \Psi^\dagger(k, 0) | \psi_0 \rangle$.

ground state, then propagated to time t , and then takes the overlap with a state with a particle at position \mathbf{r} . In general terms, we excite the ground state, let it propagate in time and then check how much is left in this state of a specific final state we are interested in. Such interpretation is illustrated in Fig. 3.2. This further indicates that the Green's function is a response function with regard to the perturbation being an excitation of the ground state.

Note that this is in strong contrast to the density functional theory Kohn-Sham formulation, which is a ground state theory. As discussed in Chapter 2, the Kohn-Sham Eigenenergies obtained as a solution to the Kohn-Sham Hamiltonian do not correspond to the true excitation energies of the real system, even though they are interpreted like this. In the Green's function formalism the concept of excitations of the ground state is incorporated correctly from the very beginning, allowing for a proper investigation of the excitation spectrum and electronic structure of a system.

But what happens when the state we are trying to create a particle in is already occupied in a fermionic system? Then it is clear that the Green's function will be identical to zero for all times $t > t'$. This motivates a more general form, in which we do not restrict ourselves to the creation of particles but excitations of the ground state, which means we create a particle if the state is empty and we annihilate a particle if the state is already occupied. This has no other meaning than just taking into account that either particles or holes can propagate. With this, we redefine the Green's function in the following way

$$G^R(\mathbf{r}, t, \mathbf{r}', t') = -i\theta(t - t') \langle \psi_0 | \{ \Psi(\mathbf{r}, t), \Psi^\dagger(\mathbf{r}', t') \} | \psi_0 \rangle. \quad (3.4.21)$$

Here $\{A, B\}$ is the fermionic anticommutator. From this definition it is clear that excitations, be it particles or holes, are propagated in time. This form also recovers the following identity

$$\lim_{t \searrow t'} G^R(\mathbf{r}, t, \mathbf{r}', t') = -i\delta(\mathbf{r} - \mathbf{r}'), \quad (3.4.22)$$

which simply means that the excitation does not propagate when there is no time evolution of the system. Without the commutator, this property would not be fulfilled. We now define Eq. (3.4.21) as the proper *many body zero temperature Green's function*. Finite temperature is not yet considered since we only measure excitations of the ground state. The ground state expectation value is just the zero temperature limit of the thermodynamic average of the finite temperature case, which leads us to the definition of the *many body finite temperature Green's function*

$$G^R(\mathbf{r}, t, \mathbf{r}', t') = -i\theta(t - t') \langle \{ \Psi(\mathbf{r}, t), \Psi^\dagger(\mathbf{r}', t') \} \rangle, \quad (3.4.23)$$

with

$$\langle A \rangle = \frac{1}{Z} \text{Tr} \left\{ e^{-\beta(H-\mu N)} A \right\}. \quad (3.4.24)$$

The Green's function is still written in the position basis, but of course it can be written in any basis. The following form has the general property of exciting a state $|b\rangle$ and then comparing it with a state $|a\rangle$ after the time $t - t'$

$$G_{a,b}^R(t, t') = -i\theta(t - t') \langle \{c_a(t), c_b^\dagger(t')\} \rangle. \quad (3.4.25)$$

For the sake of completeness, we relist our final definition of the real-time retarded and advanced Green's function

$$G_{a,b}^R(t) = -i\theta(t) \langle \{c_a(t), c_b^\dagger(0)\} \rangle \quad (3.4.26)$$

$$G_{a,b}^A(t) = +i\theta(-t) \langle \{c_a(t), c_b^\dagger(0)\} \rangle \quad (3.4.27)$$

Example: Non-interacting particle:

We now calculate the real-time Green's function for non-interacting particles in k -space. The Hamiltonian is just given by the free-particle dispersion

$$H = \sum_a \xi_a c_a^\dagger c_a \quad (3.4.28)$$

where $a = (\mathbf{k}, \sigma)$ is the combined k - and Spin-Index, and $\xi_a = \epsilon_a - \mu$, with the chemical potential μ . By using the BKH-formula one can show that the time-dependent operators can be rewritten as

$$c_a(t) = e^{-i\xi_a t} c_a \quad (3.4.29)$$

$$c_a^\dagger(t) = e^{i\xi_a t} c_a^\dagger. \quad (3.4.30)$$

With this we can evaluate the expectation values for the operator products by performing the trace over the eigenstates of the Hamiltonian. This yields

$$\langle c_a(t) c_b^\dagger(0) \rangle = e^{-i\xi_a t} \langle c_a c_b^\dagger \rangle \quad (3.4.31)$$

$$= e^{-i\xi_a t} (\delta_{ab} - \langle c_b^\dagger c_a \rangle) \quad (3.4.32)$$

$$= e^{-i\xi_a t} (1 - n_F(\xi_a)) \delta_{ab}, \quad (3.4.33)$$

where we have used the Fermi-Dirac distribution

$$\langle c_a^\dagger c_a \rangle = n_F(\xi_a) = \frac{1}{e^{\beta\xi_a} + 1}. \quad (3.4.34)$$

The other term evaluates to

$$\langle c_b^\dagger(0) c_a(t) \rangle = e^{-i\xi_a t} \langle c_b^\dagger c_a \rangle \quad (3.4.35)$$

$$= e^{-i\xi_a t} n_F(\xi_a) \delta_{ab}. \quad (3.4.36)$$

The retarded and advanced Green's function are obtained by adding up these two terms, so with this, we obtain

$$G_{a,b}^R(t) = -i\theta(t) e^{-i\xi_a t} \delta_{ab} \quad (3.4.37)$$

$$G_{a,b}^A(t) = +i\theta(-t) e^{-i\xi_a t} \delta_{ab}. \quad (3.4.38)$$

3.4.1 Finite-temperature perturbation theory

So far we have investigated the propagation of the time evolution operator $U(t, t') = e^{-iH(t-t')}$ with time-independent H . In evaluating the Green's function we encounter terms of the form

$$\sum_i \langle i | e^{-\beta H} c_a(t) c_b^\dagger(t') | i \rangle. \quad (3.4.39)$$

In the same way as we have treated the time evolution operator, we need to treat the density matrix $e^{-\beta H}$ perturbatively. We can easily transfer the previous results by realizing that actually the density matrix is nothing but the time evolution operator evaluated at $t = -i\beta$

$$e^{-\beta H} = e^{-iH(-i\beta)} = U(-i\beta, 0). \quad (3.4.40)$$

In the interaction picture, this means we have

$$U_I(-i\beta, 0) = e^{iH_0(-i\beta)} U(-i\beta, 0) e^{-iH_0 \cdot 0} \quad (3.4.41)$$

$$= e^{H_0 \beta} U(-i\beta, 0) \quad (3.4.42)$$

$$= e^{H_0 \beta} e^{-\beta H} \quad (3.4.43)$$

This expression turns out to be actually simpler than for a real time argument t , since $U_I(-i\beta, 0)$ is purely real. We will now see, that it will be indeed worthwhile to further investigate the properties for imaginary arguments in more detail.

In order to define imaginary time, we introduce a new variable τ , so that the density matrix is given as the time evolution operator evaluated at $\tau = -i\beta$, which leads to

$$U(\tau, 0) = e^{-\beta H} = e^{-iH(-i\beta)} = e^{-iH\tau}. \quad (3.4.44)$$

So we see that we can define τ as the negative imaginary part of the old time variable t extended into the whole complex plane

$$t \rightarrow z_{\text{time}} := t - i\tau, \quad \tau \in \mathbb{R}, \quad (3.4.45)$$

where t is the usual real time variable we have considered before. If $\tau > 0$, this means we are working in the lower half of the complex plane. When we encounter a function given by $f(\tau)$, what we actually mean is

$$f(\tau) := f(0 - i\tau). \quad (3.4.46)$$

For example, the time evolution operator in the complex plane is then

$$U(z_{\text{time}}, 0) = e^{-iHz} = e^{-iH(t-i\tau)} \quad (3.4.47)$$

$$\Rightarrow U(t, 0) = e^{-iHt} \quad (3.4.48)$$

$$\text{and } U(\tau, 0) = e^{-iH(-i\tau)} = e^{H\tau}. \quad (3.4.49)$$

For now, this looks just like a substitution of variables, but mathematically, we continued the time evolution operator into the whole complex plane and found, that at $z = -i\beta$ it equals the density matrix $e^{-\beta H}$. We note that

$$z \mapsto e^{-iHz}, \quad (3.4.50)$$

is a holomorphic function, because the exponential function has a complex derivative in the whole complex plane. This allows us to write down a time evolution equation for $U(z, 0)$ for general $z \in \mathbb{C}$ like Eq. (3.2.18) for z on the imaginary axis, since U in the interaction picture

$$U_I(z, 0) = e^{iH_0 z} e^{-iHz}, \quad (3.4.51)$$

as a product of holomorphic functions is also holomorphic for all $z \in \mathbb{C}$. Therefore, we can calculate the complex derivative, which indeed gives the result as expected

$$i \frac{d}{dz} U_I(z, 0) = i (iH_0 U_I(z, 0) + e^{iH_0 z} (-iH) e^{-iH z}) \quad (3.4.52)$$

$$= i \left(iH_0 U_I(z, 0) - iH_I(z) U_I(z, 0) \right) \quad (3.4.53)$$

$$= V_I(z) U_I(z, 0), \quad (3.4.54)$$

$$\Rightarrow i \frac{d}{dz} U_I(z, 0) \Big|_{z=iy} = V_I(iy) U_I(iy, 0), \quad (3.4.55)$$

for any $y \in \mathbb{R}$. Integration of Eq. 3.4.55 yields

$$U_I(z, 0) = \mathbb{1} - i \int_{\gamma} V_I(z') U_I(z', 0) dz', \quad (3.4.56)$$

where γ is the integration contour starting at $z' = 0$ and ending at $z' = z$. Assuming that $V_I(z)$ is holomorphic, the value of the integral is independent of the explicit choice of the contour γ . For the case of the density matrix $U_I(-i\beta, 0)$, we choose a parametrization just along the imaginary axis with

$$\gamma(s) := -is, \quad s \in [0, \beta], \quad (3.4.57)$$

which leads to

$$U_I(-i\beta, 0) = \mathbb{1} - \int_0^{\beta} V_I(-is) U_I(-is, 0) ds \quad (3.4.58)$$

$$= \mathbb{1} - \int_0^{\beta} V_I(-is) ds + \int_0^{\beta} V_I(-is) \int_0^s V_I(-ir) U_I(-ir, 0) dr ds, \quad (3.4.59)$$

which forms an infinite series of nested integrals like we have seen on the real axis. Since we have restricted the contour to the imaginary axis, we could rewrite the integral as a standard integral over the real variable s of a complex function. This allows us to introduce the time ordering operator T_+ , which sorts operators on the imaginary axis in the following way

$$T_+ [V_I(-is) V_I(-ir)] = \begin{cases} V_I(-is) V_I(-ir) & \text{for } s \geq r \\ V_I(-ir) V_I(-is) & \text{for } s < r \end{cases}. \quad (3.4.60)$$

Note that this would not be possible for arbitrary integration contours γ , since there is no linear order for complex numbers. Since we restricted ourselves to the imaginary axis, we have basically used the order of real numbers on the imaginary part of $\gamma(s)$. With the time ordering operator, we can rewrite the infinite series as usual

$$U_I(-i\beta, 0) = T_+ \exp \left\{ - \int_0^{\beta} V_I(-is) ds \right\}. \quad (3.4.61)$$

This result is an interesting generalization of the time evolution operator, since application of the density matrix operator corresponds to an evolution along the imaginary time axis.

To summarize, we have seen that propagating a state from time t_0 to $t > t_0$ by application of $U_I(t, t_0)$ can be evaluated by an integration of $V_I(z)$ along the straight line contour $t_0 \rightarrow t$ along the real axis, while the application of the density matrix $U_I(-i\beta, 0)$ can be evaluated by an integration of $V_I(z)$ along the straight line contour $0 \rightarrow -i\beta$.

Coming back to the matrix elements of the Green's function from the beginning of this chapter

$$\sum_i \langle i | e^{-\beta H} c_a(t) c_b^\dagger(t') | i \rangle, \quad (3.4.62)$$

we now use the obtained results for the time evolution operator to rewrite it in another way. We consider the state $|i\rangle$ to be given by some state at time t_0 , at which the system is in equilibrium and evolved to the current state at hand at $t = 0$

$$|i\rangle = U_I(0, t_0) |\psi_I(t_0)\rangle, \quad (3.4.63)$$

where in most arguments we will send t_0 to $-\infty$ later. Remember that the creation and annihilation operators $c(t), c^\dagger(t)$ were given in the Heisenberg picture. To transform them into the interaction picture we use

$$c(t) = e^{iHt} c e^{-iHt} \quad (3.4.64)$$

$$= e^{iHt} e^{-iH_0 t} c_I(t) e^{iH_0 t} e^{-iHt} \quad (3.4.65)$$

$$= U_I(0, t) c_I(t) U_I(t, 0) \quad (3.4.66)$$

$$\text{and } c^\dagger(t) = U_I(0, t) c_I^\dagger(t) U_I(t, 0). \quad (3.4.67)$$

For the density matrix we can use

$$e^{-\beta H} = e^{-iH_0(-i\beta)} e^{iH_0(-i\beta)} e^{-iH(-i\beta-0)} \quad (3.4.68)$$

$$= e^{-\beta H_0} U_I(-i\beta, 0), \quad (3.4.69)$$

which leads us to

$$\begin{aligned} & \langle i | e^{-\beta H} c_a(t) c_b^\dagger(t') | i \rangle \\ &= \langle i(t_0) | U_I(t_0, 0) e^{-\beta H_0} U_I(-i\beta, 0) U_I(0, t) c_I(t) U_I(t, 0) U_I(0, t') c_I^\dagger(t') U_I(t', 0) U_I(0, t_0) | i(t_0) \rangle \end{aligned} \quad (3.4.70)$$

$$= \langle i(t_0) | U_I(t_0, 0) e^{-\beta H_0} U_I(-i\beta, t) c_I(t) U_I(t, t') c_I^\dagger(t') U_I(t', t_0) | i(t_0) \rangle. \quad (3.4.71)$$

Let us consider the three leftmost operators

$$U_I(t_0, 0) e^{-\beta H_0} U_I(-i\beta, t) = e^{-\beta H_0} e^{\beta H_0} U_I(t_0, 0) e^{-\beta H_0} U_I(-i\beta, t_0) U_I(t_0, t) \quad (3.4.72)$$

$$= e^{-\beta H_0} U_I(t_0 - i\beta, -i\beta) U_I(-i\beta, t_0) U_I(t_0, t) \quad (3.4.73)$$

$$= e^{-\beta H_0} U_I(t_0 - i\beta, t_0) U_I(t_0, t), \quad (3.4.74)$$

so that we finally obtain

$$\begin{aligned} & \langle i | e^{-\beta H} c_a(t) c_b^\dagger(t') | i \rangle \\ &= \langle i(t_0) | e^{-\beta H_0} U_I(t_0 - i\beta, t_0) U_I(t_0, t) c_I(t) U_I(t, t') c_I^\dagger(t') U_I(t', t_0) | i(t_0) \rangle. \end{aligned} \quad (3.4.75)$$

This result is in many ways insightful: We see that in the interaction picture the thermodynamic expectation value is obtained effectively via the non-perturbed density matrix $e^{-\beta H_0}$. Each matrix element contributing to the thermodynamic average is evaluated by propagating each basis state $|i(t_0)\rangle$ from the system in equilibrium to time $t' > t_0$ and create an excitation by application of $c_I^\dagger(t')$. Then the resulting state is further propagated to $t > t'$, where the annihilation operator $c_I(t)$ is applied, and then propagated back to t_0 . Then the state is propagated along the imaginary time axis up to $t_0 - i\beta$, where the density matrix $e^{-\beta H_0}$ is multiplied for the corresponding weighting factor, and finally we calculate the overlap with the initial state $|i(t_0)\rangle$. Such a contour is called *Kadanoff-Baym contour* and is illustrated in Fig. 3.3.

This shows us that the interpretation of the Green's function is still the same as for the zero temperature Green's function in the previous chapter, namely measuring what excitations are possible and how well they survive over time. The main difference at finite temperature is the fact that we have to propagate the state also into the lower complex plane and evaluate the non-perturbed density matrix to get the correct Boltzmann weighting factor. Therefore, the finite temperature Green's function naturally leads to the concept of imaginary time, which we will make use of shortly.

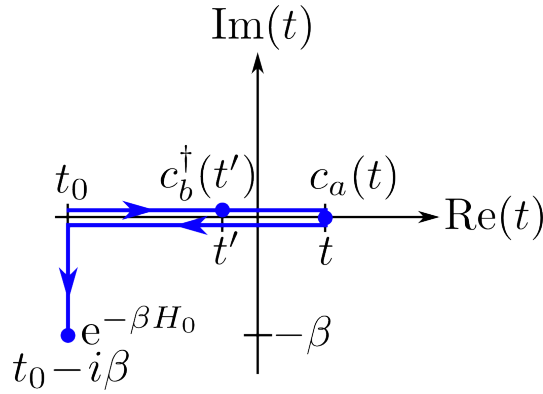


Figure 3.3: The Kadanoff-Baym contour illustrating the integration in the complex plane to evaluate the matrix element $\langle |e^{-\beta H} c_a(t) c_b^\dagger(t')| \rangle$ of the finite temperature Green's function. The dots on the contour indicate the time when each operator is evaluated. The path has a slight offset from the real axis for clarity.

To evaluate such matrix elements in practice, we only need to treat the time evolution operators perturbatively, since we usually assume we were able to solve the non-perturbed system H_0 . Since we have derived the explicit form of the time evolution operator as an exponential of $V_I(t)$, we can expand them as a power series in $V_I(t)$ and calculate the integration along the right contour with appropriate methods.

3.5 Imaginary time Green's functions

In the previous section we have seen that in order to evaluate the finite-temperature Green's function we need to calculate the time-ordered products of operators along an integration contour in the complex plane which is far from a trivial task. Therefore, we would like to simplify this contour to one which is easier to handle mathematically. Still, we are supposed to apply the creation and annihilation operators at time t , respectively t' on the real axis. Otherwise, since the functions we encounter are holomorphic, we are free to choose the integration path as long as we visit the proper points t' , t and $t_0 - i\beta$ along the way.

Since in the finite temperature Green's function we have to at some point make the transition from the real axis into the complex plane to reach $t_0 - i\beta$, we are pretty much limited to the Kadanoff-Baym contour, which is the easiest integration path since it consists only of straight lines connecting the points t' , t and $t_0 - i\beta$ etc. Any deviation from these points results in a Green's function which is different from $G(\mathbf{r}, t, \mathbf{r}', t')$, so in order to simplify the contour, we have to move away from the usual real time Green's function we know and allow for points t, t' that are not located on the real axis.

Actually, this is not a big step since in the previous section we have already seen that we have to evaluate the real frequency Green's function at points shifted slightly away from the real axis by $\eta > 0$. Additionally, the form of operators in the interaction picture becomes easier for complex time arguments, as we have seen in the discussion of the density matrix in the previous section. At some point we have to perform the integration up to a point with imaginary part $-i\beta$, otherwise we would evaluate the Green's function at a different temperature, which is a strong argument that any simplified contour should include these points in the complex plane.

We will now see that we can obtain an expression that is much easier to handle by making the transition towards *imaginary* time, *i.e.* we consider the time variables of $G(\mathbf{r}, t, \mathbf{r}', t')$ to lie only on the imaginary axis. Such analytic continuation of a general function from the real axis into the whole complex plane is a well studied subject in mathematical functional analysis, but in case

of a physical interpretation using something like imaginary time is at first sight slightly counter-intuitive. We will see that this continuation is indeed well defined and will simplify the handling and computation of Green's functions significantly, and that we mathematically are able to uniquely reconstruct the retarded or advanced Green's function from the imaginary time Green's function. In actual calculations this step will usually turn out to be a bit more cumbersome.

We will now again make use of the variable τ , which was defined as the negative imaginary part of a general complex number

$$z_{time} = t - i\tau, \quad t, \tau \in \mathbb{R}. \quad (3.5.1)$$

With this, we define the *imaginary time Green's function* $G_{ab}(\tau, \tau')$ as

$$G_{a,b}(\tau, \tau') = - \langle T_\tau c_a(\tau) c_b^\dagger(\tau') \rangle \quad (3.5.2)$$

$$= - \langle c_a(\tau) c_b^\dagger(\tau') \rangle \theta(\tau - \tau') + \langle c_b^\dagger(\tau') c_a(\tau) \rangle \theta(\tau' - \tau), \quad (3.5.3)$$

where the time ordering operator T_τ sorts all operators with larger argument τ to the left. As can be seen from the definition, the commutation of the fermionic creation and annihilation operators by the time ordering operator involves a sign change. From now on we will establish the convention that the interchange of two operators by T_τ involves a sign change for fermionic and no sign change for bosonic operators. The annihilation and creation operators are given as before in the Heisenberg picture but with imaginary time argument

$$c_a(\tau) = e^{iH(-i\tau)} c_a e^{-iH(-i\tau)} \quad (3.5.4)$$

$$= e^{H\tau} c_a e^{-H\tau} \quad (3.5.5)$$

$$\text{and } c_a^\dagger(\tau) = e^{H\tau} c_a^\dagger e^{-H\tau}. \quad (3.5.6)$$

Please remember that we should in principle write $G_{a,b}(-i\tau, -i\tau')$ and $c_a(-i\tau)$, but as stated in the previous sections, we define

$$f(\tau) := f(0 - i\tau), \quad (3.5.7)$$

without introducing further notation for better readability.

For the moment let us assume that $\beta > \tau > \tau' > 0$. If we set the time t_0 for the system to be at equilibrium to zero, we can write the matrix element of the imaginary time Green's function via the formula from Eq. (3.4.75) as

$$\begin{aligned} & \langle i | e^{-\beta H} c_a(\tau) c_b^\dagger(\tau') | i \rangle \\ &= \langle i(0) | e^{-\beta H_0} U_I(-i\beta, \tau) c_I(\tau) U_I(\tau, \tau') c_I^\dagger(\tau') U_I(\tau', 0) | i(0) \rangle. \end{aligned} \quad (3.5.8)$$

The integration contour is now only along the imaginary axis, and even for $\tau < \tau'$, the time ordering operator ensures that we always integrate from the smallest imaginary time to the larger time value and then finally until $-i\beta$, *i.e.* the contour is a straight line going from 0 to $-i\beta$, as shown in Fig. 3.4. But what happens if for example $\tau > \beta$? Intuitively, this sounds a bit strange since we integrate further than the imaginary time point that corresponds to the density matrix, and then back, which in principle should be reordered by the time ordering operator. If we interpret the density matrix $e^{-\beta H_0}$ as the operator at $\tau = \beta$, it would be put in between $c(\tau)$ and $c^\dagger(\tau')$, which would actually mean we calculate the Boltzmann weight for the intermediate state or at the wrong time. At least our physical intuition tells us that cases where $\tau > \beta$ might be a bit strange. We will indeed show in the next chapters that $|\tau| > \beta$ does not contain any additional physical information.

Before we continue, we show a few important properties of $G(\tau)$.

1. $G_{a,b}(\tau, \tau') = G_{a,b}(\tau - \tau', 0) \quad \forall \tau, \tau'$

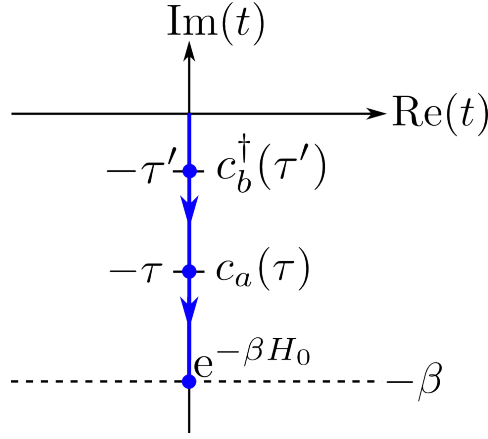


Figure 3.4: The Matsubara contour illustrating the integration in the complex plane to evaluate the matrix element $\langle |e^{-\beta H} c_a(\tau) c_b^\dagger(\tau')| \rangle$ of the finite temperature Green's function on the imaginary time axis. The dots on the contour indicate the time when each operator is evaluated.

Proof: First we consider the case $\tau > \tau'$ and use the cyclic property of the trace

$$G_{a,b}(\tau, \tau') = -\langle c_a(\tau) c_b^\dagger(\tau') \rangle \quad (3.5.9)$$

$$= -\frac{1}{Z} \text{Tr} \left\{ e^{-\beta H} e^{H\tau} c_a e^{-H\tau} e^{H\tau'} c_b^\dagger e^{-H\tau'} \right\} \quad (3.5.10)$$

$$= -\frac{1}{Z} \text{Tr} \left\{ e^{-\beta H} e^{H(\tau-\tau')} c_a e^{-H(\tau-\tau')} c_b^\dagger \right\} \quad (3.5.11)$$

$$= G_{a,b}(\tau - \tau', 0). \quad (3.5.12)$$

This means the imaginary time Green's function is time translationally invariant and only depends on the time difference $\tau - \tau'$. Therefore, from now on we will use the abbreviation

$$G_{a,b}(\tau) := G_{a,b}(\tau, 0). \quad (3.5.13)$$

The proof for $\tau < \tau'$ can be obtained in the same way, just with interchanged order of the operators.

2. $\boxed{(G_{a,b})^\dagger(\tau) = G_{b,a}(\tau) \quad \forall \tau}$

Proof: We start with $\tau > 0$ and again use the cyclic properties of the trace:

$$(G_{a,b})^\dagger(\tau) = -\left(\langle c_a(\tau) c_b^\dagger(0) \rangle \right)^\dagger \quad (3.5.14)$$

$$= -\frac{1}{Z} \text{Tr} \left\{ \left(e^{-\beta H} e^{\tau H} c_a e^{-\tau H} c_b^\dagger \right)^\dagger \right\} \quad (3.5.15)$$

$$= -\frac{1}{Z} \text{Tr} \left\{ c_b e^{-\tau H} c_a^\dagger e^{\tau H} e^{-\beta H} \right\} \quad (3.5.16)$$

$$= -\frac{1}{Z} \text{Tr} \left\{ e^{-\beta H} e^{\tau H} c_b e^{-\tau H} c_a^\dagger \right\} \quad (3.5.17)$$

$$= -\langle c_b(\tau) c_a^\dagger(0) \rangle \quad (3.5.18)$$

$$= G_{b,a}(\tau). \quad (3.5.19)$$

From this it follows directly that the diagonal Green's functions $G_{a,a}(\tau)$ are real, since

$$(G_{a,a})^\dagger(\tau) = G_{a,a}(\tau). \quad (3.5.20)$$

The proof for $\tau < 0$ is completely analogous.

$$3. \quad \boxed{G_{a,b}(-\tau) = -G_{a,b}(-\tau + \beta) \quad \forall \tau \in (0, \beta)}$$

Proof: Again, we only need the cyclic properties of the trace. Assuming that $\tau \in (0, \beta)$ we get

$$G_{a,b}(-\tau) = -\langle T_\tau c_a(-\tau) c_b^\dagger(0) \rangle \quad (3.5.21)$$

$$= \langle c_b^\dagger(0) c_a(-\tau) \rangle \quad (3.5.22)$$

$$= \frac{1}{Z} \text{Tr} \left\{ e^{-\beta H} c_b^\dagger e^{(-\tau)H} c_a e^{-(\tau)H} \right\} \quad (3.5.23)$$

$$= \frac{1}{Z} \text{Tr} \left\{ e^{(-\tau)H} c_a e^{-(\tau)H} e^{-\beta H} c_b^\dagger \right\} \quad (3.5.24)$$

$$= \frac{1}{Z} \text{Tr} \left\{ e^{-\beta H} e^{(\beta-\tau)H} c_a e^{-(\beta-\tau)H} c_b^\dagger \right\} \quad (3.5.25)$$

$$= \langle c_a(\beta - \tau) c_b^\dagger(0) \rangle \quad (3.5.26)$$

$$= \langle T_\tau c_a(\beta - \tau) c_b^\dagger(0) \rangle \quad (3.5.27)$$

$$= -G_{a,b}(-\tau + \beta) \quad (3.5.28)$$

In Eq. (3.5.27) we were able to put in the T_τ operator without any change since we choose $\tau \in (0, \beta)$, and thus $\beta - \tau > 0$. It is important to note that this relation only holds for $\tau \in (0, \beta)$, *i.e.* the Green's function in the interval $(-\beta, 0)$ is identical to the one in $(0, \beta)$ except for a minus sign. Outside this interval this is not true, because for the proof the sign change between $-\tau$ and $\beta - \tau$ is necessary.

$$4. \quad \boxed{\lim_{\tau \rightarrow 0^+} (G_{a,b}(\tau) - G_{a,b}(-\tau)) = -\delta_{ab}}$$

Proof:

$$\lim_{\tau \rightarrow 0^+} (G_{a,b}(\tau) - G_{a,b}(-\tau)) = \lim_{\tau \rightarrow 0^+} \left(-\langle c_a(\tau) c_b^\dagger(0) \rangle - \langle c_b^\dagger(0) c_a(-\tau) \rangle \right) \quad (3.5.29)$$

$$= -\langle c_a c_b^\dagger + c_b^\dagger c_a \rangle \quad (3.5.30)$$

$$= -\langle \{c_a, c_b^\dagger\} \rangle \quad (3.5.31)$$

$$= -\delta_{ab}. \quad (3.5.32)$$

This result shows us that the diagonal imaginary time Green's function is discontinuous at $\tau = 0$. This is due to the fact that we actually regain the real time Green's function from $G_{a,b}(\tau) - G_{a,b}(-\tau)$ at $\tau = t = 0$ where the real and imaginary axis intersect, except for a prefactor of i (compare Eq. 3.4.25).

Example: Non-interacting particle:

At this point let us again have a look at non-interacting particles to see an example of the properties of the imaginary time Green's function. The Hamiltonian is again given by the free particle dispersion

$$H = \sum_p \xi_p c_p^\dagger c_p. \quad (3.5.33)$$

By using the Baker-Campbell-Hausdorff formula we get

$$c_a(\tau) = e^{-\xi_a \tau} c_a \quad (3.5.34)$$

$$c_a^\dagger(\tau) = e^{-\xi_a \tau} c_a^\dagger, \quad (3.5.35)$$

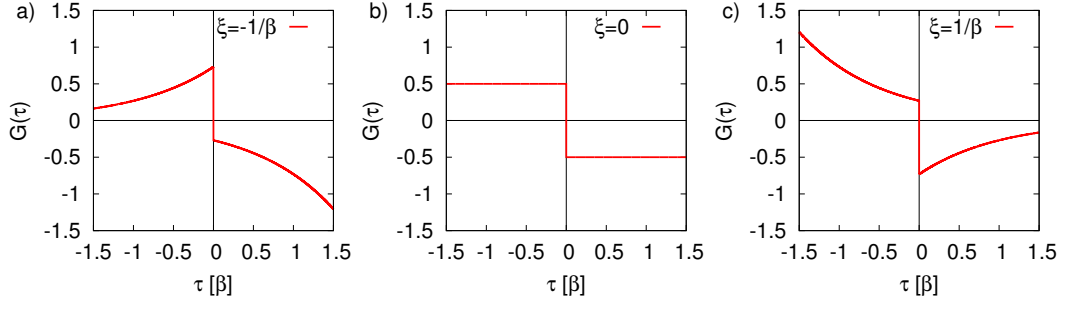


Figure 3.5: The diagonal component of the non-interacting imaginary time Green's function $G_{a,b}(\tau)$ for different values of the single particle energy $\xi = \epsilon - \mu$: a) below the Fermi level $\xi < 0$, b) at the Fermi level $\xi = 0$ and c) above the Fermi level $\xi > 0$. The imaginary time τ is given in units of the inverse temperature β . Only the diagonal component is purely real.

which leads to

$$\langle c_a(\tau)c_b^\dagger(0) \rangle = e^{-\xi_a\tau} \langle c_a c_b^\dagger \rangle \quad (3.5.36)$$

$$= e^{-\xi_a\tau} \langle \delta_{ab} - c_b^\dagger c_a \rangle \quad (3.5.37)$$

$$= e^{-\xi_a\tau} (1 - n_F(\xi_a)) \delta_{ab}, \quad (3.5.38)$$

and

$$\langle c_b^\dagger(0)c_a(\tau) \rangle = e^{-\xi_a\tau} \langle c_b^\dagger c_a \rangle \quad (3.5.39)$$

$$= e^{-\xi_a\tau} n_F(\xi_a) \delta_{ab}. \quad (3.5.40)$$

So adding up these terms we finally obtain

$$G_{a,b}(\tau) = -e^{-\xi_a\tau} (1 - n_F(\xi_a)) \delta_{ab} \theta(\tau) + e^{-\xi_a\tau} n_F(\xi_a) \delta_{ab} \theta(-\tau) \quad (3.5.41)$$

$$= \delta_{ab} e^{-\xi_a\tau} \left(n_F(\xi_a) \theta(-\tau) - (1 - n_F(\xi_a)) \theta(\tau) \right) \quad (3.5.42)$$

$$= -\delta_{ab} e^{-\xi_a\tau} \left(\theta(\tau) - n_F(\xi_a) \right). \quad (3.5.43)$$

It is easy to check that all the four properties of a Green's function from above are fulfilled. Fig. 3.5 shows a plot of the diagonal component for different values of ξ_a , where the jump of height 1 at $\tau = 0$ is clearly visible. From Eq. 3.5.43 we see that the non-interacting Green's function on the imaginary axis is basically a real exponential, originating from the factor $e^{i\xi_a t}$ that we have found on the real axis. As a result, the non-interacting Green's function diverges for large τ in one direction and converges to 0 in the other, depending on the sign of ξ_a . Therefore, the problem arises that we cannot define a Fourier transform of such Green's function, since

$$\int_{-\infty}^{\infty} e^{i\nu\tau} G_{a,b}(\tau) d\tau, \quad (3.5.44)$$

does not exist. The integral does not converge, it even diverges at $\nu = 0$ for the non-interacting particle. In the previous section we already established the notion that $|\tau| > \beta$ is physically questionable, since it would correspond to evaluate operators at times after the natural limit of $\tau = \beta$, given by the density matrix $U(-i\beta, 0) = e^{-\beta H}$. We will see soon that the restriction to the interval $(-\beta, \beta)$ can be mathematically justified and suffices to evaluate the Green's function on the real axis when we want to go back to observable quantities like the spectral function. This we will discuss now in the next section.

3.6 Matsubara Green's function

As just discussed, similar to the real frequency Green's function we would also like to define the spectral representation of $G_{a,b}(\tau)$ via a Fourier transform. Let us assume we were able to find a representation of $G_{a,b}(\tau)$ in the form of

$$G_{a,b}(\tau) = \int e^{-i\nu\tau} G_{a,b}(\nu) d\nu, \quad (3.6.1)$$

where $G_{a,b}(\nu)$ are the coefficients left to be determined. Here, the variable ν refers to the imaginary part of a complex frequency that lies on the imaginary axis, since it corresponds to the imaginary frequencies of the Fourier transform from imaginary time. For the lack of a good alternative and also to use the same notation as most existing literature about Matsubara Green's functions, we will continue to use the symbol ω in a slightly modified form to indicate the frequency on the imaginary axis. We will write $f(i\omega_n)$ when we refer to a function on the imaginary frequency axis, where $i\omega_n$ means we have to evaluate f on the imaginary axis at the value ω_n . The index n has no special meaning yet but it will acquire one shortly.

This notation is a bit inconsistent compared to the case of imaginary time, since there we explicitly decided to drop the i from $i\tau$. Since most other textbooks and publications use this notation, we will also stick to it. In hope to avoid further confusion, we explicitly list the relations between the real and imaginary cases here

Real axis:		Imaginary axis/Matsubara:	Complex plane:
t	\rightarrow	τ	$z_{time} = t - i\tau$
ω	\rightarrow	ω_n	$z_{frequency} = \omega + i\omega_n$

In summary, if we write $f(t)$, $f(\omega)$ it means that the function f should be evaluated on the real time or frequency axis, while $f(\tau)$, $f(i\omega_n)$ means that f should be evaluated on the imaginary axis with the argument $z = -i\tau$, or $z = i\omega_n$, respectively.

Coming back to the problem of how to define the Fourier transform: in case it exists, we have to fulfil the requirement from Eq. 3.5.28, namely $G_{a,b}(-\tau) = -G_{a,b}(-\tau + \beta)$ for $\tau \in (0, \beta)$. This gives the following constraint

$$0 = G_{a,b}(-\tau) + G_{a,b}(-\tau + \beta) \quad (3.6.2)$$

$$= \int \left(e^{-i\omega_n(-\tau)} + e^{-i\omega_n(\beta-\tau)} \right) G_{a,b}(i\omega_n) d\omega_n \quad (3.6.3)$$

$$= \int \left(1 + e^{-i\omega_n\beta} \right) e^{-i\omega_n(-\tau)} G_{a,b}(i\omega_n) d\omega_n. \quad (3.6.4)$$

There is no reason why this relation should be satisfied for arbitrary Green's functions. Actually this integral does not exist since no "usual" Fourier transform of $G_{a,b}(\tau)$ does exist. Therefore, one *possible* solution to this issue, which does not seem to be mathematically justified at first sight, is to require

$$1 + e^{-i\omega_n\beta} = 0, \quad (3.6.5)$$

which poses a constraint onto the frequencies ω_n we consider

$$e^{-i\omega_n\beta} = -1 \quad (3.6.6)$$

$$\Rightarrow \omega_n = (2n + 1) \frac{\pi}{\beta}, \quad n \in \mathbb{Z}. \quad (3.6.7)$$

Therefore, if we consider discrete frequencies and finally give a meaning to the index n , we can actually define the *imaginary frequency Green's function* $G_{a,b}(i\omega_n)$ by

$$G_{a,b}^{\text{FT}}(\tau) = \frac{1}{\beta} \sum_{n=-\infty}^{\infty} e^{-i\omega_n \tau} G_{a,b}(i\omega_n), \quad \omega_n = (2n+1)\frac{\pi}{\beta} \quad (3.6.8)$$

$$G_{a,b}(i\omega_n) = \int_0^\beta e^{i\omega_n \tau} G_{a,b}(\tau) d\tau, \quad (3.6.9)$$

where $G_{a,b}^{\text{FT}}(\tau)$ indicates the Green's function obtained by the inverse Fourier transform of $G_{a,b}(\omega)$, which is *not* identical to the initial $G_{a,b}(\tau)$, since this representation causes $G_{a,b}^{\text{FT}}(\tau)$ to be antiperiodic for all τ

$$G_{a,b}^{\text{FT}}(\tau + m\beta) = \frac{1}{\beta} \sum_{n=-\infty}^{\infty} e^{-i\omega_n(\tau+m\beta)} G_{a,b}(i\omega_n) \quad (3.6.10)$$

$$= e^{-i\omega_n m\beta} \frac{1}{\beta} \sum_{n=-\infty}^{\infty} e^{-i\omega_n \tau} G_{a,b}(i\omega_n) \quad (3.6.11)$$

$$= (-1)^m G_{a,b}^{\text{FT}}(\tau), \quad \text{where } m \in \mathbb{Z}, \quad (3.6.12)$$

whereas the true $G_{a,b}(\tau)$ has this property only in $(-\beta, \beta)$. From the inverse Fourier transform we see that

$$G_{a,b}^{\text{FT}}(\tau) = \frac{1}{\beta} \sum_{n=-\infty}^{\infty} e^{-i\omega_n \tau} G_{a,b}(i\omega_n) \quad (3.6.13)$$

$$= \frac{1}{\beta} \sum_{n=-\infty}^{\infty} e^{-i\omega_n \tau} \left(\int_0^\beta e^{i\omega_n \tau'} G_{a,b}(\tau') d\tau' \right) \quad (3.6.14)$$

$$= \int_0^\beta G_{a,b}(\tau') \underbrace{\left(\frac{1}{\beta} \sum_{n=-\infty}^{\infty} e^{-i\omega_n(\tau-\tau')} \right)}_{=\delta(\tau-\tau')} d\tau' \quad (3.6.15)$$

$$= G_{a,b}(\tau), \quad \text{if } \tau \in (0, \beta). \quad (3.6.16)$$

This property holds only for $\tau \in (0, \beta)$, but due to the antiperiodicity by construction $G_{a,b}^{\text{FT}}(\tau) = -G_{a,b}^{\text{FT}}(\tau - \beta)$, which is correct for the true imaginary time Green's function, we get the agreement also for $\tau \in (-\beta, \beta)$. To recapitulate what we have done by this, we restricted $G_{a,b}(\tau)$ to the interval $(-\beta, \beta)$, throwing away the information outside of this interval and replacing it antiperiodically with the data in $(0, \beta)$. This in turn allowed us to define the Fourier transform $G_{a,b}(i\omega_n)$, since it does exist for (anti)periodic form of $G_{a,b}^{\text{FT}}(\tau)$. We will see shortly that this loss of information is actually irrelevant, and that we will be able to fully and uniquely reconstruct the real time/frequency Green's function from the imaginary time/frequency Green's function which information is confined only to that interval. Therefore, from now on we will redefine the imaginary time Green's function as the inverse Fourier transform and drop the label FT

$$G_{a,b}(\tau) := G_{a,b}^{\text{FT}}(\tau), \quad (3.6.17)$$

and restrict all further investigations to the interval $(-\beta, \beta)$.

Before we come to the point of how to do the continuation from the restricted imaginary axis information to the full real axis, let us investigate the properties of the imaginary frequency Green's function:

1. $\boxed{(G_{a,b})^\dagger(i\omega_n) = G_{b,a}(-i\omega_n) \quad \forall i\omega_n}$

Proof:

$$(G_{a,b})^\dagger(i\omega_n) = \int_0^\beta e^{-i\omega_n\tau} (G_{a,b})^\dagger(\tau) d\tau \quad (3.6.18)$$

$$= \int_0^\beta e^{i(-\omega_n)\tau} G_{b,a}(\tau) d\tau \quad (3.6.19)$$

$$= G_{b,a}(-i\omega_n). \quad (3.6.20)$$

From this it directly follows that for the diagonal Green's function $G_{a,a}(i\omega_n)$ the negative frequency terms can be obtained by complex conjugation

$$G_{a,a}^*(i\omega_n) = G_{a,a}(-i\omega_n). \quad (3.6.21)$$

3.7 Validity of the periodic imaginary time Green's function

In this intermission we will give a proof that the restriction of the imaginary time Green's function on the interval $(0, \beta)$ is mathematically justified. Since this issue is usually brushed over in most textbooks about the Green's function formalism, let us spent a few sentences on recapitulating the actual problem.

In Eq. (3.6.9) we have defined the imaginary Green's function as

$$G(i\omega_n) = \int_0^\beta e^{i\omega_n\tau} G(\tau) d\tau, \quad (3.7.1)$$

where we have dropped the indices of the states a, b for convenience, since they have no effect on what we are interested in right now. This form of the Fourier transform was in principle chosen arbitrarily and so far there is no justification why we should choose especially the interval $(0, \beta)$ for the integration, because the imaginary time Green's function is *not* periodic in τ . The standard Fourier transform

$$\int_{-\infty}^{\infty} e^{i\omega_n\tau} G(\tau) d\tau, \quad (3.7.2)$$

does not even exist in the general case, as we have seen at the example of the non-interacting particle from Eq. (3.5.43)

$$- \int_{-\infty}^{\infty} e^{i\omega_n\tau} e^{-\xi\tau} (\theta(\tau) - n_F(\xi_a)) d\tau = - \int_0^{\infty} e^{(i\omega_n - \xi)\tau} d\tau + n_F(\xi) \underbrace{\int_{-\infty}^{\infty} e^{(i\omega_n - \xi)\tau} d\tau}_{\rightarrow \pm\infty}. \quad (3.7.3)$$

So why should the Fourier transform when restricted to $(0, \beta)$ in Eq. (3.7.1) give any meaningful result at all?

The advantage we have is that we can actually check whether it is meaningful and consistent with the Fourier transform on the real axis. Defining $G(i\omega_n)$ by the Fourier transform in Eq. (3.7.1) is only one way but we have additional possibility of extending the real frequency variable ω into the complex plane just as we have done with t when we introduced the imaginary time Green's function $G(\tau)$. To have a consistent unique definition of the imaginary frequency Green's function, we thus need to have the following equality

$$\int_0^\beta e^{i\omega_n\tau} G(\tau) d\tau =: G(i\omega_n) \stackrel{?}{=} G(i\omega_n) := G(\omega) \Big|_{\omega \rightarrow i\omega_n} \quad (3.7.4)$$

These two different ways of obtaining $G(i\omega_n)$ and the corresponding problem are illustrated in Fig. 3.6. The path A corresponds to the case where we first obtain the Fourier transform on the real

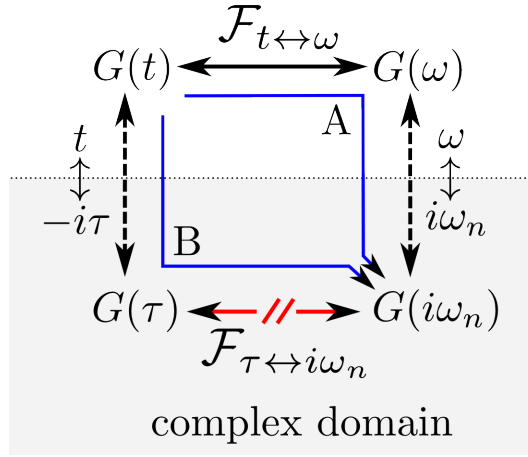


Figure 3.6: Diagram for the proof that the Fourier transform on the finite $(0, \beta)$ interval of the imaginary time Green's function is consistent with the continuation of the real frequency Green's function $G(\omega)$ extended onto the imaginary axis. Here, \mathcal{F} represents the Fourier transform between time and frequency. What one has to show is that the two paths A and B commute and give a unique relationship between the functions on the real and imaginary axis. In the general case the existence of the Fourier transform $G(\omega)$ does not imply the existence of the Fourier transform $G(i\omega_n)$. If it does exist, in general the two paths A and B will each yield a different result.

axis and then extend ω into the complex plane onto the imaginary axis $i\omega_n$. The other path B first performs the continuation into the complex plane and then applies the Fourier transform, which has to be restricted to some finite interval in order to exist.

Even if the Fourier transform in imaginary time were to exist for certain cases, Eq. (3.7.4) would not hold in the general case. For a counterexample consider the following function

$$f(z) = (1 - t^2)\theta(1 - |t|), \quad (3.7.5)$$

which is a simple quadratic function centered at the origin and equals zero outside the interval $[-1, 1]$. Other choices are possible but this function is especially easy to work with. Starting with real time arguments t , it has the Fourier transform

$$f(\omega) = \int_{-\infty}^{\infty} e^{i\omega t} (1 - t^2)\theta(1 - |t|) dt \quad (3.7.6)$$

$$= \frac{4}{\omega^3} (\sin \omega - \omega \cos \omega). \quad (3.7.7)$$

Performing the transformation onto the complex axis by substituting $\omega \rightarrow i\omega_n$, we obtain

$$f(i\omega_n) = \frac{4}{(i\omega_n)^3} (\sin i\omega_n - i\omega_n \cos i\omega_n) \quad (3.7.8)$$

$$= -\frac{4}{\omega_n^3} (\sinh \omega_n - \omega_n \cosh \omega_n). \quad (3.7.9)$$

This is the way to obtain $f(i\omega_n)$ as indicated by path A in Fig. 3.6. Now we can compare the other way indicated by B by first moving onto the imaginary axis

$$f(\tau) = (1 - (-i\tau)^2)\theta(1 - |-i\tau|) \quad (3.7.10)$$

$$= (1 + \tau^2)\theta(1 - |\tau|). \quad (3.7.11)$$

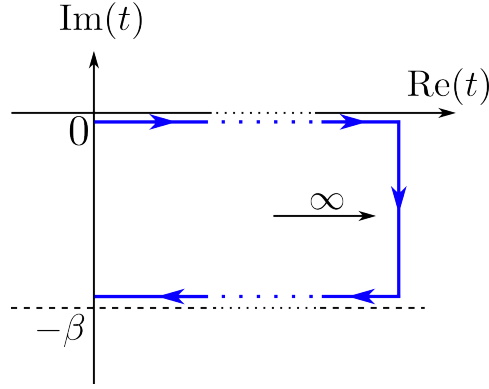


Figure 3.7: The modified integration contour to relate the Fourier transform of the imaginary time Green's function $G_{a,b}(\tau)$ to the real frequency Green's function $G_{a,b}(\omega)$. The original integration from $\tau = 0$ to $\tau = \beta$ is replaced by an integration along the real axis and then into the lower complex plane. The rightmost integration path is sent to infinity and vanishes.

Since we restricted the function to the interval $[-1, 1]$ the standard Fourier transform does exist

$$\int_{-\infty}^{\infty} e^{i\omega_n \tau} (1 + \tau^2) \theta(1 - |\tau|) d\tau = \frac{4}{\omega_n^3} (\omega_n^2 \sin \omega_n + \omega_n \cos \omega_n - \sin \omega_n), \quad (3.7.12)$$

which is in no way equal to the result we obtain by using path A in Eq. (3.7.9). Even for special choices of discretizing the ω_n values the two functions cannot be brought into agreement. This shows us that the definition of $G(i\omega_n)$ by the Fourier transform in Eq. (3.7.1) is actually quite non-trivial and needs to be justified that it is consistent with the Fourier transform on the real axis, *i.e.* that path A and B in Fig. 3.6 do commute.

With this introduction to the problem, we are finally ready to show that the definition of the imaginary frequency Green's function via

$$G_{a,b}(i\omega_n) = \int_0^\beta G_{a,b}(\tau) e^{i\omega_n \tau} d\tau, \quad (3.7.13)$$

and especially the restriction to the interval $(0, \beta)$ is mathematically justified. For this we will proceed in two steps: First, we have to show that the imaginary frequency Green's function as defined in Eq. (3.6.9) is *uniquely* determined as the continuation from the retarded Green's function $G_{a,b}^R(\omega)$ by the replacement $\omega \rightarrow i\omega_n$. This ensures that there is only one imaginary time Green's function which can be obtained from the information on the real axis. In the second step we have to show the reverse, namely that for given $G_{a,b}(i\omega_n)$, $n \in \mathbb{Z}$, there exists a unique continuation $G_{a,b}(z)$, that satisfies $G_{a,b}(z)|_{z=i\omega_n} = G_{a,b}(i\omega_n)$ and $G_{a,b}(z)|_{z=\omega+i\eta} = G_{a,b}^R(\omega)$. If this is done, we have shown that $G_{a,b}(i\omega_n)$ and $G_{a,b}^R(\omega)$ have a one-to-one correspondence, thus one can be uniquely obtained from the other, so we are free to choose whichever representation is the most convenient.

First step: We need to show that the imaginary frequency Green's function is uniquely determined as the continuation from the retarded Green's function $G_{a,b}^R(\omega)$ via $\omega \rightarrow i\omega_n$. In the definition of the imaginary frequency Green's function in Eq. (3.6.9) the integration contour is a straight line in the interval $\tau \in (0, \beta)$, resp. $z = -it'$, $t' \in (0, \beta)$. Since $G_{a,b}(\tau)$ is a holomorphic function in the lower complex plane, we are free to choose the integration contour as long as the start and end points are the same. We now modify the contour by first integration along the real axis from $z = (0, 0)$ to $z = (s, 0)$, $s > 0$, then into the lower complex plane to $z = (s, -i\beta)$, and then finally back to $z = (0, -i\beta)$. Then s will be sent to infinity. This path is illustrated in Fig. 3.7. Performing

the integration along this contour then leads to

$$G_{a,b}(i\omega_n) = \int_0^\beta G_{a,b}(\tau) e^{i\omega_n \tau} d\tau \quad (3.7.14)$$

$$= - \int_0^\beta \langle T_\tau c_a(\tau) c_b^\dagger(0) \rangle e^{i\omega_n \tau} d\tau \quad (3.7.15)$$

$$= - \int_0^\beta \langle e^{H\tau} c_a e^{-H\tau} c_b^\dagger \rangle e^{i\omega_n \tau} d\tau \quad (3.7.16)$$

$$= - \int_0^\beta \langle e^{iH(0-i\tau)} c_a e^{-iH(0-i\tau)} c_b^\dagger \rangle e^{-\omega_n(0-i\tau)} d\tau \quad (3.7.17)$$

$$= -i \int_0^\infty \langle e^{iHt} c_a e^{-iHt} c_b^\dagger \rangle e^{-\omega_n t} dt$$

$$- \underbrace{\lim_{s \rightarrow \infty} \int_0^\beta \langle e^{iH(s-iy)} c_a e^{-iH(s-iy)} c_b^\dagger \rangle e^{-\omega_n(s-iy)} dy}_{\rightarrow 0}$$

$$- i \int_\infty^0 \langle e^{iH(t-i\beta)} c_a e^{-iH(t-i\beta)} c_b^\dagger \rangle e^{-\omega_n(t-i\beta)} dt \quad (3.7.18)$$

$$= -i \int_0^\infty \langle e^{iHt} c_a e^{-iHt} c_b^\dagger \rangle e^{-\omega_n t} dt$$

$$+ i \int_0^\infty \langle e^{iH(t-i\beta)} c_a e^{-iH(t-i\beta)} c_b^\dagger \rangle (-1) e^{-\omega_n t} dt \quad (3.7.19)$$

$$= -i \int_0^\infty \langle c_a(t) c_b^\dagger(0) \rangle e^{-\omega_n t} dt - i \int_0^\infty \frac{1}{Z} \text{Tr} \left\{ e^{-\beta H} e^{iH(t-i\beta)} c_a e^{-iH(t-i\beta)} c_b^\dagger \right\} e^{-\omega_n t} dt \quad (3.7.20)$$

$$= -i \int_0^\infty \langle c_a(t) c_b^\dagger(0) \rangle e^{-\omega_n t} dt - i \int_0^\infty \langle c_b^\dagger(0) c_a(t) \rangle e^{-\omega_n t} dt \quad (3.7.21)$$

$$= -i \int_0^\infty \langle \{c_a(t), c_b^\dagger(0)\} \rangle e^{-\omega_n t} dt \quad (3.7.22)$$

$$= \int_{-\infty}^\infty G_{a,b}^R(t, 0) e^{i(\omega_n)t} dt \quad (3.7.23)$$

$$= G_{a,b}^R(\omega) \Big|_{\omega \rightarrow i\omega_n}. \quad (3.7.24)$$

For this proof we have considered the following:

1. When performing the integration along the real axis in (3.7.18) we pick up an additional factor of i due to the change of the integration measure. The parametrization on the imaginary axis is $\gamma(\tau) = -i\tau \Rightarrow d\gamma = -id\tau$, while on the real axis it is $\gamma(t) = t \rightarrow d\gamma = dt$.
2. In (3.7.18) the middle term vanishes because of the real decaying exponential factor $\lim_{s \rightarrow \infty} e^{-\omega_n s} = 0$.
3. In (3.7.19) we have used that $e^{i\omega_n \beta} = -1$, which is only true for the Matsubara frequencies $\omega_n = (2n+1)\frac{\pi}{\beta}$. This means that the result we just obtained $G_{a,b}(i\omega_n) = i G_{a,b}^R(\omega) \Big|_{\omega \rightarrow i\omega_n}$ is true *only* at the Matsubara frequencies! The proof does not hold for arbitrary values of ω_n .
4. In (3.7.21) we have used the cyclic properties of the trace to rearrange the order of the operators c_a and c_b^\dagger . For this it was crucial that the integration was performed along a contour with imaginary part $-i\beta$, otherwise the Boltzmann factor would not have been cancelled by the

Heisenberg exponential operator

$$\mathrm{Tr} \left\{ e^{-\beta H} e^{iH(t-i\beta)} c_a e^{-iH(t-i\beta)} c_b^\dagger \right\} = \mathrm{Tr} \left\{ e^{iHt} c_a e^{-iHt} e^{-\beta H} c_b^\dagger \right\} \quad (3.7.25)$$

$$= \mathrm{Tr} \left\{ e^{-\beta H} c_b^\dagger e^{iHt} c_a e^{-iHt} \right\}. \quad (3.7.26)$$

This shows that we *have* to restrict the upper limit of the integration of the Fourier transform for the imaginary frequency Green's function to $(0, \beta)$, otherwise this proof would not hold.

5. When modifying the integration contour in (3.7.18), in principle we would have to include a factor of $i\eta$ to shift the integration on the real axis slightly below into the lower complex plane. In this case it is not necessary since we have restricted us to the lower complex plane $\tau \in (0, \beta)$ and thus evaluated the time ordering operator accordingly. As soon as the time ordering operator is evaluated, we are left with the function $\langle c_a(\tau) c_b^\dagger(0) \rangle e^{i\omega_n \tau}$, which is continuous on the real axis.

Second step: We have to show that for given $G_{a,b}(i\omega_n)$, $n \in \mathbb{Z}$, there exists a unique continuation $G_{a,b}(z)$, that satisfies $G_{a,b}(z)|_{z=i\omega_n} = G_{a,b}(i\omega_n)$ and $G_{a,b}(z)|_{z=\omega+i\eta} = G_{a,b}^R(\omega)$. This step is a bit more involved since in general there exist an infinite number of functions which agree on all Matsubara points $i\omega_n$. Consider for example we have found a holomorphic function $F(z)$ which fulfils $F(z)|_{z=i\omega_n} = G_{a,b}(i\omega_n) \forall i\omega_n$. Then the following different function also has the same values at $i\omega_n$

$$F_{a,b}(z) + e^{\beta z} + 1, \quad (3.7.27)$$

since $e^{\beta i\omega_n} = -1$. Luckily, the property $\lim_{|z| \rightarrow \infty} G_{a,b}(z) = 0$ will help us to overcome this issue. This property follows from the following spectral representation of the Green's function that we will derive in Chapter 4

$$G_{a,b}(z) = \frac{1}{\pi} \int_{-\infty}^{\infty} \frac{\mathrm{Im}[G_{a,b}(\omega)]}{\omega - z} d\omega. \quad (3.7.28)$$

Since the spectral function $-\frac{1}{\pi} \mathrm{Im}[G_{a,b}(\omega)]$ is normalized to one, $G_{a,b}(z)$ will always fall off at least as $1/|z|$ for large $|z|$. This will suffice for the proof.

Baym and Mermin [88] showed that a function $f(z)$ that takes on values $f(z_n)$, $n \in \mathbb{Z}$, $z_n \notin \mathbb{R}$ and fulfils the following properties

1. f is analytic except for the real axis
2. f goes to zero along any straight line for $|z| \rightarrow \infty$ in the upper or lower half-plane,

has a unique analytic continuation $f^c(z)$ in the lower or upper complex plane that fulfils $f^c(z_n) = f(z_n)$. Since we already know from the first step of the proof that $G_{a,b}^R(\omega)$ has the property that $G_{a,b}^R(z)|_{z=i\omega_n} = G_{a,b}(i\omega_n) \forall n \in \mathbb{Z}$, it has to be the only function with this property, *i.e.* is the proper analytic continuation and we can formally write

$$\lim_{i\omega_n \rightarrow \omega+i\eta} G_{a,b}(i\omega_n) = G_{a,b}^R(\omega). \quad (3.7.29)$$

This concludes the proof. Therefore, the restriction of the imaginary time Green's function to the interval $(-\beta, \beta)$ is justified and we can work with both real and imaginary frequency Green's function without any loss of information; whichever may be more convenient. It should be clear now that the advanced Green's function can be obtained by

$$\lim_{i\omega_n \rightarrow \omega-i\eta} G_{a,b}(i\omega_n) = G_{a,b}^A(\omega), \quad (3.7.30)$$

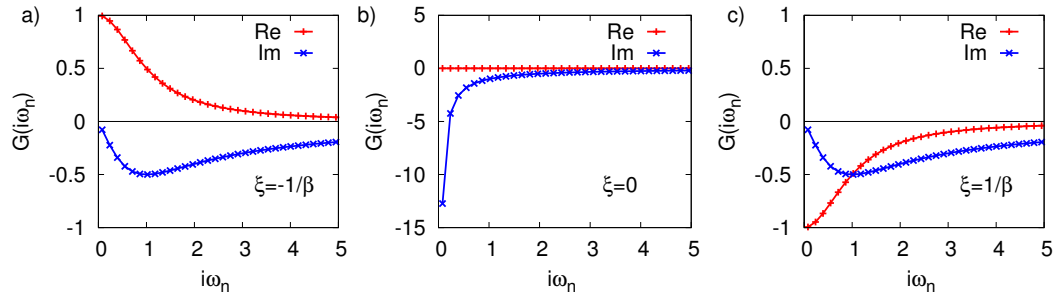


Figure 3.8: The real and imaginary part of the diagonal component of the non-interacting imaginary frequency Green's function $G_{a,b}(i\omega_n)$ for different values of the single particle energy $\xi = \epsilon - \mu$: a) below the Fermi level $\xi < 0$, b) at the Fermi level $\xi = 0$ and c) above the Fermi level $\xi > 0$. Here, the inverse temperature β corresponds to room temperature.

which follows directly if in the previous proof the integration over the imaginary axis is performed in the upper complex plane $(0, i\beta)$ instead of the lower.

For the moment let us reconsider our example of non-interacting particles. The imaginary time Green's function is (see Eq. 3.5.43)

$$G_{a,b}(\tau) = -\delta_{ab} e^{-\xi_a \tau} (\theta(\tau) - n_F(\xi_a)). \quad (3.7.31)$$

The imaginary frequency Green's function as defined in Eq. (3.6.9) then evaluates to

$$G_{a,b}(i\omega_n) = \int_0^\beta e^{i\omega_n \tau} G_{a,b}(\tau) d\tau \quad (3.7.32)$$

$$= -\delta_{ab} \int_0^\beta e^{i\omega_n \tau} e^{-\xi_a \tau} (\theta(\tau) - n_F(\xi_a)) d\tau \quad (3.7.33)$$

$$= -\delta_{ab} (1 - n_F(\xi_a)) \int_0^\beta e^{(i\omega_n - \xi_a)\tau} d\tau \quad (3.7.34)$$

$$= -\delta_{ab} (1 - n_F(\xi_a)) \frac{e^{(i\omega_n - \xi_a)\beta} - 1}{i\omega_n - \xi_a} \quad (3.7.35)$$

$$= -\delta_{ab} (1 - n_F(\xi_a)) \frac{-e^{-\beta\xi_a} - 1}{i\omega_n - \xi_a} \quad (3.7.36)$$

$$= \frac{\delta_{ab}}{i\omega_n - \xi_a}. \quad (3.7.37)$$

This is the manifestation of what we just showed in the previous proof: we can indeed obtain the imaginary frequency Green's function from the real frequency Green's function in the last chapter

$$G_{a,b}^R(\omega) = \frac{\delta_{ab}}{\omega + i\eta - \xi_a}, \quad (3.7.38)$$

just by the replacement $\omega + i\eta \rightarrow i\omega_n$ and the other way round. In Fig. 3.8 we show examples of the non-interacting Matsubara Green's function for three different values of ξ_a .

3.8 Matsubara frequency summations

When working with the Matsubara Green's function we will often encounter summations over the Matsubara frequencies of the form

$$\frac{1}{\beta} \sum_{n=-\infty}^{\infty} F(i\omega_n), \quad (3.8.1)$$

where $F(i\omega_n)$ can be the Matsubara Green's function or any other function depending on $i\omega_n$. Consider for example the inverse Fourier transform to imaginary time

$$G_{a,b}(\tau) = \frac{1}{\beta} \sum_{n=-\infty}^{\infty} e^{-i\omega_n\tau} G_{a,b}(i\omega_n), \quad \omega_n = (2n+1)\frac{\pi}{\beta}, \quad (3.8.2)$$

where $F(i\omega_n) = e^{-i\omega_n\tau} G_{a,b}(i\omega_n)$. We see that the standard sum over Matsubara frequencies in Eq. 3.8.1 is a special case of the inverse Fourier transform, namely evaluated at $\tau = 0$

$$\frac{1}{\beta} \sum_{n=-\infty}^{\infty} F(i\omega_n) = \frac{1}{\beta} \sum_{n=-\infty}^{\infty} e^{-i\omega_n 0} F(i\omega_n) \quad (3.8.3)$$

$$= F(\tau)|_{\tau=0}. \quad (3.8.4)$$

But from the previous chapter we know that basically all functions we consider, like the Green's function, are discontinuous at $\tau = 0$, which makes the Matsubara summation ambiguous. The most prominent example is the expectation value of the particle number operator $\langle c_k c_k^\dagger \rangle$, or the *filling* or *occupation* of the state $|k\rangle$. This expression is actually imaginary time Green's function evaluated at $\tau = 0^-$, since

$$\lim_{\tau \rightarrow 0^-} G_{k,k}(\tau) = \lim_{\tau \rightarrow 0^-} -\langle T_\tau c_k(\tau) c_k^\dagger(0) \rangle \quad (3.8.5)$$

$$= \lim_{\tau \rightarrow 0^-} \langle c_k^\dagger(0) c_k(\tau) \rangle, \quad \text{since } \tau < 0 \quad (3.8.6)$$

$$= \langle c_k^\dagger(0) c_k(0) \rangle \quad (3.8.7)$$

$$= \langle c_k^\dagger c_k \rangle \quad (3.8.8)$$

$$= n_k, \quad (3.8.9)$$

while for $\tau = 0^+$ we have

$$\lim_{\tau \rightarrow 0^+} G_{k,k}(\tau) = \lim_{\tau \rightarrow 0^+} -\langle c_k(\tau) c_k^\dagger(0) \rangle \quad (3.8.10)$$

$$= -\langle c_k c_k^\dagger \rangle \quad (3.8.11)$$

$$= -\langle 1 - c_k^\dagger c_k \rangle \quad (3.8.12)$$

$$= n_k - 1. \quad (3.8.13)$$

If we use the definition of the inverse Fourier transform we can obtain the filling as

$$n_k = \lim_{\tau \rightarrow 0^-} G_{k,k}(\tau) \quad (3.8.14)$$

$$= \lim_{\tau \rightarrow 0^-} \frac{1}{\beta} \sum_{n=-\infty}^{\infty} e^{-i\omega_n\tau} G_{k,k}(i\omega_n), \quad (3.8.15)$$

where we cannot exchange the limit and the summation, since the sum is not continuous in $\tau = 0$, as we have just seen. Therefore, any summation over Matsubara frequencies that involves functions that are discontinuous at $\tau = 0$ need to be handled carefully. For example, calculating the filling for

a state at the Fermi level with $\xi_k = 0$, which should be half filled with $n_k = 0.5$, without the factor $e^{-i\omega_n 0^-}$ leads to neither n_k nor $n_k - 1$, since the behaviour is undefined

$$\frac{1}{\beta} \sum_{n=-\infty}^{\infty} \frac{1}{i\omega_n} = \frac{1}{\beta} \sum_{n=0}^{\infty} \left(\frac{1}{i\omega_n} + \frac{1}{i\omega_{-n-1}} \right) \quad (3.8.16)$$

$$= 0, \quad (3.8.17)$$

$$\begin{aligned} \text{since } \omega_{-n-1} &= (2(-n-1) + 1) \frac{\pi}{\beta} \\ &= -(2n+1) \frac{\pi}{\beta} \\ &= -\omega_n. \end{aligned} \quad (3.8.18)$$

Including the limit $\tau \rightarrow 0^-$ we get the expected result

$$\lim_{\tau \rightarrow 0^-} \frac{1}{\beta} \sum_{n=-\infty}^{\infty} \frac{e^{-i\omega_n \tau}}{i\omega_n} = \lim_{\tau \rightarrow 0^-} \frac{1}{\beta} \sum_{n=0}^{\infty} \left(\frac{e^{-i\omega_n \tau}}{i\omega_n} + \frac{e^{i\omega_n \tau}}{-i\omega_n} \right) \quad (3.8.19)$$

$$= \lim_{\tau \rightarrow 0^-} \frac{1}{\beta} \sum_{n=0}^{\infty} \frac{-2i \sin(\omega_n \tau)}{i\omega_n} \quad (3.8.20)$$

$$= \lim_{\tau \rightarrow 0^-} \frac{-2}{\beta} \sum_{n=0}^{\infty} \frac{\sin(\omega_n \tau)}{\omega_n} \quad (3.8.21)$$

$$= \lim_{\tau \rightarrow 0^-} \frac{-2}{\beta} \left(\beta \frac{\text{sgn}(\tau)}{4} \right), \text{ see Appendix} \quad (3.8.22)$$

$$= \frac{1}{2}. \quad (3.8.23)$$

Therefore, a correct treatment of Matsubara sums is absolutely crucial, since the error is completely uncontrolled.

General summations over Matsubara frequencies will always have the form

$$\frac{1}{\beta} \sum_{n=-\infty}^{\infty} F(i\omega_n) e^{-i\omega_n \tau}, \quad (3.8.24)$$

for some function $F(i\omega_n)$ with a finite $\tau \neq 0$. Except for special cases like we have just seen for the non-interacting Green's function in Eq. (3.8.23) we will usually not be able to evaluate these sums analytically. Since in the computer we can only sum up a finite number of values, we not only have to ensure a correct treatment of the infinite sum but also of the limit $\tau \rightarrow 0^\pm$. It should be clear that the more terms in the sum we can analytically evaluate before employing a numerical procedure the better. In practice, we always need to perform a cut-off of the number of Matsubara frequencies we can store in the computer

$$\frac{1}{\beta} \sum_{n=-\infty}^{\infty} F(i\omega_n) e^{-i\omega_n \tau} \approx \frac{1}{\beta} \sum_{n=-N}^N F(i\omega_n) e^{-i\omega_n \tau}, \quad (3.8.25)$$

so we have to make sure that either the infinite number of terms we miss are indeed negligible or treat them separately. A possible way is to expand the function $F(i\omega)$ for large ω_n (the data for small ω_n we will store in the computer) and treat these high frequency tails exactly, while summing only the remaining terms in the computer and then adding the analytic ones at the end. For the general case we expand F at high frequencies up to some, *e.g.* fourth order

$$F(i\omega_n) \approx c_0 + \frac{c_1}{i\omega_n} + \frac{c_2}{(i\omega_n)^2} + \frac{c_3}{(i\omega_n)^3} + \frac{c_4}{(i\omega_n)^4} \text{ for large } \omega_n. \quad (3.8.26)$$

The first coefficient c_0 has to be zero in order for the Fourier transform to converge. Then we split up the summation into the first N terms that we have stored in the computer and the remaining terms from $N + 1$ to ∞ , that can be well approximated by Eq. (3.8.26)

$$F(\tau) = \frac{1}{\beta} \sum_{n=-N}^N F(i\omega_n) e^{-i\omega_n \tau} + \frac{1}{\beta} \sum_{\substack{n=-\infty \\ n \notin [-N..N]}}^{\infty} F(i\omega_n) e^{-i\omega_n \tau} \quad (3.8.27)$$

$$\approx \frac{1}{\beta} \sum_{n=-N}^N F(i\omega_n) e^{-i\omega_n \tau} + \frac{1}{\beta} \sum_{\substack{n=-\infty \\ n \notin [-N..N]}}^{\infty} e^{-i\omega_n \tau} \left(\frac{c_1}{i\omega_n} + \frac{c_2}{(i\omega_n)^2} + \frac{c_3}{(i\omega_n)^3} + \frac{c_4}{(i\omega_n)^4} \right). \quad (3.8.28)$$

We now add and subtract the remaining terms to complete the sum in the right term

$$F(\tau) \approx \frac{1}{\beta} \sum_{n=-N}^N e^{-i\omega_n \tau} \left(F(i\omega_n) - \frac{c_1}{i\omega_n} - \frac{c_2}{(i\omega_n)^2} - \frac{c_3}{(i\omega_n)^3} - \frac{c_4}{(i\omega_n)^4} \right) \quad (3.8.29)$$

$$+ \frac{1}{\beta} \sum_{n=-\infty}^{\infty} e^{-i\omega_n \tau} \left(\frac{c_1}{i\omega_n} + \frac{c_2}{(i\omega_n)^2} + \frac{c_3}{(i\omega_n)^3} + \frac{c_4}{(i\omega_n)^4} \right) \quad (3.8.30)$$

The right term can be evaluated analytically with (see Appendix)

$$\frac{1}{\beta} \sum_{n=-\infty}^{\infty} e^{-i\omega_n \tau} \frac{c_1}{i\omega_n} = -\frac{c_1}{2} \operatorname{sgn}(\tau) \quad (3.8.31)$$

$$\frac{1}{\beta} \sum_{n=-\infty}^{\infty} e^{-i\omega_n \tau} \frac{c_2}{(i\omega_n)^2} = \frac{c_2}{4} (2\tau - \beta) \quad (3.8.32)$$

$$\frac{1}{\beta} \sum_{n=-\infty}^{\infty} e^{-i\omega_n \tau} \frac{c_3}{(i\omega_n)^3} = \frac{c_3}{4} \tau (\beta - \tau) \operatorname{sgn}(\tau) \quad (3.8.33)$$

$$\frac{1}{\beta} \sum_{n=-\infty}^{\infty} e^{-i\omega_n \tau} \frac{c_4}{(i\omega_n)^4} = \frac{c_4}{48} (2\tau - \beta)(2\tau^2 - 2\tau\beta - \beta^2) \quad (3.8.34)$$

By using the symmetry $F(-i\omega_n) = F^*(i\omega_n)$, which holds for the diagonal components of most

Matsubara functions we consider, and $\omega_{-n-1} = -\omega_n$, the first sum can be simplified as

$$F(\tau) = \frac{1}{\beta} \sum_{n=-N}^N \left(F(i\omega_n) - \frac{c_1}{i\omega_n} - \frac{c_2}{(i\omega_n)^2} - \frac{c_3}{(i\omega_n)^3} - \frac{c_4}{(i\omega_n)^4} \right) e^{-i\omega_n\tau} \quad (3.8.35)$$

$$= \frac{1}{\beta} \left[\sum_{n=0}^N \left(F(i\omega_n) - \frac{c_1}{i\omega_n} - \frac{c_2}{(i\omega_n)^2} - \frac{c_3}{(i\omega_n)^3} - \frac{c_4}{(i\omega_n)^4} \right) e^{-i\omega_n\tau} + \left(F(-i\omega_n) - \frac{c_1}{-i\omega_n} - \frac{c_2}{(-i\omega_n)^2} - \frac{c_3}{(-i\omega_n)^3} - \frac{c_4}{(-i\omega_n)^4} \right) e^{i\omega_n\tau} \right] \quad (3.8.36)$$

$$= \frac{1}{\beta} \sum_{n=0}^N \left[\left(F(i\omega_n) e^{-i\omega_n\tau} + [F(i\omega_n) e^{-i\omega_n\tau}]^* \right) + c_1 \frac{e^{i\omega_n\tau} - e^{-i\omega_n\tau}}{i\omega_n} - c_2 \frac{e^{i\omega_n\tau} + e^{-i\omega_n\tau}}{(i\omega_n)^2} + c_3 \frac{e^{i\omega_n\tau} - e^{-i\omega_n\tau}}{(i\omega_n)^3} - c_4 \frac{e^{i\omega_n\tau} + e^{-i\omega_n\tau}}{(i\omega_n)^4} \right] \quad (3.8.37)$$

$$= \frac{1}{\beta} \sum_{n=0}^N \left[2 \operatorname{Re} [F(i\omega_n) e^{-i\omega_n\tau}] + c_1 \frac{2i \sin(\omega_n\tau)}{\omega_n} - c_2 \frac{2 \cos(\omega_n\tau)}{(\omega_n)^2} + c_3 \frac{2i \sin(\omega_n\tau)}{(\omega_n)^3} - c_4 \frac{2 \cos(\omega_n\tau)}{(\omega_n)^4} \right] \quad (3.8.38)$$

$$= \frac{2}{\beta} \sum_{n=0}^N \left[\operatorname{Re} [F(i\omega_n) e^{-i\omega_n\tau}] + c_1 \frac{\sin(\omega_n\tau)}{\omega_n} + c_2 \frac{\cos(\omega_n\tau)}{\omega_n^2} - c_3 \frac{\sin(\omega_n\tau)}{\omega_n^3} - c_4 \frac{\cos(\omega_n\tau)}{\omega_n^4} \right] \quad (3.8.39)$$

$$= \frac{2}{\beta} \sum_{n=0}^N \left[\operatorname{Re} [F(i\omega_n)] \cos(\omega_n\tau) + \operatorname{Im} [F(i\omega_n)] \sin(\omega_n\tau) + c_1 \frac{\sin(\omega_n\tau)}{\omega_n} + c_2 \frac{\cos(\omega_n\tau)}{\omega_n^2} - c_3 \frac{\sin(\omega_n\tau)}{\omega_n^3} - c_4 \frac{\cos(\omega_n\tau)}{\omega_n^4} \right] \quad (3.8.40)$$

Therefore, we obtain in total for the summation

$$F(\tau) = \left(\frac{2}{\beta} \sum_{n=0}^N \operatorname{Re} [F(i\omega_n)] \cos(\omega_n\tau) + \operatorname{Im} [F(i\omega_n)] \sin(\omega_n\tau) + c_1 \frac{\sin(\omega_n\tau)}{\omega_n} + c_2 \frac{\cos(\omega_n\tau)}{\omega_n^2} - c_3 \frac{\sin(\omega_n\tau)}{\omega_n^3} - c_4 \frac{\cos(\omega_n\tau)}{\omega_n^4} \right) - \frac{c_1}{2} \operatorname{sgn}(\tau) + \frac{c_2}{4} (2\tau - \beta) + \frac{c_3}{4} \tau (\beta - \tau) \operatorname{sgn}(\tau) + \frac{c_4}{48} (2\tau - \beta)(2\tau^2 - 2\tau\beta - \beta^2) \quad (3.8.41)$$

This is a general expression for any $\tau \in (-\beta, \beta)$. In many cases like the filling we need the limit of $\tau \rightarrow 0^-$. Since we now have a finite sum, we can evaluate the limit of (3.8.41) explicitly taking the limit of every term in the sum

$$\lim_{\tau \rightarrow 0^-} F(\tau) = \frac{c_1}{2} - \frac{c_2}{4} \beta + \frac{c_4}{48} \beta^3 + \frac{2}{\beta} \sum_{n=0}^N \left(\operatorname{Re} [F(i\omega_n)] + \frac{c_2}{\omega_n^2} - \frac{c_4}{\omega_n^4} \right). \quad (3.8.42)$$

We see that the third order correction vanishes, so considering only the second order terms

$$\lim_{\tau \rightarrow 0^-} F(\tau) = \frac{c_1}{2} - \frac{c_2}{4} \beta + \frac{2}{\beta} \sum_{n=0}^N \left(\operatorname{Re} [F(i\omega_n)] + \frac{c_2}{\omega_n^2} \right), \quad (3.8.43)$$

already corresponds to a high frequency correction up to third order. Higher order terms can be included, but the analytical evaluation becomes more involved and the subtraction of the correction terms numerically unstable. This is due to the fact that the factors c^k/ω_n^k become quite large for the lowest frequencies, especially at low temperature, and have to be subtracted by another large analytical term, to finally yield a small number like the occupation. This leads to numerical noise that can grow quite fast with higher order corrections. Therefore, in practice a good compromise is to use a high frequency correction only up to fourth order.

Chapter 4

Analytic continuation

4.1 Introduction

Since in the Green's function formalism we will mostly work in the Matsubara representation on imaginary frequencies we are faced with the problem how to obtain the real frequency data only from the imaginary frequency information, *i.e.* how to go from

$$F(i\omega_n) \rightarrow F(\omega \pm i\eta), \quad (4.1.1)$$

for some function $F(z)$, $z \in \mathbb{C}$, where $\omega \in \mathbb{R}$ is on the real axis and $i\omega_n$ are the Matsubara frequencies on the imaginary axis. $\eta > 0$ is a small convergence parameter since F is usually discontinuous at the real axis. We restrict our analysis from now on to the open subset U given by

$$U := \{z \in \mathbb{C} : \text{Im}[z] > 0\}, \quad (4.1.2)$$

i.e. the upper complex plane. We assume that $F(i\omega_n)$, which could be the Green's function, Selfenergy or any other Matsubara function

$$F : U \rightarrow \mathbb{C}, \quad (4.1.3)$$

is a holomorphic function. We cannot extend U any further, since $F(z)$, resp. the Green's function has a discontinuity at the real axis. For holomorphic functions we have the Cauchy's integral formula, which states that

$$F(a) = \frac{1}{2\pi i} \oint_{\gamma} \frac{F(z)}{z - a} dz. \quad (4.1.4)$$

This formula holds for all functions that are holomorphic (complex differentiable) in a set $U \subset \mathbb{C}$ for all $a \in U$. The closed integration contour γ has to enclose the point a with a winding number of 1. Therefore, for the diagonal components of the Green's function $G_{a,a}(z)$, U needs to be either the lower or upper half of the complex plane and cannot intersect the real axis. For the positive Matsubara frequencies $\omega_n > 0$ on the imaginary axis, we obtain the relation

$$G_{a,a}(i\omega_n) = \frac{1}{2\pi i} \oint_{\gamma} \frac{G_{a,a}(z)}{z - i\omega_n} dz. \quad (4.1.5)$$

We now choose the integration path where we deform γ into a semicircle along the real axis but slightly shifted upwards $z = \omega + i\eta$, $\omega \in \mathbb{R}$, $\eta > 0$ small, and close the circle in the upper complex plane, as illustrated in Fig. 4.1. By this we do not leave the subset U on which the Green's function is holomorphic. Then we extend the integration along the real axis from $-\infty$ to ∞ which sends the radius of the semicircle contour also to ∞ . Since the Green's function decays at least as $\mathcal{O}(1/|z|)$,

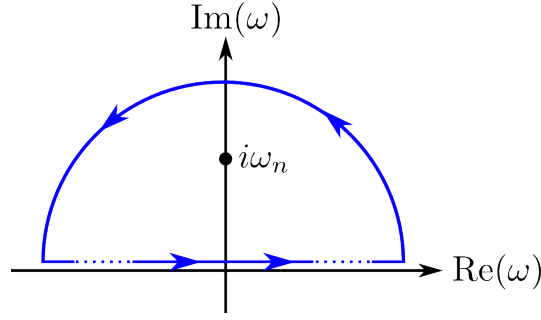


Figure 4.1: The integration contour to obtain the Green's function $G(i\omega_n)$ on the Matsubara axis by an integration along the real frequency axis via Cauchy's integral formula.

the contribution of the semi circle vanishes and we get

$$G_{a,a}(i\omega_n) = \lim_{\eta \rightarrow 0^+} \frac{1}{2\pi i} \int_{-\infty}^{\infty} \frac{G_{a,a}(\omega + i\eta)}{\omega + i\eta - i\omega_n} d\omega \quad (4.1.6)$$

$$= \frac{1}{2\pi i} \int_{-\infty}^{\infty} \frac{G_{a,a}^R(\omega)}{\omega - i\omega_n} d\omega, \quad (4.1.7)$$

where $\omega \in \mathbb{R}$ is the frequency on the real axis. We were able to evaluate the limit of $\eta \rightarrow 0$, since we defined the retarded Green's function as

$$\lim_{\eta \rightarrow 0^+} G_{a,a}(\omega + i\eta) = G_{a,a}^R(\omega), \quad (4.1.8)$$

and

$$\lim_{\eta \rightarrow 0^+} \frac{1}{\omega + i\eta - i\omega_n} = \frac{1}{\omega - i\omega_n}, \quad (4.1.9)$$

since for any real ω_n it follows that $\omega - i\omega_n \neq 0$.

One is tempted to simplify the result in Eq. (4.1.7) a little bit more by using the symmetry relation $G_{a,a}(i\omega_n) = G_{a,a}^*(-i\omega_n)$. This will actually lead to a wrong result, since we restricted our domain to the upper complex plane U , while $G_{a,a}^*(-i\omega_n)$ is in the lower complex plane! Since Cauchy's integral formula assumes the function to be holomorphic, the function does not have a discontinuity at the real axis if we were to extend U to the whole complex plane. Therefore, the function obtained by Cauchy's integral formula at negative Matsubara frequencies will in general be different from $G_{a,a}^*(i|\omega_n|)$. Using this property leads to the following wrong result

$$0 = G_{a,a}(i\omega_n) - G_{a,a}^*(-i\omega_n) \quad (4.1.10)$$

$$= \frac{1}{2\pi i} \int_{-\infty}^{\infty} \frac{G_{a,a}^R(\omega)}{\omega - i\omega_n} d\omega - \frac{1}{2\pi(-i)} \int_{-\infty}^{\infty} \frac{(G^R)_{a,a}^*(\omega)}{\omega - (-i)(-\omega_n)} d\omega \quad (4.1.11)$$

$$= \frac{1}{2\pi i} \int_{-\infty}^{\infty} \frac{G_{a,a}^R(\omega) + (G^R)_{a,a}^*(\omega)}{\omega - i\omega_n} d\omega \quad (4.1.12)$$

$$= \frac{1}{\pi i} \int_{-\infty}^{\infty} \frac{\text{Re}[G_{a,a}^R(\omega)]}{\omega - i\omega_n} d\omega \quad (4.1.13)$$

From this it seems when evaluating the integral at the Matsubara frequencies, the contribution of the real part of $G_{a,a}(\omega)$ drops out and we have

$$G_{a,a}(i\omega_n) = \frac{1}{2\pi} \int_{-\infty}^{\infty} \frac{\text{Im}[G_{a,a}^R(\omega)]}{\omega - i\omega_n} d\omega, \quad (4.1.14)$$

which is wrong by a factor of 2, as we will see now. To simplify Eq. (4.1.7), we use the same idea of removing the real part from the integration, but for this we make use of the relations between the real and imaginary part of a holomorphic function given by the Kramers-Kronig relations. Remember that we are still restricted to the open subset U above the real axis. For a holomorphic function $F : U \rightarrow \mathbb{C}$ the Kramers-Kronig relations state

$$\operatorname{Re}[F(\omega)] = \frac{1}{\pi} \mathcal{P} \int_{-\infty}^{\infty} \frac{\operatorname{Im}[F(\omega')]}{\omega' - \omega} d\omega' \quad (4.1.15)$$

$$\operatorname{Im}[F(\omega)] = -\frac{1}{\pi} \mathcal{P} \int_{-\infty}^{\infty} \frac{\operatorname{Re}[F(\omega')]}{\omega' - \omega} d\omega', \quad (4.1.16)$$

where both $\omega, \omega' \in \mathbb{R}$. Since we restricted ourselves to U , $F(\omega)$ is to be understood as $\lim_{\eta \rightarrow 0^+} F(\omega + i\eta)$. The Kramers-Kronig relations are just a special case of Cauchy's integral formula, which is quite evident due to their similar form. By replacing the real part in the Cauchy formula in Eq. (4.1.7) with the Kramers-Kronig relations from Eq. (4.1.15), we get

$$G_{a,a}(i\omega_n) = \frac{1}{2\pi i} \int_{-\infty}^{\infty} \frac{G_{a,a}^R(\omega)}{\omega - i\omega_n} d\omega \quad (4.1.17)$$

$$= \frac{1}{2\pi i} \int_{-\infty}^{\infty} \frac{\operatorname{Re}[G_{a,a}^R(\omega)]}{\omega - i\omega_n} d\omega + \frac{1}{2\pi} \int_{-\infty}^{\infty} \frac{\operatorname{Im}[G_{a,a}^R(\omega)]}{\omega - i\omega_n} d\omega \quad (4.1.18)$$

$$= \frac{1}{2\pi^2 i} \int_{-\infty}^{\infty} \mathcal{P} \int_{-\infty}^{\infty} \frac{1}{\omega - i\omega_n} \frac{\operatorname{Im}[G_{a,a}^R(\omega')]}{\omega' - \omega} d\omega' d\omega + \frac{1}{2\pi} \int_{-\infty}^{\infty} \frac{\operatorname{Im}[G_{a,a}^R(\omega)]}{\omega - i\omega_n} d\omega \quad (4.1.19)$$

$$= \frac{1}{2\pi^2 i} \int_{-\infty}^{\infty} \frac{\pi i \operatorname{Im}[G_{a,a}^R(\omega')]}{\omega' - i\omega_n} d\omega' + \frac{1}{2\pi} \int_{-\infty}^{\infty} \frac{\operatorname{Im}[G_{a,a}^R(\omega)]}{\omega - i\omega_n} d\omega \quad (4.1.20)$$

$$= \frac{1}{\pi} \int_{-\infty}^{\infty} \frac{\operatorname{Im}[G_{a,a}^R(\omega)]}{\omega - i\omega_n} d\omega, \quad (4.1.21)$$

where we have used that

$$\mathcal{P} \int_{-\infty}^{\infty} \frac{1}{\omega - i\omega_n} \frac{1}{\omega' - \omega} d\omega = \frac{\pi i}{\omega' - i\omega_n}. \quad (4.1.22)$$

Similarly, if we use the Kramers-Kronig relation to replace the imaginary part we get

$$G_{a,a}(i\omega_n) = \frac{1}{\pi i} \int_{-\infty}^{\infty} \frac{\operatorname{Re}[G_{a,a}^R(\omega)]}{\omega - i\omega_n} d\omega. \quad (4.1.23)$$

Since we have made no restriction for $i\omega_n$ except to lie in the upper complex plane U , this relation also holds for all points z in U , *i.e.*

$$G_{a,a}(z) = \frac{1}{\pi} \int_{-\infty}^{\infty} \frac{\operatorname{Im}[G_{a,a}^R(\omega)]}{\omega - z} d\omega \quad (4.1.24)$$

$$= \frac{1}{\pi i} \int_{-\infty}^{\infty} \frac{\operatorname{Re}[G_{a,a}^R(\omega)]}{\omega - z} d\omega. \quad (4.1.25)$$

This result now provides us with a way of how to generate the Matsubara Green's function from the retarded Green's function. In practice the problem of analytic continuation is to go from $G_{a,a}(i\omega_n) \rightarrow G_{a,a}^R(\omega)$, so Cauchy's integral formula actually does exactly the opposite of what we need! The most intuitive approach to obtain $G_{a,a}^R(\omega)$ from $G_{a,a}(i\omega_n)$ is to discretize Eq. (4.1.21) on some real frequency interval $[\omega_{min}, \omega_{max}]$ into N bins with $\omega_0 = \omega_{min}$, $\omega_N = \omega_{max}$ where we

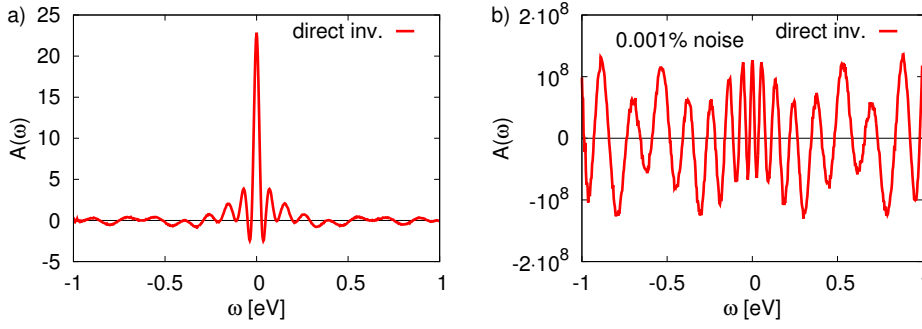


Figure 4.2: a) The negative imaginary part of the retarded Green's function on the real axis as obtained by direct inversion (see Eq. (4.1.33)) from $G(i\omega_n) = \frac{1}{i\omega_n}$. The correct analytic continuation is $\text{Im} G^R(\omega) = -\pi\delta(\omega)$. b) $-\text{Im} G^R(\omega)$ for the same input data, but with only 0.001% of random noise added to $G(i\omega_n)$. Since the problem is ill-conditioned, even very small changes in the input lead to strong modifications and unphysical features in the output.

assume $A(\omega) \neq 0$ and then invert the resulting Matrix equation

$$G_{a,a}(i\omega_n) = \frac{1}{\pi} \int_{-\infty}^{\infty} \frac{\text{Im}[G_{a,a}^R(\omega)]}{\omega - i\omega_n} d\omega \quad (4.1.26)$$

$$= \lim_{N \rightarrow \infty} \sum_{m=0}^N \frac{1}{\pi} \frac{\omega_{m+1} - \omega_m}{\omega_m - i\omega_n} \text{Im}[G_{a,a}^R(\omega_m)] \quad (4.1.27)$$

$$\Rightarrow \mathbf{g}_n = (A\mathbf{g}^R)_n, \quad (4.1.28)$$

with

$$A_{nm} = \frac{1}{\pi} \frac{\omega_{m+1} - \omega_m}{\omega_m - i\omega_n} \quad (4.1.29)$$

$$\mathbf{g}_n = G_{a,a}(i\omega_n) \quad (4.1.30)$$

$$\mathbf{g}_m^R = \text{Im}[G_{a,a}^R(\omega_m)] \quad (4.1.31)$$

$$(4.1.32)$$

which leads to

$$\text{Im}[G_{a,a}^R(\omega_m)] = (A^{-1}\mathbf{g})_m, \quad (4.1.33)$$

where A^{-1} is the pseudo inverse of A , which means that A^{-1} is the matrix which solves the least-squares problem $A\mathbf{x} = \mathbf{b}$, *i.e.* it minimizes $|A\mathbf{x} - \mathbf{b}|^2$. While being exact, the problem with Eq. (4.1.33) is that the Matrix elements fall off very quickly for large n, m , which leads to A^{-1} being almost singular and ill-conditioned. In practice this will lead to large numerical errors that are extremely sensitive to very small changes in the input data $\mathbf{g}_n = G_{a,a}(i\omega_n)$. As an example we have performed the direct inversion on the Green's function $G(i\omega_n) = \frac{1}{i\omega_n}$, which corresponds to just a Delta peak on the real axis $\text{Im}[G^R(\omega)] = -\pi\delta(\omega)$, and plotted the result in Fig. 4.2 a). Even though $G(i\omega_n)$ was generated within double precision, the direct inversion shows an oscillatory behaviour and only qualitatively resembles the correct result. Since we will later use a Monte Carlo approach to generate the Matsubara Green's function, the input data will always contain some numerical noise. Since the inversion is ill-conditioned, even a very small amount of noise will lead to large fluctuations on the real axis, rendering the result completely unphysical, as can be seen in Fig. 4.2 b).

This extreme sensitivity to noise is the result of Cauchy's integral equation (see Eq. (4.1.21)), which ensures that $G(i\omega_n)$ is a smooth function even if $G^R(\omega)$ is not smooth, since the integral

of a continuous function will always be differentiable. But in practice $G(i\omega_n)$ will always contain some degree of noise, which causes the function to become non-smooth and thus delta function-like features have to appear in $G^R(\omega)$ to create the kinks in $G(i\omega_n)$ introduced by the noise. Therefore, since the true solution does not generate exactly the input data $G(i\omega_n)$, we have to resort to approximate analytic continuation schemes that allow for some deviation and do not “fit” the noise on the imaginary axis.

4.2 The Padé approximation

One possible way of obtaining a function $f(z)$ in the whole complex plane that approximately resembles $G(i\omega_n)$ on the imaginary axis is the Padé approximation [89, 90]. The Padé approximant is an approximation of a function by a ratio of two power series of a given order. Its power series agrees with the power series of the approximated function but due to being a rational function poles can also be well represented, which makes the Padé approximation in this regard superior to the Taylor series. The general form of the Padé approximant is the rational function

$$R(z) := \frac{\sum_{k=0}^N a_k z^k}{1 + \sum_{m=1}^M b_m z^m}, \quad (4.2.1)$$

with polynomials in the nominator and denominator of order $N \geq 0$, resp. $M \geq 1$. While the coefficients can in general be obtained by solving the equation

$$f(z) - \frac{\sum_{k=0}^N a_k z^k}{1 + \sum_{m=1}^M b_m z^m} = 0, \quad (4.2.2)$$

for $N + M + 1$ points, a more direct way is to make use of Padé tables [90] which coefficients can be used to express $R(z)$ as a continued fraction. Let us assume that we have a set of N points $z_n, n = 0..N - 1$, where we know the values of $f_n := f(z_n)$. Then the coefficients of the Padé table $P_{n,m}$ are given by

$$P_{0,m} = f_m, \quad \text{for } m = 0..N - 1 \quad (4.2.3)$$

$$P_{n,m} = \frac{P_{n-1,n-1} - P_{n-1,m}}{P_{n-1,m}(z_m - z_{n-1})}, \quad \text{for } m = 1..N - 1, n = 1..m. \quad (4.2.4)$$

Note that only the upper triangle of P is needed. The Padé approximant is then given as

$$R(z) = \frac{P_{0,0}}{1 + \frac{P_{1,1}(z - z_0)}{1 + \frac{P_{2,2}(z - z_1)}{1 + \frac{P_{3,3}(z - z_2)}{1 + \dots}}}}. \quad (4.2.5)$$

For example, the Padé approximation can exactly represent the function $f(z) = \frac{1}{z}$ and the expansion stops at the second coefficient for any points $z_0, z_1, z_2, \dots \neq 0$

$$P = \begin{pmatrix} 1/z_0 & 1/z_1 & 1/z_2 \\ & 1/z_0 & 1/z_0 \\ & & 0 \end{pmatrix}, \quad (4.2.6)$$

which leads to

$$R(z) = \frac{1/z_0}{1 + \frac{1/z_0(z - z_0)}{1 + 0}} = \frac{1}{z}. \quad (4.2.7)$$

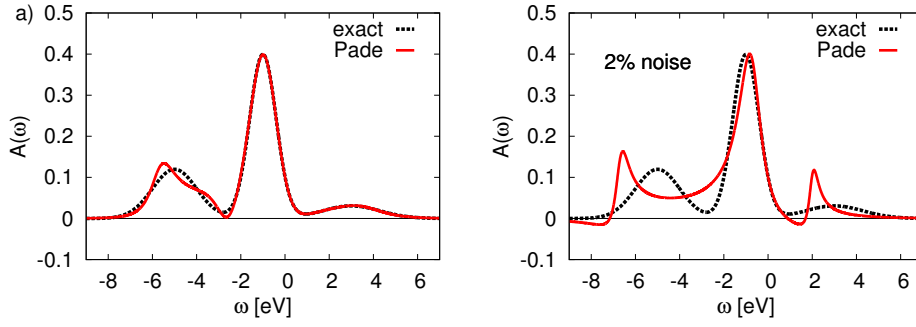


Figure 4.3: a) The negative imaginary part of the retarded Green's function on the real axis as obtained by the Padé approximation (red line) compared to the correct spectral function (black dashed line). If the input on the Matsubara axis is completely free of any numerical noise the Padé approximation is able to reproduce the original spectra with high accuracy.

b) $-\text{Im} G^R(\omega)$ for the same input data, but with 2% of random noise added to $G(i\omega_n)$. Since the Padé approximation approximates $G(z)$ by a rational function and no other restrictions like positivity can be easily imposed, even small numerical noise in the input data can lead to significant unphysical features on the real axis.

In general the Padé approximation is far superior over the direct inversion method, since it does not exactly reproduce the noisy data $G(i\omega_n)$ but only approximately, which can filter out most of the unphysical poles on the real axis that would result from an exact “fit”. In practice, if the quality of the input is very high, this method can give quite reliable results. Still, it does not respect important properties like positivity or normalization of the spectral function and is very unreliable for small amounts of noise as can be seen in Fig. 4.3.

4.3 The maximum entropy method

A famous and widely used approach for filtering out unphysical noise and requiring non-negativity of the spectral function is the so called *maximum entropy method* (MEM) [91] based on Bayesian statistical inference. It is most commonly formulated in imaginary time τ , so we will shortly review the main ideas for Matsubara Green's functions in imaginary time $G(\tau)$, but will change later to imaginary frequencies for most parts of the thesis. Recall that the equation we want to solve for $\text{Im} G^R(\omega)$ was

$$G(i\omega_n) = \frac{1}{\pi} \int_{-\infty}^{\infty} \frac{\text{Im}[G^R(\omega)]}{\omega - i\omega_n} d\omega, \quad (4.3.1)$$

where we omit the orbital- and spin degrees of freedom for better readability. When the input data is given on the imaginary time axis $G(\tau)$ instead of Matsubara frequency, we do not have to calculate the Fourier transform of $F(\tau)$, which introduces further numerical errors, but instead we can work directly in imaginary time. Application of the Fourier transform to Cauchy's equation (4.1.21)

yields

$$G(\tau) = \frac{1}{\beta} \sum_{n=-\infty}^{\infty} e^{-i\omega_n \tau} G(i\omega_n) \quad (4.3.2)$$

$$= \frac{1}{\pi} \int_{-\infty}^{\infty} \text{Im}[G^R(\omega)] \left(\frac{1}{\beta} \sum_{n=-\infty}^{\infty} \frac{e^{-i\omega_n \tau}}{\omega - i\omega_n} \right) d\omega \quad (4.3.3)$$

$$= \frac{1}{\pi} \int_{-\infty}^{\infty} \text{Im}[G^R(\omega)] \frac{e^{-\tau\omega}}{e^{-\beta\omega} + 1} d\omega \quad (4.3.4)$$

$$= \frac{1}{\pi} \int_{-\infty}^{\infty} \frac{\text{Im}[G^R(\omega)]}{e^{(\tau-\beta)\omega} + e^{\tau\omega}} d\omega \quad (4.3.5)$$

$$= - \int_{-\infty}^{\infty} A(\omega) \frac{e^{-\tau\omega}}{e^{-\beta\omega} + 1} d\omega, \quad (4.3.6)$$

where we have defined $A(\omega) = -\frac{1}{\pi} \text{Im}[G^R(\omega)]$. Note that this form ensures (the diagonal components of) $G(\tau)$ to be purely real, as we have found in chapter 3.5 as well as negative semi-definiteness. Please note that our definition of the Kernel has a negative sign compared to most other publications. Let us assume we have the input data given as the numerically obtained $G_{meas}(\tau)$, which contains some degree of unphysical noise. Proposing a possible function for $A(\omega)$, we use Eq. (4.3.6) to obtain $G(\tau)$. How well this function agrees with the measured data $G_{meas}(\tau)$ can be characterized with the goodness-of-fit-measure χ^2

$$\chi^2 = \int_0^\beta \frac{1}{\sigma^2(\tau)} |G_{meas}(\tau) - G(\tau)|^2 d\tau \quad (4.3.7)$$

$$= \int_0^\beta \frac{1}{\sigma^2(\tau)} \left| G_{meas}(\tau) - \int_{-\infty}^{\infty} K(\tau, \omega) A(\omega) d\omega \right|^2 d\tau, \quad (4.3.8)$$

with the integration kernel $K(\tau, \omega) = -e^{-\tau\omega} / (e^{-\beta\omega} + 1)$. Here, $\sigma(\tau)$ specifies a best-guess estimate of the measurement error in the input data $G_{meas}(\tau)$ at each point τ . Since the search for the function $A(\omega)$ which minimizes χ^2 will not yield any physical result due to the numerical noise contained in $G_{meas}(\tau)$, the maximum entropy method is based on a different approach that makes use of Bayesian interference and the principle of maximum entropy. Assume we have given two events a, b with corresponding probabilities $\text{Pr}[a]$ and $\text{Pr}[b]$. Then Baye's theorem states that

$$\text{Pr}[a|b] = \frac{\text{Pr}[b|a] \text{Pr}[a]}{\text{Pr}[b]} \quad (4.3.9)$$

where $\text{Pr}[a|b]$ is the conditional probability of a given knowledge of the result b , and $\text{Pr}[b|a]$ vice versa. For our analytic continuation the event a is the spectral function $A(\omega)$ and b is the input $G_{meas}(\tau)$. Therefore, $\text{Pr}[A|G_{meas}]$ corresponds to the probability of $A(\omega)$ being the true spectral function given the knowledge of G_{meas} . In the maximum entropy method the criterion for the best solution is the function $A(\omega)$ that maximizes $\text{Pr}[A|G_{meas}]$. For this, a so-called *default model* $D(\omega)$ for the spectral function $A(\omega)$ is introduced, which is a smooth function that already includes all prior information known about the true result, like normalization or maxima of the spectral weight. $D(\omega)$ is then used as the reference model that serves as the zero entropy configuration, so we can define the entropy $S[A]$ relative to the smooth default model as

$$S[A] = - \int A(\omega) \ln \left(\frac{A(\omega)}{D(\omega)} \right) d\omega. \quad (4.3.10)$$

This entropy has a maximum value of zero when $A(\omega)$ equals the default model $D(\omega)$ and becomes more negative the more $A(\omega)$ differs from the default model. It can then be shown that the conditional probability can be written as

$$\text{Pr}[A|G_{meas}] \propto e^{\alpha S - \frac{1}{2}\chi^2}, \quad (4.3.11)$$

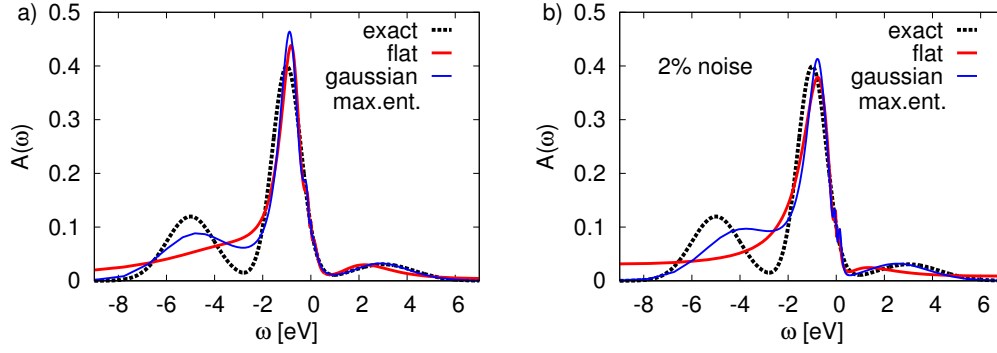


Figure 4.4: a) The negative imaginary part of the retarded Green's function on the real axis as obtained by the maximum entropy method (code provided by Ref. [94]) for a flat (red line) and Gaussian (blue line) default model, compared to the correct spectral function (black dashed line). The MEM is able to capture the main features quite well when there is no noise in the input data but depends quite strongly on the default model.

b) $-\text{Im} G^R(\omega)$ for the same input data, but with 2% of random noise added to $G(i\omega_n)$. The MEM still obtains the correct qualitative aspects of the spectral function but in general sharp features like the maximum at negative energies become washed out.

where α is a regularization parameter. Finding the function $A(\omega)$ that maximizes $\text{Pr}[A|G_{meas}]$ is thus equivalent to maximizing $\alpha S - \frac{1}{2}\chi^2$. In this sense the parameter α acts like a regulator for $A(\omega)$, defining how much importance is given to either minimizing the deviation χ^2 or the difference to the default model specified by S . Therefore, the result will in general depend on the value of α . Multiple methods have been suggested (see for example Ref. [91]) of how to determine the best value for α , like choosing α in a way that it maximizes $\text{Pr}[\alpha, G_{meas}]$, *i.e.* the conditional probability for α given G_{meas} , which is called the *classic maximum entropy solution*. Other methods suggest to use an average over all $A_\alpha(\omega)$, or similar, Bryan [92] proposed an average of all spectral functions but with a corresponding weight $\text{Pr}[\alpha|G_{meas}, D]$.

In practice, one employs numerical optimization algorithms like gradient search techniques for maximization of $\alpha S - \frac{1}{2}\chi^2$. Nonetheless, a formal solution for the maximizing spectrum $\bar{A}(\omega)$ can be found [93], which takes the self-consistent form

$$\bar{A}(\omega) = e^{\alpha\mu} D(\omega) \exp \left\{ -2\alpha \int_0^\beta \frac{1}{\sigma^2(\tau)} \left(\int_{-\infty}^\infty \bar{A}(\omega') K(\tau, \omega') d\omega' - G_{meas}(\tau) \right) K(\tau, \omega) d\tau \right\}, \quad (4.3.12)$$

where μ is a Lagrange multiplier for enforcing the right normalization of the solution $\bar{A}(\omega)$. Investigation of the limit $\alpha \rightarrow 0$ results in $\bar{A}(\omega) = e^{\alpha\mu} D(\omega)$, *i.e.* the spectrum is equal to the default model and $S[A]$ is maximized. For the other limit $\alpha \rightarrow \infty$, Eq. (4.3.12) demands that $\int_{-\infty}^\infty \bar{A}(\omega') K(\tau, \omega') d\omega' - G_{meas}(\tau) \rightarrow 0$, *i.e.* the spectrum exactly reproduces the noisy input data.

In Fig. 4.4 we show an example of Bryan's maximum entropy method using the code from Ref. [94] applied to the same spectrum used in the example for the Padé approximation in Fig. 4.3. A flat and a Gaussian default model was used with variance 2 eV, and we compare the case where the data on the Matsubara axis was generated exactly and the case where a small amount of noise was included. We see that the MEM is able to reproduce the original data to very high accuracy with the Gaussian default model, but does not capture the lower Hubbard band-like feature when using the flat default model. Otherwise the agreement is quite good and only small deviations can be found in the width of the quasiparticle peak, which turns out to be more narrow than the correct result.

When adding 2% of random noise to the data on the Matsubara axis, the result of the MEM

becomes more sensitive to the default model and the error estimate σ . What we generally find is that the width of the quasiparticle peak becomes even more narrow and the maximum at negative energies, if captured at all, moves up in energy so that the small dip is almost completely gone. Directly at the Fermi level small artefacts also appear but qualitatively the result is much more accurate and controlled than the Padé approximation. Still, the proper choice of the default model remains an open issue.

4.4 Stochastic analytic continuation

As we have seen, in the process of finding an appropriate function $f(z)$ for analytic continuation in practice we always have to make a compromise between how well we can represent the noisy input data on the one hand and the smoothness of $f(z)$ on the other hand. Recall that the equation we want to solve for $\text{Im } G^R(\omega)$ is

$$G(i\omega_n) = \frac{1}{\pi} \int_{-\infty}^{\infty} \frac{\text{Im}[G^R(\omega)]}{\omega - i\omega_n} d\omega. \quad (4.4.1)$$

Since we know the left side $G(i\omega_n)$ of the integral equation, one can think of numerically generating physically reasonable functions $\text{Im } G^R(\omega)$ that have the proper sign, normalization, no unphysical divergences etc., perform the integral and compare the result to $G(i\omega_n)$. Indeed, early on it was proposed, for example in Ref. [95], to take the average of a large sequence of possible solutions that approximately generate the right values $G(i\omega_n)$ as the final result. By this, one hopes that spurious features that are supposed to appear at random average out, while physical and robust features are reinforced. However, this method does not hold any physical justification and we have no means of specifying when the procedure is converged or if we actually have included the right functions in the sequence. Still, in practice one usually observes that the average of possible spectra produce a better result than the most likely spectrum as obtained from the maximum entropy method. For example, Sandvik [96] has shown that a “thermal average” of all possible spectra, weighted with the Boltzmann factor $e^{-\alpha\chi^2}$, where χ^2 is the goodness-of-fit-measure, *i.e.* the squared deviation on the imaginary axis and α an artificial inverse sampling temperature, consistently yields results that are closer to the true spectrum obtained by exact diagonalization. This averaging approach was made systematic by Beach [93], who showed that the “thermal” sampling of spectral functions at a fictitious inverse temperature α is a very natural way to analytic continuation and resembles the simulation of a physical ensemble. In fact, it is the dynamical generalization of the maximum entropy method, which is realized as the mean-field solution of this fictitious physical system. In the following we will now show the most important aspects of Stochastic analytic continuation, following the ideas of the original paper by Beach [93].

Let us assume that we have given the function $G(i\omega_n)$ on N Matsubara points $i\omega_n$, obtained by some numerical procedure so that it contains some degree of numerical noise. Then every physical form of the function $\text{Im } G^R(\omega)$ will not exactly generate $G(i\omega_n)$ on the imaginary axis, which can be characterized by the goodness-of-fit-measure χ^2

$$\chi^2[A] = \sum_{n=0}^{N-1} \frac{1}{\sigma^2(i\omega_n)} \left| G(i\omega_n) - \int_{-\infty}^{\infty} \frac{A(\omega)}{i\omega_n - \omega} d\omega \right|^2, \quad (4.4.2)$$

where we have set $A(\omega) = -\frac{1}{\pi} \text{Im } G^R(\omega)$. $\sigma(i\omega_n)$ is the estimate for the stochastic error in $G(i\omega_n)$ at $i\omega_n$, *i.e.* the deviation at each Matsubara frequency is weighted according to the accuracy of the measured data point (for example as obtained from a Monte Carlo procedure). We now interpret Eq. (4.4.2) as the Hamiltonian for a system of classical fields $A(\omega)$, so they describe a fictitious system where each “configuration” can be ascribed a fictitious energy

$$H[A] = \chi^2[A]. \quad (4.4.3)$$

Then let us assume we keep the system at the artificial inverse temperature α , so that we can define the usual partition function as

$$Z = \int e^{-\alpha H[A]} dA, \quad (4.4.4)$$

and the thermal average of $A(\omega)$ is then

$$\langle A(\omega) \rangle = \frac{1}{Z} \int A(\omega) e^{-\alpha H[A]} dA. \quad (4.4.5)$$

For the limiting case of zero temperature $\alpha \rightarrow \infty$, $\langle A(\omega) \rangle$ will be simply the ground-state configuration with the lowest value of $\chi^2 = 0$. This corresponds to the spectrum which exactly reproduces the data on the imaginary axis and thus will contain unphysical features. In other limit of infinite temperature $\alpha \rightarrow 0$ all possible spectral functions $A(\omega)$ will equally contribute with the same weight to $\langle A(\omega) \rangle$ and thus the result will be independent of the input $G(i\omega_n)$ and just a constant $\left(\int_{-\infty}^{\infty} A(\omega) d\omega \right)^{-1}$. These limits are exactly the limits of the maximum entropy method with a constant default model, with the fictitious temperature being the regularization parameter.

For further insight we can now turn to approximate solutions of the Hamiltonian in Eq. (4.4.2). Expanding the square and dropping the constant term that does not depend on $A(\omega)$ we obtain

$$H[A] = H_0 + H_{int} \quad (4.4.6)$$

$$= \int_{-\infty}^{\infty} \epsilon(\omega) A(\omega) d\omega + \frac{1}{2} \int_{-\infty}^{\infty} \int_{-\infty}^{\infty} A(\omega) V(\omega, \omega') A(\omega') d\omega' d\omega, \quad (4.4.7)$$

where the free dispersion is given by

$$\epsilon(\omega) = -2 \sum_{n=0}^{N-1} \frac{1}{\sigma^2(i\omega_n)} \frac{G(i\omega_n)}{i\omega_n - \omega}, \quad (4.4.8)$$

and the interacting potential

$$V(\omega, \omega') = 2 \sum_{n=0}^{N-1} \frac{1}{\sigma^2(i\omega_n)} \frac{1}{(i\omega_n - \omega)(i\omega_n - \omega')}. \quad (4.4.9)$$

As the first test case let us consider the non-interacting system $H = H_0$. In addition, let us introduce the requirement that all functions $A(\omega)$ should be normalized to some constant $C = \int_{-\infty}^{\infty} A(\omega) d\omega$. With this, we can write the partition function as

$$Z = \int \delta \left(\int_{-\infty}^{\infty} A(\omega) d\omega - C \right) e^{-\alpha H_0[A]} dA. \quad (4.4.10)$$

If we use the representation of the delta function given by

$$\delta(X) = \int_{-\infty}^{\infty} e^{iyX} dy, \quad (4.4.11)$$

we can rewrite the partition function as

$$Z = \int_{-\infty}^{\infty} e^{-iyC} \int e^{-\alpha \int_{-\infty}^{\infty} (\epsilon(\omega) - iy/\alpha) A(\omega) d\omega} dA dy. \quad (4.4.12)$$

Since the Hamiltonian corresponds to a non-interacting system in thermal equilibrium at temperature $1/\alpha$, the distribution of configurations is exactly given by the Maxwell-Boltzmann statistics

$$Z = \int_{-\infty}^{\infty} e^{-\alpha(\epsilon(\omega) - iy/\alpha)} d\omega, \quad (4.4.13)$$

from which the average spectrum follows as

$$\langle A(\omega) \rangle = -\frac{1}{\alpha} \frac{\partial}{\partial \epsilon(\omega)} \ln Z = e^{-\alpha(\epsilon(\omega) - \mu)}, \quad (4.4.14)$$

which means that the spectra are distributed according to the Maxwell-Boltzmann statistics with respect to their energy relative to the fictitious chemical potential $\mu = iy/\alpha$. μ is then the controlling factor for the normalization of $\langle A(\omega) \rangle$, corresponding to the number of particles in a physical system.

Now let us switch on the interaction $V(\omega, \omega')$, but we assume that the fluctuations of $A(\omega)$ about its mean $\langle A(\omega) \rangle$ are negligible, *i.e.*

$$(A(\omega) - \langle A(\omega) \rangle)(A(\omega') - \langle A(\omega') \rangle) \approx 0, \quad (4.4.15)$$

which leads, using the standard mean-field approach, to the following Hamiltonian

$$H_{MF} = \int_{-\infty}^{\infty} E(\omega) A(\omega) d\omega + \text{const.}, \quad (4.4.16)$$

where

$$E(\omega) = \left. \frac{\delta H[A]}{\delta A(\omega)} \right|_{A(\omega) = \langle A(\omega) \rangle} = \epsilon(\omega) + \int_{-\infty}^{\infty} V(\omega, \omega') \langle A(\omega') \rangle d\omega'. \quad (4.4.17)$$

Since $E(\omega)$ does no longer depend explicitly on $A(\omega)$ but only on $\langle A(\omega) \rangle$, the expression for the partition function and thermal averaged spectrum are identical to the ones in Eq. (4.4.13) and (4.4.14) with $\epsilon(\omega)$ replaced by the effective field $E(\omega)$, which leads to the self-consistent equation

$$\langle A(\omega) \rangle_{MF} = e^{\alpha\mu} \exp \left\{ -\alpha \left(\epsilon(\omega) + \int_{-\infty}^{\infty} V(\omega, \omega') \langle A(\omega') \rangle d\omega' \right) \right\}. \quad (4.4.18)$$

This is formally completely identical to the expression of the maximum entropy method in Eq. (4.3.12) for a constant default model, which in turn means that the maximum entropy method is the mean-field solution of the interacting classical system described by the Hamiltonian H . In contrast, the thermal averaging method introduced by Sandvik [96] then corresponds to the fully dynamical solution at the inverse temperature α . This explains the observation that the maximum entropy method usually prefers smoother solutions with less sharp features than found in the sampling method at low temperature. Furthermore, Beach additionally showed [93] that different default models in the MEM correspond to a change of the integration measure $d\omega$ in the stochastic sampling method. If we were to make a change of variables $x = \phi(\omega)$, the default model would be equal to $D(x) = N\phi'(x)$, with N being a normalization factor. Thus, the stochastic sampling approach to analytic continuation relates in the same way to the maximum entropy method as the well-known Metropolis sampling relates to the mean-field solution of the Ising model, which as a matter of principle makes it superior to the maximum entropy method. It still retains the free parameter α , though, acting as a fictitious temperature that controls how well the sampled function has to agree with the noisy Matsubara data. Both Sandvik [96] and Beach [93] noticed that the error $\chi^2(\alpha)$ shows similar features of a phase transition from an ordered to a disordered phase which is interpreted as the transition from the good-fitting to the ill-fitting regime as a function of α . Therefore, Beach suggested the sum over all average spectral functions $A_\alpha(\omega)$ in the ordered regime in combination with a parallel tempering approach [93, 97] as the final spectral function.

In Fig. 4.5 we show an example of the stochastic analytic continuation applied to the same input data as in the Padé (Fig. 4.3) and MEM (Fig. 4.4) case, making use of the parallel tempering algorithm suggested in [93], which removes the necessity of choosing a certain value of α . We can see that the stochastic approach is very similar to the maximum entropy method for zero noise and only provides a small improvement for the representation of the dip at lower energies, but the small maximum at positive energies is not as well represented as in the MEM. Inclusion of 2% random noise on the input data leads surprisingly to hardly any noticeable difference in the resulting

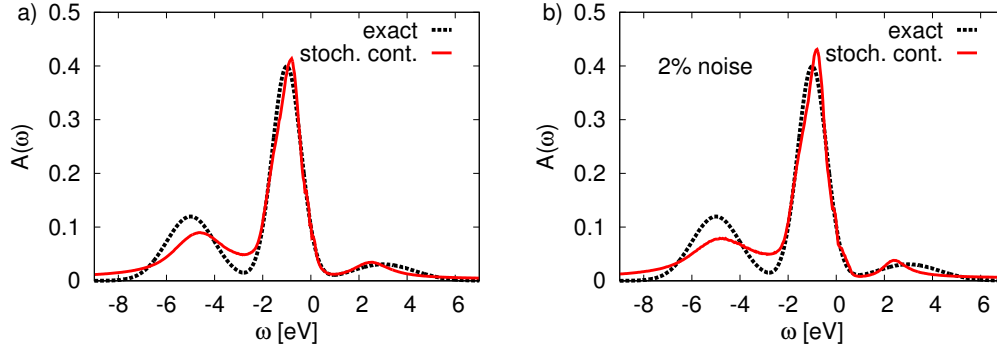


Figure 4.5: *a)* The negative imaginary part of the retarded Green's function on the real axis as obtained by stochastic analytic continuation (red line) compared to the correct spectral function (black dashed line). While the stochastic analytic continuation does a good job of capturing the main features if there is no noise in the input data, it still does not fully recover the original spectral function.

b) $-\text{Im} G^R(\omega)$ for the same input data, but with 2% of random noise added to $G(i\omega_n)$. The main strength of the stochastic analytical continuation is its robustness and its ability to extract the main features of the original spectral function even in the presence of numerical noise.

spectrum. We attribute this to the fact that the stochastic continuation method samples many spectra that fit quite well to the noisy input data, and their average still provides a very robust quantity.

Guided by these results, we will from now on use the stochastic approach to analytic continuation throughout this thesis to obtain the real-frequency data from the Matsubara result, unless otherwise noted. If we also need the real part $\text{Re}[G^R(\omega)]$, the Kramers-Kronig relations from Eq. (4.1.15) are applied to obtain $\text{Re}[G^R(\omega)]$ from $\text{Im}[G^R(\omega)]$. This for example is often the case for the Selfenergy, which is discussed in the following section.

4.5 Analytic continuation of general Matsubara functions

Until now, we have formulated the analytic continuation procedure for the Matsubara Green's function $G(i\omega_n)$ but since the result from Cauchy's integral formula holds for any holomorphic function $F(z)$ we have the relation

$$F(i\omega_n) = \frac{1}{\pi} \int_{-\infty}^{\infty} \frac{\text{Im}[F(\omega)]}{\omega - i\omega_n} d\omega, \quad (4.5.1)$$

and we can use the stochastic analytic continuation also for example for the Selfenergy $\Sigma(i\omega_n)$. Nonetheless, since the Selfenergy has the constant Hartree term $\lim_{n \rightarrow \infty} \Sigma(i\omega_n) = \Sigma_0$ and a normalization which is different from that of a Green's function and depends on the strength of the interaction, we have to adjust our scheme slightly. Since we only want to sample functions with the right normalization, we need to extract this information from the input $F(i\omega_n)$ and use it in our sampling procedure. It can be obtained in the limit of large ω_n as follows: Let us divide the integration along the real frequency axis into two parts, namely the interval $[-a, a]$, $a > 0$ and the remaining $\mathbb{R} \setminus [-a, a]$. Since we only consider normalizable functions, a finite value of a exists that includes (almost) all spectral weight so that we will obtain the correct result since the remaining contribution outside of this interval will be negligible

$$F(i\omega_n) = \frac{1}{\pi} \int_{-a}^a \frac{\text{Im}(F(\omega))}{\omega - i\omega_n} d\omega. \quad (4.5.2)$$

Now we consider $\omega_n \gg a$, which allows us to get the following

$$F(i\omega_n) = \frac{1}{\pi} \lim_{a \rightarrow \infty} \int_{-a}^a \frac{\text{Im}[F(\omega)]}{\omega - i\omega_n} d\omega \quad (4.5.3)$$

$$= \frac{1}{\pi} \lim_{a \rightarrow \infty} \int_{-a}^a \text{Im}[F(\omega)] \frac{\omega + i\omega_n}{\omega^2 + \omega_n^2} d\omega \quad (4.5.4)$$

$$\approx \frac{1}{\pi} \lim_{a \rightarrow \infty} \int_{-a}^a \text{Im}[F(\omega)] \frac{\omega + i\omega_n}{\omega_n^2} d\omega \quad (4.5.5)$$

$$\approx \frac{1}{\pi} \lim_{a \rightarrow \infty} \int_{-a}^a \text{Im}[F(\omega)] \frac{i}{\omega_n} d\omega \quad (4.5.6)$$

$$= -\frac{1}{i\omega_n} \frac{1}{\pi} \lim_{a \rightarrow \infty} \int_{-a}^a \text{Im}[F(\omega)] d\omega \quad (4.5.7)$$

$$= \frac{c_1}{i\omega_n}, \quad (4.5.8)$$

with $c_1 = -\frac{1}{\pi} \int_{-\infty}^{\infty} \text{Im}[F(\omega)] d\omega$. Therefore, in the case of a Green's function with $c_1 = 1$, the imaginary part is normalized to $-\pi$, which is in correspondence with the original definition of the spectral function

$$A(\omega) = -\frac{1}{\pi} \text{Im}[G(\omega)]. \quad (4.5.9)$$

In other cases, *e.g.* of the Selfenergy $\Sigma(i\omega_n)$, we have in general $c_1 \neq 1$, so we can extract the normalization N from the high frequency behaviour as

$$N = -\pi c_1, \quad (4.5.10)$$

and use only functions obeying this normalization in the sampling process.

We have just seen that for large ω_n , the Cauchy formula poses the restriction on $F(i\omega_n)$ to fall off as $c_1/i\omega_n$, which is not the case for the Selfenergy

$$\Sigma(i\omega_n) = c_0 + \frac{c_1}{i\omega_n} + \dots, \quad (4.5.11)$$

where c_0 is the real constant Hartree term. Therefore, instead of $\Sigma(i\omega_n)$ the function $\Sigma(i\omega_n) - c_0$ has the right behaviour at large ω_n , so the standard analytic continuation procedure can be applied. After $\Sigma(\omega) - c_0$ is obtained on the real axis, the constant term c_0 can be added back to the result to finally obtain $\Sigma(\omega)$.

4.6 Practical implementation

We will now present an exemplary procedure of how to implement the stochastic analytic continuation approach. For this we assume that we have given the input data $F_{meas}(i\omega_n)$ on N Matsubara points $i\omega_n$. The function on the real frequency axis will be discretized and its function values are updated by a Metropolis-like Monte Carlo algorithm, similar to the Delta function walkers by Beach [93]. Multiple runs for different values of α are performed at once in order to make use of the parallel tempering method and generate the final spectral function at the end as discussed in the previous sections. The procedure is then as follows:

1. Choose an interval $[a, b]$ on the real axis which is large enough to include basically all weight of $\text{Im}[F(\omega)]$. Usually this will be a guess of the same order as the relevant bandwidth in case of a physical system and then can be optimized during the iterations.
2. Initialize and normalize $\text{Im}[F(\omega)]$, for example as a constant $\text{Im}[F(\omega)] = -\pi c_1/(b - a)$.

3. Calculate $F(i\omega_n)$ by using

$$F(i\omega_n) = \frac{1}{\pi} \int_{-\infty}^{\infty} \frac{\text{Im}[F(\omega)]}{\omega - i\omega_n} d\omega. \quad (4.6.1)$$

4. Calculate deviation

$$\chi_0^2 = \sum_{n=0}^{N-1} \frac{1}{\sigma^2(i\omega_n)} |F_{meas}(i\omega_n) - F(i\omega_n)|^2. \quad (4.6.2)$$

5. Modify the values of $\text{Im}[F(\omega)]$ by a norm-conserving operation, recalculate $F(i\omega_n)$ and calculate the new deviation χ_{new}^2 .

6. Accept the modification with probability

$$p = \min \left\{ 1, e^{-\alpha(\chi_{new}^2 - \chi_0^2)} \right\}, \quad (4.6.3)$$

and update $\chi_0^2 := \chi_{new}^2$, otherwise revert the modification.

7. Measure $\text{Im}[F(\omega)]$, *i.e.* save the values for calculating the average afterwards.

8. Go back to 5).

This process is iterated many times until $\text{Im}[F(\omega)]$ is sufficiently converged and reasonably smooth. Then the Kramers-Kronig relations are used to obtain $\text{Re}[F(\omega)]$ if needed.

Chapter 5

Electronic correlations

The study of electronic correlations has been and still is one of the main important and interesting fields of research in condensed matter physics. In general, one refers to electronic correlations as the collection of all effects in an interacting electronic system that cannot be described by a Slater determinant of single-particle states, where the interaction is incorporated by the electrons interacting with an effective field instead of interacting directly with each other, which is the basis for approximate methods like Hartree-Fock theory. The effects of electronic correlations can be quite significant, with the Mott-Hubbard metal-insulator transition in lattice systems being the most famous example. The metal-insulator transition arises from the limit of the Coulomb repulsion of the electrons becoming dominant over the tendency to delocalize in order to reduce the kinetic energy. In this chapter, we will first provide a short introduction of what we actually mean with correlations, and then different approaches of how we can treat them theoretically. One possible way is to improve the state-of-the-art DFT method by more elaborate functionals, or include Selfenergy effects perturbatively by the LDA+U approach. Another quite successful approach is the dynamical mean-field theory,

When we speak of correlations, what we usually mean is that something like an object or event does depend on something else, another object or event, and is not free. Its actions or behaviour cannot be understood without taking that of the other into account. Looking up the meaning of *correlation* in a dictionary [98], what we usually find is something along the lines of

- “mutual relation of two or more things, parts, etc.”
- “the degree to which two or more attributes or measurements on the same group of elements show a tendency to vary together.”

These definitions also pronounce the attribute of *dependency*, *i.e.* correlated objects “show a tendency to vary together”. Quite similar to that, correlation in mathematics is defined as a property of two random variables X, Y , where the expectation value of the random variable XY does not factorize into the product of the expectation value of X times the expectation value of Y . The general expression is given by

$$E[XY] = E[X]E[Y] + \text{cov}(X, Y). \quad (5.0.1)$$

Thus, in the mathematical sense two random variables X, Y are said to be *uncorrelated* if $\text{cov}(X, Y) = 0$, and vice versa, where $\text{cov}(X, Y) = 0$ “measures” the degree of *correlation* between X and Y

$$\text{cov}(X, Y) = E[(X - E[X])(Y - E[Y])]. \quad (5.0.2)$$

For example, in physics we can ask whether the charge density $n(\mathbf{r})$ in an electronic system at two different points $\mathbf{r}_i, \mathbf{r}_j$ is uncorrelated, which in general for an interacting system is not true

$$\langle n(\mathbf{r}_i)n(\mathbf{r}_j) \rangle \neq \langle n(\mathbf{r}_i) \rangle \langle n(\mathbf{r}_j) \rangle. \quad (5.0.3)$$

This is due to the fact that the electrons interact with each other via the Coulomb interacting and Pauli principle, which causes $n(\mathbf{r}_j)$ to be usually small if $n(\mathbf{r}_i)$ is large when \mathbf{r}_i and \mathbf{r}_j are close. If the expectation value were to separate, this would imply that we can calculate the probability for one electron to be at position \mathbf{r}_i independently from where all the other electrons are, which is true only for a purely non-interacting system.

This factorization is the key property that defines electronic correlations in the physical sense: correlations are the effects that go beyond approximations based on the factorization of correlation functions, *i.e.* beyond static mean-field theories like the Weiss mean-field theory for the Ising model, the Hartree approximation for the Hubbard model or, to some degree, density functional theory. These approximations do not neglect the interactions between the electrons, but they include them via an effective background potential that has to be determined self-consistently, in which the non-interacting electrons are embedded. By this, the single-particle picture is preserved, since the resulting Hamiltonian, after being determined self-consistently, is effectively non-interacting.

Consider as an example the most simple tight-binding model of a one-dimensional atomic chain with lattice spacing a , with a single s -orbital and σ -bonds between the sites, so the Hamiltonian can be written as

$$H_{TB} = -t \sum_{\langle i,j \rangle, \sigma} c_{i,\sigma}^\dagger c_{j,\sigma}, \quad (5.0.4)$$

where $\langle i, j \rangle$ indicates a summation only over the nearest-neighbouring sites i, j . The hopping integral is given by

$$t = \int \langle \phi_\sigma(r-a) | H | \phi_\sigma(r) \rangle dr, \quad (5.0.5)$$

and thus will usually decrease exponentially as a function of a . This Hamiltonian can be solved by a Fourier transformation, yielding the dispersion

$$\epsilon(k) = -2t \cos(ka). \quad (5.0.6)$$

Assuming one electron per site, the system is at half filling with the Fermi level $E_F = 0$, so the system is metallic, since at $k = (n+1)\frac{\pi}{2a}$ the single band crosses the Fermi level. Now assume we increase the lattice spacing a , for example up to the order of one meter. The only thing that will happen is that the band width will decrease since t is reduced, and the bands will become extremely flat around the Fermi level but the system will still stay metallic at half filling. This is of course quite counter-intuitive and unphysical, but what exactly goes wrong with this approach? The reason is that in the tight-binding model the electrons are assumed to be tightly bound to the individual atoms and the atomic-like orbitals on one atom do not significantly spread onto the neighbouring atoms but only have a small overlap with the neighbouring orbitals in the interstitial. Due to this we neglect the energy cost of U for one electron that delocalizes to another site and interacts with the other electrons via the Coulomb repulsion, *i.e.* U/t is assumed to be small. If we now increase the atomic distance, the value of U is mostly unchanged but t will decrease significantly, so that U/t becomes large. Since we neglected the contribution of U , *i.e.* the correlation of electrons on the same site in the Hamiltonian in Eq. (5.0.4), delocalization will always be favoured in order to reduce the energy, so the system will not become insulating for any value of a .

In a very simplified picture we can see that a small band width will in general correspond to strong electronic correlations. Consider similar to the previous tight-binding model that the energy of the electrons can be described by the dispersion $\epsilon(\mathbf{k})$. From the dispersion we can derive the mean velocity of the electrons as $v(\mathbf{k}) = \frac{1}{\hbar} |\nabla_{\mathbf{k}} \epsilon(\mathbf{k})| \sim \frac{1}{\hbar} a W$, where W is the band width. For example, in the tight-binding model we have $v(\mathbf{k}) = 2ta |\sin(\mathbf{k}a)|$. On the other hand, the typical velocity for delocalized electrons should be approximately a/t , where t is the average time an electron spends on an atom. Comparing these two results we get that

$$t \sim \frac{\hbar}{W}. \quad (5.0.7)$$

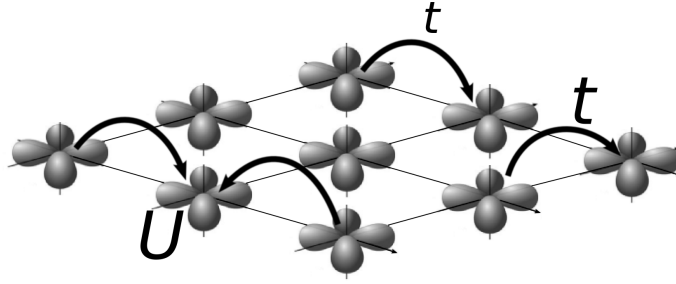


Figure 5.1: Illustration of the one-band Hubbard model in two dimensions. The model consists of a lattice of atomic sites occupied by electrons that can hop between neighbouring sites with the hopping amplitude t . Double occupation of an atomic site with two electrons of the opposite spin incurs an energy penalty of U to mimic the screened short-range Coulomb interaction. .

In this simple picture, we can interpret the effect of a narrow band width as the electrons staying longer on an atomic site and thereby feeling the other electrons much more strongly. Thus, a narrow band width implies in general strong electronic correlations and the importance of U in the Hamiltonian.

5.1 The Hubbard model

In order to find a way of appropriately treating electronic correlations we should also consider alternative ways of treating the Coulomb repulsion. Since the Coulomb interaction is a long-range interaction due to the potential falling off as $\sim \frac{1}{r}$, the problem is notoriously difficult since we need to take the contribution of many particles into account. However, in real systems the range of the interaction is effectively reduced due to screening effects of the electronic charge. Consider electrons moving in a positive background potential given by the atomic lattice. Focussing on a specific electron, one will observe a region of reduced electronic density in the vicinity of said electron due to the Coulomb repulsion, that creates an effective positively charged cloud that will move around with the electron. From large distances, the resulting potential seen by other electrons will thus be reduced by the positive cloud compared to the bare electron. Therefore, the effective potential will fall off much faster than the bare Coulomb repulsion, making it an effective short-range interaction. This is why approximative models like the Hubbard model [2–4], which assume the Coulomb repulsion to be completely local, can be quite appropriate to describe correlated lattice systems.

The most simple variant is the one-band fermionic Hubbard model, given by the Hamiltonian

$$H = \sum_{\langle i,j \rangle, \sigma} t_{ij} c_{i\sigma}^\dagger c_{j\sigma} + U \sum_i n_{i\uparrow} n_{i\downarrow}, \quad (5.1.1)$$

with the hopping amplitudes t_{ij} between neighbouring sites i, j . The Coulomb interaction is represented by a local on-site interaction U , that has to be paid if two electrons of opposite spin occupy the same site. Fig. 5.1 shows an example of the two-dimensional Hubbard model. It can encompass basically all types of lattice systems by appropriately choosing the hopping integrals t_{ij} . Even though this model appears to be very simple, it is not only impossible to be solved analytically in more than one dimensions [5], but also includes the main effects of the competition between the kinetic energy and Coulomb interaction. Considering for example the limit $U/t \rightarrow 0$, the Hamiltonian corresponds to that of free particles with a dispersion corresponding to the Fourier transform of t_{ij} For the linear chain we already had as an example $\epsilon(k) = -2t \cos(ka)$ and, since the Hamiltonian separates into a sum of single-particle terms, all expectation values can be calculated independently.

Thus, all correlation functions factorize, *e.g.*

$$\langle n_{i\uparrow} n_{i\downarrow} \rangle = \langle n_{i\uparrow} \rangle \langle n_{i\downarrow} \rangle. \quad (5.1.2)$$

Considering the other limit of $U/t \rightarrow \infty$, the Hamiltonian becomes just the sum of the double occupations times U . At half filling the ground state which minimizes the energy thus corresponds to each electron being localized on an atomic site with zero probability on all other sites. As a result, the system is now in an insulating state due to the electronic correlations and the correlation functions no longer factorize

$$\underbrace{\langle n_{i\uparrow} n_{i\downarrow} \rangle}_{=0} \neq \underbrace{\langle n_{i\uparrow} \rangle}_{=0.5} \underbrace{\langle n_{i\downarrow} \rangle}_{=0.5}. \quad (5.1.3)$$

Thus, even though the Hubbard model is quite simple, it can show the non-trivial effect of a metal-insulator transition as U/t is increased. Approximations like Hartree-Fock mean-field theories that are based on the separation of correlation functions are, therefore, also insufficient to correctly describe the physics in the Hubbard model for strong interactions.

5.2 Dynamical mean-field theory

In the previous section we have seen that standard Hartree-Fock mean-field theories based on the factorization of correlation functions are insufficient to describe electronic systems like the Hubbard model in the presence of strong electronic interactions. Still, good and controlled approximative techniques are needed since analytic solutions are mostly restricted to special limiting cases, and most too often to one dimensional systems. Lots of approximations are of perturbative nature, in the sense that they focus on special cases where a certain parameter becomes very large or very small. Most of the time, even when said parameter is in the intermediate range, these approximations can give valuable insight into the physics and trends of the system. dynamical mean-field theory itself corresponds to a mean-field theory in the limit of large coordination number $1/Z \rightarrow 0$, *i.e.* the number of nearest-neighbours is large, but as we will see it still retains the full dynamics of the system. By this, it is different from, for example the well known Weiss molecular-field theory for the Ising model [99], which becomes exact also for the limit of infinite coordination number Z . It contains no other approximation or restriction of the values of the physical parameters like interactions or temperature, and is diagrammatically controlled [87], which makes it already a very good starting point for further improvements.

In most of physically interesting systems the parameters like temperature and interaction are in the intermediate range, and especially in the relevant case of three dimensions the coordination number Z can be very large. Consider for example the cubic lattice $Z = 6$, the body-centered cubic (bcc) lattice $Z = 8$ or the face-centered cubic (fcc) lattice $Z = 12$, which already have quite a small value of $1/Z$, so an expansion in $1/Z$ is quite attractive if other limits of small U or large T are not applicable.

5.2.1 Weiss mean-field theory

In this sense, and in order to pave the way for introducing the variant the dynamical mean-field theory, it is instructional to revisit the concept of the Weiss mean-field theory as a precursor at the example of the Ising model. Its Hamiltonian with nearest-neighbour coupling $J > 0$ is given by

$$H = -\frac{J}{2} \sum_{\langle i,j \rangle} S_i S_j, \quad (5.2.1)$$

where S_i corresponds to only the z -component of the spin. Focussing on a specific site i , the energy contribution is given by a multiplication with a local field

$$h_i = J \sum_{\langle j \rangle \text{ of } i} S_j, \quad (5.2.2)$$

surrounding site i , so we can also write Eq. (5.2.1) as

$$H = -\frac{1}{2} \sum_i S_i h_i. \quad (5.2.3)$$

The local field h_i is in general different for each site i and changes dynamically due to quantum fluctuations. Let us assume the system has an *average* magnetization $\langle M \rangle = \frac{1}{N} \sum_i \langle S_i \rangle$, where $\langle \cdot \rangle$ is the quantum mechanical thermal average and N the number of lattice sites. By the very definition of the average magnetization we know that each spin $\langle S_i \rangle$ will on average be equal to M , *especially* if the standard deviation, or resp., the fluctuations around the mean value are small. This means, each value $\langle S_i \rangle$ can be interpreted as a random variable that can take values between $[-|S|, |S|]$ (usually $\pm\hbar/2$ for the Ising model), and the distribution has a mean of $\langle M \rangle$. Since the local field h_i is a sum over the Z nearest-neighbouring random variables, on average we usually would expect the local field to be equal to

$$\langle h_i \rangle = J \sum_{\langle j \rangle \text{ of } i} \langle S_j \rangle \quad (5.2.4)$$

$$\approx JZ \langle M \rangle. \quad (5.2.5)$$

In general the local field will be different, since we only draw Z random variables from the distribution, which average value is in general not equal to the true mean value of the distribution. For example, consider the system to be in the paramagnetic unordered phase where $\langle M \rangle = 0$. For a specific configuration at a given point in time the local field $\langle h_i \rangle$ will fluctuate significantly from site to site and will in general be not equal to $\langle M \rangle$, since at high temperature the probability for the system to be in high energy states is similar to that of the low energy states. For example, for a specific site all neighbouring spins could be polarized, while for a different site the average polarization of the neighbouring spins is zero. Only the average over many sites and configurations over time will approach the true value of $\langle M \rangle$.

This motivates the following limit: consider the case of $Z \rightarrow \infty$, *i.e.* the number of nearest-neighbours goes to infinity. This means the local field is a sum over infinitely many random variables from a distribution with mean $\langle M \rangle$. From the central limit theorem we know that the average of an infinite number of random variables becomes equal to its mean (the deviation from the mean decays as $1/\sqrt{Z}$), so the replacement of $\langle h_i \rangle$ by $JZ \langle M \rangle$ actually becomes exact [100, 101]. For now, in order to keep $\langle h_i \rangle$ finite, we will rescale J as

$$J = \frac{J^*}{Z}, \quad (5.2.6)$$

so that the limit $Z \rightarrow \infty$ of $\langle h_i \rangle$ exists. In this limit we have the true equality of

$$\lim_{Z \rightarrow \infty} \langle h_i \rangle = J^* \langle M \rangle, \quad (5.2.7)$$

which is *independent* of the lattice site i . This simplified picture is illustrated in Fig. 5.2.

This notion can be made rigorous and one arrives at the mean-field Hamiltonian [99]

$$H_{MF} = -h_{MF} \sum_i S_i + \frac{1}{2} N J^* \langle M \rangle^2 \quad (5.2.8)$$

$$\text{with } h_{MF} = J^* \langle M \rangle. \quad (5.2.9)$$

Obtaining a solution to the mean-field Hamiltonian now has to be done self-consistently, since the effective field h_{MF} depends on the spin configuration, which we simply do not know for given input parameters J, T etc., otherwise we would have solved the system right away. The important aspect of Eq. (5.2.8) is that the Hamiltonian has become a purely local quantity

$$H_{MF} = \sum_i H_i + \text{const.} \quad (5.2.10)$$

$$\text{with } H_i = -h_{MF} S_i, \quad (5.2.11)$$

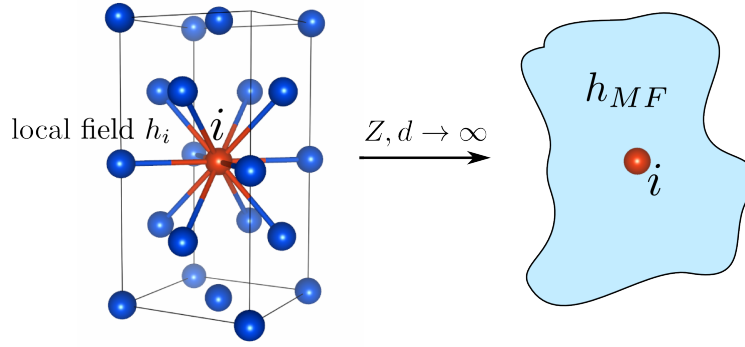


Figure 5.2: Illustration of the local field h_i surrounding a single atom in a crystal environment. In three dimensions the number of nearest-neighbours can be quite high, like $Z = 12$ for the fcc lattice. In the limit of infinite dimensions this local field can be described by an effective field h_{MF} with no spatial but only temporal fluctuations. Static mean-field theories also neglect the temporal fluctuations of the effective field and replace it by an average effective field that has to be determined self-consistently.

i.e. it has reduced to an effective *single-site* problem, where the interaction with the neighbouring sites has been replaced by an effective field.

5.2.2 The Hubbard model in infinite dimensions

Motivated by the investigations of $d \rightarrow \infty$ in the Ising model we will now study the behaviour of the Hubbard model in this limit, following the ideas of Metzner and Vollhardt [6, 102]. The Hamiltonian for the one-band model is given by

$$H = \sum_{\langle i,j \rangle, \sigma} t_{ij} c_{i\sigma}^\dagger c_{j\sigma} + U \sum_i n_{i\uparrow} n_{i\downarrow}. \quad (5.2.12)$$

As we have already pointed out, the Coulomb interaction is assumed to be purely local and thus the last term in Eq. (5.2.12) is independent of the number of nearest-neighbours or resp., the spatial dimension d . Only the kinetic term, which has a similar structure as the interaction term in the Ising model (5.2.1), is non-local and depends on d . Considering a d -dimensional hypercubic lattice with lattice spacing a , the dispersion of the non-interacting system, obtained by a Fourier transform of the kinetic term, is given by

$$\epsilon_{\mathbf{k}} = -2t \sum_{i=1}^d \cos(k_i a). \quad (5.2.13)$$

Taking a different point of view on this relations, the sum over dimensions can also be interpreted as a summation of d random variables $X_i = -2t \cos(k_i a)$. They are drawn from the same distribution, corresponding to choosing a certain \mathbf{k} -vector and can take on the values $\epsilon \in [-2t, 2t]$. In mathematical terms we have the random variable $X : \Omega \rightarrow E$, where the probability space Ω is the set of all \mathbf{k} -vectors and the measurable space $E = [-2t, 2t]$.

In this context we now make use of the central limit theorem: It states that as the number of random variables in the sum, or resp., the dimension d , approaches infinity, the probability of the sum to take on a certain value converges to a normal distribution with the corresponding mean and variance of the random variables. But this probability of the sum assuming a certain value (=energy) is just what is measured by the local density of states, given by

$$D(\omega) = \sum_{\mathbf{k}} \delta(\omega - \epsilon_{\mathbf{k}}). \quad (5.2.14)$$

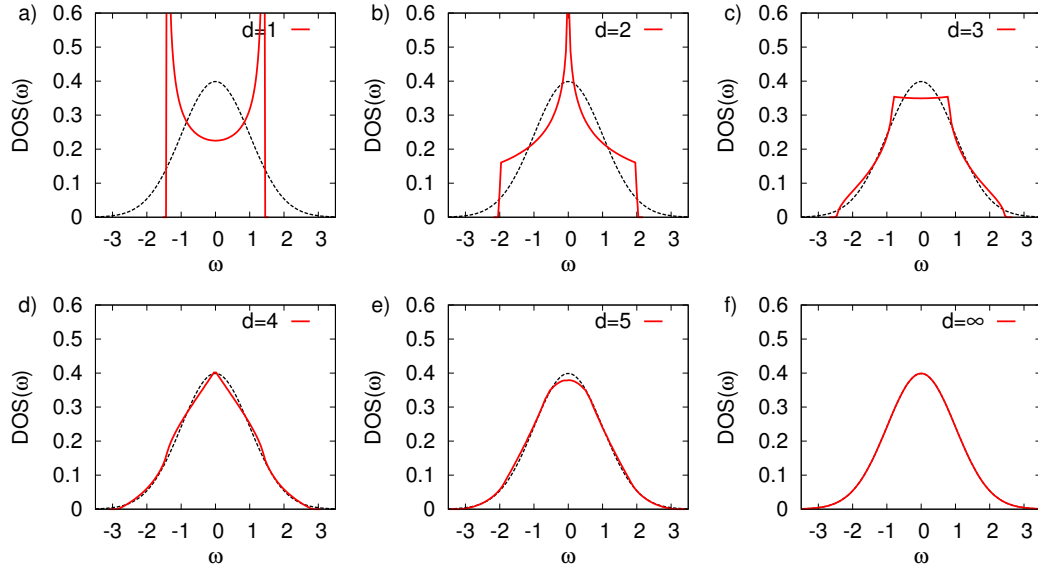


Figure 5.3: The density of states of the hypercubic lattice with dispersion $\epsilon_k = -2t \sum_{i=1}^d \cos(k_i a)$ for increasing dimension d . The hopping parameter has been rescaled as $t \rightarrow t^*/\sqrt{2d}$ with $t^* = 1$ constant. For large dimensions the DOS converges to a Gaussian distribution with mean $\langle \epsilon_k \rangle = 0$ and variance $\sigma = t\sqrt{2d} = t^*$.

Therefore, the DOS for large d is approximately given by

$$D_d(\omega) = \frac{1}{\sqrt{2\pi}t\sqrt{2d}} \exp \left\{ -\frac{1}{2} \left(\frac{\omega}{t\sqrt{2d}} \right)^2 \right\} \quad (5.2.15)$$

with variance $\sigma = t\sqrt{2d} = t\sqrt{Z}$. Similar to the Ising model, we have to rescale the hopping amplitude t in order to define the DOS in the limit of $d \rightarrow \infty$. Choosing the scaling

$$t \rightarrow \frac{t^*}{\sqrt{Z}}, \quad (5.2.16)$$

we obtain the DOS in the limit of infinite dimensions as [6]

$$D(\omega) = \frac{1}{\sqrt{2\pi}t^*} \exp \left\{ -\frac{1}{2} \left(\frac{\omega}{t^*} \right)^2 \right\}. \quad (5.2.17)$$

The resulting DOS at the example of the hypercubic lattice in different dimensions is shown in Fig. 5.3. We observe that the DOS converges quite quickly to the $d = \infty$ result. Already at $d = 3$, where $Z = 6$, the shape is very similar to the Gaussian limit, which is a promising result for possible approximate approaches of the $d \rightarrow \infty$ also to finite dimensions.

Hence, we have just seen that the Hubbard Hamiltonian scaled as

$$H = \frac{1}{\sqrt{Z}} \sum_{\langle i,j \rangle, \sigma} t_{ij} c_{i\sigma}^\dagger c_{j\sigma} + U \sum_i n_{i\uparrow} n_{i\downarrow}, \quad (5.2.18)$$

has a non-trivial limit in infinite dimensions, with a non-interacting DOS given by the Gaussian in Eq. (5.2.17). Choosing the scaling as $t \rightarrow t^*/\sqrt{Z}$ is not obvious at first glance. Another possible option is to use $t \rightarrow t^*/Z$, which would suppress the kinetic energy to zero in the $d \rightarrow \infty$ limit. This yields a model which is not unphysical by itself, but usually infeasible to describe realistic systems

where the competition between the kinetic energy and local interaction U is finite. A more detailed discussion about the scaling can be found in Ref. [103].

As we have seen the convergence to this limit can be quite fast, so that possible simplifications that arise in the $d \rightarrow \infty$ limit are quite promising candidates for approximations for realistic systems in $d = 3$. In the next section we will investigate what kind of simplifications follow in infinite dimensions.

5.2.3 Simplifications in infinite dimensions - dynamical mean-field theory

Considering the limit of infinite dimensions, we will now again turn on the interactions perturbatively and investigate possible simplifications in this limit. One important aspect of the Hubbard model was that we had to rescale the hopping amplitude by a factor of $1/\sqrt{Z}$. Thus, certain terms in a perturbative expansion that scale with the hopping amplitude are expected to vanish for $d \rightarrow \infty$, reducing the terms that we have to calculate when we want to solve the interacting system.

In order to see what kind of terms are effected, let us consider the kinetic energy term for the non-interacting system in the Green's function language. For simplicity, we also assume that the hopping is identical for different sites $t_{ij} = t$. The kinetic energy is given by the non-interacting Green's function via (see also chapter 3)

$$\langle T_{\text{kin}} \rangle = -t \sum_{\langle i,j \rangle, \sigma} \langle c_{i\sigma}^\dagger c_{j\sigma} \rangle \quad (5.2.19)$$

$$= -t \sum_{\langle i,j \rangle, \sigma} G_{ij,\sigma}^0(\tau \rightarrow 0^-). \quad (5.2.20)$$

Since the one-particle density matrix $\langle c_{i\sigma}^\dagger c_{j\sigma} \rangle = G_{ij,\sigma}^0(\tau \rightarrow 0^-)$ describes the amplitude for an electron hopping from site j to site i , the probability for this process is given by $|G_{ij,\sigma}^0(0^-)|^2$. Summation for a given site j over all neighbouring sites and j itself must equal to probability one, since the electron has to go to some other site or remain on the present site. For Z nearest-neighbours we thus have

$$1 = |G_{ii,\sigma}^0(0^-)|^2 + \underbrace{\sum_{\langle j \rangle \text{ of } i} |G_{ij,\sigma}^0(0^-)|^2}_{\sim \mathcal{O}(Z) \text{ terms}}. \quad (5.2.21)$$

This not only shows that we have to scale the hopping as $t \rightarrow t^*/\sqrt{Z}$ as we have found in the previous section, but also that each term in the sum has to fall off as

$$G_{ij,\sigma}^0(0^-) \sim \mathcal{O}\left(\frac{1}{\sqrt{Z}}\right), \text{ for } i \neq j \text{ and large } Z, \quad (5.2.22)$$

in order to yield a normalized probability. The diagonal term $G_{ii,\sigma}^0(0^-) = \langle n_{i\sigma} \rangle$ is in general allowed to stay finite, since its contribution to the total probability does not scale as $\mathcal{O}(Z)$. This scaling has to hold also for the general case $\tau \neq 0^-$, since this property does not depend on whether there is a finite time $\tau \neq 0$ between the annihilation and creation of an electron at site j and i . Also the Fourier transform does not change this behaviour, since $G(i\omega_n)$ depends linearly on $G(\tau)$. This leads to the general result

$$G_{ij,\sigma}^0(\tau) \sim \mathcal{O}\left(\frac{1}{\sqrt{Z}}\right) \quad (5.2.23)$$

$$G_{ij,\sigma}^0(i\omega_n) \sim \mathcal{O}\left(\frac{1}{\sqrt{Z}}\right), \text{ for } i \neq j \text{ and large } Z. \quad (5.2.24)$$

Thus, the off-diagonal terms of the non-interacting Green's function vanish in the limit of $Z \rightarrow \infty$.

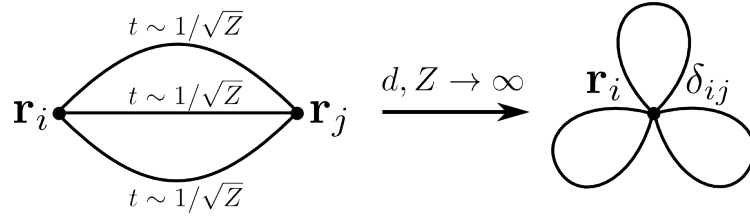


Figure 5.4: A diagram for the irreducible Selfenergy Σ_{ij} from second-order perturbation theory in real space. For infinite dimension or $Z \rightarrow \infty$, all diagrams collapse and become local since each process connecting different sites $i \neq j$ scales as $\mathcal{O}(1/\sqrt{Z})$.

It is important to note that this does not imply that the electrons automatically become localized in infinite dimensions. The kinetic energy is still finite and can compete with the interaction U because we have introduced the appropriate scaling t^*/\sqrt{Z} , which causes T_{kin} to be finite. Since the number of nearest-neighbours becomes infinite, the hopping probability for a given process $j \rightarrow i$ becomes arbitrarily small, but the total probability integrated over the whole surrounding is of the order of one. This gives us the impression that in this limit a single site i sees its surrounding as a continuous bath, where electrons can hop from the bath to the site i and back. Since the bath is continuous, the probability to hop into a specific “bath site” is arbitrarily small but the total probability to hop into the bath is finite. We will see later that indeed this picture will be the key step to solving the Hubbard model in the $d \rightarrow \infty$ limit.

For the general sites i, j one can show [104, 105] that the non-interacting Green’s function obeys the following scaling

$$G_{ij,\sigma}^0 \sim \mathcal{O}\left(d^{-\|\mathbf{r}_i - \mathbf{r}_j\|/2}\right), \quad (5.2.25)$$

where $\|\cdot\|$ is the Manhattan metric (the distance is the shortest connection between two sites, always along connecting bonds). This special property of the non-interacting Green’s function is responsible for far-reaching simplifications for perturbation theory. For example, in the language of Feynman diagrams when we construct the interacting Green’s function or the irreducible Selfenergy in real space, we draw the non-interacting propagator as lines connecting different sites i and j . Since in the limit $d \rightarrow \infty$, the non-interacting propagator lines scale as $\mathcal{O}(1/\sqrt{d})$ for $i \neq j$, all connected diagrams collapse to local diagrams and do not contribute to off-diagonal i, j components [6, 104, 106]. This behaviour is shown in Fig. 5.4 for the example of a second-order diagram for the irreducible Selfenergy Σ_{ij} . In second order the three non-interacting Green’s function lines will contribute a factor of the order of $\mathcal{O}(1/d^{3/2})$ and summation over all neighbouring sites gives only a factor of $\mathcal{O}(d)$. Therefore, this contribution to Σ_{ij} will vanish as $\mathcal{O}(1/\sqrt{d})$ and only the diagonal components Σ_{ij} will survive. This can be illustrated by the collapsed diagram in Fig. 5.4. Any two vertices that are connected by more than three separate Green’s function lines will thus collapse onto a single vertex, and the diagram becomes local. As a result, in the limit of $d \rightarrow \infty$ the irreducible Selfenergy becomes a purely local quantity [6, 106]

$$\lim_{d \rightarrow \infty} \Sigma_{ij}(i\omega_n) = \delta_{ij} \Sigma_{ii}(i\omega_n). \quad (5.2.26)$$

Correspondingly, taking the Fourier transform of a local Selfenergy in real-space we get the momentum-independent Selfenergy

$$\lim_{d \rightarrow \infty} \Sigma_k(i\omega_n) = \Sigma(i\omega_n). \quad (5.2.27)$$

This results in tremendous simplifications in the perturbative treatment for the Hubbard model. Recall that the non-interacting Green’s function in momentum-space is given by

$$G_k^0(i\omega_n) = \frac{1}{i\omega_n + \mu - \epsilon_k}. \quad (5.2.28)$$

Due to the collapse of all diagrams to local diagrams, the momentum summations in the diagrammatic calculation of the interacting Green's function or Selfenergy over the inner momentum degrees of freedom simplify and can be substituted by an integration over the non-interacting density of states (DOS) [6, 102, 106] due to the momentum-independence of the Selfenergy. At the example of the local interacting Green's function

$$G(i\omega_n) = \frac{1}{N_k} \sum_{\mathbf{k}} \frac{1}{i\omega_n + \mu - \epsilon_k - \Sigma(i\omega_n)} \quad (5.2.29)$$

$$= \int \frac{D(\epsilon)}{i\omega_n + \mu - \epsilon - \Sigma(i\omega_n)} d\epsilon, \quad (5.2.30)$$

where $D(\epsilon)$ is the non-interacting DOS. For simplicity we have suppressed further orbital- or spin-indices and used the representation of the Green's function on the Matsubara axis, but of course these simplifications in $d \rightarrow \infty$ are independent of whether we use real or imaginary time, or work in frequency space. It is important to note that nowhere a simplification or approximation was made to the dynamics of the system, *i.e.* the time or frequency dependence is not affected and there is no "collapse" in the diagrams with respect to these variables. Thus, even if the $d \rightarrow \infty$ limit is used as an approximation to systems in finite dimension, the problem retains its full dynamics, which is in contrast to the standard Weiss mean-field theories. This property coined the term *dynamical mean-field theory*, because the local dynamics are fully preserved. Only the non-local fluctuations are not considered, which is still exact in infinite dimensions but an approximation for real systems in, *e.g.* $d = 3$.

5.2.4 Derivation of the DMFT equations - effective Anderson impurity model

Dynamical mean-field theory has provided an important contribution to the understanding and possible approximative solutions of the Hubbard model. The collapse of all connected diagrams into local ones is a significant simplification towards obtaining, for example, the Selfenergy of the interacting system. Still, even though the problem has been simplified to a great extent, it remains challenging and in general cannot be solved analytically. Perturbatively summing up local diagrams up to a certain order is much simpler compared to non-local diagrams but will not provide valuable insight into the physically interesting regimes at low temperature and moderate to strong interactions.

The major breakthrough which made the numerical treatment of the Hubbard model in $d \rightarrow \infty$ possible was the insight by Ohkawa [107] and Georges and Kotliar [7], who showed that the functional equations of the Hubbard model in this limit can be made equivalent to that of an Anderson impurity model (AIM) [108] with an effective bath that has to be determined self-consistently. They show that a direct extension from the classical mean-field to the dynamical quantum case can be made, where the classical Weiss-field becomes a dynamical quantum bath in which a single lattice site is embedded. Like in the classical case the single site only interacts with the effective bath, which is in contrast a time-dependent quantity and thus retains the temporal quantum fluctuations present in the DMFT.

This correspondence to the Anderson impurity model is extremely helpful, since a plethora of numerical methods exist for solving the AIM that can be applied right away to treat the DMFT equations. Examples are the Hirsch-Fye quantum Monte Carlo solver [109, 110], continuous-time quantum Monte Carlo [8, 9], exact diagonalization [111, 112] or renormalization group approaches [113].

The derivation of the DMFT equations for the Hubbard model follow the same idea as for the Ising model but with formal differences. In the limit $d \rightarrow \infty$ the surrounding of a single lattice site can be described by an effective field similar to the Ising case, but in the quantum case it retains its time or frequency dependence, resembling the dynamical quantum fluctuations. This can be achieved by a generalized coherent potential approximation [114, 115], or by the so-called "cavity" method [7, 116]. The derivation we present here will be based on the latter. One proceeds by focussing on a specific site i , usually by convention set to $i = 0$, and integrate out all other degrees of freedom for the lattice site. By this, one obtains an effective dynamical Weiss field in which the lattice site i is embedded (see Fig. 5.5 for an illustration). At the same time one can write down

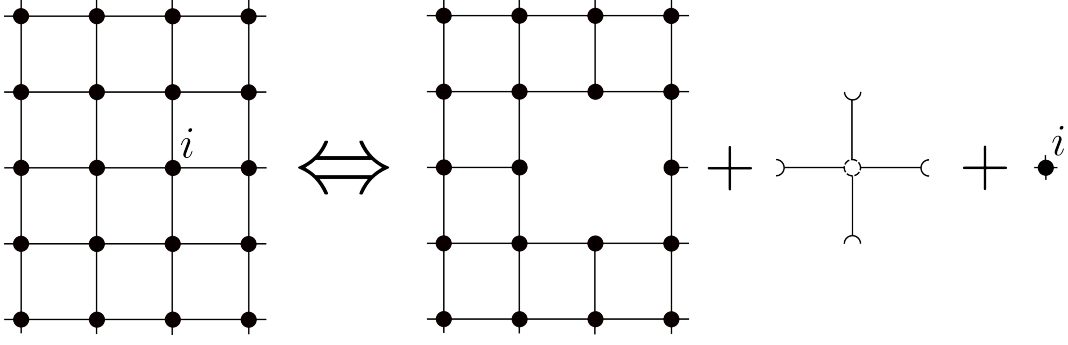


Figure 5.5: Illustration of the cavity method to derive the DMFT equations. The idea of this method is to focus on a particular site i and separate the total action S into a sum of the contributions arising from the lattice without the site $S^{(0)}$, the hybridization between the site and the lattice ΔS and the action S_0 of the site itself. In the limit $d \rightarrow \infty$ all other degrees of freedom of the lattice are integrated out in order to obtain an effective dynamical field in which site i is embedded.

the equations defining the effective bath of an Anderson impurity model, which describes a single impurity site in a non-interacting bath. This model can be used for example to describe an isolated magnetic impurity in a metal, in which the impurity orbitals hybridize with the conduction states of the surrounding. Investigating these equations one observes that the equations of the AIM and the Hubbard lattice site embedded in the effective Weiss field become equivalent if one chooses a specific form of the hybridization between impurity site and the effective bath in the AIM. This finding then allows us to obtain the solution of the Hubbard model in $d \rightarrow \infty$ by solving an effective AIM after we have chosen the correct form of the hybridization. Since the effective field and thus the hybridization is unknown at the beginning, it has to be found by a self-consistent procedure. After convergence, we have obtained a hybridization function of the impurity site that exactly represents the effective field surrounding the single site in the Hubbard model. The solution of the AIM, the impurity Green's function, will then correspond to the solution of the Hubbard model with the correct effective field.

For the derivation of the DMFT equations we will start with the formulation of the effective action of the Hubbard model, and identify it with the action of the Anderson impurity model to obtain a relation with the hybridization and effective field.

In the grand canonical ensemble the partition function \mathcal{Z} is sufficient to fully describe a thermodynamic system

$$\mathcal{Z} = \int \prod_i Dc_{i\sigma}^* Dc_{i\sigma} e^{-S}, \quad (5.2.31)$$

where $c_{i\sigma}^*, c_{i\sigma}$ are anticommuting Grassmann variables [117], and the action S [87], which is given for the Hubbard model as

$$S = \int_0^\beta d\tau \left(\sum_{i\sigma} c_{i\sigma}^*(\tau) \left[\frac{\partial}{\partial \tau} - \mu \right] c_{i\sigma}(\tau) - \sum_{ij\sigma} t_{ij} c_{i\sigma}^*(\tau) c_{j\sigma}(\tau) \right. \\ \left. + U \sum_i c_{i\uparrow}^*(\tau) c_{i\uparrow}(\tau) c_{i\downarrow}^*(\tau) c_{i\downarrow}(\tau) \right). \quad (5.2.32)$$

Now we split the lattice system into three parts, namely the ‘‘impurity’’ site $i = 0$, the remaining lattice without site $i = 0$ and the part that connects the two. The action correspondingly is separated into three parts

$$S = S_0 + \Delta S + S^{(0)}, \quad (5.2.33)$$

where S_0 is the action only on site $i = 0$

$$S_0 = \int_0^\beta d\tau \left(\sum_\sigma c_{0\sigma}^*(\tau) \left[\frac{\partial}{\partial \tau} - \mu \right] c_{0\sigma}(\tau) + U c_{0\uparrow}^*(\tau) c_{0\uparrow}(\tau) c_{0\downarrow}^*(\tau) c_{0\downarrow}(\tau) \right), \quad (5.2.34)$$

ΔS contains the hopping processes or hybridization between site 0 and the other sites

$$\Delta S = - \int_0^\beta d\tau \sum_{i\sigma} (t_{i0} c_{i\sigma}^*(\tau) c_{0\sigma}(\tau) + t_{0i} c_{0\sigma}^*(\tau) c_{i\sigma}(\tau)), \quad (5.2.35)$$

and finally $S^{(0)}$ is the action of the lattice with site 0 and the bonds connecting to it are removed

$$S^{(0)} = \int_0^\beta d\tau \left(\sum_{i \neq 0, \sigma} c_{i\sigma}^*(\tau) \left[\frac{\partial}{\partial \tau} - \mu \right] c_{i\sigma}(\tau) - \sum_{ij \neq 0, \sigma} t_{ij} c_{i\sigma}^*(\tau) c_{j\sigma}(\tau) + U \sum_{i \neq 0} c_{i\uparrow}^*(\tau) c_{i\uparrow}(\tau) c_{i\downarrow}^*(\tau) c_{i\downarrow}(\tau) \right). \quad (5.2.36)$$

We now define the thermodynamic average $\langle \cdot \rangle_{(0)}$ as the trace over the system with the impurity removed

$$\langle A \rangle_{(0)} = \frac{1}{Z_{(0)}} \int \prod_i Dc_{i\sigma}^* Dc_{i\sigma} A e^{-S^{(0)}}, \quad (5.2.37)$$

where $Z_{(0)}$ is the corresponding partition function. Expanding the full partition function Z with respect to ΔS , one obtains

$$Z = Z^{(0)} \int \prod_\sigma Dc_{0\sigma}^* Dc_{0\sigma} e^{-S_0} \left(1 - \int_0^\beta \langle \Delta S(\tau) \rangle_{(0)} d\tau + \frac{1}{2!} \int_0^\beta \int_0^\beta \langle \Delta S(\tau_1) \Delta S(\tau_2) \rangle_{(0)} d\tau_2 d\tau_1 + \dots \right), \quad (5.2.38)$$

where $\Delta S = \Delta S(\beta)$. For fermionic systems only the correlation functions $\langle \Delta S(\tau_1) \dots \Delta S(\tau_n) \rangle_{(0)}$ with equal number of c^* and c are non-zero. Using the definition of the one-particle correlation function, namely the Green's function of the lattice without the site 0

$$G_{jk\sigma}^{(0)}(\tau_1 - \tau_2) = - \langle T_\tau c_{j\sigma}(\tau_1) c_{k\sigma}^*(\tau_2) \rangle_{(0)}, \quad (5.2.39)$$

for example the second order term can be written as

$$\begin{aligned} & \frac{1}{2!} \int_0^\beta \int_0^\beta \langle \Delta S(\tau_1) \Delta S(\tau_2) \rangle_{(0)} d\tau_2 d\tau_1 \\ &= - \sum_{jk \neq 0, \sigma} t_{j0} t_{k0} \int_0^\beta \int_0^\beta G_{jk\sigma}^{(0)}(\tau_1 - \tau_2) c_{0\sigma}^*(\tau_1) c_{0\sigma}(\tau_2) d\tau_2 d\tau_1. \end{aligned} \quad (5.2.40)$$

The next terms of higher order can be written in a similar way by using the expressions for n -particle correlation functions. The important property of the terms in the expansion of Z in Eq. (5.2.38) is that terms of n -th order contain n factors of hopping amplitudes t_{j0} . In the limit of $d \rightarrow \infty$ we know that each hopping amplitude has to be rescaled by a factor of $Z^{\|\mathbf{r}_0 - \mathbf{r}_j\|/2}$ since the one-particle correlation function scales as $Z^{-\|\mathbf{r}_0 - \mathbf{r}_j\|/2}$, as discussed before. Therefore, the first term is of order 1, while all other terms of higher order scale at least as $\mathcal{O}(1/Z)$, so in the limit $d \rightarrow \infty$ only

contributions of $G_{jk\sigma}^{(0)}$ remain. This leads to the *effective local DMFT action*

$$S_{\text{loc}} = \int_0^\beta d\tau \sum_\sigma c_{0\sigma}^*(\tau) \left[\frac{\partial}{\partial \tau} - \mu \right] c_{0\sigma}(\tau) + U \int_0^\beta d\tau c_{0\uparrow}^*(\tau) c_{0\uparrow}(\tau) c_{0\downarrow}^*(\tau) c_{0\downarrow}(\tau) \\ + \sum_{jk \neq 0, \sigma} t_{j0}^* t_{k0}^* \int_0^\beta d\tau_1 \int_0^\beta d\tau_2 G_{jk\sigma}^{(0)}(\tau_1 - \tau_2) c_{0\sigma}^*(\tau_1) c_{0\sigma}(\tau_2), \quad (5.2.41)$$

where the rescaled hopping amplitudes are indicated by t_{j0}^* . We introduce the *hybridization function* Δ_σ as

$$\Delta_\sigma(\tau_1 - \tau_2) = \sum_{jk \neq 0} t_{j0}^* t_{k0}^* G_{jk\sigma}^{(0)}(\tau_1 - \tau_2), \quad (5.2.42)$$

and define the so-called effective *Weiss field* \mathcal{G}_σ for the Hubbard model in the $d \rightarrow \infty$ limit as

$$\mathcal{G}_\sigma^{-1}(\tau_1 - \tau_2) = -\delta(\tau_1 - \tau_2) \left[\frac{\partial}{\partial \tau_1} - \mu \right] - \Delta_\sigma(\tau_1 - \tau_2), \quad (5.2.43)$$

which allows us to write the local action in the following form

$$S_{\text{loc}} = - \int_0^\beta d\tau_1 \int_0^\beta d\tau_2 \sum_\sigma c_\sigma^*(\tau_1) \mathcal{G}_\sigma^{-1}(\tau_1 - \tau_2) c_\sigma(\tau_2) \\ + U \int_0^\beta d\tau c_\uparrow^*(\tau) c_\uparrow(\tau) c_\downarrow^*(\tau) c_\downarrow(\tau), \quad (5.2.44)$$

where we have omitted the index $i = 0$ for readability (the choice of $i = 0$ is, after all, arbitrary). This is an important result, since it shows that the action of the Hubbard model in the $d \rightarrow \infty$ limit becomes identical to the action of a single site embedded in an effective field \mathcal{G}_σ^{-1} plus the local Coulomb interaction on this site. The definition of the Weiss field in Eq. (5.2.43) shows some resemblance to the classical case, since it relates the effective field, which defines the full partition function and thus all information of the system, with the Green's function $G_{jk\sigma}^{(0)}$ of the original Hubbard model with one site removed. If we were to relate $G_{jk\sigma}^{(0)}$ to the Green's function of the original full lattice $G_{jk\sigma}$, Eq. (5.2.44) would form a self-consistent relation, since the calculation of Z now requires knowledge of the Green's function and vice versa.

The Fourier transform of the Weiss field in Eq. (5.2.43) takes on a slightly simpler form

$$\mathcal{G}_\sigma^{-1}(i\omega_n) = i\omega_n + \mu - \Delta_\sigma(i\omega_n) \quad (5.2.45)$$

$$\text{with } \Delta_\sigma(i\omega_n) = \sum_{jk \neq 0} t_{j0}^* t_{k0}^* G_{jk\sigma}^{(0)}(i\omega_n). \quad (5.2.46)$$

To make the connection back to the original lattice, one can expand the Green's functions in terms of the hopping matrix elements, leading to [116]

$$G_{jk\sigma}^{(0)} = G_{jk\sigma} - G_{j0\sigma} G_{00\sigma}^{-1} G_{0k\sigma}, \quad (5.2.47)$$

where $G_{jk\sigma}$ corresponds to the Green's function of the full lattice. This relation allows one to express the local Green's function $G_{00\sigma} = G_\sigma$ by the dynamical Weiss field in the form of a Dyson equation

$$G_\sigma^{-1}(i\omega_n) = \mathcal{G}_\sigma^{-1}(i\omega_n) - \Sigma_\sigma(i\omega_n) \quad (5.2.48)$$

$$= i\omega_n + \mu - \Delta_\sigma(i\omega_n) - \Sigma_\sigma(i\omega_n). \quad (5.2.49)$$

The original momentum-dependent lattice Green's function in the DMFT limit is given by

$$G_\sigma(\mathbf{k}, i\omega_n) = \frac{1}{i\omega_n + \mu - \epsilon_{\mathbf{k}} - \Sigma_\sigma(i\omega_n)}, \quad (5.2.50)$$

which finally leads to the equation for the effective Weiss field

$$\mathcal{G}_\sigma^{-1}(i\omega_n) = \Sigma_\sigma(i\omega_n) + G_\sigma^{-1}(i\omega_n) \quad (5.2.51)$$

$$= \Sigma_\sigma(i\omega_n) + \left[\int \frac{D(\epsilon)}{i\omega_n + \mu - \epsilon - \Sigma_\sigma(i\omega_n)} d\epsilon \right]^{-1}, \quad (5.2.52)$$

where $D(\epsilon)$ is the non-interacting density of states of the original lattice. The equations for the effective action (5.2.44), for the Weiss field (5.2.45), the Dyson equation for the local Green's function (5.2.49) and the relation of the Weiss field with the non-interacting DOS (5.2.52) form a set of self-consistent equations that can in principle be solved iteratively. The only unknown property in these relations is the Selfenergy $\Sigma_\sigma(i\omega_n)$. Starting with an initial guess for $\Sigma_\sigma(i\omega_n)$, one uses Eq. (5.2.52) to obtain the Weiss field, then solve the corresponding local problem defined by the action S_{loc} in Eq. (5.2.44), and then obtain a new Selfenergy from the Dyson equation in Eq. (5.2.49). After convergence, one has found the correct Weiss field \mathcal{G}_σ^{-1} , that parametrizes the effective field surrounding a lattice site of the Hubbard model in $d \rightarrow \infty$, with the corresponding interacting Green's function G_σ and Selfenergy Σ_σ . The local interacting Green's function is then equal to the momentum-averaged interacting lattice Green's function. Solving the local system is still a difficult interacting many-body problem, which in general cannot be done analytically.

It is important to note that the interacting Green's function of the original lattice in Eq. (5.2.50) is still a momentum-dependent quantity. In the DMFT limit the Selfenergy Σ_σ becomes a local quantity, but the lattice Green's function retains its momentum-dependence via the non-interacting lattice dispersion $\epsilon_{\mathbf{k}}$, with no *additional* dependence on momentum by the Selfenergy.

Having established the DMFT equations and the local problem to be solved, we can finally compare them to the Anderson impurity model. Recall that the AIM consists of an impurity site embedded in a non-interacting bath, from which electrons can hop into the impurity site, interact via the local Coulomb repulsion, get dressed by the Selfenergy, and eventually hop back into the bath. The Hamiltonian of the AIM is given by

$$H_{\text{AIM}} = \sum_{\mathbf{k}\sigma} \tilde{\epsilon}_{\mathbf{k}} a_{\mathbf{k}\sigma}^\dagger a_{\mathbf{k}\sigma} + \sum_{\mathbf{k}\sigma} V_{\mathbf{k}} \left(a_{\mathbf{k}\sigma}^\dagger c_\sigma + c_\sigma^\dagger a_{\mathbf{k}\sigma} \right) - \tilde{\mu} \sum_\sigma c_\sigma^\dagger c_\sigma + U c_\uparrow^\dagger c_\uparrow c_\downarrow^\dagger c_\downarrow, \quad (5.2.53)$$

where $a_{\mathbf{k}\sigma}, a_{\mathbf{k}\sigma}^\dagger$ are the annihilation and creation operators for the bath states with dispersion $\tilde{\epsilon}_{\mathbf{k}}$, and $c_\sigma, c_\sigma^\dagger$ are the annihilation and creation operators for an electron on the impurity site. The impurity hybridizes with the bath via the amplitude $V_{\mathbf{k}}$, which corresponds to the annihilation of one electron in the bath and creation of one electron on the impurity site, and vice versa. $\tilde{\mu}$ corresponds to the chemical potential on the impurity and U to the Coulomb interaction term. It can be shown [7, 116] that this model generates an action S_{AIM} of exactly the same functional form as the effective action S_{loc} of the Hubbard model in Eq. (5.2.44)

$$S_{\text{AIM}} = - \int_0^\beta d\tau_1 \int_0^\beta d\tau_2 \sum_\sigma c_\sigma^*(\tau_1) \mathcal{G}_\sigma^{-1}(\tau_1 - \tau_2) c_\sigma(\tau_2) + U \int_0^\beta d\tau c_\uparrow^*(\tau) c_\uparrow(\tau) c_\downarrow^*(\tau) c_\downarrow(\tau), \quad (5.2.54)$$

with the Weiss field given by

$$\mathcal{G}_\sigma^{-1}(\tau_1 - \tau_2) = -\delta(\tau_1 - \tau_2) \left[\frac{\partial}{\partial \tau_1} - \tilde{\mu} \right] + \sum_{\mathbf{k}} |V_{\mathbf{k}}|^2 (\theta(\tau_1 - \tau_2) - n_F(\tilde{\epsilon}_{\mathbf{k}})), \quad (5.2.55)$$

or with Matsubara frequencies

$$\mathcal{G}_\sigma^{-1}(i\omega_n) = i\omega_n + \tilde{\mu} - \sum_{\mathbf{k}} \frac{|V_{\mathbf{k}}|^2}{i\omega_n - \tilde{\epsilon}_{\mathbf{k}}}. \quad (5.2.56)$$

The equivalence of the action S_{AIM} and S_{loc} tells us that indeed the solution of the Hubbard model in $d \rightarrow \infty$ can be obtained by solving an Anderson impurity model with the special choice of the Weiss field given by Eq. 5.2.52. The solution for a given Weiss field will consist in general of the interacting local Green's function and the Selfenergy, so that we have to iterate the mapping and solving procedure self-consistently until convergence as explained above.

This concludes the derivation of the DMFT equations and the ways to solve them by relating the effective field in $d \rightarrow \infty$ to the bath of an Anderson impurity model. This method can now be applied to all kinds of lattice systems for the Hubbard model for which the non-interacting dispersion or density of states is known. The DMFT itself is non-perturbative in the sense that it is valid for the complete range of U/t and temperature T . It only relies on the approximation that $1/Z$ is small, which we assume is quite a good approximation for realistic systems, like the cubic lattice ($Z = 6$), the body-centered cubic (bcc) lattice ($Z = 8$) or the face-centered cubic (fcc) lattice ($Z = 12$). However, DMFT as it is right now is only applied to a “toy model”-like approximation of a real lattice, namely the Hubbard model, where the hopping parameters t_{ij} are basically free parameters. In the next section we will now discuss how we can extend the DMFT method to realistic systems.

Chapter 6

The LDA+DMFT approach

6.1 Making the transition to realistic systems

In the previous section we have discussed the DMFT self-consistency cycle for solving the Hubbard model in the $d \rightarrow \infty$ limit. The parameters that define the type of lattice we are dealing with are the hopping parameters t_{ij} . By appropriately choosing these parameters, in principle any lattice can be realized. Though, in practice this is not an easy task if one wants to construct a lattice for a realistic system, since a realistic model for a multiorbital system will usually consist of thousands or ten thousands of hopping parameters.

One of the most promising approaches for applying the DMFT equations to realistic systems is the so-called LDA+DMFT approach [118–121], which employs density functional theory for the extraction of the non-interacting dispersion $\epsilon_{\mathbf{k}}$, which is used to construct the lattice Green's function and then solving the corresponding lattice model within dynamical mean-field theory. This way of extending DMFT to realistic systems is very valuable, since it makes the LDA+DMFT method in principle an *ab initio* approach.

One drawback is obviously the fact that using the DFT Hamiltonian H_{DFT} for the non-interacting Hamiltonian H_0 is not correct but only an approximation. DFT itself, though being based by an exact mapping onto a non-interacting system, is by no means a non-interacting theory and includes electronic correlation to the extent given by the quality of the approximation to the exchange-correlation potential, for example on the level of the local density approximation. This gives rise to the so-called double counting problem, discussed in chapter 6.4, since we partially add electronic correlations via DMFT which have already been treated within density functional theory.

Furthermore, DFT is usually formulated in the Bloch basis $|\Psi_n(\mathbf{k})\rangle$, in contrast to the lattice model in DMFT, which is formulated in terms of electronic wave functions localized on a specific lattice site, which will make a proper change of basis a necessity. We will now review the DMFT self-consistency cycle and discuss the adoption of basically any general Hamiltonian H_0 into the framework of DMFT.

In DMFT the starting point for the self-consistency cycle is the Green's function of the original lattice

$$G_{\sigma}(\mathbf{k}, i\omega_n) = \frac{1}{i\omega_n + \mu - \epsilon_{\mathbf{k}} - \Sigma_{\sigma}(i\omega_n)}, \quad (6.1.1)$$

with the non-interacting dispersion and a first guess for the Selfenergy $\Sigma_{\sigma}(i\omega_n)$, that is going to be determined self-consistently. Recall the more general form of the interacting Green's function from chapter 3 given in terms of operators

$$G_{\sigma}(i\omega_n) = [(i\omega_n + \mu)\mathbb{1} - H_0 - \Sigma_{\sigma}(i\omega_n)]^{-1}, \quad (6.1.2)$$

where H_0 is the Hamiltonian of the non-interacting system that generates the dispersion $\epsilon_{\mathbf{k}}$ in the momentum basis. Since the Selfenergy is connected to the interacting and non-interacting Green's

function via the Dyson equation, $\Sigma_\sigma(i\omega_n)$ lives in the same Hilbert space as H_0 and will have the same dimension in terms of a matrix representation of operators. As we know, we can in general choose any basis we deem appropriate for the system at hand, for example in chapter 3 we also encountered the position basis

$$G_\sigma(\mathbf{r}, \mathbf{r}', i\omega_n) = \langle \mathbf{r} | [(i\omega_n + \mu)\mathbb{1} - H_0 - \Sigma_\sigma(i\omega_n)]^{-1} | \mathbf{r}' \rangle. \quad (6.1.3)$$

If we want to apply the DMFT method to a realistic system for which we can construct the non-interacting Hamiltonian H_0 , we can work in the orthonormal basis $|\phi_k\rangle$ that diagonalizes H_0 , *i.e.*

$$\langle \phi_k | \phi_{k'} \rangle = \delta_{kk'}, \quad \sum_k |\phi_k\rangle \langle \phi_k| = \mathbb{1} \quad (6.1.4)$$

$$H_0 |\phi_k\rangle = \epsilon_k |\phi_k\rangle, \quad (6.1.5)$$

which then determines the Green's function as

$$G_\sigma(k, k', i\omega_n) = \langle \phi_k | [(i\omega_n + \mu)\mathbb{1} - H_0 - \Sigma_\sigma(i\omega_n)]^{-1} | \phi_{k'} \rangle \quad (6.1.6)$$

$$= \frac{\delta_{kk'}}{i\omega_n + \mu - \epsilon_k - \Sigma_{k\sigma}(i\omega_n)}, \quad (6.1.7)$$

here $\Sigma_{k\sigma}(i\omega_n)$ is again just a first guess, for example $\Sigma_{k\sigma}(i\omega_n) \equiv 0$, and will be determined self-consistently.

While the representation of the Green's function is of course possible in any basis, most choices will not be appropriate in practice. To see why, reconsider that we have to solve an effective Anderson impurity model that generates the solution for the Hubbard model in the DMFT limit. The action of the Anderson impurity model is given by

$$S_{\text{AIM}} = - \int_0^\beta d\tau_1 \int_0^\beta d\tau_2 \sum_\sigma c_\sigma^*(\tau_1) \mathcal{G}_\sigma^{-1}(\tau_1 - \tau_2) c_\sigma(\tau_2) \\ + U \int_0^\beta d\tau c_\uparrow^*(\tau) c_\uparrow(\tau) c_\downarrow^*(\tau) c_\downarrow(\tau), \quad (6.1.8)$$

where the Grassman variables $c_\sigma^*(\tau), c_\sigma(\tau)$ correspond to creation and annihilation operators on the impurity site, which is obviously a very localized basis. In a local basis for a single orbital corresponding to electronic states localized on the lattice sites i the Coulomb interaction term takes on the simple diagonal form $U n_\uparrow n_\downarrow$. But if we were to change to a delocalized basis that in turn diagonalizes H_0 , the Coulomb interaction term would be much more complicated. Of course this is a possible choice but since the AIM is naturally formulated in a basis where the electronic wave functions are localized on the lattice sites, the Weiss field \mathcal{G}_σ^{-1} and thus the Green's function used to construct the effective AIM should be given in a localized basis. On the other hand, a non-interacting Hamiltonian H_0 of the form

$$H_0 = \sum_{\langle ij \rangle \sigma} t_{ij} c_{i\sigma}^\dagger c_{j\sigma}, \quad (6.1.9)$$

can usually be diagonalized only in a delocalized basis, *e.g.* by a Fourier transform. Thus, at some point we will be forced to perform a change of basis from a delocalized to a localized basis.

6.2 Localized basis for the Green's function

The choice of a localized basis set for realistic systems is in principle arbitrary, but most of the time corresponds to atomic orbital-like wave functions on a specific atomic site. One example are the orbital wave functions $|s_{\sigma i}\rangle, |p_{k\sigma i}\rangle, |d_{m\sigma i}\rangle$ for the atomic s, p, d orbitals with spin σ on site i , assuming they retain a similar shape in the solid compared to an isolated atom. In the context

of LDA+DMFT many choices of a localized basis have been explored, like linear muffin-tin orbitals (LMTO) [118, 119, 122], N -th order muffin-tin orbitals (NMTO) [123], Wannier functions constructed by a projection onto a subset of Bloch wave functions [124, 125], maximally localized Wannier functions [53] or projection onto local orbitals in the full-potential linear augmented plane-wave (FLAPW) method [36, 126].

In the following we will present the method of projection onto local orbitals as proposed by Aichhorn *et al.* [36]. It is based on the construction of a projection operator that projects the lattice Green's function from the Bloch basis onto localized orbitals in the "correlated subspace", in which the impurity problem is formulated.

The starting point to construct a local Green's function for defining an effective Anderson impurity model is the lattice Green's function

$$G_\sigma(i\omega_n) = [(i\omega_n + \mu)\mathbb{1} - H_0 - \Sigma_\sigma(i\omega_n)]^{-1}, \quad (6.2.1)$$

where H_0 corresponds to the DFT Hamiltonian. Please note that this equation corresponds to the full interacting Green's function of the lattice in the DMFT approximation by the inclusion of the Selfenergy $\Sigma_\sigma(i\omega_n)$. In the beginning $\Sigma_\sigma(i\omega_n)$ is not known, so for starting the self-consistency cycle we will use a reasonable guess, like $\Sigma_\sigma(i\omega_n) \equiv 0$, which means our best estimate to the interacting Green's function will be the non-interacting Green's function.

In DFT our main basis is usually the set of Bloch states $|\Psi_n(\mathbf{k})\rangle$ that diagonalizes the DFT Hamiltonian H_0 and forms a complete orthonormal basis set at each k-point

$$\langle \Psi_\nu(\mathbf{k}) | \Psi_{\nu'}(\mathbf{k}) \rangle = \delta_{\nu\nu'}, \quad \sum_\nu |\Psi_\nu(\mathbf{k})\rangle \langle \Psi_\nu(\mathbf{k})| = \mathbb{1} \quad (6.2.2)$$

$$H_0 |\Psi_\nu(\mathbf{k})\rangle = \epsilon_\nu(\mathbf{k}) |\Psi_\nu(\mathbf{k})\rangle, \quad (6.2.3)$$

where ν, ν' are the band indices. Since this basis is orthonormal and complete, the lattice Green's function takes the form

$$(G^{-1})_{\nu\nu',\sigma}(i\omega_n) = \langle \Psi_\nu(\mathbf{k}) | G_\sigma^{-1}(i\omega_n) | \Psi_{\nu'}(\mathbf{k}) \rangle \quad (6.2.4)$$

$$= (i\omega_n + \mu - \epsilon_\nu(\mathbf{k}))\delta_{\nu\nu'} - \Sigma_{\nu\nu',\sigma}(i\omega_n). \quad (6.2.5)$$

Please note that $G_{\nu\nu',\sigma}(i\omega_n)$ has to be obtained by a matrix inversion of the matrix $G_\sigma^{-1}(i\omega_n)$ which entries are given by Eq. (6.2.5), and not by inverting each entry separately. In general we have

$$(G^{-1})_{\nu\nu',\sigma}(i\omega_n) \neq [G_{\nu\nu',\sigma}(i\omega_n)]^{-1}. \quad (6.2.6)$$

We now want to project $G_\sigma(i\omega_n)$ from the Bloch basis onto localized orbital states $|\tilde{\chi}_m\rangle$. For a realistic system these states would correspond for example to the atomic s, p, d, \dots orbitals but can in general be any set of Wannier function-like localized wave functions. In this context we introduce the projection operator $\tilde{P}(\mathbf{k})$, defined by

$$\tilde{P}_{m\nu}(\mathbf{k}) = \langle \tilde{\chi}_m | \Psi_\nu(\mathbf{k}) \rangle, \quad (6.2.7)$$

which corresponds to the overlap of the Bloch wave function and the localized orbital (spin indices are suppressed). Note that this operator has the general form of a unitary matrix for a basis change from the Bloch to the local orbital basis, as long as both basis sets are complete and orthonormal. In practice this is not the case.

First, the number of bands ν will be restricted to some finite number N_ν , since the construction of the Green's function in Eq. (6.2.5) involves the exact inversion of an $N_\nu \times N_\nu$ matrix, which cannot be made arbitrarily large.

Second, the number of local orbitals m will usually be between 1 to 7 and involve only complete shells like the $3d$ orbitals, because more orbitals become numerically infeasible and one usually assumes that correlation effects are mostly restricted to a specific set of orbitals. This is of course an approximation and has to be carefully checked, if possible, or based on a sound physical reasoning.

As a result, the projection operator is neither unitary because the basis sets are not complete, nor is it a square matrix since the number of Bloch states will usually be different than the number of local orbitals

$$\mathbf{1} \neq \tilde{P}^\dagger(\mathbf{k})\tilde{P}(\mathbf{k}) \neq \tilde{P}(\mathbf{k})\tilde{P}^\dagger(\mathbf{k}) \neq \mathbf{1}. \quad (6.2.8)$$

As a result, the local orbital set will also not be orthonormal

$$\left(\tilde{P}(\mathbf{k})\tilde{P}^\dagger(\mathbf{k})\right)_{mm'} = \sum_{\nu=1}^{N_\nu} \langle \tilde{\chi}_m | \Psi_\nu(\mathbf{k}) \rangle \langle \Psi_\nu(\mathbf{k}) | \tilde{\chi}'_{m'} \rangle \neq \delta_{mm'}. \quad (6.2.9)$$

In order to restore the orthonormality of the local basis set, which is needed to define the local impurity problem, we define the overlap matrix as

$$O_{mm'}(\mathbf{k}) = \left[\tilde{P}(\mathbf{k})\tilde{P}^\dagger(\mathbf{k})\right]_{mm'} \quad (6.2.10)$$

$$= \sum_{\nu} \langle \tilde{\chi}_m | \Psi_\nu(\mathbf{k}) \rangle \langle \Psi_\nu(\mathbf{k}) | \tilde{\chi}'_{m'} \rangle. \quad (6.2.11)$$

Orthonormalized local orbitals are then obtained by

$$|\chi_m\rangle = \sum_{m'} [O(\mathbf{k})]_{mm'}^{-1/2} |\tilde{\chi}_m\rangle, \quad (6.2.12)$$

and correspondingly the orthonormalized projectors

$$P(\mathbf{k}) = [O(\mathbf{k})]^{-1/2} \tilde{P}(\mathbf{k}). \quad (6.2.13)$$

The proof of the orthonormality is straightforward

$$(P(\mathbf{k})P^\dagger(\mathbf{k}))_{mm'} = \left(\frac{\tilde{P}(\mathbf{k})\tilde{P}^\dagger(\mathbf{k})}{\tilde{P}(\mathbf{k})\tilde{P}^\dagger(\mathbf{k})}\right)_{mm'} = \delta_{mm'}. \quad (6.2.14)$$

Nevertheless, the projectors do not form a complete orthonormal basis in Bloch space

$$(P^\dagger(\mathbf{k})P(\mathbf{k}))_{\nu\nu'} = \delta_{\nu\nu'}, \quad (6.2.15)$$

which simply corresponds to the fact that some local orbitals only have very small overlap with other Bloch wave functions or none at all, rendering parts of the diagonal entries of $P^\dagger(\mathbf{k})P(\mathbf{k})$ smaller than one. This is the reason why this method is a projection instead of a unitary transformation, since we project from the Bloch space to a (usually smaller) local orbital space, so we lose information about the bands that do not have any overlap with our choice of local orbitals. The influence of the choice of bands and orbitals to take into account will be discussed shortly in Chapter 6.3.

With the orthonormalized projectors $P(\mathbf{k})$ the lattice Green's function can be projected onto the local orbitals via

$$G_{mm'}(\mathbf{k}, i\omega_n) = \sum_{\nu\nu'} \langle \chi_m | \Psi_\nu(\mathbf{k}) \rangle G_{\nu\nu'}(\mathbf{k}, i\omega_n) \langle \Psi_{\nu'}(\mathbf{k}) | \chi_{m'} \rangle \quad (6.2.16)$$

$$= [P(\mathbf{k})G(\mathbf{k}, i\omega_n)P^\dagger(\mathbf{k})]_{mm'}, \quad (6.2.17)$$

from which the local Green's function follows as

$$G_{mm'}(i\omega_n) = \sum_{\mathbf{k}} G_{mm'}(\mathbf{k}, i\omega_n). \quad (6.2.18)$$

Please note that exchanging the sum over \mathbf{k} by an integration over the energy and density of states as in Eq. (5.2.52) cannot be used since the projections also depend on the momentum. From now on

we can proceed via the standard DMFT cycle and obtain the effective Weiss field $\mathcal{G}_{mm'}(i\omega_n)$ from the local Green's function by Eq. (5.2.51).

From the solution of the effective impurity model, we obtain either directly the Selfenergy $\Sigma(i\omega_n)$ or the interacting impurity Green's function $G^{\text{imp}}(i\omega_n)$. If the latter is the case, the Dyson equation (5.2.49) is used to obtain the Selfenergy.

In the next step we have to construct the interacting lattice Green's function. One can think of "upfolding" the local impurity Green's function $G^{\text{imp}}(i\omega_n)$ to the Bloch basis, but this is not appropriate since the local orbitals do not form a complete basis set in the large Bloch space, which would lead to loss of information in the bands that cannot be fully represented as a linear combination of the local basis. Thus, we promote the Selfenergy which contains the full information of the correlated subspace into the larger Bloch space via the inverse projection

$$\Sigma_{\nu\nu'}(\mathbf{k}, i\omega_n) = \sum_{mm'} [P(\mathbf{k})]_{\nu m}^\dagger (\Sigma_{mm'}(i\omega_n) - \Sigma_{\text{DC}}) P(\mathbf{k})_{m'\nu'}, \quad (6.2.19)$$

where Σ_{DC} is a correction of the double counting, which we will discuss in chapter 6.4. This object is also called the *lattice Selfenergy*. It is important to note that the resulting Selfenergy is a momentum-dependent object even though the Selfenergy of the effective impurity model is local. The additional \mathbf{k} -dependence originates only from the momentum-dependence of the hybridization, causing the Bloch bands to be composed of different orbital character that changes as a function of \mathbf{k} . This can be understood in the illustrative way that the Selfenergy is only distributed to these bands and \mathbf{k} -points that have significant weight of the correlated orbitals.

The lattice Selfenergy (6.2.19) can then be used to update the lattice Green's function in Eq. (6.2.5), and thus closes the DMFT cycle.

6.3 The choice of the energy window

In the construction of the projection operator $P(\mathbf{k})$ we restricted the number of bands taken into account for the projection to some number N_ν . The choice of bands is guided by the principle that we want to represent the local orbitals $|\chi_m\rangle$ as accurate as possible, *i.e.* we have to choose these bands $|\Psi_\nu(\mathbf{k})\rangle$ so that

$$|\chi_m\rangle \approx \sum_{\nu=1}^{N_\nu} |\Psi_\nu(\mathbf{k})\rangle \langle \Psi_\nu(\mathbf{k}) | \chi_m \rangle, \quad (6.3.1)$$

is fulfilled as best as possible. The relation becomes an equality only if all bands are taken into account, so that the Bloch basis is complete. This sets a lower bound for N_ν , because the dimension of the restricted Bloch space needs to be at least as large as the dimension of the local orbital space in order to construct N_{lo} (approximately) orthogonal wave function $|\chi_m\rangle$ as a linear combination of the Bloch states $|\Psi_\nu(\mathbf{k})\rangle$.

The choice of the bands or energy window should also include basically all of the weight of the local orbitals in order to maximize the overlap of a specific local orbital with the set of Bloch wave functions. For example, if a local orbital has almost all of its weight inside a small energy window of $[E_{\text{min}}, E_{\text{max}}]$, the natural choice is to select all bands inside this window for use in the projection scheme.

This is illustrated at the example of the cubic perovskite SrVO_3 in Fig. 6.1. This material features three-fold degenerate t_{2g} and two-fold degenerate e_g states of the vanadium $3d$ orbitals close to the Fermi level. The vanadium states hybridize partially with the oxygen p states, as can be seen by residual weight of oxygen at the Fermi level and vanadium $3d$ states at negative energies in the position of the bonding oxygen p -states. For the local orbitals $|\chi_m\rangle$ to project on we choose the set of the vanadium t_{2g} and e_g orbitals.

Let us consider the first case of an energy window which is as small as possible, shown by the window A in Fig. 6.1, that includes all the weight around the Fermi level but neglects the contribution

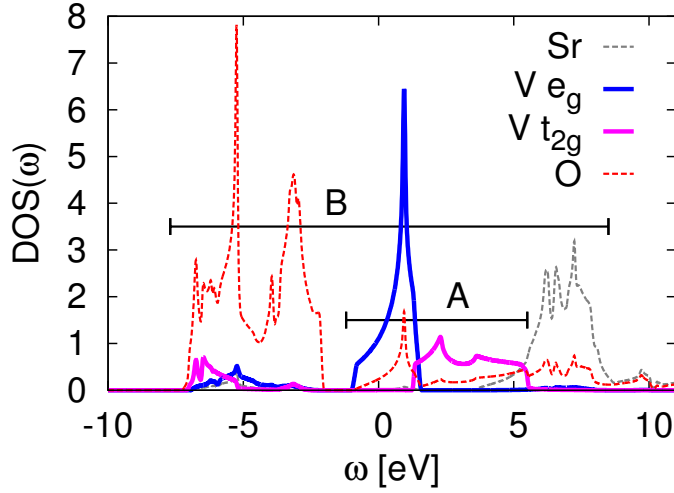


Figure 6.1: The DOS for the cubic perovskite SrVO_3 . Two different choices A,B for the energy window used for the projection from the Bloch bands onto the local vanadium t_{2g} and e_g states are shown. The smaller window A encompasses only the ~ 6 Bloch bands close to the Fermi level, leading to more spatially extended local orbitals. The larger window B contains ~ 20 bands that contain also the vanadium t_{2g} and e_g weight at low energies originating from the hybridization with oxygen, leading to local orbitals that are more localized in real space.

of the hybridization with oxygen. Choosing the window as $[-1.5, 6]$ eV we obtain ~ 6 Bloch bands, of which 5 correspond to bands with mostly vanadium $3d$ character and one band with mostly O- p character. Since the O- p character contained in the V- t_{2g} band around E_F claims a certain amount of weight, while at the same time we neglect the V- t_{2g} at lower energies, the total weight of the V- t_{2g} orbital in this window does not sum up to one so we cannot recover the original shape of the atomic orbital. By the orthonormalization procedure the local orbitals will show some leakage to the oxygen site in real space, the remnant of the hybridization with the O- p states, creating more extended and less localized wave function.

On the other hand we can consider the opposite case of a larger energy window like the one indicated by B in Fig. 6.1. This energy range of $[-8, 9]$ eV encompasses ~ 20 Bloch bands, including the bands corresponding the hybridization of the V- d states with O- p . This results in a very accurate representation of the atomic wave function since the Bloch basis is more complete. Thus, the resulting local orbitals are more localized in space with almost no leakage to the neighbouring oxygen sites. The information about the hybridization in this large window is now encoded in the off-diagonal entries of the lattice Green's function.

When calculating the effective matrix elements of the Coulomb interaction, less localized orbitals lead to smaller values of the interaction parameters U , while for localized orbitals the parameters will be larger. Additionally, by restricting the number of bands in the Bloch basis the Coulomb interaction is reduced by screening processes [36, 56, 127–129]. When the chosen energy window is small, the remaining large subset of Bloch bands not considered for the projection effectively screens the interaction to a small value. For a larger energy window the screening is less effective because more states are excluded from the screening process, resulting in a larger effective U . As a result, a smaller value of U has to be used in the effective impurity model for a small window, while a larger value of U has to be used for a larger window.

For fixed interaction parameters, the degree of correlation is thus reduced if the energy window is enlarged. This is illustrated in Fig. 6.2 at the example of SrVO_3 , using the same energy windows as in Fig. 6.1 for the interaction values of $U = 4$ eV, $J_H = 0.65$ eV. While keeping these parameters

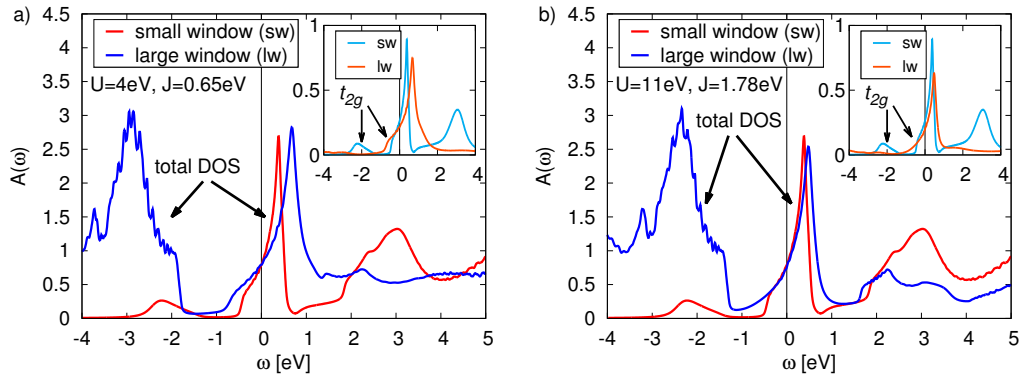


Figure 6.2: The spectral function of SrVO_3 as obtained from LDA+DMFT for a small and large energy window corresponding to the windows A and B in Fig. 6.1. The small inset shows the projection on the degenerate $V-t_{2g}$ orbitals. The weight at lower energies that can be found in the larger window is of oxygen p -character and not included in the smaller window.

a) shows the resulting spectral function for fixed interaction parameters $U = 4 \text{ eV}$, $J_H = 0.65 \text{ eV}$, which clearly results in a decrease of correlation in the larger window. No Hubbard bands are present in the case of the larger window and the renormalization factor reduces by about 40%.

b) shows the result for the same windows, but the interaction parameters are increased to $U = 11 \text{ eV}$, $J_H = 1.78 \text{ eV}$ for the larger window to account for the less effective screening. This leads to a better qualitative agreement, where the renormalization factor in the large window is now even 16% higher compared to the small window. Still, no clear signs of upper and lower Hubbard band are present.

fixed and enlarging the energy window, correlations are significantly reduced, as can be seen from the enlarged width of the quasiparticle peak. Correspondingly, the mass enhancement of the $V-t_{2g}$ orbital drops from ~ 2.4 in the small window to ~ 1.4 in the larger window. Also, there is no upper and lower t_{2g} Hubbard band present in the case of the larger window. This is the result from the inclusion of the hybridizing states at negative energies which increase the kinetic energy of the $V-t_{2g}$ orbitals significantly and thus increase the effective t/U ratio.

When increasing the interaction parameters almost by a factor of three up to $U = 11 \text{ eV}$, $J_H = 1.78 \text{ eV}$ to account for the reduced screening in the larger window, we can only qualitatively regain the results and strength of correlations found for the smaller window. While the mass enhancement of the $V-t_{2g}$ orbital is now even larger with ~ 2.8 , we do not observe any emergence of a lower Hubbard band.

The larger window includes significant weight of the $O-p$ states hybridizing with the $V-3d$ states, but these states are not considered for the local orbital projection and the impurity problem. For a consistent treatment of correlations these states should also be subject to correlations but interactions between two distinct atoms is out of the scope of DMFT, which is an effective single-site theory. A possible approximative way of treating more than one atom within LDA+DMFT is discussed in chapter 6.5.

Therefore, a proper choice of the energy window in combination with the proper interaction parameters is of crucial importance and can have significant effects on the degree of electronic correlations. In practice one will usually use a compromise between, on the one hand, an energy window that is large enough in order to capture as much weight of the correlated orbitals as possible, while on the other hand keeping the window small enough so that weight from other orbitals that are not treated in the impurity problem is as small as possible. A way of determining effective screened interaction parameters depending on the energy window is for example the constrained random-phase approximation (cRPA) [127, 130, 131], which uses the non-interacting polarization arising only from the excluded states to screen the bare Coulomb interaction. More discussion of the effects of different energy windows can also be found in the literature, for example in Ref. [36, 53].

6.4 The double counting problem

Let us now discuss the aspect of the double counting problem already mentioned in Chapter 6.2. It arises every time we combine two or more approaches of solving an interacting many-body problem where the same interaction term in the Hamiltonian is treated by more than one of them. In the case of LDA+DMFT the interaction term is the Coulomb term in the electronic Hamiltonian, and the double counting problem arises because both density functional theory and DMFT treat the electronic interactions in their own way. This leads to the effect that some terms of the interaction are “counted twice”.

DFT itself is based on an exact mapping of the interacting electronic system onto a non-interacting one, with the Coulomb interaction incorporated by an effective potential that is determined self-consistently. The only approximation is done to the exchange-correlation potential, *e.g.* by assuming a homogeneous electron gas in the local density approximation. Therefore, the dispersion $\epsilon^{\text{DFT}}(\mathbf{k})$ obtained in DFT corresponds to the (approximate) Eigenvalues of the interacting electronic system. In contrast to that, within the DMFT Hamiltonian $\epsilon(\mathbf{k})$ is regarded as the dispersion of the non-interacting system. Still, in the combination of LDA+DMFT we assume that

$$\epsilon(\mathbf{k}) \approx \epsilon^{\text{DFT}}(\mathbf{k}), \quad (6.4.1)$$

and replace $\epsilon(\mathbf{k})$ in the non-interacting Green’s function by $\epsilon^{\text{DFT}}(\mathbf{k})$. By this we have already incorporated the effects of correlation on the level of LDA in the non-interacting Green’s function, which leads to the double counting of correlation effects when solving the effective interacting impurity model. We are also faced with the exceptional situation that the more accurate the exchange-correlation part is treated in DFT, for example by using improved functionals like the generalized gradient approximation [64] or hybrid functionals [69, 70, 73, 75, 76, 132, 133] (see Chapter 2.4), the more severe the double counting becomes.

In order to prevent this double counting effect, we have to correct the correlations added by DMFT by a double counting correction term Σ_{DC} . Deriving such a term is inherently difficult in the framework of DFT combined with DMFT, since the two approaches are based on fundamentally different formalism. DFT itself is based on periodic Kohn-Sham wave functions and is not an orbital resolved theory in its usual form (though, orbital resolved quantities can be obtained by projection) and based on total energy functionals that do not have a diagrammatic representation, so one cannot identify and subtract terms that correspond solely to a local Coulomb interaction. On the other hand, DMFT is a diagrammatic theory based on Green’s functions with a clear separation between the non-interacting and interacting case.

Multiple approximative expressions for Σ_{DC} have been derived and used in practice. Many of them were originally derived for use in the LDA+U framework, like the “around mean-field” (AMF) [63] approximation, which is based on the conjecture that the local density approximation corresponds to an approximative mean-field solution of the interacting many-body problem. In this case the modified LDA+U potential that includes the subtraction of the contribution from the average mean-field occupations can be written as a fluctuation around these values

$$\begin{aligned} E_{\text{LDA+U}}^{\text{AMF}} = & \frac{1}{2} \sum_{mm'\sigma} U_{mm'} (n_{m\sigma} - \bar{n}_\sigma)(n_{m\bar{\sigma}} - \bar{n}_{\bar{\sigma}}) \\ & + \sum_{m>m'\sigma} (U_{mm'} - J_{mm'}) (n_{m\sigma} - \bar{n}_\sigma)(n_{m'\sigma} - \bar{n}_\sigma), \end{aligned} \quad (6.4.2)$$

where $\bar{n}_\sigma = \frac{1}{2l+1} \sum_m n_{m\sigma} = \frac{1}{2l+1} N_\sigma$ are the orbitally averaged occupations. If we compare this effective form of the LDA+U with the explicit interaction term that was given as in Eq. (2.5.4)

$$E^{\text{Hub}}[n_{mm'}^\sigma] = \frac{1}{2} \sum_{mm'\sigma} U_{mm'} n_{m\sigma} n_{m'\bar{\sigma}} + \sum_{m>m'\sigma} (U_{mm'} - J_{mm'}) n_{m\sigma} n_{m'\sigma}, \quad (6.4.3)$$

we can derive the double counting functional term as

$$E_{\text{DC}}^{\text{AMF}} = \frac{1}{2} \sum_{mm'\sigma} U_{mm'} (n_{m\sigma} \bar{n}_{\sigma} + n_{m\bar{\sigma}} n_{m\sigma} - \bar{n}_{\sigma} \bar{n}_{\bar{\sigma}}) + \sum_{m>m'\sigma} (U_{mm'} - J_{mm'}) (n_{m\sigma} \bar{n}_{\sigma} + n_{m'\sigma} \bar{n}_{\sigma} - \bar{n}_{\sigma} \bar{n}_{\sigma}) \quad (6.4.4)$$

$$= U_{\text{avg}} N_{\uparrow} N_{\downarrow} + \frac{1}{2} \frac{2l}{2l+1} (U_{\text{avg}} - J_{\text{avg}}) \sum_{\sigma} N_{\sigma}^2, \quad (6.4.5)$$

where we have used the summation rules for a spherically symmetric potential $\sum_{m'} U_{mm'} = U_{\text{avg}}$ and $\sum_{m'} (U_{mm'} - J_{mm'}) = 2l(U_{\text{avg}} - J_{\text{avg}})$ (see Chapter 6.6).

Another approach is the “fully-localized limit” (FLL) [118, 134], which starts from the atomic limit of an ensemble of $N = \sum_{m\sigma} n_{m\sigma}$ electrons where the total Coulomb energy is given by

$$E_{\text{DC}}^{\text{FLL}} = \frac{1}{2} U_{\text{avg}} N(N-1) - \frac{1}{2} J_{\text{avg}} \sum_{\sigma} N_{\sigma}(N_{\sigma}-1). \quad (6.4.6)$$

This form of the FLL functional has the property of the exact density functional which shows a discontinuity at integer filling, which is not observed in LDA or GGA [82].

To derive the orbital potentials of the AMF and FLL double counting correction we evaluate the derivative with respect to $n_{m\sigma}$

$$\Sigma_{\text{DC},\sigma}^{\text{AMF}} = U_{\text{avg}} \left(N - \frac{N_{\sigma}}{2l+1} \right) - J_{\text{avg}} \left(N_{\sigma} - \frac{N_{\sigma}}{2l+1} \right) \quad (6.4.7)$$

$$\Sigma_{\text{DC},\sigma}^{\text{FLL}} = U_{\text{avg}} \left(N - \frac{1}{2} \right) - J_{\text{avg}} \left(N_{\sigma} - \frac{1}{2} \right). \quad (6.4.8)$$

We see that in general the FLL double counting will give a larger correction than the AMF double counting. The resulting effects on the LDA+DMFT calculation will be discussed shortly.

Other methods have been proposed [135], like subtracting the average Hartree term from the impurity Selfenergy so that

$$\Sigma_{\text{DC}} = \lim_{\omega_n \rightarrow \infty} \sum_{m\sigma} \Sigma_{m\sigma}(i\omega_n). \quad (6.4.9)$$

By this construction, the orbital levels experience no static shift on average but still allow for orbital differentiation and insulating solutions. This is motivated by the idea that the orbitals treated as correlated are not shifted relative to the other orbitals on average.

Another similar approach is to constrain the total charge of the impurity Green’s function to be equal to that of the non-interacting local Green’s function [126]. By this, no net charge is pushed out of the correlated orbitals but only redistributed. This method can work well for metals but not for materials that become insulators due to correlations since this double counting pushes the system away from half-filling unless the non-interacting system is half filled.

Others have proposed small modifications to existing schemes [136], like the so-called nominal double counting, which is based on the FLL variant of the double counting correction but replaces the orbital fillings by the nominal valence [137, 138]. This scheme usually yields a smaller correction than the standard FLL method and an improved agreement with experiment.

Recently, another highly-sophisticated double counting was presented [139], which promoted the DMFT functionals into a real-space continuum representation, in which the LDA is defined, and calculating the overlap of the two methods by solving an effective LDA impurity model, *i.e.* a uniform electron gas with a charge density being equal to the local impurity filling and a screened Coulomb interaction. This method was shown to give encouraging results similar to the nominal double counting [139]. Still, the contribution of other orbitals that hybridize with the impurity orbitals, thus are included in the energy window but are not treated as correlated is not clear.

All these different methods have in common that they use a real constant Σ_{DC} for the double counting correction which can be spin-resolved for magnetic systems but is orbitally and frequency independent, since the Hartree and exchange terms included in DFT are static. All the methods only differ by the value of this constant and the way how it is obtained. Therefore, it is very insightful to investigate the qualitative effect of such correction independent of the method by which it is obtained, and quantify the changes due to larger or smaller values of Σ_{DC} in order to be able to properly judge the effects of different double counting schemes.

In LDA+DMFT all orbitals and the corresponding bands that are not treated as correlated do not experience any effects of the impurity Selfenergy and thus should also not be influenced by the double counting. Therefore, it is customary to subtract the double counting directly from the impurity Selfenergy

$$\Sigma(i\omega_n) = \Sigma^{\text{imp}}(i\omega_n) - \Sigma_{\text{DC}}, \quad (6.4.10)$$

which is then upfolded into the Bloch space to create the interacting lattice Green's function (see Chapter 6.2)

$$[G^{-1}]_{\nu\nu'}(\mathbf{k}, i\omega_n) = (i\omega_n + \mu - \epsilon_\nu)\delta_{\nu\nu'} - \sum_{mm'} [P(\mathbf{k})]_{\nu m}^\dagger (\Sigma_{mm'}(i\omega_n) - \Sigma_{\text{DC}}\delta_{mm'}) P(\mathbf{k})_{m'\nu}. \quad (6.4.11)$$

For simplicity let us assume that the Hartree term $\Sigma_{m,\infty} = \lim_{\omega_n \rightarrow \infty} \Sigma_{mm}(i\omega_n)$ will be approximately equal for all correlated orbitals $\Sigma_\infty \approx \Sigma_{m,\infty}$. Since $\Sigma_\infty - \Sigma_{\text{DC}}$ will usually be different from zero, unless we make the special choice $\Sigma_\infty = \Sigma_{\text{DC}}$, the Selfenergy will introduce a net shift of all correlated orbitals that will result in a change of the total electron number, so we have to readjust the chemical potential μ in order to keep the total charge of the system constant (see Chapter 6.8)

$$\mu \rightarrow \mu + \Delta\mu. \quad (6.4.12)$$

The diagonal components of the Green's function are then given by

$$[G^{-1}]_{\nu\nu}(\mathbf{k}, i\omega_n) = i\omega_n + \mu + \Delta\mu - \epsilon_\nu - \sum_{mm'} [P(\mathbf{k})]_{\nu m}^\dagger (\Sigma_{mm'}(i\omega_n) - \Sigma_{\text{DC}}\delta_{mm'}) P(\mathbf{k})_{m'\nu} \quad (6.4.13)$$

$$= i\omega_n + \mu - (\epsilon_\nu - \Delta\mu + (\Sigma_\infty - \Sigma_{\text{DC}}) [P^\dagger P]_{\nu\nu}) - P^\dagger(\mathbf{k})\Sigma'(i\omega_n)P(\mathbf{k}), \quad (6.4.14)$$

where $\Sigma'_{mm'}(i\omega_n) = \Sigma_{mm'}(i\omega_n) - \Sigma_\infty$. Under the assumption that the imaginary part of the Selfenergy is small and that $\Sigma'(i\omega_n)$ is similar for all orbitals, we can identify the new energies of the quasiparticle excitations in LDA+DMFT as

$$\epsilon_\nu^{\text{QP}} \approx \epsilon_\nu - \Delta\mu + (\Sigma_\infty - \Sigma_{\text{DC}}) [P^\dagger P]_{\nu\nu}. \quad (6.4.15)$$

If the hybridization between the correlated orbitals and uncorrelated orbitals is small, we can obtain a good representation of the bands that have correlated orbital character, *i.e.* $[P^\dagger P]_{\nu\nu} \approx 1$ for a band ν with mostly correlated character and resp. 0 for mostly uncorrelated character. This leads to the approximative total shift of the quasiparticle excitation energies given by

$$\Delta\epsilon_\nu \approx \begin{cases} -\Delta\mu & \nu \text{ uncorrelated} \\ -\Delta\mu + \Sigma_\infty - \Sigma_{\text{DC}} & \nu \text{ correlated} \end{cases}. \quad (6.4.16)$$

As a result the correlated and uncorrelated bands are separated by the energy $\Sigma_\infty - \Sigma_{\text{DC}}$, which is just a linear function of Σ_{DC} . This tells us that different values of the double counting basically define the separation of the correlated and uncorrelated states. We can distinguish two cases:

1. The subset of correlated bands is well separated from the uncorrelated bands, so that the energy window used for the projection does not include the the uncorrelated states:

If this is the case, $[P^\dagger P]_{\nu\nu} \approx 1$ for all ν considered, so that all bands will shifted approximately by the same constant which can be absorbed in the chemical potential. Therefore, the choice of the double counting can be arbitrary and will not change the results. Thus it can be even neglected, which is done for example in calculations based on a tight-binding model where the number of correlated orbitals equals the number of bands.

2. The subset of correlated bands overlaps with the uncorrelated bands which are then included in the energy window:

In this case the correlated bands are pushed to higher energies compared to the uncorrelated depending on the value of the double counting correction. This can change the hybridizations between the two kinds of bands and thus the localization of the orbitals, which can lead to a difference in correlation strength. In general, the filling of the correlated orbitals reduces while for the uncorrelated orbitals it increases much more than if the two sets were separated. This is because the first are pushed to higher energies while the latter are pushed to lower energies. In case when they are separated, the double counting acts like an overall shift, which is absorbed in the chemical potential by requiring overall charge conservation, so charge can only be redistributed in the correlated orbitals.

In the most extreme case uncorrelated bands that are above the Fermi level in the energy range of about $\Delta\mu$ can be pushed below E_F even though they do not experience any Selfenergy effects. In these cases the it is not the DMFT approximation that is at fault in general but more the restriction to only a *single* effective impurity. Since the correlated atom hybridizes strongly with one of its neighbours these neighbouring atom should also pick up a finite Selfenergy which would resolve the problem of the unphysical separation between them.

We now discuss the difference of the double counting schemes at the example of two realistic systems. The iron-based superconductor FeSe falls in-between these two cases discussed above. The states at the Fermi level are almost exclusively of Fe $3d$ nature in the energy window of about $[-2.5, 2]$ eV, so we will treat them as correlated in the impurity problem. They are separated by a gap from the selenium states that are lower in energy. Though, there is a sizeable hybridization between these low-energy selenium states and the Fe $3d$ orbitals which we would like to include in the energy window in order for the total Fe $3d$ weight to be normalized to one as close as possible. By doing so, we also include the selenium states but since they have significant weight only away from the Fermi level, the separation of the correlated from the uncorrelated sector due to the double counting will not be of significance around the Fermi level.

As a result, we observe only small quantitative changes in the spectral function obtained from LDA+DMFT for the two FLL and AMF double counting methods shown in Fig. 6.3, even though the two corrections are quite different $\Sigma_{DC}^{FLL} - \Sigma_{DC}^{AMF} \approx 1$ eV. Naturally, one would expect the uncorrelated selenium states to differ in their energy about the same value between the two schemes, while we only observe a difference of about 0.25 eV. This is a general trend we find when performing the calculation fully charge self-consistent (see Chapter 6.7), where the self-consistent calculation also of the DFT charge moderates the different double countings, which was also observed in Ref. [139]. Still, the smaller AMF double counting results in an increased average mass enhancement of about 2.6 compared to the FLL double counting of about 1.9 (for parameters $U = 4$ eV, $J_H = 0.8$ eV, $\beta = 100$ 1/eV).

As a second example where the double counting becomes more important is the iron-pnictide superconductor KFe_2As_2 , shown in Fig. 6.4. In this system the Fe $3d$ hybridize to a notable degree with the As $4p$ states also close to the Fermi level and there is no gap that separates the bands of majority iron and majority arsenic weight like in FeSe. As a result the double counting will have a significant impact on the relative fillings of the Fe and As orbitals since smaller values of the double counting will lead to an increase in separation of the correlated and uncorrelated sector.

Though, the qualitative agreement between the FLL and AMF double counting is still quite good but not on the same level as in FeSe, even though the difference is very similar

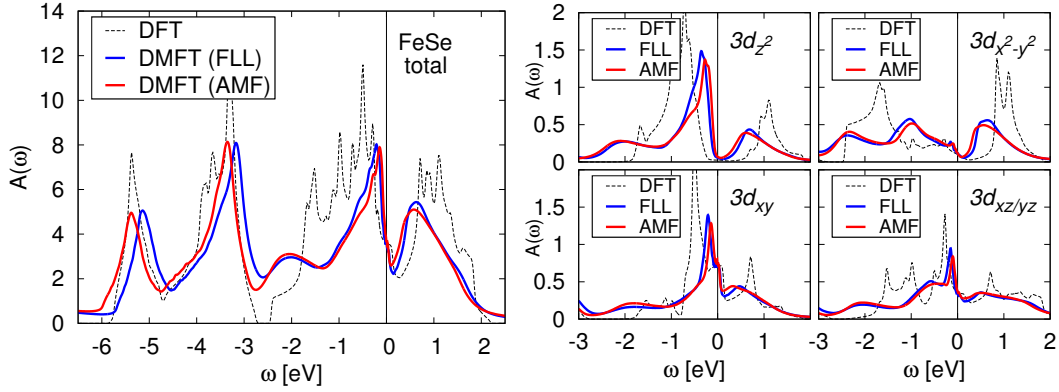


Figure 6.3: The spectral function of FeSe within LDA+DMFT, comparing the two different double counting schemes of the fully-localized limit (FLL) and around mean-field (AMF) approximations. Left: The total spectral function and right: orbital resolved spectral functions of the iron 3d orbitals. The most prominent difference between the two double counting schemes is the shift of the uncorrelated selenium states since the double counting defines the effective separation between the correlated and the uncorrelated sector (see explanation in the text). The smaller AMF double counting results in an increased average mass enhancement of about 2.6 compared to the FLL double counting of about 1.9 (for parameters $U = 4$ eV, $J_H = 0.8$ eV, $\beta = 100$ 1/eV).

$\Sigma_{DC}^{FLL} - \Sigma_{DC}^{AMF} \approx 1.1$ eV. Apart from the shift in energy of the uncorrelated states at lower energy, we also observe a shoulder-like feature in the Fe $3d_{z^2}$, $3d_{xy}$ and $3d_{xz/yz}$ spectral function at negative energies which is absent for the FLL calculation. Since the smaller value of the AMF double counting brings the system closer to half-filling, we interpret this feature as an effect of the increase in correlation strength, which is discussed in Chapter 8, also indicated by the increase in the average mass enhancement of up to 2.8 compared to the FLL double counting of about 2.3 (for parameters $U = 4$ eV, $J_H = 0.8$ eV, $\beta = 80$ 1/eV).

Despite all the effort that has been devoted to solving the double counting problem, a satisfying solution is not in sight and probably will never be. Since the double counting problem arises whenever states that are not included in the DMFT model hybridize with the correlated states, the straightforward solution would be to treat all states inside the energy window used for projection on the same footing, with no separation into correlated and uncorrelated subsets. While this is in principle possible for atomic orbitals on one atomic site, it immediately moves out of the scope of DMFT as soon as more than one atomic site becomes relevant.

While fully charge self-consistent calculations (see Chapter 6.7) by our experience are found to relieve the difference between the double counting procedures by updating the projectors and thus the DFT potential in the presence of the modified DMFT charge density self-consistently, qualitative differences can still remain (see for example our results on KFe_2As_2 in Chapter 7).

This makes modified approaches of LDA+DMFT method that aim to avoid the double counting problem from the start highly attractive. While retaining the DMFT approach for its accuracy of solving the interacting local problem also for strong interactions, it was suggested to replace the DFT part in LDA+DMFT by a Green's function based method like GW, called GW+DMFT (see Outlook in Chapter 10), which allows for a unique identification of the correlations accounted for in both methods.

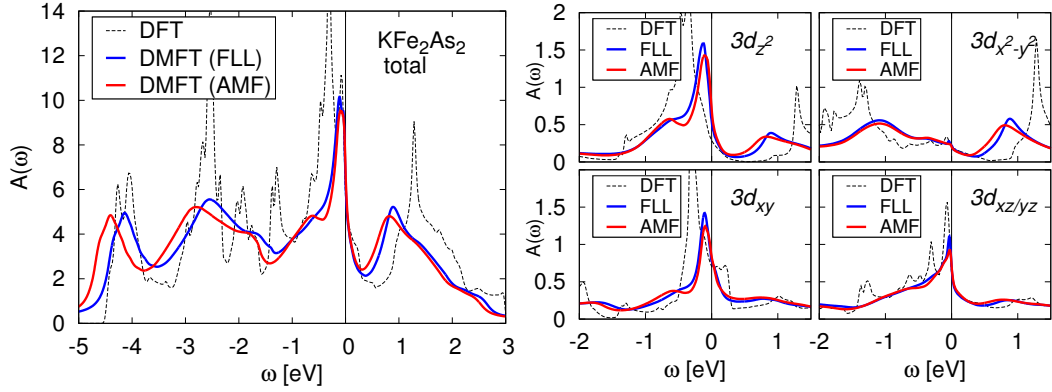


Figure 6.4: The spectral function of KFe_2As_2 within LDA+DMFT, comparing the two different double counting schemes of the fully-localized limit (FLL) and around mean-field (AMF) approximations.

Left: The total spectral function and right: orbital resolved spectral functions of the iron 3d orbitals. Similar to FeSe in Fig. 6.3 the shift of the uncorrelated states differs between the two methods but one also observes a slightly different form of the Fe 3d spectral functions close to the Fermi level, where in the AMF scheme a shoulder-like feature emerges at negative energies for most orbitals. This feature will be discussed in more detail in Chapter 8. The smaller AMF double counting results in an increased average mass enhancement of about 2.8 compared to the FLL double counting of about 2.3 (for parameters $U = 4$ eV, $J_H = 0.8$ eV, $\beta = 80$ 1/eV).

6.5 Multiple correlated atoms

Often we are faced with a system that contains more than one correlated atom in the unit cell. This raises the question of how we can actually treat multiple atoms within LDA+DMFT, since DMFT is an effective single impurity method. In the derivation of the DMFT method in Chapter 5.2 we saw that the Selfenergy Σ_{ij} became site-diagonal in the limit of infinite dimensions

$$\lim_{d \rightarrow \infty} \Sigma_{ij} = \delta_{ij} \Sigma_{ii}, \quad (6.5.1)$$

where i, j label the lattice sites. There are no off-diagonal terms in the Selfenergy since the hybridization of an atom with only one specific neighbour becomes negligible for an infinite number of neighbours and can be described instead by an effective bath \mathcal{G} . In the original derivation we considered the periodic Hubbard model where all sites are equivalent, which allowed us to choose a unit cell that contained only a single atom and solve the impurity model only for this site. Focusing on another atom does not change this result and by symmetry we know that each site i will pick up the same Selfenergy site-diagonal $\Sigma_{ii} = \Sigma$ in the DMFT limit.

In the same way we can apply the DMFT approximations to two different sites i and j , that will have no off-site Selfenergy $\Sigma_{ij} = 0$ for $i \neq j$ for $d \rightarrow \infty$. They only interact via a global bath \mathcal{G} in which the two atoms are embedded that has to be determined self-consistently, as illustrated in Fig. 6.5. In a realistic system with a finite coordination number Z this approximation will be appropriate if the surrounding of the multiple impurity atoms is approximately homogeneous, *i.e.* the impurity atoms do not hybridize directly with each other so there is no dimerization or clustering of correlated atoms.

In the simplest case all correlated atoms are equivalent and related by symmetry, for example most iron-based superconductors contain two or more Fe atoms in their unit cell which are related by glide-mirror symmetry. This allows us to solve the resulting impurity model only once, and obtain the Selfenergy for the other equivalent atoms by the corresponding symmetry operation O^α , where

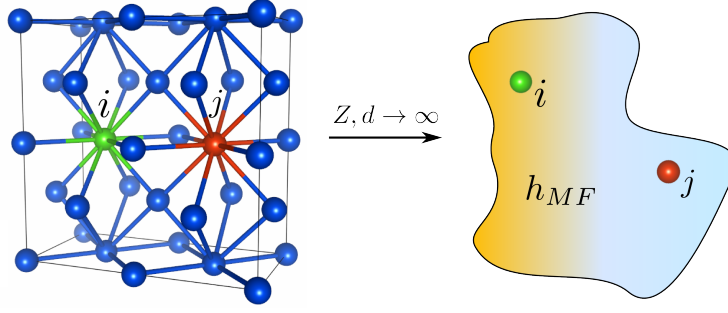


Figure 6.5: Illustration of two impurity atoms in the DMFT limit. For large coordination number Z (or dimension d) the two impurities do not interact directly with each other but only via an effective bath \mathcal{G} that has to be found self-consistently. For equivalent atoms in the unit cell the effective local environment for each atom is identical so only one impurity problem has to be solved. In general the local bath is different for each atom.

α labels the equivalent atoms

$$\Sigma^\alpha = O^{\alpha,\dagger} \Sigma O^\alpha. \quad (6.5.2)$$

For an example let us consider two correlated atoms in the unit cell with two orbitals a, b taken as the local basis. The two sites are related by the symmetry transformation $x, y, z \rightarrow y, x, -z$, so the full local Selfenergy is then of the form

$$\Sigma = \begin{array}{c} |a\rangle_1 \\ |b\rangle_1 \\ |a\rangle_2 \\ |b\rangle_2 \end{array} \begin{pmatrix} \Sigma_{aa}^1 & \Sigma_{ab}^1 & 0 & 0 \\ \Sigma_{ba}^1 & \Sigma_{bb}^1 & 0 & 0 \\ 0 & 0 & \Sigma_{aa}^1 & -\Sigma_{ab}^1 \\ 0 & 0 & -\Sigma_{ba}^1 & \Sigma_{bb}^1 \end{pmatrix}. \quad (6.5.3)$$

The projection operators P^α from the Bloch basis to the local orbital basis (see Chapter 6.2) now also depend on the atomic site since the local orbitals $|\chi_{\alpha,m}\rangle$ are different on each site (but related by symmetry). The local Green's function for the equivalent atoms α is then given by

$$G_{mm'}^\alpha(i\omega_n) = \sum_{\mathbf{k}} [P^\alpha(\mathbf{k}) G(\mathbf{k}, i\omega_n) P^{\alpha,\dagger}(\mathbf{k})]_{mm'}. \quad (6.5.4)$$

The impurity problem is then solved for only one of the equivalent atoms, *e.g.* $\alpha = 1$, since the resulting Selfenergy $\Sigma^1(i\omega_n)$ can be used to construct the Selfenergy for all other atoms by using Eq. (6.5.2). The full lattice Selfenergy is then given by

$$\Sigma_{\nu\nu'}(i\omega_n) = \sum_{\alpha} [P^{\alpha,\dagger}(\mathbf{k}) O^{\alpha,\dagger} (\Sigma^1(i\omega_n) - \Sigma_{\text{DC}}^1) O^\alpha P^\alpha(\mathbf{k})]_{\nu\nu'}, \quad (6.5.5)$$

which is then used to construct the lattice Green's function via Eq. (6.2.5). Here we have set $O^{\alpha=1} = \mathbb{1}$.

For two atoms or more in the unit cell that are not equivalent we cannot resort to symmetry operations to obtain the Selfenergy from only one of them. In this case we have to solve each impurity problem separately and obtain different Selfenergies $\Sigma^\alpha(i\omega_n)$ for each site α . The final lattice Selfenergy is then of the same form as Eq. (6.5.5) just without the symmetry operations

$$\Sigma_{\nu\nu'}(i\omega_n) = \sum_{\alpha} [P^{\alpha,\dagger}(\mathbf{k}) (\Sigma^\alpha(i\omega_n) - \Sigma_{\text{DC}}^\alpha) P^\alpha(\mathbf{k})]_{\nu\nu'}. \quad (6.5.6)$$

6.6 Coulomb matrix

After the projection onto the local orbitals and application of the DMFT approximation the Hamiltonian in this local subspace is given by an effective Anderson impurity model (AIM), as discussed in Chapter 5.2. The resulting AIM Hamiltonian we have to solve is of the form

$$H_{\text{AIM}} = H_{\text{bath}} + H_{\text{hyb}} + H_{\text{int}}, \quad (6.6.1)$$

where H_{bath} contains the kinetic contribution of the effective bath and H_{hyb} the hybridization of the bath with the impurity site, which both correspond to the non-interacting part of the Hamiltonian. The difficult problem is contained in the interacting part H_{int} , describing the Coulomb interaction of electrons on the impurity site.

Since the Coulomb interaction is spin-independent and thus preserves the spin of the interacting electrons, the general form of H_{int} can be written as

$$H_{\text{int}} = \frac{1}{2} \sum_{\substack{mm' \\ m''m'''}} \sum_{\sigma\sigma'} \langle mm' | V_{\text{Coulomb}} | m''m''' \rangle c_{m\sigma}^\dagger c_{m'\sigma'}^\dagger c_{m''\sigma} c_{m'''\sigma'}, \quad (6.6.2)$$

where the matrix elements are given by

$$\langle mm' | V_{\text{Coulomb}} | m''m''' \rangle = \int d\mathbf{r} \int d\mathbf{r}' \psi_{m\sigma}^*(\mathbf{r}) \psi_{m'\sigma'}^*(\mathbf{r}') \frac{1}{|\mathbf{r} - \mathbf{r}'|} \psi_{m''\sigma}(\mathbf{r}') \psi_{m'''\sigma}(\mathbf{r}). \quad (6.6.3)$$

For the case of a one-orbital model the Coulomb interaction takes the simple form

$$H_{\text{int}}^1 = \frac{1}{2} \sum_{\sigma\sigma'} V c_{\sigma}^\dagger c_{\sigma'}^\dagger c_{\sigma'} c_{\sigma} \quad (6.6.4)$$

$$= V n_{\uparrow} n_{\downarrow}. \quad (6.6.5)$$

For a multi-orbital system the interaction terms become much more complicated. Often one neglects terms with matrix elements that connect more than two different orbitals because they are assumed to be small or spin-flip and pair-hopping terms due to numerical efficiency. For the construction of the proper interaction matrix we follow the outline given in Ref. [140].

The case of a three-orbital system is still rather simple, but quite relevant in the context of transition metals in an octahedral environment, where three t_{2g} orbitals form the states close to the Fermi level. This leads to the so-called Kanamori form [4, 38] of the Coulomb interaction, which can be shown to be fully parametrized by the three matrix elements

$$U = \langle mm | V_{\text{Coulomb}} | mm \rangle = \int d\mathbf{r} \int d\mathbf{r}' |\psi_{m\sigma}(\mathbf{r})|^2 \frac{1}{|\mathbf{r} - \mathbf{r}'|} |\psi_{m\bar{\sigma}}(\mathbf{r}')|^2, \quad (6.6.6)$$

$$U' = \langle mm' | V_{\text{Coulomb}} | mm' \rangle = \int d\mathbf{r} \int d\mathbf{r}' |\psi_{m\sigma}(\mathbf{r})|^2 \frac{1}{|\mathbf{r} - \mathbf{r}'|} |\psi_{m'\bar{\sigma}}(\mathbf{r}')|^2, \quad (6.6.7)$$

$$J = \langle mm' | V_{\text{Coulomb}} | m'm \rangle = \int d\mathbf{r} \int d\mathbf{r}' \psi_{m\sigma}^*(\mathbf{r}) \psi_{m'\sigma}^*(\mathbf{r}') \frac{1}{|\mathbf{r} - \mathbf{r}'|} \psi_{m\sigma}(\mathbf{r}') \psi_{m'\sigma}(\mathbf{r}). \quad (6.6.8)$$

This leads to the Kanamori Hamiltonian

$$\begin{aligned} H_{\text{int}}^3 = & U \sum_m n_{m\uparrow} n_{m\downarrow} + U' \sum_{m \neq m'} n_{m\uparrow} n_{m'\downarrow} + (U' - J) \sum_{m < m', \sigma} n_{m\sigma} n_{m'\sigma} \\ & - J \sum_{m \neq m'} c_{m\uparrow}^\dagger c_{m\downarrow} c_{m'\downarrow}^\dagger c_{m'\uparrow} + J \sum_{m \neq m'} c_{m\uparrow}^\dagger c_{m\downarrow}^\dagger c_{m'\downarrow} c_{m'\uparrow}. \end{aligned} \quad (6.6.9)$$

The first term corresponds to the interaction of two electrons in the same orbital with opposite spin, the second term to the same case in different orbitals, and the third term to different orbitals but with the same spin. The energy for this state ($U' - J$) is reduced by J , reflecting the Hund's rules of

maximizing the total spin. The second last term is called the spin-flip term, since its form looks like it flips the spin of each electron in the different orbitals m and m' . This is just an effective description of the process of exchanging the orbitals of the two electrons, since the Coulomb interaction is spin-independent. The last term is known as the pair-hopping term, since it effectively transfers a pair of electrons in the same orbital to another different orbital.

The U' parameter can be determined by requesting H_{int}^3 to be rotationally invariant. By calculating the action of H_{int}^3 on a state which is not an S_z Eigenstate one obtains the requirement

$$U' = U - 2J. \quad (6.6.10)$$

Therefore, the full Kanamori Hamiltonian can be parametrized by only the on-site Coulomb term U and Hund's coupling J as

$$\begin{aligned} H_{\text{int}}^3 = & U \sum_m n_{m\uparrow} n_{m\downarrow} + (U - 2J) \sum_{m \neq m'} n_{m\uparrow} n_{m'\downarrow} + (U - 3J) \sum_{m < m', \sigma} n_{m\sigma} n_{m'\sigma} \\ & - J \sum_{m \neq m'} c_{m\uparrow}^\dagger c_{m\downarrow} c_{m'\downarrow}^\dagger c_{m'\uparrow} + J \sum_{m \neq m'} c_{m\uparrow}^\dagger c_{m\downarrow}^\dagger c_{m'\downarrow} c_{m'\uparrow}. \end{aligned} \quad (6.6.11)$$

The next relevant case is that of a full d -shell with five orbitals, encountered in most iron-pnictide superconductors (see our results in Chapter 7,8 and 9). A compact notation of the Coulomb matrix for five orbitals is given by the use of Slater integrals [84, 141], which also allow a full parametrization in terms of an on-site Coulomb term and Hund's coupling.

For this, we rewrite the Coulomb interaction in spherical coordinates, where the transformation is given by $\mathbf{r} = r(\cos \phi \sin \theta, \sin \phi \sin \theta, \cos \theta)$, leading to the form

$$\frac{1}{|\mathbf{r} - \mathbf{r}'|} = \sum_{l=0}^{\infty} \frac{r_{<}^l}{r_{>}^{l+1}} \frac{4\pi}{2l+1} \sum_{m=-l}^l Y_{l,m}(\theta', \phi') Y_{l,m}^*(\theta, \phi), \quad (6.6.12)$$

where $r_{<}$ is the smaller of r, r' and $r_{>}$ the larger, respectively. We assume that the local orbitals we use for the basis of the impurity model are close to the atomic orbitals and thus evaluate the Coulomb matrix elements in the basis of the states $|n, l, m\rangle$, where n is the principal, l the orbital and m the magnetic quantum number. With this the matrix elements can be written as

$$\langle mm' | V_{\text{Coulomb}} | m'' m''' \rangle = \sum_{k=0}^{2l} a_k (mm'', m' m''') F_k, \quad (6.6.13)$$

where a_k contain the integrals over the angular part

$$a_k (mm'', m' m''') = \frac{4\pi}{2k+1} \sum_{q=-k}^k \langle nlm | Y_{k,q} | nlm'' \rangle \langle nlm' | Y_{k,q}^* | nlm''' \rangle, \quad (6.6.14)$$

and F_k the Slater integrals given by

$$F_k = \int d\mathbf{r} \int d\mathbf{r}' r'^2 R_{nl}^2(r) \frac{r_{<}^k}{r_{>}^{k+1}} R_{nl}^2(r'). \quad (6.6.15)$$

The radial functions $R_{nl}(r)$ are given by the usual form

$$R_{nl}(r) = \sqrt{\left(\frac{2}{na_0}\right)^3 \frac{(n-l-1)!}{2n[(n+l)!]^3}} e^{-\rho/2} \rho^l L_{n-l-1}^{2l+1}(\rho), \quad (6.6.16)$$

where a_0 is the Bohr radius, $\rho = \frac{2r}{na_0}$ and L_{n-l-1}^{2l+1} are the generalized Laguerre polynomials.

In applications for electronic structure calculations the real form Y_{lm}^{real} of the spherical harmonics are usually used. Therefore, we will now formulate the Coulomb matrix elements for the d shell in the real harmonics basis.

Similar to the three-orbital case we define the direct $U_{mm'}$ and exchange $J_{mm'}$ integrals as

$$\langle mm' | V_{\text{Coulomb}} | mm' \rangle = U_{mm'} = \sum_{k=0}^{2l} a_k(mm, m'm') F_k \quad (6.6.17)$$

$$\langle mm' | V_{\text{Coulomb}} | m'm \rangle = J_{mm'} = \sum_{k=0}^{2l} a_k(mm', m'm) F_k. \quad (6.6.18)$$

With the aim of introducing a simple parametrization we define the average Coulomb parameters as

$$U_{\text{avg}} = \frac{1}{(2l+1)^2} \sum_{mm'} U_{mm'} = F_0 \quad (6.6.19)$$

$$J_{\text{avg}} = U_{\text{avg}} - \frac{1}{2l(2l+1)} \sum_{mm'} (U_{mm'} - J_{mm'}) = \frac{F_2 + F_4}{14}. \quad (6.6.20)$$

It can be shown that for d -electrons only the F_0, F_2 and F_4 Slater integrals contribute and that $F_4/F_2 \approx 5/8$ for realistic $3d$ orbitals. With this, we can parametrize the direct $U_{mm'}$ and exchange $J_{mm'}$ Coulomb matrices as

$$U_{mm'} \begin{array}{l} |z^2\rangle \\ |x^2 - y^2\rangle \\ |xy\rangle \\ |xz\rangle \\ |yz\rangle \end{array} \begin{pmatrix} |z^2\rangle & |x^2 - y^2\rangle & |xy\rangle & |xz\rangle & |yz\rangle \\ U_0 & U_0 - 2J_2 & U_0 - 2J_2 & U_0 - 2J_4 & U_0 - 2J_4 \\ U_0 - 2J_2 & U_0 & U_0 - 2J_3 & U_0 - 2J_1 & U_0 - 2J_1 \\ U_0 - 2J_2 & U_0 - 2J_3 & U_0 & U_0 - 2J_1 & U_0 - 2J_1 \\ U_0 - 2J_4 & U_0 - 2J_1 & U_0 - 2J_1 & U_0 & U_0 - 2J_1 \\ U_0 - 2J_4 & U_0 - 2J_1 & U_0 - 2J_1 & U_0 - 2J_1 & U_0 \end{pmatrix} \quad (6.6.21)$$

$$J_{mm'} \begin{array}{l} |z^2\rangle \\ |x^2 - y^2\rangle \\ |xy\rangle \\ |xz\rangle \\ |yz\rangle \end{array} \begin{pmatrix} |z^2\rangle & |x^2 - y^2\rangle & |xy\rangle & |xz\rangle & |yz\rangle \\ 0 & J_2 & J_2 & J_4 & J_4 \\ J_2 & 0 & J_3 & J_1 & J_1 \\ J_2 & J_3 & 0 & J_1 & J_1 \\ J_4 & J_1 & J_1 & 0 & J_1 \\ J_4 & J_1 & J_1 & J_1 & 0 \end{pmatrix}, \quad (6.6.22)$$

where

$$U_0 = U_{\text{avg}} + \frac{8}{7} J_{\text{avg}} \quad (6.6.23)$$

$$J_1 = \frac{3}{49} F_2 + \frac{20}{9} \frac{1}{49} F_4 \quad (6.6.24)$$

$$J_2 = -\frac{10}{7} J_{\text{avg}} + 3J_1 \quad (6.6.25)$$

$$J_3 = \frac{30}{7} J_{\text{avg}} - 5J_1 \quad (6.6.26)$$

$$J_4 = \frac{20}{7} J_{\text{avg}} - 3J_1. \quad (6.6.27)$$

Within this parametrization, the Hamiltonian for the Coulomb interaction is given by

$$\begin{aligned} H_{\text{int}}^5 &= \sum_{mm'} U_{mm'} n_{m\uparrow} n_{m'\downarrow} + \sum_{m < m', \sigma} (U_{mm'} - J_{mm'}) n_{m\sigma} n_{m'\sigma} \\ &- \sum_{m \neq m'} J_{mm'} c_{m\uparrow}^\dagger c_{m\downarrow} c_{m'\downarrow}^\dagger c_{m'\uparrow} + \sum_{m \neq m'} J_{mm'} c_{m\uparrow}^\dagger c_{m\downarrow}^\dagger c_{m'\downarrow} c_{m'\uparrow}. \end{aligned} \quad (6.6.28)$$

Again the Coulomb interaction can be parametrized by only the two parameters U_{avg} and J_{avg} .

Please note that in this definition U_{avg} is very different from U_0 , which corresponds to the interaction of two electrons with opposite spin in the same orbital, when $J_{\text{avg}} > 0$. Therefore, care must be taken when comparing calculations with different notations, since U_0 is usually much larger than U_{avg} .

As discussed in Chapter 6.3, the matrix elements of the Coulomb interaction $\langle mm' | V_{\text{Coulomb}} | mm' \rangle$ cannot be used directly in the Hamiltonian of the Anderson impurity model since they are screened to lower values by the remaining uncorrelated states. For example, the monopole Slater Integral $F_0 = U_{\text{avg}}$ is usually of the order of 15 – 20 eV for 3d orbitals, but is screened down to a few eV's at low energies, while the Hund's rule coupling corresponding to J_{avg} is approximately reduced by 20 – 30 % [142].

The effective screened interaction parameters depend on the energy window, since the more number of bands are outside of the window the more efficient is the screening. From methods like constrained random-phase approximation (cRPA) [127, 130, 131], which calculate the non-interacting polarization arising only from the excluded states that screens the bare Coulomb interaction, one even obtains a frequency dependent interaction $U(\omega)$, since the screening is less efficient and recovers the bare value at high frequencies [127, 128, 130]. Taking these effects into account can lead to plasmon satellites and transfer of spectral weight away from the Fermi level to high energies [56, 127, 128]. Since the numerical effort becomes quite involved in this case, we will not consider the explicit treatment of the frequency dependence of the interactions in this work. A simple approximation to capture the most important effects of the frequency dependence in transition-metal oxides will be discussed in Chapter 9.

6.7 Full charge self-consistency

The original LDA+DMFT approach was based on a fixed set of non-interacting $\epsilon_{\mathbf{k}}$ that were obtained from a converged DFT calculation. This scheme is usually called “one-shot” LDA+DMFT. In principle this approach is correct since the starting point for DMFT is the non-interacting dispersion. On the other hand, due to the self-consistent determination of the charge density in combination with the approximations applied to the exchange-correlation potential in DFT, the mapping to the non-interacting electron system and the resulting effective one-particle potentials will also be only approximative. It is quite natural for electronic correlations introduced by DMFT to induce a redistribution of electronic charge density and thus the one-electron potentials.

This becomes especially important for total energy calculations within LDA+DMFT. The modified charge and one-electron potentials due to correlations will also effect the electron-nuclei and exchange-correlation energy, that also contribute to the total LDA+DMFT energy. Therefore, a *full charge self-consistent* scheme is necessary, where the charge density in DFT is self-consistently updated and the one-electron potentials are recalculated within the LDA+DMFT cycle. In the description of this scheme we will follow the outline of [31].

After the convergence of the DMFT cycle for a given set of non-interacting $\epsilon(\mathbf{k})$ we can obtain the LDA+DMFT density matrix for all bands ν, ν' that were considered in the energy window \mathcal{W} for projection on the local orbitals as

$$\rho_{\nu\nu'}(\mathbf{k}) = \lim_{\tau \rightarrow 0^-} \frac{1}{\beta} \sum_{i\omega_n} G_{\nu\nu'}(\mathbf{k}, i\omega_n) e^{-i\omega_n \tau}. \quad (6.7.1)$$

In real space the full charge density matrix including also the bands outside the window \mathcal{W} is then given by

$$\rho^{\text{LDA+DMFT}}(\mathbf{r}) = \rho^{\text{OW}}(\mathbf{r}) + \sum_{\mathbf{k}, \nu, \nu'} \langle \mathbf{r} | \Psi_{\nu}(\mathbf{k}) \rangle \rho_{\nu\nu'}(\mathbf{k}) \langle \Psi_{\nu'}(\mathbf{k}) | \mathbf{r} \rangle, \quad (6.7.2)$$

where $\rho^{\text{OW}}(\mathbf{r})$ (OW=outside window) is the density matrix for the contribution of the states outside the window \mathcal{W} , which is identical to the DFT result. Depending on the basis of the DFT code, one inserts the expansion of the Bloch wave function $\langle \mathbf{r} | \Psi_{\nu}(\mathbf{k}) \rangle$ into Eq. (6.7.2) to obtain an expression

for the density matrix in the corresponding basis. For further details of the implementation in specific basis sets we refer to Refs. [31, 137, 143, 144].

The total energy has the same form as the DFT total energy with the DFT density replaced by the one obtained from LDA+DMFT plus the additional correlation energy corrected by a double counting term [145] (see Chapter 6.4)

$$E_{\text{tot}} = E_{\text{kin}} + E_c[\rho^{\text{LDA+DMFT}}] + E_{\text{H}}[\rho^{\text{LDA+DMFT}}] + E_{\text{XC}}[\rho^{\text{LDA+DMFT}}] \quad (6.7.3)$$

$$+ \langle H_U \rangle - E_{\text{DC}}. \quad (6.7.4)$$

The different contributions to the total energy are the kinetic term E_{kin} , the electron-nuclei and nuclei-nuclei term $E_{\text{H}}[\rho^{\text{LDA+DMFT}}]$, the Hartree contribution $E_{\text{H}}[\rho^{\text{LDA+DMFT}}]$, the exchange-correlation contribution $E_{\text{XC}}[\rho^{\text{LDA+DMFT}}]$ and the Hubbard term $\langle H_U \rangle$ with the double counting correction E_{DC} . The kinetic term is modified as

$$E_{\text{kin}} = E_{\text{band}} - \int v_{\text{KS}}(\mathbf{r}) \rho^{\text{LDA+DMFT}}(\mathbf{r}) \, \text{d}\mathbf{r} \quad (6.7.5)$$

$$= E_{\text{band}}^{\text{OW}} + \sum_{\mathbf{k}, \nu} \epsilon_{\nu}(\mathbf{k}) \rho_{\nu\nu}(\mathbf{k}) - \int v_{\text{KS}}(\mathbf{r}) \rho^{\text{LDA+DMFT}}(\mathbf{r}) \, \text{d}\mathbf{r}, \quad (6.7.6)$$

with the Kohn-Sham potential $v_{\text{KS}}(\mathbf{r})$. The first term on the right is the sum over the energy of the occupied Kohn-Sham states outside the window and the second term is the sum over the states inside the window \mathcal{W} with the LDA+DMFT occupations.

The Hubbard term $\langle H_U \rangle$ can be obtained by either sampling the corresponding quantity directly in the impurity solver, *e.g.* for density-density interactions the $\langle n_m n_{m'} \rangle$ correlation function

$$\langle H_U \rangle = \sum_{mm'} U_{mm'} \langle n_m n_{m'} \rangle, \quad (6.7.7)$$

where $U_{mm'}$ are the Coulomb matrix elements with m, m' including both orbital and spin indices. Otherwise the Migdal formula can be used

$$\langle H_U \rangle = \frac{1}{2\beta} \lim_{\tau \rightarrow 0^+} \sum_{i\omega_n, m} [\Sigma(i\omega_n) G(i\omega_n)]_{mm} e^{-i\omega_n \tau}, \quad (6.7.8)$$

where $\Sigma(i\omega_n), G(i\omega_n)$ are the impurity Selfenergy and Green's function.

For the double counting correction E_{DC} the same approaches as described in Chapter 6.4 are used, and the corresponding double counting energies are obtained by a formal integration over the impurity charge. For example, the FLL and AMF corrections are given by the corresponding energies in Chapter 6.4 (see Eqs. (6.4.5) and (6.4.6))

$$E_{\text{DC}}^{\text{AMF}} = U_{\text{avg}} N_{\uparrow} N_{\downarrow} + \frac{1}{2} \frac{2l}{2l+1} (U_{\text{avg}} - J_{\text{avg}}) \sum_{\sigma} N_{\sigma}^2 \quad (6.7.9)$$

$$E_{\text{DC}}^{\text{FLL}} = \frac{1}{2} U_{\text{avg}} N(N-1) - \frac{1}{2} J_{\text{avg}} \sum_{\sigma} N_{\sigma}(N_{\sigma}-1), \quad (6.7.10)$$

where N is the total impurity charge and N_{σ} is the total impurity charge for given spin σ . l is the orbital quantum number and $U_{\text{avg}}, J_{\text{avg}}$ defined in terms of Slater integrals (see Chapter 6.6).

6.8 The complete LDA+DMFT cycle

After having established all the necessary tools for LDA+DMFT, we now give an example of the complete self-consistency cycle that can be used for numerical implementations of the method. During this cycle the important quantities are the impurity Selfenergy $\Sigma(i\omega_n)$ and the local and impurity Green's functions $G^{\text{loc}}(i\omega_n), G^{\text{imp}}(i\omega_n)$. Convergence will be reached when the difference in the

Selfenergy from one iteration to the next is smaller than a given threshold or, equivalently, when the difference between the local and impurity Green's function is smaller than a desired accuracy. Details can vary depending on the system and numerical complexity. For example, most of the time we perform three self-consistent DMFT iterations before feeding back the charge into DFT for the full charge self-consistency step. This ratio can be adjusted if the DFT or DMFT takes much longer than the other, or converges at a different speed.

1. Set up the DFT calculation and perform a couple of self-consistent pure DFT iterations to obtain a reasonable charge density.
2. Obtain the Eigenenergies $\epsilon(\mathbf{k})$, the chemical potential μ and the projectors $P(\mathbf{k})$ (see Chapter 6.2) from DFT, set up the initial non-interacting lattice Green's function

$$[G^{-1}]_{\nu\nu'}(\mathbf{k}, i\omega_n) = (i\omega_n + \mu - \epsilon(\mathbf{k}))\delta_{\nu\nu'}, \quad (6.8.1)$$

and calculate the total number of electrons by (see Chapter 3.8)

$$N_e = \lim_{\tau \rightarrow 0^-} \frac{1}{\beta N_k} \sum_{i\omega_n} \sum_{\nu, \mathbf{k}} G_{\nu\nu}(\mathbf{k}, i\omega_n) e^{-i\omega_n \tau}. \quad (6.8.2)$$

Perform the downfolding of the lattice Green's function on the local orbitals

$$G_{mm'}(\mathbf{k}, i\omega_n) = [P(\mathbf{k})G(\mathbf{k}, i\omega_n)P^\dagger(\mathbf{k})]_{mm'}, \quad (6.8.3)$$

and obtain the local charge

$$N_{e,\text{loc}} = \lim_{\tau \rightarrow 0^-} \frac{1}{\beta N_k} \sum_{i\omega_n} \sum_{m, \mathbf{k}} G_{mm}(\mathbf{k}, i\omega_n) e^{-i\omega_n \tau}, \quad (6.8.4)$$

to get the initial value for the double counting correction $\Sigma_{\text{DC}}[N_{e,\text{loc}}]$ (see Chapter 6.4). If the double counting is already given from a previous iteration or does not depend on the local charge, this step can be omitted.

3. Set up the initial interacting lattice Green's function

$$[G^{-1}]_{\nu\nu'}(\mathbf{k}, i\omega_n) = (i\omega_n + \mu - \epsilon(\mathbf{k}))\delta_{\nu\nu'} - [P^\dagger(\Sigma(i\omega_n) - \Sigma_{\text{DC}})P]_{\nu\nu'}, \quad (6.8.5)$$

with the Selfenergy $\Sigma(i\omega_n)$ given from a previous iteration or a first guess. For example, it can be set equal to the Hartree term or $\Sigma(i\omega_n) = \Sigma_{\text{DC}}$. In the latter case, the local Green's functions from the previous step can be used.

4. Obtain the local Green's function by

$$G_{mm'}^{\text{loc}}(i\omega_n) = \frac{1}{N_k} \sum_{\mathbf{k}} [P(\mathbf{k})G(\mathbf{k}, i\omega_n)P^\dagger(\mathbf{k})]_{mm'}. \quad (6.8.6)$$

5. Obtain the effective Weiss field via the Dyson equation

$$\mathcal{G}^{-1}(i\omega_n) = [G^{\text{loc}}]^{-1}(i\omega_n) + \Sigma(i\omega_n), \quad (6.8.7)$$

and calculate the hybridization function (see Chapter 5.2)

$$\Delta(i\omega_n) = (i\omega_n + \tilde{\mu})\mathbb{1} - \mathcal{G}^{-1}(i\omega_n). \quad (6.8.8)$$

The value of the effective local orbital levels $\tilde{\mu}$, which is in general different from the chemical potential μ , is determined by the special form of the hybridization function for the Anderson impurity model, which real part vanishes for $\omega_n \rightarrow \infty$ (see Eq. 5.2.56). This requirement fixes $\tilde{\mu}$ as

$$\tilde{\mu} = \lim_{\omega_n \rightarrow \infty} \text{Re} [\mathcal{G}^{-1}(i\omega_n)]. \quad (6.8.9)$$

Note that per construction $\tilde{\mu}$ depends on the orbital and spin.

6. Calculate the hybridization function $\Delta(\tau)$

$$\Delta(\tau) = \frac{1}{\beta} \sum_{i\omega_n} \Delta(i\omega_n) e^{-i\omega_n \tau}, \quad (6.8.10)$$

and solve the effective impurity model with $\Delta(\tau)$, $\tilde{\mu}$ and the Coulomb matrix (see Chapter 6.6 as the input).

7. From the impurity model obtain $G^{\text{imp}}(i\omega_n)$ and $\Sigma(i\omega_n)$. If the Selfenergy is not calculated in the impurity solver, use the Dyson equation to get $\Sigma(i\omega_n)$. Update the double counting Σ_{DC} by calculating the impurity charge from $G^{\text{imp}}(i\omega_n)$. Project the Selfenergy back into Bloch space by

$$\Sigma_{\nu\nu'}(\mathbf{k}, i\omega_n) = [P(\mathbf{k})^\dagger (\Sigma(i\omega_n) - \Sigma_{\text{DC}}) P(\mathbf{k})]_{\nu\nu'}. \quad (6.8.11)$$

8. Calculate the new lattice Green's function

$$[G^{-1}]_{\nu\nu'}(\mathbf{k}, i\omega_n) = (i\omega_n + \mu - \epsilon(\mathbf{k}))\delta_{\nu\nu'} - \Sigma_{\nu\nu'}(\mathbf{k}, i\omega_n), \quad (6.8.12)$$

which will now have a total charge different from N_e due to the Selfenergy effects. Use a root-finding algorithm to adjust the chemical potential μ like regula-falsi or bisection search so that the total electron number N_e is preserved.

9. Check for convergence of the DMFT cycle, *i.e.* whether $G^{\text{imp}} = G^{\text{loc}}$ and the Selfenergy did not change compared to the previous iteration within a desired accuracy. If convergence has not been reached, go back to step 4. Otherwise, continue with step 10.

10. Calculate the density matrix

$$\rho_{\nu\nu'}(\mathbf{k}) = \lim_{\tau \rightarrow 0^-} \frac{1}{\beta} \sum_{i\omega_n} G_{\nu\nu'}(\mathbf{k}, i\omega_n) e^{-i\omega_n \tau}, \quad (6.8.13)$$

and feed the result back into the DFT code. Perform another DFT iteration and go back to step 2.

The whole cycle is then iterated until the local and impurity Green's function have become equal, the Selfenergy is converged and also the DFT cycle (charge, energy, chemical potential) is converged. The full cycle is illustrated in Fig. 6.6. After convergence is reached, observables of interest can be calculated from the interacting Green's function or Selfenergy (see Chapter 6.9).

6.9 Observables

After the convergence of the LDA+DMFT calculation we can start investigating the effect of electronic correlations on the properties of the system. Possible observables are for example the density of states, the band structure, Fermi surface, effective mass of the quasiparticles, their lifetime, etc. Many of them require an analytic continuation of either the Green's function or Selfenergy, others can be directly derived from the data on the imaginary frequency or time axis.

In this section we want to give an overview over the most important observables and how one can obtain them from the LDA+DMFT calculation. This list does not claim to be exhaustive but will include the most essential ones that we use to analyze our results for correlated systems like iron-pnictide superconductors.

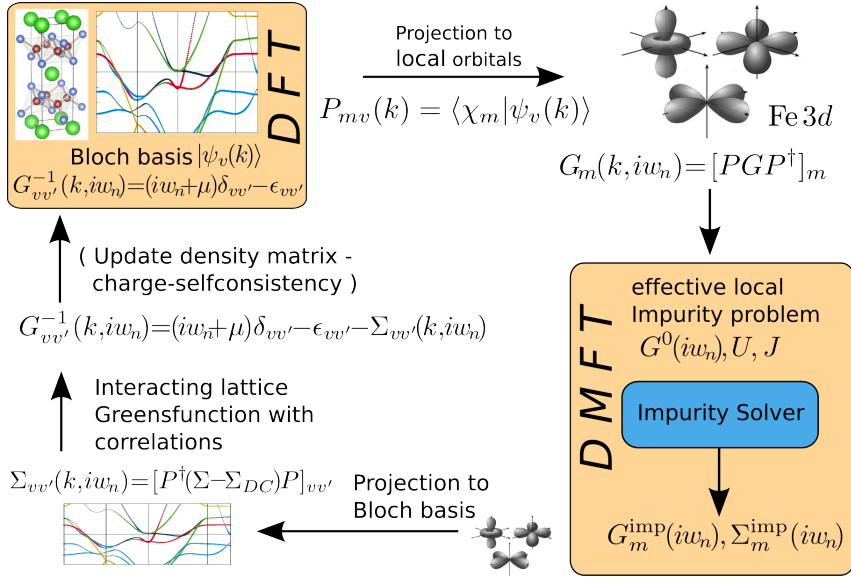


Figure 6.6: Illustration of the LDA+DMFT full charge self-consistency cycle. The full lattice Green's function in Bloch space $G_{vv'}(\mathbf{k}, iw_n)$ is projected onto local orbitals to obtain the Weiss field $\mathcal{G}(iw_n)$, defining the effective Anderson impurity model (AIM). From the solution of the AIM, the Selfenergy $\Sigma(iw_n)$ is projected back into the Bloch space to update the lattice Green's function. Iteration of this cycle is called “one-shot” LDA+DMFT, while the additional step of recalculating the DFT potentials self-consistently by feeding back the density matrix into DFT is called “full charge self-consistency”.

6.9.1 Quasiparticle weight, lifetime and mass enhancement

A very important aspect of an interacting electronic system is the concept of quasiparticles. In the presence of interactions, the electrons can no longer follow their non-interacting dispersion but become dressed by the Selfenergy and pick up a larger effective mass which tends to make them “heavier”, *i.e.* more localized. The new possible excitations of the system are called quasiparticles, which energies will thus be different from the non-interacting system. In general they will also have a finite lifetime, since an excitation of the system, *i.e.* the creation of a quasiparticle, will decay over time due to scattering effects. These properties, amplitude and lifetime, of the excitations are exactly the properties that are “measured” by the interacting Green's function (see Chapter 3).

We will now shortly review the concept of quasiparticles in Fermi liquid theory in order to derive the equations for their effective mass and lifetime. The interacting Green's function on the real axis that encodes the possible excitations of the system is given by

$$G^R(\mathbf{k}, \omega) = \frac{1}{\omega + i\eta + \mu - \epsilon(\mathbf{k}) - \Sigma^R(\mathbf{k}, \omega)}, \quad (6.9.1)$$

with the corresponding spectral function (neglecting $i\eta$, since $\text{Im} \Sigma^R(\mathbf{k}, \omega)$ will usually be small but finite at any frequency)

$$A(\mathbf{k}, \omega) = -\frac{1}{\pi} \text{Im} [G^R(\mathbf{k}, \omega)] \quad (6.9.2)$$

$$= \frac{1}{\pi} \frac{-\text{Im} \Sigma^R(\mathbf{k}, \omega)}{\left(\omega + \mu - \epsilon(\mathbf{k}) - \text{Re} \Sigma^R(\mathbf{k}, \omega)\right)^2 + \left(\text{Im} \Sigma^R(\mathbf{k}, \omega)\right)^2}. \quad (6.9.3)$$

As we already know from Chapter 3, the imaginary part of the Selfenergy introduces a broadening of the original Delta function-like excitation poles, while the real part is responsible for a shift of

the excitation energies. If the imaginary part is small and varies smoothly with frequency, the new excitation energies or, correspondingly, maxima in the spectral function are defined by

$$\omega + \mu - \epsilon(\mathbf{k}) - \text{Re} \Sigma^R(\mathbf{k}, \omega) = 0. \quad (6.9.4)$$

We define the *quasiparticle energy* $E_{\mathbf{k}} - \mu$ as the energy which fulfils this relation so that

$$E_{\mathbf{k}} - \mu = \epsilon(\mathbf{k}) - \mu + \text{Re} \Sigma^R(\mathbf{k}, E_{\mathbf{k}} - \mu). \quad (6.9.5)$$

Expanding $\omega + \mu - \epsilon(\mathbf{k}) - \text{Re} \Sigma^R(\mathbf{k}, \omega)$ as a function of ω around the maximum at $E_{\mathbf{k}} - \mu$ we obtain

$$\omega + \mu - \epsilon(\mathbf{k}) - \text{Re} \Sigma^R(\mathbf{k}, \omega) \approx \left(1 - \left. \frac{\partial \text{Re} \Sigma^R(\mathbf{k}, \omega)}{\partial \omega} \right|_{\omega=E_{\mathbf{k}}-\mu} \right) (\omega - E_{\mathbf{k}} + \mu) + \dots \quad (6.9.6)$$

$$= Z_{\mathbf{k}}^{-1} (\omega - E_{\mathbf{k}} + \mu) + \dots \quad (6.9.7)$$

where we have introduced the renormalization factor or also called *quasiparticle weight* as

$$Z_{\mathbf{k}} = \left[1 - \left. \frac{\partial \text{Re} \Sigma^R(\mathbf{k}, \omega)}{\partial \omega} \right|_{\omega=E_{\mathbf{k}}-\mu} \right]^{-1}. \quad (6.9.8)$$

Using the definition of $Z_{\mathbf{k}}$ we can now rewrite the spectral function close to the maximum $E_{\mathbf{k}} - \mu$ as

$$A(\mathbf{k}, \omega) \approx \frac{1}{\pi} \frac{-\text{Im} \Sigma^R(\mathbf{k}, \omega)}{Z_{\mathbf{k}}^{-2} (\omega - E_{\mathbf{k}} + \mu)^2 + (\text{Im} \Sigma^R(\mathbf{k}, \omega))^2} + \text{inc.} \quad (6.9.9)$$

$$= Z_{\mathbf{k}} \frac{1}{\pi} \frac{\Gamma_{\mathbf{k}}(\omega)}{(\omega - E_{\mathbf{k}} + \mu)^2 + (\Gamma_{\mathbf{k}}(\omega))^2} + \text{inc.}, \quad (6.9.10)$$

with the *quasiparticle scattering rate*, or inverse *quasiparticle lifetime*

$$\Gamma_{\mathbf{k}}(\omega) = -Z_{\mathbf{k}} \text{Im} \Sigma^R(\mathbf{k}, \omega). \quad (6.9.11)$$

The first term in Eq. (6.9.10) has a functional form which is identical to a Lorentzian centered at $E_{\mathbf{k}} - \mu$ and a width of $\Gamma_{\mathbf{k}}(\omega)$, multiplied by the quasiparticle weight $Z_{\mathbf{k}}$. It is called the *quasiparticle peak*, since it corresponds to the peak in the excitation spectrum of the new quasiparticles with energy $E_{\mathbf{k}} - \mu$ and lifetime $\Gamma_{\mathbf{k}}^{-1}(\omega)$. Because the Lorentzian is normalized to one, the total weight of the peak is indeed equal to the quasiparticle weight $Z_{\mathbf{k}}$, which is, therefore, necessarily bound to be positive and ≤ 1 .

This Lorentzian shape of the quasiparticle peak is only valid close the excitation energy. All other weight which is not contained in the peak is called *incoherent* spectral weight because it does not belong to the coherent excitation of a quasiparticle with energy $E_{\mathbf{k}} - \mu$. For weak correlations, the Selfenergy will be small and renormalize the spectrum only by a small value, thus $Z_{\mathbf{k}} \approx 1$ and all spectral weight is contained in the quasiparticle peak, which will be very similar to the Delta peak-like spectrum in the non-interacting system. For strong correlations, $Z_{\mathbf{k}} \lesssim 1$ and spectral weight is transferred into the incoherent part away from the quasiparticle peak. If $Z_{\mathbf{k}}$ becomes zero, the quasiparticle peak vanishes and all weight is contained in the incoherent part away from the original quasiparticle energy $E_{\mathbf{k}} - \mu$. This corresponds to the metal-insulator transition in the Hubbard model.

Since we are often interested in orbitally resolved features at the Fermi level at $\omega = 0$, we can obtain the quasiparticle weight and scattering rate directly from the impurity Selfenergy on the real axis

$$Z_m = \left[1 - \left. \frac{\partial \text{Re} \Sigma_m^R(\omega)}{\partial \omega} \right|_{\omega=0} \right]^{-1} \quad (6.9.12)$$

$$\Gamma_m = -Z_m \text{Im} \Sigma_m^R(\omega = 0). \quad (6.9.13)$$

The inverse of the scattering is called the *quasiparticle mass enhancement* $\frac{m^*}{m_{\text{nonint}}}$ and diverges if the electrons in the corresponding orbital localize

$$\frac{m_m^*}{m_{\text{nonint},m}} = 1 - \left. \frac{\partial \text{Re} \Sigma_m^R(\omega)}{\partial \omega} \right|_{\omega=0}. \quad (6.9.14)$$

We can now make use of the fact that at $\omega = 0$, the retarded Green's function and Selfenergy agree with the corresponding functions on the Matsubara axis for $\omega_n \rightarrow 0^+$. This allows us to directly calculate the quasiparticle scattering rate from the Selfenergy on the imaginary axis without analytic continuation. For the quasiparticle weight and mass enhancement we make use of the Cauchy-Riemann differential equations, which provide a relationship between the differentials along the real and imaginary axis. For a holomorphic function of the form $f(z) = u(z) + iv(z)$, where u, v are real-valued functions, and $z = x + iy$, the Cauchy-Riemann differential equations state that

$$\frac{\partial u}{\partial x} = \frac{\partial v}{\partial y} \quad \text{and} \quad \frac{\partial u}{\partial y} = -\frac{\partial v}{\partial x}, \quad (6.9.15)$$

which directly leads to the following results

$$Z_m = \left[1 - \left. \frac{\partial \text{Im} \Sigma_m(i\omega_n)}{\partial i\omega_n} \right|_{\omega_n \rightarrow 0^+} \right]^{-1} \quad (6.9.16)$$

$$\Gamma_m = - \lim_{\omega_n \rightarrow 0^+} Z_m \text{Im} \Sigma_m(i\omega_n) \quad (6.9.17)$$

$$\frac{m_m^*}{m_{\text{nonint},m}} = Z_m^{-1}. \quad (6.9.18)$$

This has the important advantage that no analytic continuation to the real axis is necessary, avoiding possible errors introduced by the continuation procedure. Since we only know the Selfenergy on the discrete Matsubara points $i\omega_n$, an extrapolation to $\omega_n \rightarrow 0^+$ has to be performed, for example by fitting a polynomial to the first few Matsubara frequencies. This procedure will only be accurate at small temperatures because the Matsubara grid will move further away from the origin due to $i\omega_n(T)$ being a linear function of the temperature T , making the extrapolation prone to errors.

6.9.2 Band structure and Fermi surface

Upon the inclusion of correlation the finite imaginary part of the Selfenergy replaces the Delta peak-like excitation spectrum of the non-interacting system with the smooth spectral function $A(\mathbf{k}, \omega)$, which in general does not allow for an identification of a single excitation energy. Only a quasiparticle energy in the sense of the energy where the spectral function approaches a maximum can be defined for the case where the imaginary part of the Selfenergy is small.

Therefore, the usual ‘‘spaghetti plot’’ of the band structure is replaced by a plot of the spectral function

$$A(\mathbf{k}, \omega) = -\frac{1}{\pi} \text{Im} [G^R(\mathbf{k}, \omega)], \quad (6.9.19)$$

which can be directly compared to experiments like angular-resolved photoemission spectroscopy (ARPES). This makes an analytic continuation of the Selfenergy or Green's function from the Matsubara to the real axis necessary.

For the Fermi surface, which is given by $A(\mathbf{k}, \omega = 0)$, we can avoid an explicit analytic continuation by obtaining the value of $A(\mathbf{k}, \omega = 0)$ by extrapolation of the Green's function on the Matsubara axis, similar to the procedure for the quasiparticle weight described in Chapter 6.9.1. For simplicity, the extrapolation can be applied to the Selfenergy, which only needs to be performed for all orbitals instead of all bands and \mathbf{k} -points, and then constructing the lattice Green's function and spectral function.

6.9.3 Local spectral function $A(\omega)$

The local spectral function $A(\omega)$ is usually the most difficult observable to construct, since it involves an accurate analytic continuation of either the Selfenergy or Green's function onto a large frequency interval of several electron volts on the real axis. In our experience performing the analytic continuation on the Selfenergy instead of the local Green's function gives more accurate results, since possible errors introduced by the continuation are only contained in the correlated part of the spectrum while the uncorrelated terms $\epsilon(\mathbf{k})$ are exactly known.

After continuation of the Selfenergy to the real axis, the local $\Sigma^R(\omega)$ is upfolded into the Bloch space (see Chapter 6.2) to construct the lattice Green's function $G^R(\mathbf{k}, \omega)$, from which the momentum-integrated spectrum is obtained by

$$A(\omega) = -\frac{1}{\pi N_k} \sum_{\mathbf{k}\nu} \text{Im} G_{\nu\nu}^R(\mathbf{k}, \omega). \quad (6.9.20)$$

Orbital resolved quantities can be obtained by a further downfolding to the local orbital basis in the same way

$$A_m(\omega) = -\frac{1}{\pi N_k} \sum_{\mathbf{k}} \text{Im} [P(\mathbf{k})G^R(\mathbf{k}, \omega)P^\dagger(\mathbf{k})]_{mm}. \quad (6.9.21)$$

Chapter 7

Effects of electronic correlations in KFe_2As_2

S. Backes, D. Guterding, H. O. Jeschke, R. Valentí
New J. Phys. 16, 083025 (2014)

As we have already discussed in the introduction in Chapter 1.3, many members of the ironpnictide family show effects of strong electronic correlations that cannot be described reasonably well within DFT. We will now use the LDA+DMFT method we introduced in Chapter 6 to study the hole-doped 122 compound KFe_2As_2 and compare our obtained results for the electronic structure to DFT calculations as well as experimental data.

Our calculations indicate that KFe_2As_2 is a moderately correlated metal with a mass renormalization factor of the Fe $3d$ orbitals between 1.6 and 2.7. We also find that the obtained Fermi surface is in good agreement with angular-resolved photoemission spectroscopy (ARPES) measurements, since we observe specific changes with respect of the Fermi surface pockets with respect to DFT. By this, we obtain de Haas-van Alphen (dHvA) frequencies that are in much better agreement with experiments than the DFT results. This shows that correlation effects are important for a proper understanding of the electronic structure of KFe_2As_2 .

7.1 Introduction

The system KFe_2As_2 is the hole-doped end member of the $\text{Ba}_{1-x}\text{K}_x\text{Fe}_2\text{As}_2$ family of iron-based superconductors [146]. It shows a superconducting transition with $T_c = 3.4$ K under ambient pressure [147]. In this material the origin of the superconducting phase and the pairing symmetry is still unclear [148–150], both on the experimental and theoretical sides. On the one hand laser-based angle-resolved photoemission (laser ARPES) measurements found the superconducting order parameter to be of s -wave character [151], while in contrast to that theoretical studies based on the functional renormalization group [152] predicted a d -wave symmetry, which in turn are backed by measurements of the thermal conductivity [153]. Other theoretical studies [154, 155] based on spin pairing theory within the random phase approximation found that s - and d -wave pairing channels are strong competitors in this system and both might be possible in KFe_2As_2 . Also transport measurements under pressure [156] suggested the presence of a possible phase transition from d -wave to s -wave around 1.75 GPa.

Quantum oscillation experiments [23] also predicted high effective charge carrier masses of up to $19 m_e$ with an average mass enhancement factor m^*/m_{band} of about 9. Estimates from ARPES [20] and cyclotron resonance experiments [157] on the other hand reported mass enhancements of about 3 for certain regions of the Fermi surface.

On the theoretical side, DFT calculations for KFe_2As_2 are known to show poor agreement with ARPES measurements [19–21] and also to dHvA measurements [23, 158]. This makes the system a

very promising candidate for a study within LDA+DMFT. Additionally, there was only one existing publication in the literature so far [28] that considered an LDA+DMFT study for KFe_2As_2 . From the obtained mass enhancement and Fermi surface at $k_z=0$ a promising improvement in the agreement with ARPES data was evident, which motivated a deeper analysis of this system.

Therefore, we will perform a comprehensive LDA+DMFT investigation focused on features of the KFe_2As_2 compound that have not been dealt with in past studies [28]. We will also study the effects of the different FLL and AMF double counting schemes that were discussed in Chapter 6.4 on the electronic Fermi surface. This will allow us to perform a critical benchmark of our LDA+DMFT calculations to see in which way they can help to improve the agreement with experimental ARPES and dHvA measurements as well as how they can contribute to the understanding of the electronic structure of this system.

7.2 Computational details

For our calculations we will use the experimentally determined tetragonal $I4/mmm$ structures of KFe_2As_2 by Tafti *et al.* [159], which are given for pressure values starting at 0.23 GPa. For the zero pressure structure we perform a linear extrapolation of the available data points. A comparison of this structure to the existing crystal structure by Rosza and Schuster [160] used in previous theoretical investigations shows that while lattice parameters a , b , and c are consistent, the As z position differs significantly between both structures. The As z position was consistently determined over a large pressure range in the above mentioned study by Tafti *et al.* [159] and the As z position determined by Rosza and Schuster does not follow the trend shown by those data. Here we use the new structure with the following parameters: $a = b = 3.8488 \text{ \AA}$, $c = 13.883 \text{ \AA}$, fractional As $z = 0.140663$. Additionally, we will also compare to the results obtained for the structure by Rosza and Schuster [160].

For the DFT calculation we employed the full-potential linear augmented plane-wave (FLAPW) framework as implemented in WIEN2k [161], using the local density approximation (LDA) as well as the generalized gradient approximation (GGA) by Perdew, Burke and Ernzerhof [162] to the exchange-correlation functional. We used a grid of 726 k points in the irreducible Brillouin zone in our calculations. Additionally, we also included the effects of spin-orbit coupling (SO) in the DFT calculation and compared to the case when its contribution is neglected. The LDA+DMFT calculations were performed without the inclusion of SO.

The LDA+DMFT calculations were performed fully charge self-consistent by making use of the implementations in the WIEN2K code for updating the DFT electronic density. The projection from Bloch eigenstates to the correlated Fe $3d$ orbitals was carried out with our adoption [163] of the projection method as described by Aichhorn *et al.* [36]. The energy window for the projection onto the localized basis was chosen comparatively large, ranging from -5 eV to 13 eV to capture the higher energy contribution of the Fe $3d$ orbitals to the density of states arising from the hybridization with the As $4p$ orbitals. Compared to other materials no clear separation with the correlated Fe $3d$ and uncorrelated As $4p$ states can be obtained. As a result we expect the different double counting schemes to have a more noticeable effect on the results as discussed in Chapter 6.4.

The effective Anderson impurity model was solved using the continuous-time hybridization expansion quantum Monte Carlo solver as implemented in the ALPS [164] code. We made use of the Legendre polynomial representation [165] of the impurity Green's function and improved estimators for the Selfenergy [166], which allow for an improved representation on the Matsubara axis in the presence of numerical noise from the Monte Carlo sampling. About 6×10^6 Monte-Carlo sweeps were performed at an inverse temperature $\beta = 40 \text{ eV}^{-1}$, corresponding to room temperature. The effective local interaction parameters U and J_H were chosen as $U = 4 \text{ eV}$ and $J_H = 0.8 \text{ eV}$ in terms of Slater integrals F^0 , F^2 and F^4 , where for the Fe $3d$ -electrons we used $U = F^0$, $J_H = (F^2 + F^4)/14$, and $F^2/F^4 = 0.625$ [118], as discussed in Chapter 6.6.

For the double-counting correction the fully-localized limit [82, 167] (FLL) and around mean-field (AMF) [63] scheme were used. All orbital characters presented here are defined in a coordinate system which is rotated by 45° around the crystallographic z axis, *i.e.* x and y are pointing along Fe-

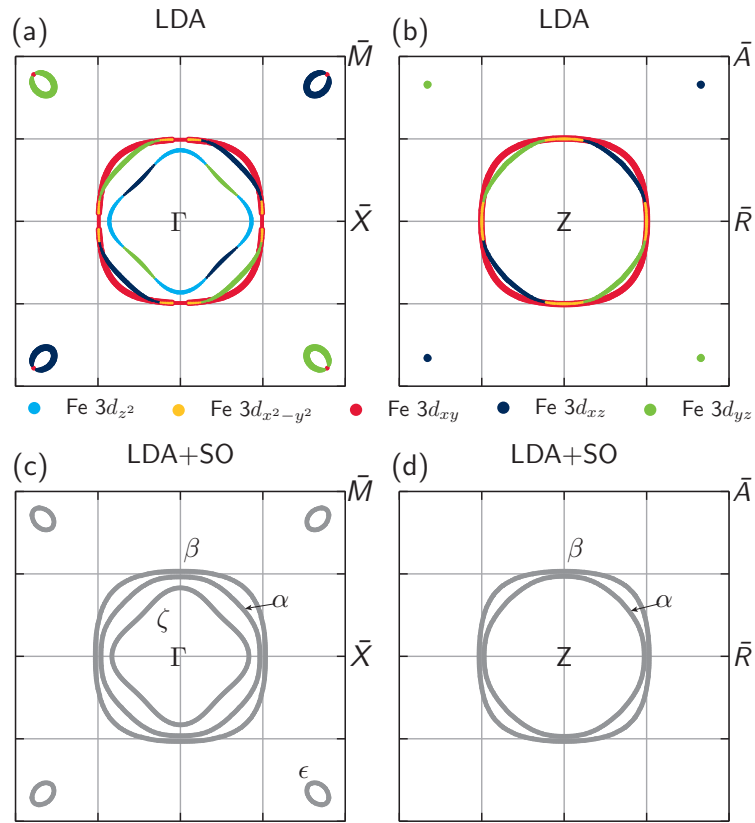


Figure 7.1: Overview of Fermi surface cuts at $k_z = 0$ and $k_z = \pi$ in KFe_2As_2 obtained from DFT using the LDA exchange correlation functional with and without spin-orbit coupling (SO). Inclusion of spin-orbit coupling only leads to small quantitative changes, in particular a lifting of all apparent degeneracies of Fermi surface sheets. Fermi surfaces are shown in the two-Fe Brillouin zone representation.

Fe nearest neighbour bonds. For determining the LDA+DMFT excitation energies that we used to define the Fermi surface, we tracked the maximum of the real-frequency spectral function throughout the Brillouin zone. Analytic continuation of imaginary frequency data to the real frequency axis was performed by using the Padé approximation for the impurity Selfenergy and we checked the results against the stochastic analytic continuation method [93].

The dHvA frequencies were obtained from the electronic band structure using our own implementation of the dHvA frequency extraction algorithm by Rourke and Julian [168].

7.3 Results

7.3.1 Electronic structure

We first investigated the band structure of KFe_2As_2 obtained by the DFT calculation within LDA and LDA+SO. Results obtained with the GGA functional were nearly identical to the LDA result and are therefore not shown. At the Γ point (see Fig. 7.1 (a) and Fig. 7.2 (a)) we see three bands crossing the Fermi level, forming hole pockets of Fe $3d_{xy}$, $3d_{xz}$ and $3d_{yz}$ character. The two outer hole pockets form cylinders along k_z between the Γ and Z points, while the cylinder of the third inner hole pocket closes shortly before the Z point. This leads to two hole pockets at the Z point, being mostly of Fe $3d_{xy}$, $3d_{xz/yz}$ character. Around the \bar{M} point, we observe very small hole pockets with Fe $3d_{xy}$,

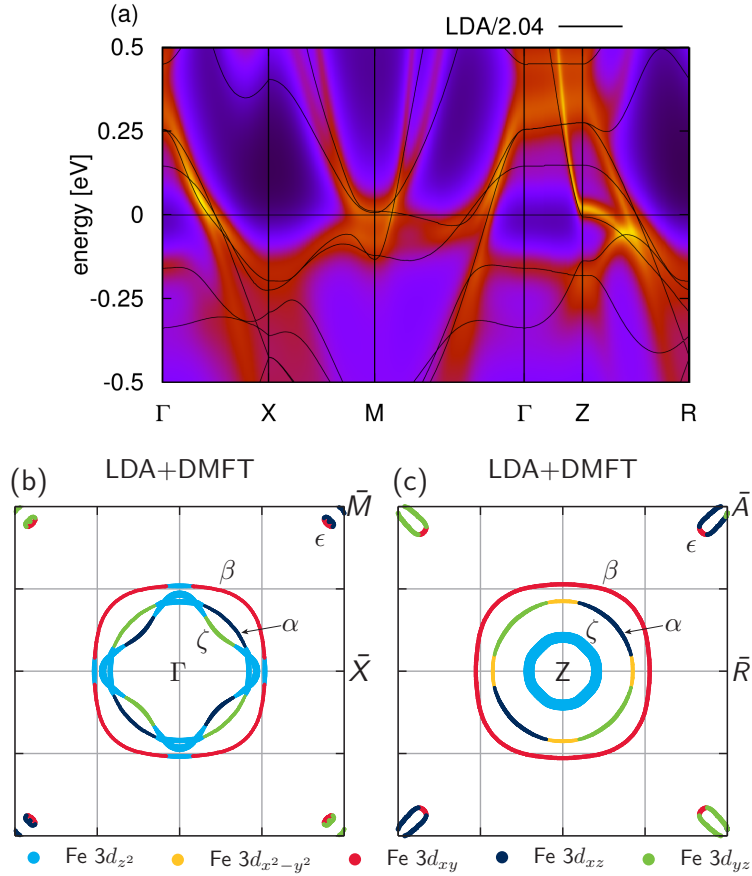


Figure 7.2: The k -resolved spectral function and orbital-resolved Fermi surface of KFe_2As_2 within LDA+DMFT. The LDA bands (black lines) are rescaled by the average mass enhancement of 2.04 for comparison. Dominant orbital characters are indicated by the colour scale. Fermi surfaces are shown in the two-Fe Brillouin zone representation.

$3d_{xz/yz}$ character, where the bands with mostly Fe $3d_{xz/yz}$ character are very shallow right above E_F , which leads to a high sensitivity to input parameters and total electron charge in the calculation.

By including the spin-orbit interaction we observe an overall repulsion between touching or degenerate bands, which leads to clear separation of the hole pockets along the high symmetry directions (see Fig. 7.1 (c), (d)).

Comparing these DFT results to ARPES measurements [19–21] we find that the agreement in size and shape of the hole pockets along the high symmetry directions is quite poor. This disagreement has already been noted in the publications cited above. The inner two pockets (α , ζ) are too large while the outer one (β) is too small. The topology of the Fermi surface also differs from experimental observations. ARPES clearly shows a separated outer hole cylinder at Γ , while the two inner ones overlap considerably [19–21]. The closure of the inner hole cylinder is not seen in ARPES [19–21] or dHvA [23, 158] measurements, leading to a third inner hole pocket at Z in experiments. Also, the hole pockets (ϵ) close to \bar{M} are too small in DFT.

When including correlations on the Fe $3d$ orbitals via LDA+DMFT, the electronic structure of KFe_2As_2 changes significantly. The different approximations to the exchange-correlation potential of LDA and GGA do not result in noticeable changes in the electronic structure. In the band structure shown in Fig. 7.2 we observe a strong renormalization of the bands around the Fermi level, with mass enhancements for the Fe $3d$ orbitals ranging from 1.56 to 2.72, as shown in table 7.1.

These results are in agreement with a previous LDA+DMFT study [28], but still very different from experimentally reported mass enhancements, that can reach values of up to 24 for the

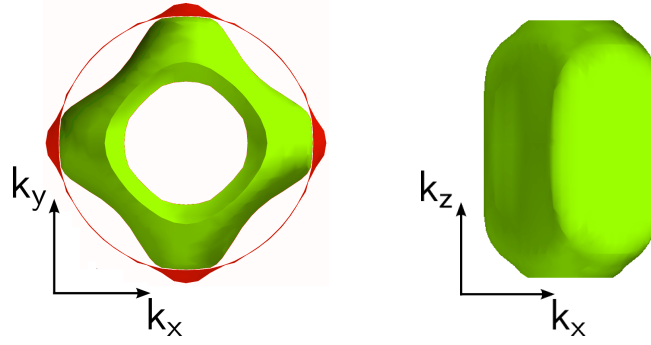


Figure 7.3: Three dimensional view of the Fermi surface obtained from LDA+DMFT in the two-Fe Brillouin zone representation. Figure (a) shows the intersection nodes between the inner (green) and middle (red) Fermi surface sheet. The configuration used in calculating de Haas-van Alphen frequencies is indicated by the colours. Figure (b) shows the dispersion of the inner Fermi surface sheet along the k_z -axis.

small pockets (ϵ) and up to 6.9 for the large pockets (α , β , ζ) in the centre of the reciprocal unit cell [23, 158]. We attribute the discrepancy between our results and the experimentally observed mass enhancements partly to the restriction of the interactions in our method to be only of density-density type, since it is known that including the full four-index rotationally invariant U-tensor (compare Chapter 6.6) can increase obtained mass enhancements significantly [29]. Also the inclusion of other effects missing in our current LDA+DMFT method like non-local correlations and electron-phonon interactions should be able to further reduce the differences between theory and experiment. It was already pointed out in [158] that flattening of the bands near the Fermi level caused by coupling to low-energy bosonic excitations [169] that originate from strong spin fluctuations present in KFe_2As_2 [170–172], also contribute to the mass enhancement, but are not accounted for in the DMFT method. On the other hand overall the bandwidth renormalization as seen in ARPES, which is independent of such low-energy bosonic excitations, is well reproduced in DMFT. Therefore, our results support the interpretation given in [158].

Orbital	d_{xy}	d_{z^2}	$d_{x^2-y^2}$	$d_{xz/yz}$
$\frac{m^*}{m_{LDA}}$	2.72	1.89	1.56	2.02

Table 7.1: The orbital-resolved mass enhancements for the Fe 3d orbitals in KFe_2As_2 .

We also observe a reordering of bands along the high symmetry directions with significant changes in the size of the hole cylinders. Both the inner sheets (α , ζ) at the Γ point at $k_z = 0$ shrink in size, while the outer one (β) gets enlarged, as seen in the LDA+DMFT Fermi surface in Fig. 7.2. This is in better agreement with experimental observations. Moreover, we observe a small overlap of the centre (ζ) and middle hole pocket (α) with small intersection nodes around Γ , which are also observed in ARPES but were absent in the DFT calculation and previous LDA+DMFT studies [28]. Most importantly, at $k_z = \pi$ around the Z point the band of mostly $3d_{z^2}$ character that was located just below the Fermi level is pushed above E_F due to correlations, opening the hole cylinder that was previously closed in the DFT calculation. By also investigating the structure from Rosza and Schuster [160], we found a strong dependence of the shape of this hole pocket on the As- z position. Within DFT alone, an opening of a new hole pocket can be observed by increasing the As height above the Fe plane. Since the band in question originates from the hybridization of Fe 3d with As 4p states, it is extremely sensitive to the arsenic position. The LDA+DMFT middle hole pocket around Z reduces in size compared to LDA, forming an almost k_z -dispersionless hole cylinder between the Γ and Z points. In Fig. 7.3 we show three-dimensional plots of the hole cylinders throughout the Brillouin zone.

Recent ARPES experiments [19–21] and dHvA measurements [23, 158] also observe three hole pockets around the Z point, agreeing well with our calculations. The strong Fe $3d_{z^2}$ character around Z reported from ARPES [21] is also reproduced by our calculation. A detailed comparison shows, however, still some differences between theory and ARPES experiment: the size of the middle hole pocket in the k_x - k_y -plane at both the Γ and Z points is smaller in ARPES, while the inner pocket at Z seems to be larger compared to our results.

The small hole pockets at the \bar{M} point emerge from the crossing of two bands at an energy of about 5 meV above E_F , with very weak dispersion of one of the bands. Therefore, these pockets are extremely sensitive to the Fermi level which makes them strongly dependent on the details of the calculation like the double-counting scheme or the chosen DFT functional. On the experimental side this indicates a strong dependence on the actual composition and possible impurities in the sample; this is a possible explanation for the different sizes of these pockets in ARPES experiments [19–21]. In Chapter 7.3.3 we show that for the structure by Rosza and Schuster [160] we indeed observe larger hole pockets at the \bar{M} point compared to Tafti *et al.* [159]. In our calculations, we carefully checked the results for different double-counting procedures and analytic continuation methods and found overall qualitatively good agreement. Finally, we note that in order to obtain a better agreement with experiment, the middle hole cylinder would have to be shifted inside of the inner cylinder in our calculations. This cannot be achieved by inclusion of local correlations only since in this system the necessary shifts of the band energies cannot be obtained with a k -independent Selfenergy only. Instead, a k -dependent shift would be required to improve the agreement of the position of the middle hole cylinder at Γ with experiments while retaining the otherwise satisfactory agreement at other k -points.

The Fermi surface obtained from LDA+DMFT offers a natural explanation for the magnetic breakdown junctions between orbits α and ζ observed by Terashima *et al.* [23, 158]. Taking spin-orbit coupling into account will likely lift the exact degeneracies at the intersection nodes as seen in our LDA+SO calculation. A shift of the maxima of the spectral function however does not forbid transition processes between Fermi surface sheets if the spectral weight between them remains finite. We conclude that the degeneracy of the lines found in ARPES might be due to both experimental resolution and overestimation of the distance between sheets in our calculation. Furthermore we would like to point out that our Fermi surface strongly resembles the octet line-node structure observed in laser ARPES measurements of the superconducting order parameter [151].

7.3.2 De Haas-van Alphen frequencies

Comparing our findings to measurements of quantum oscillations [158] we can confirm that DFT is not able to describe the Fermi surface of KFe_2As_2 correctly. An overview of our results is presented in Fig. 7.4. LDA and LDA+SO calculations for the structure by Rosza and Schuster are given in Chapter 7.3.3. They reproduce the DFT results by Terashima *et al.* [23, 158].

The two inner hole pockets (α , ζ) around the Γ point are too large compared to experimental frequencies, while the outermost hole pocket (β) is too small (Fig. 7.4 left panel). The size of the hole pocket close to \bar{M} (ϵ) is already well described in DFT. Adding spin-orbit coupling already shows the correct tendency to increase the size of the outer hole pocket and decrease the size of the two inner hole pockets. Deviations from experimentally observed frequencies are nevertheless large (Fig. 7.4 middle panel). The good agreement with experiment for the largest and smallest frequencies comes with persisting disagreement for the two intermediate frequencies.

In the LDA+DMFT calculation (Fig. 7.4 right panel) the two innermost orbits (α, ζ) intersect around the Γ point (Fig. 7.2). For the analysis of the dHvA frequencies we take into account the outermost and innermost possible configuration of these two orbits as shown in Fig. 7.2. The same configuration was attributed to fundamental frequencies observed in dHvA experiment [23, 158]. The outer hole pocket (β) is considerably enlarged. As the corresponding electronic band is flattened, it becomes susceptible to tiny energy shifts. Both inner hole pockets (α , ζ) are shifted to lower frequencies and thus decreased in size. The small orbit (ϵ) close to \bar{M} is enlarged around the Z point, but decreases in size around Γ as shown in Fig. 7.2. Therefore we only find the maximum frequency for this sheet.

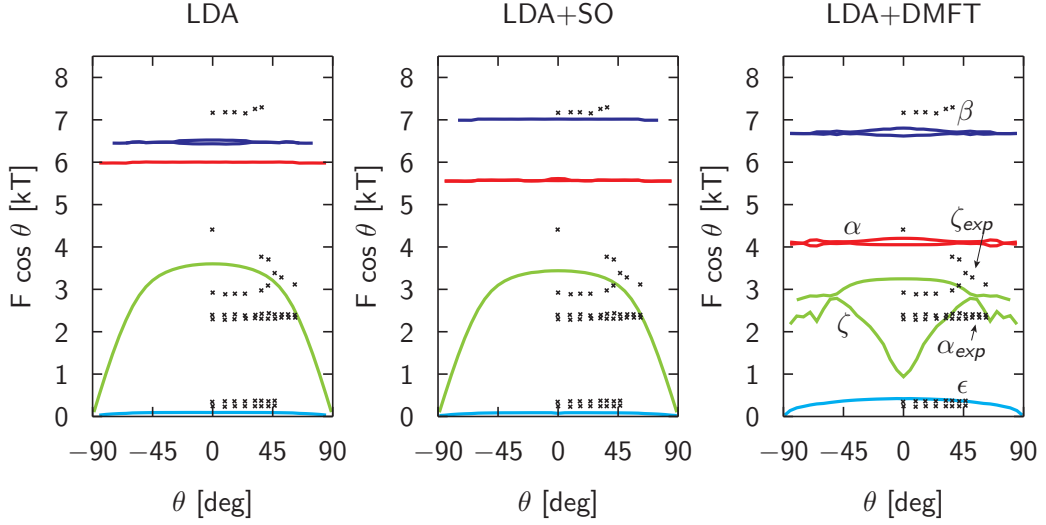


Figure 7.4: Overview of de Haas-van Alphen frequencies in KFe_2As_2 calculated from density functional theory and LDA+DMFT. Lines represent our calculations, while crosses represent experimental frequencies taken from [158]. Colour coding is the same as in Fig. 7.2. The ζ -orbit (innermost) is shown in green, while the frequencies originating from the middle sheet (α) are shown in red. The outermost orbits (β , ϵ) are drawn in blue.

We would like to note that quantum oscillation experiments [173] and ARPES [20, 21] reported the existence of a fourth very small pocket centred at the Z point which was not seen in our calculations for the most recent structure. This fourth pocket is however present in the DFT calculation when using the structure from Rosza and Schuster [160], but we found it to vanish when adding correlations in LDA+DMFT, depending on the double-counting. This will be discussed in more detail in the next Chapter 7.3.3.

The opening of the innermost hole pocket ζ is clearly observed in the LDA+DMFT calculated dHvA frequencies by the appearance of a lower extremal frequency. As pointed out before in the ARPES section, the middle hole cylinder would have to be decreased in size considerably to match the experimental frequencies. This would in turn increase the enclosed volume of the sheet labelled ζ and thus shift it towards experimentally observed values. A comparison of experimental and LDA+DMFT frequencies for $B \parallel (001)$ is given in Table 7.2.

	ϵ_l	ϵ_h	α_l	α_h	ζ_l	ζ_h	β_l	β_h
exp.	0.24	0.36	2.30	2.39	2.89	4.40	7.16	-
LDA+DMFT	-	0.42	4.05	4.20	0.94	3.25	6.62	6.81

Table 7.2: De Haas-van Alphen frequencies in kT (kiloTesla) for $B \parallel (001)$ obtained from DMFT calculations compared to experimental values [158].

Furthermore we calculated effective masses averaged over extremal orbits on the Fermi surface from the LDA+DMFT excitation energies. These masses correspond to the effective masses observed in dHvA experiments (Table 7.3). Note that values given in this table are *absolute* masses in contrast to mass *enhancements* given in Table 7.1.

Qualitatively our calculation captures the trends that are observed in sheet-resolved effective masses, however, as discussed above, the differences might be attributed to the restriction to density-density type interactions and effects originating from other than electron-electron interactions missing in DMFT, which increase effective masses seen in dHvA experiments such as electron-phonon coupling.

For comparison with dHvA experiment, we have obtained the Fermi surface within LDA+DMFT

	ϵ_Γ	ϵ_Z	α_Γ	α_Z	ζ_Γ	ζ_Z	β_Γ	β_Z
exp.	6.0	7.2	6.0	6.5	8.5	18.0	19.0	19.0
LDA+DMFT	-	5.9	3.4	4.6	2.4	5.3	8.3	8.3

Table 7.3: Electron orbit averaged effective masses in m_e for $B \parallel (001)$ obtained from DMFT calculations compared to experimental values [158].

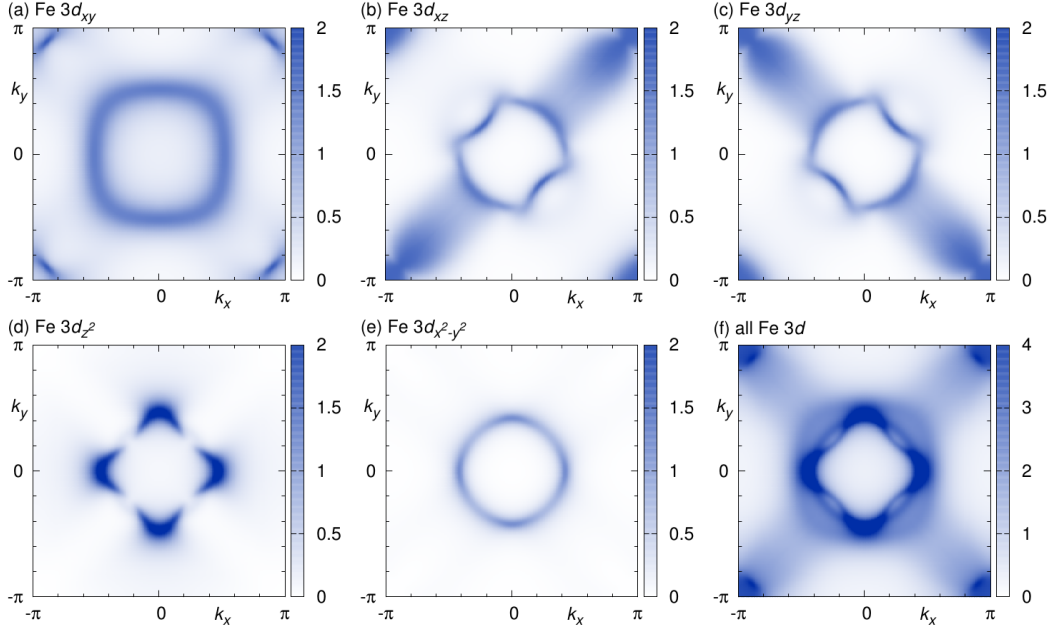


Figure 7.5: The orbital-resolved spectral function of KFe_2As_2 at $k_z = 0$ and $E = 0$ for the structure by Tafti *et al.* [159]. The colour intensity indicates the value of the spectral function. Subfigure (f) shows the summed Fe 3d orbital contributions to the spectral function.

by tracing the maxima of the spectral function throughout the Brillouin zone that is shown in Fig 7.2. This approach is insensitive to the broadening of the excitation energies. Experimentally observed dHvA frequencies correspond to orbits with extremal areas and maximal spectral weight, which we take into account with our method. Fermi surface plots generated from the maxima of the spectral function can however mask the true extent of the Fermi surface pockets as seen in ARPES experiments. To allow for a better comparison with ARPES experiments and to visualize the broadening of the excitation energies, we show the orbital resolved spectral function at the chemical potential in Fig. 7.5. Compared to the Fermi surface in Fig. 7.2 a strong broadening of the bands can be observed, especially in the Fe $3d_{xy}$ and $3d_{xz/yz}$ orbitals. This is in correspondence with the fact that these orbitals also have the strongest renormalization in LDA+DMFT. The small pockets at the \bar{M} point can be seen to represent a very extended structure with no well defined maxima. Note that in the Fermi surface plot obtained using spectral function maxima (Fig. 7.2 (b) and (c)) the true extent of these pockets is not properly accounted for. From this we conclude that the spectral function in LDA+DMFT (Fig. 7.5) is better suited for comparison with photoemission experiments.

7.3.3 Sensitivity analysis

Previous theoretical work on KFe_2As_2 was based on the structural data obtained by Rosza and Schuster [160], while new results for elevated pressure by Tafti *et al.* [159] became available recently. These structures differ most noticeably in the As z -position, where the old structure has a fractional coordinate of $z = 0.1475$, while the new one yields $z = 0.140663$ by interpolation to 0 GPa.

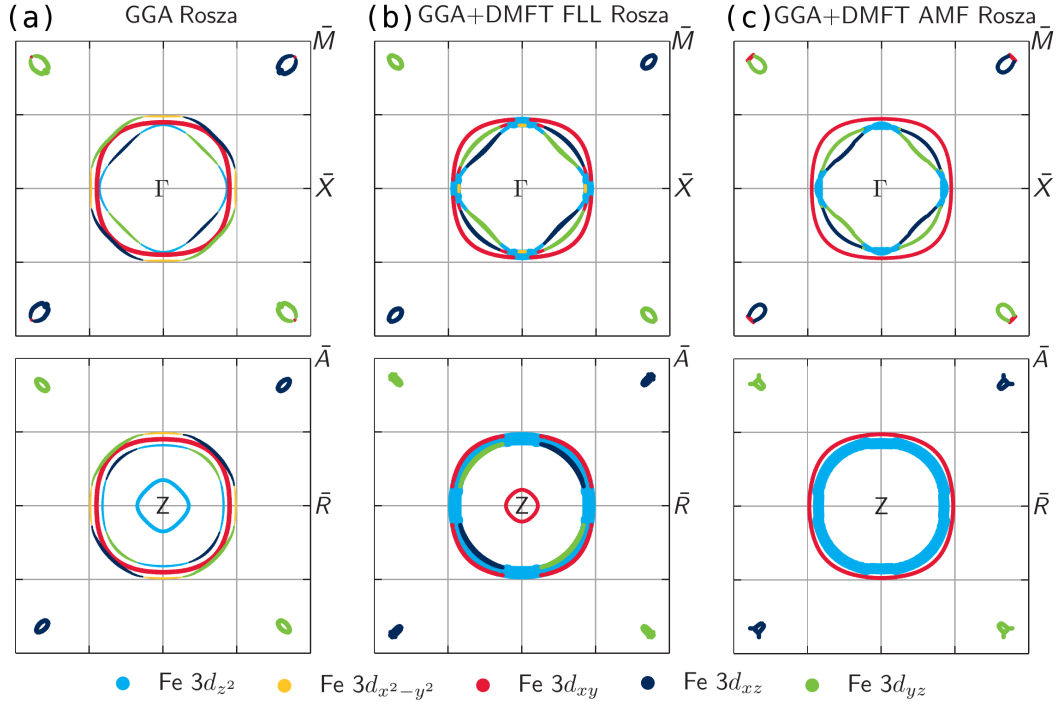


Figure 7.6: The orbital-resolved Fermi surface of KFe_2As_2 within (a) DFT for the structural data by Rosza and Schuster [160], within (b) LDA+DMFT for with the FLL double counting scheme and (c) the AMF double counting scheme. The GGA+DMFT indicates that the GGA functional has been used in the DFT part. Dominant orbital characters are indicated by the colour scale. Fermi surfaces are shown in the two-Fe Brillouin zone representation.

Therefore, to interpret current theoretical investigations correctly, we investigate the dependence of the Fermi surface and de Haas-van Alphen frequencies of KFe_2As_2 on the two different structures and also on different double-counting methods within LDA+DMFT. We also tested the dependence of these quantities upon considering LDA versus GGA and found only minor changes. Here we present GGA results.

We find very different behaviour for the two structural configurations: The Fermi surfaces for the Rosza and Schuster [160] structure can be seen in Fig. 7.6 (a), to be compared to the Tafti *et al.* [159] structure in Fig. 7.1. The cut at $k_z = 0$ is qualitatively identical but the Fermi surface topology at the Z point is different, where the structure of Rosza and Schuster with the higher As z -position features two additional inner hole pockets around Z . The inner one emerges from a small hole pocket centred at Z , while the second inner one corresponds to the open ζ -hole cylinder, which closes shortly before $k_z = \pi$ in the structure by Tafti *et al.* [159]. From our calculations we can deduce that the As z -position is the key factor for the existence of these hole pockets. This makes sense since their main orbital character is either Fe $3d_{z^2}$ or As $4p$, giving rise to a strong dependence on the Fe-As bonding distance. By lowering the As z -position, and thus enhancing the hybridization of the Fe $3d$ with the As $4p$ orbitals, the two inner pockets become smaller and finally vanish.

In Fig. 7.6 (b) and (c) we show cuts of the Fermi surface in LDA+DMFT, calculated for the structure by Rosza and Schuster. The electronic structure depends on the double-counting correction. With the FLL double-counting the fourth inner hole pocket stays present at the Z point, whereas with the around mean-field (AMF) double-counting it vanishes. This can be explained by the large As $4p$ character of the inner hole pocket, which makes it sensitive to the double-counting method. Since AMF reduces the Selfenergy by a smaller degree than FLL, this band is pushed below the Fermi level when using the AMF method. In the structure by Tafti *et al.* this band is farther away from the Fermi level already in the DFT calculation, lowering the As $4p$ contribution to the density of states

at E_F . Therefore, we see only slight differences between the two double-counting corrections in the Tafti *et al.* structure without qualitative changes.

7.4 Conclusion

In summary, in this chapter we have presented the results of our LDA+DMFT calculations of the Fermi surface and de Haas-van Alphen frequencies in KFe_2As_2 . We first showed that DFT calculations with LDA or GGA exchange correlation functionals, with or without spin-orbit coupling fail to reproduce the experimentally observed electronic structure of KFe_2As_2 .

Most notably, DFT predicts no third inner hole pocket at the Z point, which we find to open in our LDA+DMFT calculation, in agreement with experiment. We also obtain a qualitatively correct k_z dispersion of the iron bands, where between the Γ and Z points the dispersion of the inner hole cylinder is greatly increased while the middle hole cylinder shows almost no dispersion, giving a much better agreement with dHvA measurements when identifying them in different order in experiment.

The intersection nodes we found on the inner two hole cylinders offer a natural explanation for magnetic breakdown orbits observed in dHvA measurements [158].

The obtained effective mass-enhancements about 1.6 – 2.7 show that KFe_2As_2 is a moderately correlated metal and thus a DFT calculation fails to capture the important features that lead to the experimentally observed electronic structure. This has strong implications for the obtained dHvA frequencies, where LDA+DMFT gives distinctively different results than DFT. Our results are in better agreement with both ARPES [20, 21] and quantum oscillation [23, 158] experiments. The observed strong flattening of electronic bands gives a possible explanation for the spread of experimental results in this compound in terms of extreme sensitivity to the experimental stoichiometry. We conclude that LDA+DMFT captures most of the important correlation effects in KFe_2As_2 and such a treatment may be necessary in order to understand the controversial nature of superconductivity in this system.

We also find strong broadening effects of the quasiparticle excitations at the Fermi level, leading to a diffusive Fermi surface. While we considered different double counting schemes and structures, we did not investigate the temperature dependence of the coherence properties in this system. This will be the subject of the next Chapter 8.

Chapter 8

Strong electronic correlations in $A\text{Fe}_2\text{As}_2$ ($A = \text{K, Rb, Cs}$): Hund's coupling versus Coulomb repulsion

S. Backes, H. O. Jeschke, R. Valentí
Phys. Rev. B 92, 195128 (2015)

In this chapter we will now extend our analysis of the hole-doped iron-pnictide superconductors by considering the isovalent 122 family of KFe_2As_2 , RbFe_2As_2 and CsFe_2As_2 . Along this series we find that the hybridization between the Fe $3d$ orbitals is reduced because the increase in atomic radius of the Rb and Cs atoms induces a lattice expansion in these systems. As a result we see an increase in electronic correlations and especially a strong increase of the incoherence properties, with shift of spectral weight from the Fermi level to negative energies. We attribute these observations to the effect of the Hund's coupling which also causes the incoherent weight not to show the typical Hubbard-band behaviour.

8.1 Introduction

In addition to the Fermi surface changes and mass enhancements we investigated in the last chapter, a significant amount of work on the iron-pnictide superconductors has been concentrated on the description of effects of strong electronic correlations like possible non-Fermi liquid behavior or Hubbard band-like features [27–29, 32–35]. Due to the multi-orbital nature of these systems, governed by the Fe $3d$ orbitals at the Fermi level, the Hund's coupling J_H has been shown to play a key role in the determination of their electronic properties [27, 32–38]. However, there is an ongoing debate regarding the role of J_H versus the on-site Coulomb repulsion U and the interpretation of the correlated nature of Fe-pnictides and Fe-chalcogenides [28, 33, 34, 38–41, 174]. A main conclusion drawn in many of these studies is that, depending on the electronic filling, the Hund's coupling J_H on the one hand renders a moderately correlated system even more correlated and pushes it into a bad metal regime, while on the other hand it can also reestablish a metallic behavior, albeit orbital selective, in a strongly correlated system [38, 41]. The main question for the Fe-based superconductors and especially the hole-doped members narrows down to which regime of parameters do they belong to and how do correlations manifest in a wide range of binding energies as a function of doping and/or pressure?

In the hole-doped 122 materials $A\text{Fe}_2\text{As}_2$ ($A = \text{K, Rb, Cs}$) the substitution of Ba in the parent system BaFe_2As_2 by K, Rb or Cs accounts for a doping of one hole per formula unit and is accompanied by a complete suppression of any structural or magnetic phase transition [175, 176] and by the appearance of superconductivity at low temperatures. This behavior is common [46, 48, 147, 177, 178] to all hole-doped end members $A\text{Fe}_2\text{As}_2$ and they all seem to have a nodal gap structure [178, 179],

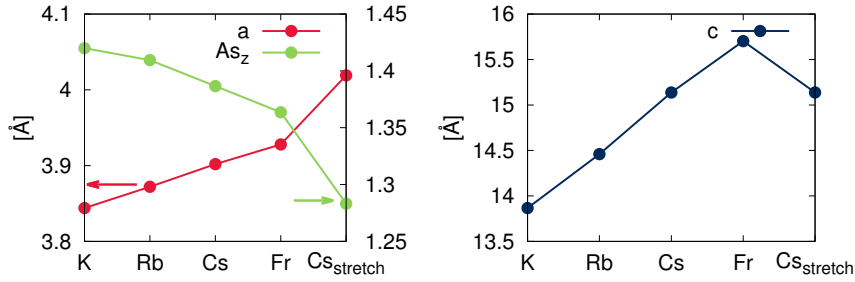


Figure 8.1: The structural parameters for the considered materials KFe_2As_2 (K), RbFe_2As_2 (Rb), CsFe_2As_2 (Cs) (from Ref. [46]), and the fictitious systems FrFe_2As_2 (Fr) and stretched CsFe_2As_2 ($\text{Cs}_{\text{stretch}}$). (a) The a -parameter (short side of the tetragonal unit cell) and absolute height of the As-atom above the Fe plane and (b) the c -lattice parameter, corresponding to the long side of the tetragonal unit cell.

which is different to the nodeless gap structure found in the parent BaFe_2As_2 system [180–182]. Further, experimentally $\text{Ba}_{1-x}\text{K}_x\text{Fe}_2\text{As}_2$ is thought to undergo a coherence-incoherence transition [42, 43, 183] as a function of temperature, that has been interpreted in terms of a strong increase in correlations [23, 184, 185]. Measurements of the Sommerfeld coefficient suggest that the hole-doped end systems are among the strongest correlated 122 iron-pnictide superconductors [42, 46], which is also corroborated by theoretical investigations on KFe_2As_2 [28, 40, 42, 49] and our results in the previous chapter. The measured Sommerfeld coefficient increases from BaFe_2As_2 to KFe_2As_2 by more than an order of magnitude [42, 44, 45] and increases further as K is substituted by Rb and Cs [47, 48]. In view of these observations, the hole doped end members $A\text{Fe}_2\text{As}_2$ provide an ideal background for investigating strong correlation effects as function of *negative* pressure.

Therefore, in this chapter we will again use LDA+DMFT to study the electronic structure of the series $A\text{Fe}_2\text{As}_2$ ($A = \text{K}, \text{Rb}, \text{Cs}$) as well as the fictitious FrFe_2As_2 and a -axis stretched CsFe_2As_2 in an extended range of binding energies. While a compression of the unit cell has been found to usually decrease correlation effects in the 122 iron pnictides [186–188], similarly, the opposite is to be expected when lattice parameters are expanded since the larger interatomic distances should reduce the hybridization of neighboring atomic orbitals and lead to stronger localization of the electronic states. We will show in the following that these considerations are correct only at first sight; actually, the strong correlation effects in these systems are mostly governed by a subtle interplay of J_H and U .

8.2 Computational details

For our study we use the structural parameters from Ref. [46] for the tetragonal structures of KFe_2As_2 , RbFe_2As_2 and CsFe_2As_2 at room temperature. Due to the almost perfect linear dependence of the lattice parameters as a function of atomic radius, we further use linear extrapolation to obtain structural parameters for fictitious FrFe_2As_2 , avoiding possible ambiguities from DFT-based relaxation methods which do not work satisfactorily for these systems. Additionally, we prepare a structure for CsFe_2As_2 that is extended along the a/b -axis by 3% and has a reduced relative As_z height of 2% to mimic a small expansion of the lattice. The expansion is performed in both the x - and y -direction so that tetragonal symmetry is preserved. The lattice parameters and As_z position are shown in Fig. 8.1.

For the DFT calculations we again used the WIEN2K [161] implementation of the full-potential linear augmented plane wave (FLAPW) method in the local density approximation. The Kohn-Sham equations were solved on 726 k -points in the irreducible Brillouin zone, resulting in a $21 \times 21 \times 21$ k mesh in the conventional Brillouin zone. For the local orbital basis we used the coordinate system

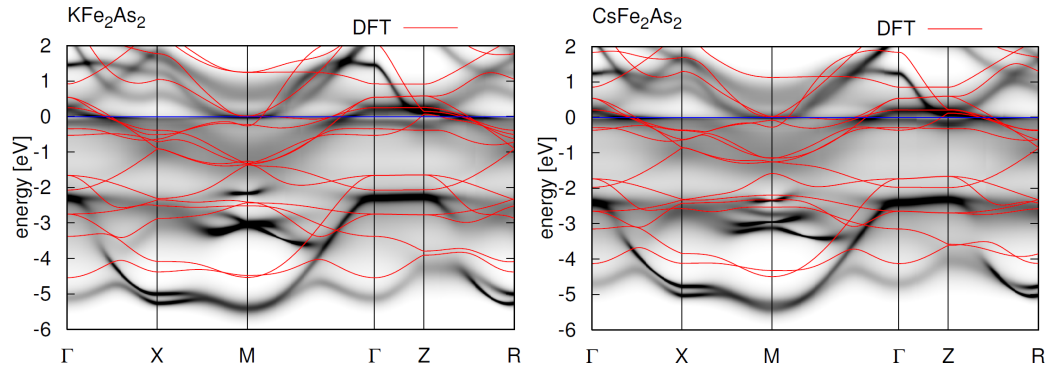


Figure 8.2: Momentum-resolved spectral function of KFe_2As_2 (top) and $CsFe_2As_2$ (bottom). Strong correlations in these materials introduce renormalization effects as well as broadening in the spectral function due to finite quasiparticle lifetimes compared to DFT(LDA). We observe a notable broadening and suppression of spectral features especially in the energy range $[-2.0, -0.5]$ eV.

which is rotated by 45° around the z -axis with respect to the conventional $I4/mmm$ unit cell. Thus, the x - and y -axis point towards neighboring Fe atoms. The energy window for the bands to be considered for projection was chosen to be $[-6, 13]$ eV, with the lower boundary lying in a gap in the density of states. Consequently, 35 bands on average were taken into account for the projection, resulting in a representation of the k -dependent and local non-interacting spectral function for each orbital that is indistinguishable from the DFT result in the chosen energy window.

The effective Anderson impurity model was solved with the continuous-time quantum Monte Carlo method in the hybridization expansion [8] as implemented in the ALPS [9, 164] project. In the calculations we used an inverse temperature of $\beta = 80 \text{ eV}^{-1}$, corresponding to the temperature of 145 K, unless stated differently. A total number of at least 50×10^6 Monte-Carlo sweeps were performed for each solution of the impurity model and up to 90×10^6 sweeps for the larger interaction parameters. For the double counting correction we used the nominal double counting [138, 139], which has been shown to yield significantly better agreement with photoemission experiments [139], especially for low and high binding energies, while other methods like the FLL [82, 167] double counting scheme can overestimate the valence charge and underestimate a possible Mott gap [139]. The interaction parameters were used in the definition of the Slater integrals [85] F^k with $U = F^0$ and $J_H = (F^2 + F^4)/14$, like described in Chapter 6.6. For the on-site Coulomb interaction we considered a value of $U = 4 \text{ eV}$ and for Hund's rule coupling $J_H = 0.8 \text{ eV}$, unless stated differently. We calculate the effective masses directly from the impurity Selfenergy as described in Chapter 6.9.1. The continuation of the Monte Carlo data to the real axis was done by stochastic analytic continuation [93] as described in Chapter 4.

To study the hopping matrix elements we obtained a tight-binding Hamiltonian from projective Wannier functions [189] from DFT, generated by the all-electron full-potential local orbital (FPLO) [190] code, using a 10 (16) orbital model, including the Fe $3d$ only (10-orbital model) [191] or Fe $3d$ and As $4p$ orbitals (16-orbital model).

8.3 Results

8.3.1 Momentum-resolved spectral function $A(\mathbf{k}, \omega)$

In Fig. 8.2 we show the momentum-resolved spectral function for KFe_2As_2 and $CsFe_2As_2$ as obtained within LDA+DMFT (gray density plot) at a temperature $T = 145 \text{ K}$ and compare it to the DFT bandstructure (red). We estimate for both systems Fe $3d$ effective masses m^*/m_{LDA} between 2.2 and 4.1 (depending on the orbital) which lead to a renormalization of the DFT(LDA) band energies and overall reduction of bandwidth. The average effective mass increases slightly from 2.89 to

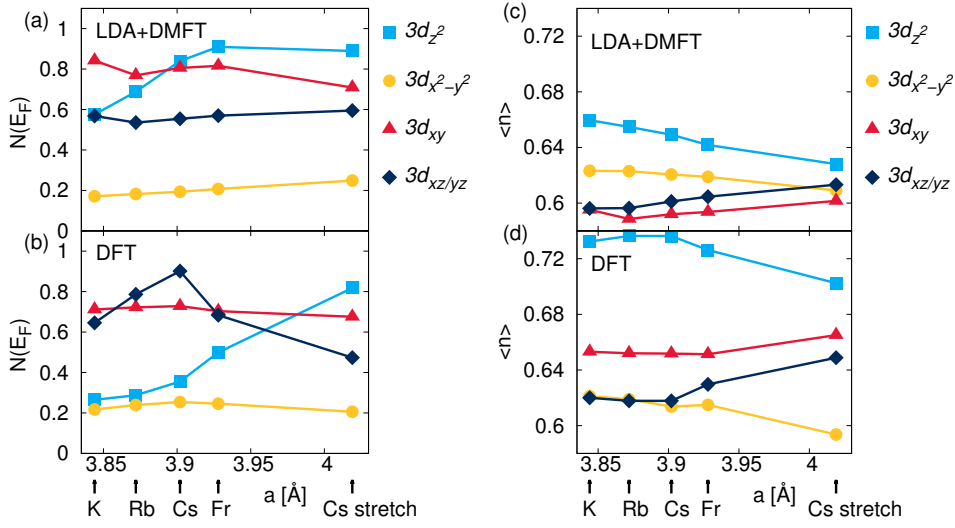


Figure 8.3: (a) and (b): The density of states of the Fe 3d orbitals at the Fermi level as obtained from (a) LDA+DMFT and in comparison with (b) DFT. The electronic correlations induce a marked deviation from the DFT results: The contribution of the Fe $3d_{z^2}$ orbital is strongly enhanced, while a more pronounced decrease of the Fe $3d_{xy}$ orbital is found towards the end system of stretched CsFe_2As_2 . Also, the trend in the Fe $3d_{xz/yz}$ orbital in DFT is completely evened out in LDA+DMFT. (c) and (d): Filling of the Fe 3d orbitals as obtained from (c) LDA+DMFT and (d) DFT(LDA). Correlations reduce the overall Fe 3d filling, with the most correlated $3d_{xy}$ and $3d_{xz/yz}$ orbitals being the closest to half filling in contrast to the DFT result. Along the alkali metal series, the occupation of Fe $3d_{z^2}$ and $3d_{x^2-y^2}$ orbitals reduces, while that of the $3d_{xy}$ and $3d_{xz/yz}$ orbitals increases after a local minimum in RbFe_2As_2 , which has the smallest $3d_{xy}$ occupation of all systems studied.

2.95, which indicates an increase in correlation along the $A\text{Fe}_2\text{As}_2$ series due to enhanced localization of electrons on Fe. The difference in the effective masses compared to our previous investigation are due to the different double counting scheme (see also discussion in Chapter 6.4), as well as the lower temperature. The effect of the temperature on the calculated mass enhancements will be discussed in more detail shortly.

Already at the Fermi level we obtain diffuse structures corresponding to incoherent quasi-particle excitations with finite lifetimes. At energies below -0.5 eV all coherent features are basically washed out due to correlation. This effect is present in all systems in the series $\text{KFe}_2\text{As}_2 \rightarrow \text{CsFe}_2\text{As}_2$, where we observe in the energy range of $[-2.0, -0.5]$ eV effects of strong broadening and depletion of spectral weight compared to the DFT bandstructure. At energies below -2 eV coherent features become visible again, which correspond to the As p states that partially hybridize with Fe $3d$ states. Even though the Selfenergy in DMFT has no momentum dependence, an effective momentum dependence is present in the results due to the momentum dependent orbital character of the original DFT bands. This leads to k-dependent broadening effects in LDA+DMFT.

8.3.2 Spectral weight at the Fermi level and orbital-resolved electronic filling

We first analyze the manifestation of correlation effects near the Fermi level. For that we compare in Fig. 8.3 LDA+DMFT (Fig. 8.3 (a)) with DFT(LDA) (Fig. 8.3 (b)) orbital-resolved density of states at the Fermi level $N(E_F)$ for all studied systems. The LDA+DMFT calculations show an increasing and pronounced dominance of $3d_{z^2}$ contribution at E_F along the series. This is in contrast to the DFT results where the Fe $3d_{z^2}$ orbital contribution also increases, but is much lower and only significant

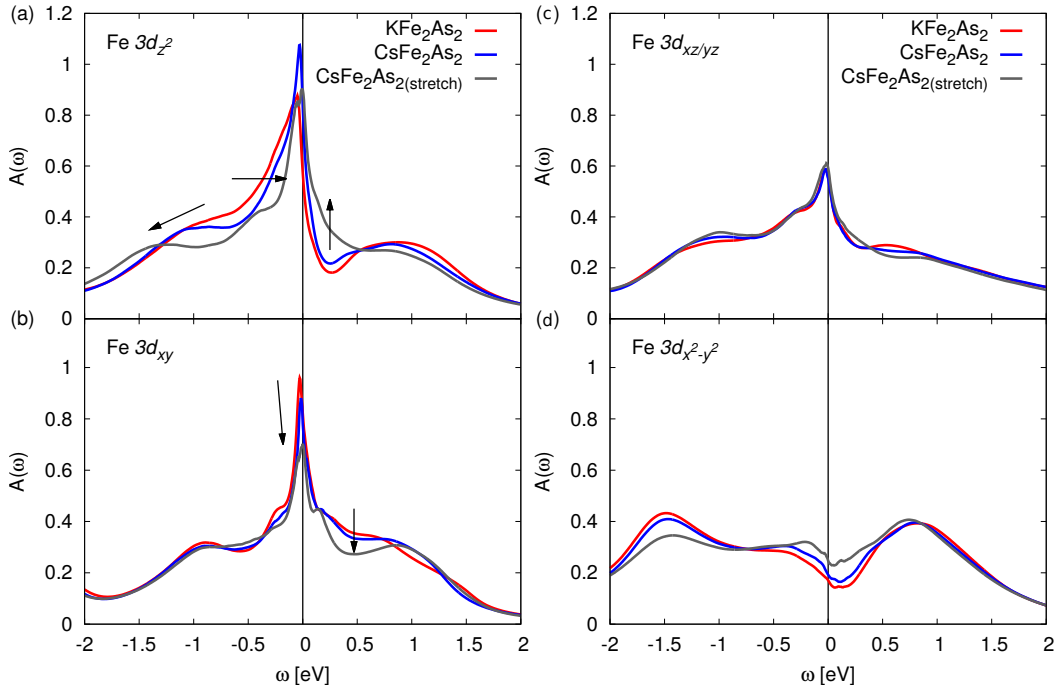


Figure 8.4: The local spectral function for (a) the Fe $3d_{z^2}$ orbital, (b) the Fe $3d_{xy}$ orbital, (c) the Fe $3d_{xz/yz}$ orbital and (d) the Fe $3d_{x^2-y^2}$ orbital as obtained from LDA+DMFT for the three compounds KFe_2As_2 , CsFe_2As_2 and an a -axis stretched CsFe_2As_2 . Note the emergence of a Hubbard-like peaks around -1.2 eV and $+1$ eV for $3d_{z^2}$ and around -1 eV and $+1$ eV for $3d_{xy}$. With arrows we mark the trend of the changes in the spectral function along the series. The interaction parameters are given as $U = 4$ eV and $J_H = 0.8$ eV.

for a -axis stretched CsFe_2As_2 with shortest As height. The non-monotonous behaviour of the Fe $3d_{xz/yz}$ contribution in DFT is a result of the special electronic structure of these systems at the M point. This feature is greatly suppressed by broadening effects in the LDA+DMFT calculation.

Linked to these results is the behavior of the LDA+DMFT orbitally-resolved electronic filling (see Fig. 8.3 (c) and (d)). We observe that inclusion of correlation effects not only reduces the overall Fe $3d$ filling due to the additional cost of the Coulomb interaction energy for doubly occupying a certain orbital, but also introduces orbital-dependent effects (see Section 8.3.4). While the Fe $3d_{z^2}$ and $3d_{x^2-y^2}$ filling decreases along the series, it increases for $3d_{xz/yz}$ and $3d_{xy}$.

8.3.3 Spectral function $A(\omega)$

In order to understand the origin of the changes in $N(E_F)$ and orbital filling, we show in Fig. 8.4 the local spectral function $A(\omega)$ for the Fe $3d$ orbitals in the energy range $[-2, 2]$ eV for the representatives KFe_2As_2 , CsFe_2As_2 and a -axis stretched CsFe_2As_2 . The orbitals (a) $3d_{z^2}$ and (b) $3d_{xy}$ are the most affected along the series: $3d_{z^2}$ because of the decrease in As height from KFe_2As_2 to CsFe_2As_2 and $3d_{xy}$ because of the increase in the orbital localization with increasing a lattice parameter. Fe $3d_{z^2}$ shows a shift of orbital weight to negative energies (high binding energies) and a narrowing of the quasiparticle-like peak structure at E_F from KFe_2As_2 to CsFe_2As_2 . Since the electronic filling of the iron $3d$ orbitals is larger than half-filling in these systems, the quasiparticle-like peak is located close to but below the Fermi level. In Fe $3d_{z^2}$ due to the reduction of the filling from 0.66 in KFe_2As_2 to 0.63 in stretched CsFe_2As_2 (see Fig. 8.3) caused by an increase of electronic correlations, the quasiparticle peak-like structure is shifted even closer towards the Fermi level along the series, which in turn leads to the observed increase of the density of states at the Fermi level (Fig. 8.3(a)). Such a shift of the quasiparticle peak-like structure in KFe_2As_2 was already noted

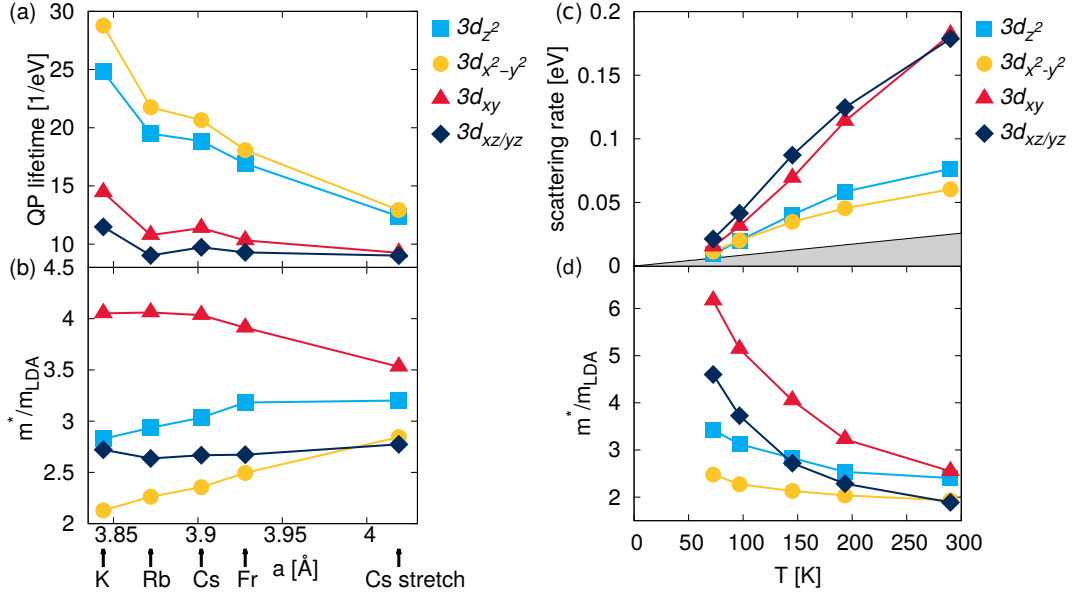


Figure 8.5: (a) Quasiparticle lifetimes given by $\tau_m = -(Z_m \text{Im}\Sigma_m(i0^+))^{-1}$ of the Fe 3d orbitals along the $A\text{Fe}_2\text{As}_2$ series and (b) the corresponding effective masses $\frac{m^*}{m_{\text{LDA}}}$. On the right we show the temperature dependence of the (c) scattering rates $-Z_m \text{Im}\Sigma_m(i0^+)$ of the Fe 3d orbitals of KFe_2As_2 . The shaded area indicates the coherent domain. The coherence temperature estimate T^* as deduced from the scattering rate is quite low, located around 50 K. (d) The corresponding effective masses evaluated at the same temperatures.

in Ref. [49]. For the $3d_{xy}$ orbital, the quasiparticle peak is much closer to the Fermi level since the filling is closer to half filling at $n_{xy} \approx 0.59$. This orbital shows a strong suppression of the quasiparticle peak (up to $\approx 30\%$) from KFe_2As_2 to the a -axis stretched CsFe_2As_2 which points to an important increase of decoherence along the series. This increase of decoherence will be studied in more detail in the next section. Reduction of the maximum of the quasiparticle peak combined with a slight change of its position results in the almost constant spectral function at the Fermi level for the $3d_{xy}$ orbital observed in Fig. 8.3 (a).

Additionally, a shoulder-like feature appears in the spectral function at 1 eV and -1 eV in CsFe_2As_2 , closely resembling the typical spectral function shape of a quasiparticle peak and a lower and upper Hubbard band. These features do not correspond to any property found in the non-interacting DOS and are purely an effect of correlations and, at first sight, are similar to the emergence of Hubbard bands as a function of U in strongly correlated systems. This is also in agreement with the $3d_{xy}$ orbital being the strongest correlated one, whereas these features are far less developed in the $3d_{z^2}$ and other orbitals. However, as we will show in Section 8.3.6, these peaks do not behave as expected for Hubbard bands in a one-band Hubbard model.

The Fe $3d_{xz/yz}$ and $3d_{x^2-y^2}$ orbitals are less affected by an increase of the lattice parameter a . Similar to the $3d_{z^2}$ and $3d_{xy}$ orbital a small Hubbard-like peak becomes more pronounced in the $3d_{xz/yz}$ orbital, while the $3d_{x^2-y^2}$ orbital shows the opposite trend, increasing its spectral function at the Fermi level at the cost of decreasing it at negative energies.

8.3.4 Effective masses and quasiparticle lifetimes

In order to quantify the change in correlation along the series $A\text{Fe}_2\text{As}_2$ we plot in Fig. 8.5 (a) and (b) the orbitally resolved quasiparticle lifetimes and effective masses $\frac{m^*}{m_{\text{LDA}}}$. The effective masses for Fe $3d_{z^2}$ and $3d_{x^2-y^2}$ increase along the $A\text{Fe}_2\text{As}_2$ series but remain constant or even slightly decrease for $3d_{xz/yz}$ and $3d_{xy}$. This last result cannot be explained solely by the behavior of the DFT-derived tight binding parameters (see Fig. 8.3.7).

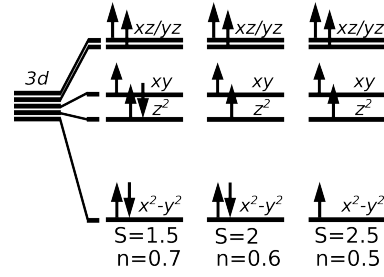


Figure 8.6: Sketch of some of the most likely Fe atomic orbital configurations in hole-doped 122 iron pnictide systems. The electronic filling is indicated by n and the total spin by S .

Information on the origin of this behavior can be obtained from the quasiparticle lifetimes which strongly decrease for all orbitals along the series (Fig. 8.5 (b)). This indicates that the coherent quasiparticle picture, being the basis for the calculation of the effective masses, becomes less appropriate along the $A\text{Fe}_2\text{As}_2$ series, and accordingly, the effective masses obtained by this procedure are underestimated compared of the true value. This result shows that already at the temperature of $T = 145$ K these systems are quite incoherent. With increasing lattice parameter incoherence significantly increases, albeit leading to an orbital dependent change in localization of the Fe $3d$ electrons. In particular, we find a pronounced decrease of the quasiparticle lifetime from KFe_2As_2 to RbFe_2As_2 , which we attribute to the competing effects of decrease of Fe-Fe direct hopping and increase in Fe-Fe indirect hopping through As, which seem to have a crossover point between RbFe_2As_2 and CsFe_2As_2 (see Fig. 8.3.7).

In Fig. 8.5 (c) and (d) we show the temperature dependence of the quasiparticle scattering rates and effective masses of KFe_2As_2 . We find a similar temperature dependence as also observed for multi-orbital SrRuO_3 and CaRuO_3 in Ref. [192]. As the temperature is lowered in the calculation, the quasiparticle picture, which is suppressed at high temperatures, is partially restored, leading to an exponential increase in the quasiparticle lifetimes. Still, even at the lowest studied temperature of $T = 72$ K the width (scattering rate) of the quasiparticle peak $-\text{Z}_m \text{Im} \Sigma_m(i0^+)$ (compare Chapter 6.9.1) is still larger than the temperature, indicating that coherent quasiparticle excitations are still in the minority. From our results for the scattering rate we estimate that the temperature T^* for the incoherent-coherent phase transition for our chosen interaction parameters $U = 4$ eV, $J_H = 0.8$ eV is around 50 K, and is even lower for RbFe_2As_2 and CsFe_2As_2 . This is in qualitative agreement with previous LDA+DMFT estimates for KFe_2As_2 [49] and with magnetic susceptibility and thermal expansion measurements which predict the coherence scale of KFe_2As_2 to be around 100 K [42, 43, 45] and even lower for RbFe_2As_2 and CsFe_2As_2 [45, 46]. We expect that inclusion of the full rotationally invariant Hund's coupling, which is beyond the scope of the present work, will shift the transition to higher temperatures in the calculation [29, 33, 193] and, therefore, closer to experiment. The consequences of inclusion of rotationally invariant interactions have been extensively discussed in previous works in the framework of the two-band [194] and three-band [195] Hubbard models. The computational effort of including these terms in the five-band cases studied here is beyond the scope of the present work. However, we performed some benchmarking calculations with fully rotational Hund's coupling and find that the coherence transition shifts to higher temperatures as found in other studies [29, 33, 193]. In this sense the presented results can be considered as a lower bound to the experimental observations.

The increase of effective masses as shown in Fig. 8.5 (d) at lower temperatures in our calculation is precisely the effect of restoring the coherent quasiparticle picture, so that the effective masses at the lowest temperature (72 K) we investigated can be considered as the closest approximation to the true values, *i.e.* 6.1 ($3d_{xy}$), 4.6 ($3d_{xz/yz}$), 3.4 ($3d_{z^2}$) and 2.5 ($3d_{x^2-y^2}$).

Combining these observations along the series we conclude that alkali 122 systems show typical signs of strong correlations but, in the studied range of temperatures, are actually quite deep in the incoherent bad metal region with a well defined, albeit strongly suppressed, quasiparticle peak.

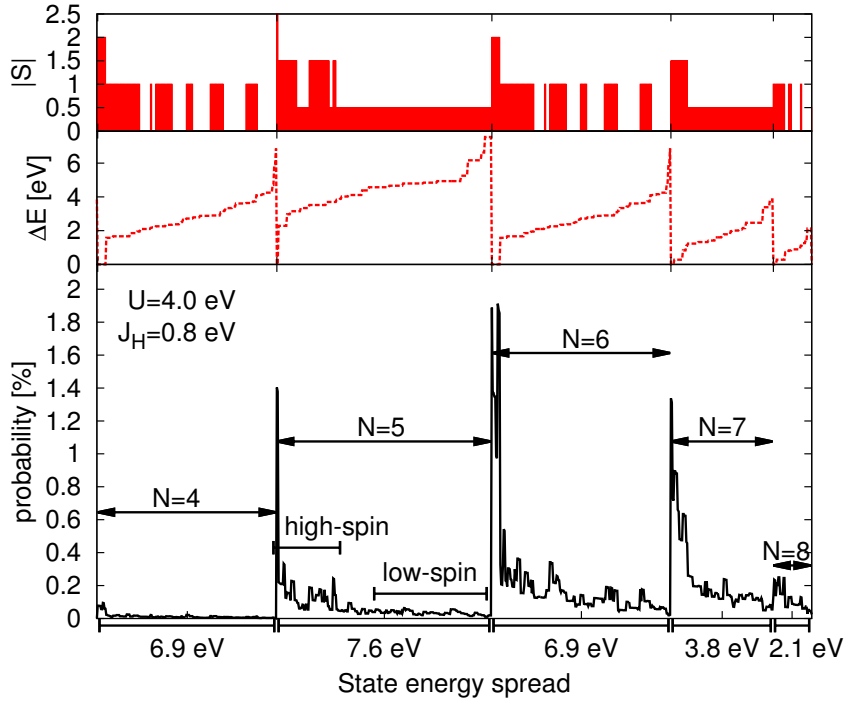


Figure 8.7: The histogram of the Fe 3d atomic state for KFe_2As_2 at $T = 145$ K. The probability corresponds to the fraction of time the Fe 3d orbitals spend in one of the $2^{10} = 1024$ possible states. Within the interval of constant electron number N the states are sorted by increasing energy, i.e. the leftmost states within an interval correspond to high-spin states, while the rightmost states correspond to low-spin states.

8.3.5 Nature of the Fe 3d wave function

We proceed now with an analysis of the wave function in terms of the Fe atomic basis states, similar to what has been done for other pnictide systems [28, 33]. In Fig. 8.6 we show a sketch for a few typical orbital configurations in these systems with the orbital splittings obtained from the down-folded charge self-consistent LDA Hamiltonian. Since the nominal electronic filling for Fe 3d for these systems is 5.5 electrons per Fe, one would expect atomic Fe 3d states with 5 and 6 electrons to be the most likely states. However, as shown in Fig. 8.3, the actual average Fe 3d filling is slightly larger than 6 and this can be analysed in the histogram of Fig. 8.6. For the interacting system there is a non-trivial competition between the energy contribution due to the crystal field splitting, which prefers to occupy the lowest states first, the on-site U interaction, which tends to decrease the filling of the localized states and the Hund's coupling J_H , which prefers orbital states with maximum total spin. When the Hund's coupling J_H is large compared to the total crystal field splitting, the high-spin states will have the highest probability and the low-spin states will be suppressed. This is indeed true for the hole-doped 122 iron-pnictides.

In Fig. 8.7 we show for KFe_2As_2 the atomic histogram of the Fe 3d shell, i.e. the projection of the wave function onto the Fe 3d atomic basis states. The states are sorted by the number of electrons N , and inside the interval of constant filling the states are sorted by energy. Because of the Hund's coupling, the leftmost states in such an interval correspond to the high-spin states, while the rightmost states correspond to low-spin states. The probability assigned to each state corresponds to the fraction of time in the calculation the 3d orbitals spend in a specific configuration. Due to the Hund's coupling the high-spin states clearly dominate the histogram, although their probabilities are quite low with less than 2%. Even for the low-spin states at higher energy the probability,

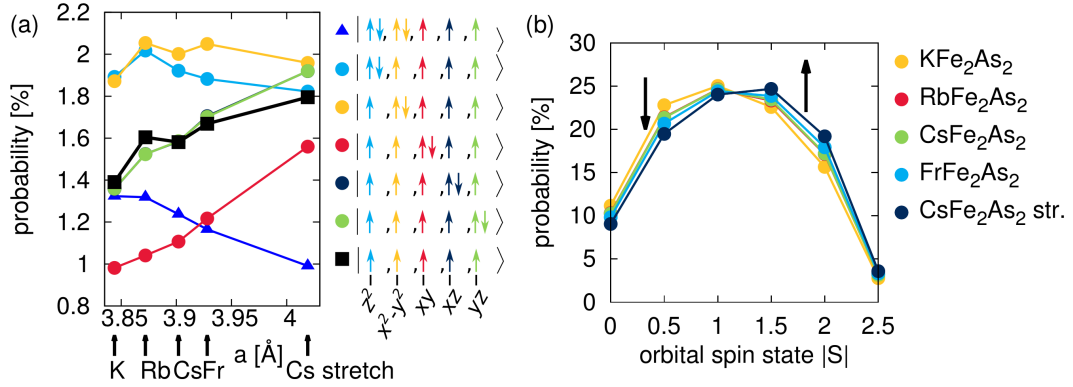


Figure 8.8: (a) Probabilities of the most likely atomic states of the Fe 3d atomic orbitals for the $A\text{Fe}_2\text{As}_2$ series. The probability corresponds to the fraction of time the atom in the DMFT calculation spends in a specific state. (b) The summed probability of all atomic states with a given total spin S . High-spin states become more likely for increasing lattice parameter a , while the probability of low-spin states is reduced.

while being smaller, is never close to zero, which causes the Fe 3d orbitals to visit a large number of accessible states over time even when they are much higher in energy. Since all these states contribute with a finite fraction to the Fe 3d spectral function, no well defined atomic like excitations can be expected. This leads to the observed suppression of the quasiparticle peak and subtle high-binding energy features in the spectral function without well defined Hubbard bands, which is the distinctive property of Hund's metals [28, 41].

This behavior becomes even more pronounced when we perform this analysis along the $A\text{Fe}_2\text{As}_2$ series. In Fig. 8.8 (a) we analyze the most likely atomic states from the histogram of the Fe 3d orbitals for $A\text{Fe}_2\text{As}_2$. For all systems, six out of the seven most likely atomic states are solely composed of the maximal high-spin states with $S = 2.5$ and $S = 2$. For the earth alkali (undoped) 122 iron-pnictides like BaFe_2As_2 the atomic ground state of the Fe atom with a valence charge of 6 has a maximum possible spin of $S = 2$. Since for the systems studied here one electron per formula unit has been removed by hole doping, the probability for the fully polarized half-filled $S = 2.5$ state with 5 electrons in the Fe 3d orbitals is among the most likely states with a comparably high probability of 1.4% (or 2.8% when accounting for spin degeneracy) in KFe_2As_2 , that increases up to 1.8% (or 3.6%) in the stretched CsFe_2As_2 system. Along the series the low-spin states become suppressed while the high-spin states increase in probability, as can be seen in Fig. 8.8 (b).

Generally, the systems can reduce their energy by assigning a higher probability to high-spin states due to the Hund's coupling J_H . This leads to a significant increase of localization caused by the orbital blocking mechanism [28]. Since J_H enforces a high-spin state, orbital mixing is greatly suppressed compared to a vanishing Hund's coupling where high- and low-spin states would have equal energies and, therefore, probabilities. This is the typical behavior of a so-called Hund's metal, in which the electronic correlations are much more sensitive to the value of J_H than to the on-site Coulomb interaction U . Therefore, in the hole-doped end systems like CsFe_2As_2 and especially the a -axis stretched CsFe_2As_2 the Hund's coupling becomes the most important interaction that governs the physical properties of these systems.

8.3.6 Dependence on U and J_H

In order to investigate the effects of U and J_H more explicitly and to determine the nature of the peak/shoulder at $[-1.5, -1]$ eV we performed calculations for different interaction parameters for the most correlated case, the a -axis stretched CsFe_2As_2 system. For computational efficiency these calculations were done at higher temperature $\beta = 40 \text{ eV}^{-1}$. While the height of the quasiparticle

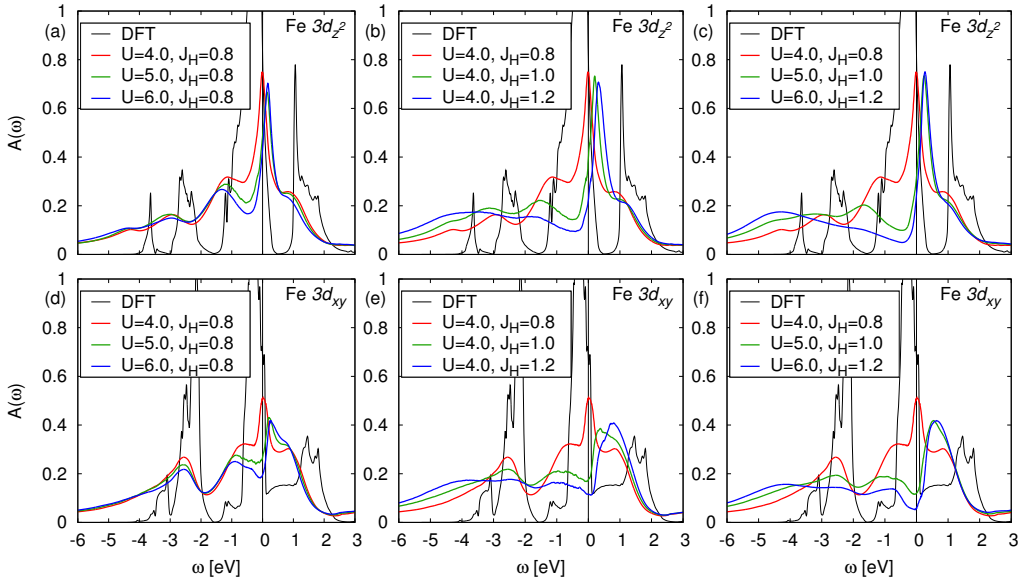


Figure 8.9: The local spectral function $A(\omega)$ for the Fe $3d_{z^2}$ orbital (upper row, (a)-(c)) and the Fe $3d_{xy}$ orbital (lower row, (d)-(f)) of the stretched CsFe_2As_2 compound as a function of the on-site Coulomb repulsion U and Hund's coupling J_H . (a) An increase only in U leads to an increase in renormalization, i.e. effective masses and a pronounced Hubbard-like peak at -1.5 eV but no other qualitative changes are observed. (b) The Hund's coupling J_H greatly increases the decoherence of the electronic states at the Fermi level and leads to a significant shift of spectral weight down to lower energies. (c) The combined effect of U and J_H is qualitatively similar to an increase in J_H alone.

In the Fe $3d_{xy}$ orbital we see the similar result that the shift of spectral weight to lower energies is almost exclusively dependent on the Hund's coupling J_H . Being the most correlated orbital, the spectral function of the Fe $3d_{xy}$ orbital at the Fermi level is almost gapped for $U = 6$ eV and $J_H = 1.2$ eV.

peak is reduced at higher temperatures, the behavior of the spectral function at $[-2, -1]$ eV is quite robust. We considered on-site Coulomb values $U = 4, 5$ and 6 eV and Hund's couplings of $J_H = 0.8, 1.0$ and 1.2 eV. In Fig. 8.9 we show the spectral function $A(\omega)$ for Fe $3d_{z^2}$ and $3d_{xy}$. An increase of U from 4 eV to 6 eV at a fixed J_H implies only moderate changes in the spectral function in general for all Fe $3d$ orbitals. The Hubbard-like shoulder at -1.2 eV becomes more pronounced for larger U values and its maximum moves only slightly to negative energies (-1.4 eV). Due to particle-hole asymmetry, we obtain a quasiparticle like peak shifted away from the Fermi level. On the other hand, an increase in the Hund's coupling J_H for fixed U immediately renders the system very incoherent, with a strong increase in the scattering rate and a reduction of the quasiparticle lifetime. This leads to a strong suppression of the spectral function at the Fermi level and a significant shift of spectral weight to lower energies, forming a broad lower Hubbard band located between -4 and -5 eV. Finally, the combined effect of U and J_H yields an even more well pronounced lower Hubbard-like band at around -4.5 eV. While this characteristic dependence on U and J_H is similar for all Fe $3d$ orbitals, we still find a strong orbital selection regarding the remaining spectral weight at the Fermi level. Especially the Fe $3d_{xy}$ orbital is almost gapped at the Fermi level for the largest interaction values considered (see Fig. 8.9).

In Fig. 8.10 we show the dependence of the Fe $3d_{xz/yz}$ and $3d_{x^2-y^2}$ orbital spectral function on U and J_H . The results are very similar to the other orbitals, with the effect of increasing U being much less extreme than that of J_H . While at higher U the spectral functions still mimics the LDA result, an increase in J_H results in a large shift of spectral weight to negative energies. The $3d_{x^2-y^2}$

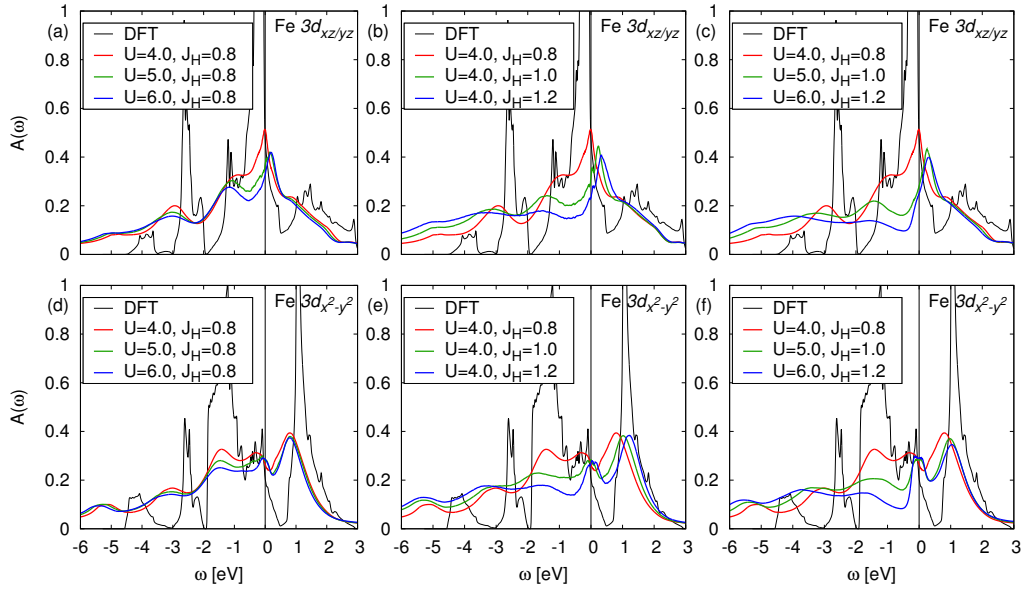


Figure 8.10: The spectral function for the Fe $3d_{xz/yz}$ and $3d_{x^2-y^2}$ orbital of the stretched CsFe_2As_2 compound as a function of the on-site Coulomb repulsion U and Hund's coupling J_H . (a)+(d) An increase only in U leads to a slightly better pronounced lower Hubbard band-like feature but otherwise no qualitative changes to the high energy features. (b)+(e) The Hund's coupling J_H greatly increases the decoherence of the electronic states at the Fermi level and leads to a significant shift of spectral weight down to negative energies. (c)+(f) The combined effect of U and J_H is qualitatively very similar to an increase in J_H alone.

orbital shows the smallest degree of correlations and experiences basically no suppression of the spectral function at the Fermi level, regardless of the interaction parameters and instead retains a well defined quasiparticle peak for higher values of U and J_H .

Our results confirm the general picture of the iron pnictides being "Hund's metals" with strong orbital separation, especially for the strongly correlated hole-doped end systems considered in this chapter. In this case, a slight increase of J_H renders the system much more incoherent and "bad metal"-like for the same value of U , while the spectral weight at the Fermi level differs strongly between the orbitals but remains finite even for larger values of U .

We also checked the case of negligible Hund's coupling by setting $J_H = 0$, which recovered the coherence properties even at $T = 300$ K, with low effective masses around 1.4 and a spectral function that resembled quite well the DFT density of states.

8.3.7 Tight binding analysis

In order to quantify at the level of DFT the effects of negative pressure introduced by isovalent doping in $A\text{Fe}_2\text{As}_2$ ($A = \text{K}, \text{Rb}, \text{Cs}, \text{Fr}$), we calculated the Fe-Fe hopping matrix elements via projective Wannier functions. The absolute values of the hopping parameters from a 10-band tight binding fit to the Fe $3d$ orbitals are plotted in Fig. 8.11 (a). In this model the hoppings through the arsenic site are integrated out and thus are included in the effective hopping. There are two main contributions that affect the values of the Fe-Fe hopping parameters: First, the increase of the interatomic distances due to increasing atomic radii of the alkali ions implies a decrease of the direct Fe-Fe hopping. Second, due to elongation of the Fe-As tetrahedron, the As atom moves closer to the Fe-Fe plane. This reduction of the As_z height leads to an increase of the indirect hopping along the path Fe-As-Fe. The total contribution of these two effects translates into a non-trivial behavior of the Fe-Fe effective hoppings along the doping series $(\text{K,Rb,Cs})\text{Fe}_2\text{As}_2$. The Fe $3d_{xy}$ -

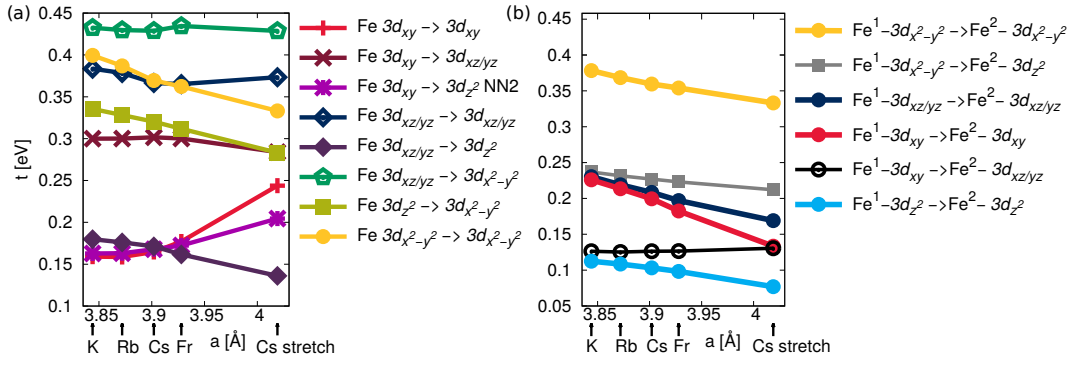


Figure 8.11: (a) The eight largest effective Fe-Fe hopping parameters t obtained from a 10-band tight binding fit to the Fe $3d$ orbitals. In this model the hoppings through the arsenic site are integrated out and thus included in the effective hopping. Also shown are some second nearest neighbour parameters indicated by the label NN2. The non-trivial evolution of the hopping values with increasing lattice parameter and reduced As_z height leads to different degrees of localization and effects of correlation in the Fe $3d$ orbitals along the series KFe_2As_2 , RbFe_2As_2 , CsFe_2As_2 and FrFe_2As_2 . In comparison (b) shows the first six largest hopping parameters t for the Fe-Fe hopping obtained from a 16-band tight binding fit, where the arsenic contribution is excluded. As a result, the increasing lattice parameter results in an almost perfect linear decrease of the hoppings. Fe^i denotes the i -th atom out of the two equivalent iron atoms in the irreducible Brillouin zone.

Fe $3d_{xy}$ effective hopping is the smallest in KFe_2As_2 due to the almost perfect cancellation of the two contributions as pointed out in Ref. [28]. As the lattice parameter increases, the indirect Fe-As-Fe hopping contribution outweighs the contribution coming from the direct Fe-Fe orbital overlap. This causes a slight increase of the hopping parameters from KFe_2As_2 to CsFe_2As_2 . These two contributions are very similar for hoppings between Fe $3d_{xz/yz}$ orbitals. The trend in the hoppings between Fe $3d_{z^2}$ and $3d_{x^2-y^2}$ orbitals is less affected by changes of the indirect hopping contribution and shows a small overall decrease in the hopping to the neighboring Fe $3d$ orbitals.

In comparison we also show in Fig. 8.11 (b) the six largest Fe-Fe hopping parameters obtained from a 16-band tight binding fit, encompassing the Fe $3d$ and As $4p$ orbitals. By this, the effective hopping through the arsenic site is not included in the Fe hopping parameters. The overall monotonous decrease resembles the increase of the interatomic distance that leads to a reduced overlap of the neighboring Fe $3d$ orbitals. As already noted, the indirect hopping through the As $4p$ orbitals has an important effect on the effective hopping parameters. Taking only the direct Fe-Fe hopping into account, we observe the expected decrease of the hopping parameters which resembles the reduced hybridization as the lattice parameters are increased.

8.4 Conclusions

From our extended analysis of the hole-doped iron-pnictide series $A\text{Fe}_2\text{As}_2$ ($A = \text{K, Rb, Cs}$) as well as the fictitious FrFe_2As_2 and a -axis stretched CsFe_2As_2 we conclude that the monotonous increase of the a lattice parameters and a decrease of the As_z height are responsible for an increase in correlation and incoherence of the Fe $3d$ orbitals, albeit orbitally selective, and the systems show clear features of a Hund's metal. In this case the Hund's coupling plays the major role and renders these materials much more incoherent than expected from the value of the Coulomb repulsion U alone. While the most correlated orbitals (d_{xy}) show features that resemble those of being close to an orbital selective Mott transition, specially for a -stretched CsFe_2As_2 , the system is deep in the incoherent bad metal regime with a finite spectral weight at the Fermi level even for $U = 6$ eV and $J_H = 1.2$ eV.

Experimentally, we predict that an increase of the Fe-Fe distance in CsFe_2As_2 by stretching will

induce an orbital dependent increase in correlations and incoherence of the Fe $3d$ orbitals, where the Fe $3d_{z^2}$ and Fe $3d_{xy}$ orbitals are strongly, but not fully localized and the other Fe $3d$ orbitals retain a bad metallic behaviour. From our results we estimate the coherence temperature to be located around 50 K in KFe_2As_2 and even lower for RbFe_2As_2 and CsFe_2As_2 in qualitative agreement with the experimental observations. This justifies the choice of the nominal double counting scheme, since in our previous study of KFe_2As_2 in Chapter 7 within the FLL scheme we obtained a very similar spectral function away from the Fermi level, but states that were too coherent at the Fermi level compared to experiment. In general, these features make the hole doped end systems of the 122 iron pnictides, namely KFe_2As_2 , RbFe_2As_2 and especially CsFe_2As_2 and a -axis stretched CsFe_2As_2 a valuable test bed to study the behavior of strongly correlated Hund's metals and orbital-selective bad metallicity and its interplay with superconductivity.

Chapter 9

Interplay of electronic correlations and oxygen vacancies in SrVO₃

S. Backes, T. C. Rödel, A. J. Kim, F. Lechermann, H. O. Jeschke,
M. J. Rozenberg, R. Valentí, A. F. Santander-Syro *et al.*
arXiv:1602.06909 (2016)

In this chapter we come back to a system that has been the drosophila of correlated electron methods: the strongly correlated cubic perovskite SrVO₃. Being one of the first systems studied within LDA+DMFT, it can basically be seen as the starting point for its success. While being structurally very simple, it shows effects of strong electronic correlations that are interpreted as upper and lower Hubbard bands in the spectral function, where LDA+DMFT can obtain a very good agreement with experimental observations.

However, in this investigation which was done in collaboration with the experimental group of Santander-Syro *et al.* (Université Paris-Sud, France), we show that the interpretation of the spectral features found in SrVO₃ solely in terms of Hubbard bands is not correct and oxygen vacancies play an important role in the final spectrum. Moreover, we demonstrate that LDA+DMFT is not only able to capture the contribution of incoherent spectral weight arising from a Hubbard band, but in addition can also describe coherent states arising from oxygen vacancies below the Fermi level on the same footing.

By this, the theoretical investigation in combination with experiments enables us to disentangle the contributions coming from the oxygen vacancy states and from the lower Hubbard band in SrVO₃. Our results show the relevance of potential spurious states affecting angular-resolved photoemission spectroscopy (ARPES) experiments in correlated metals, which are associated to the ubiquitous oxygen vacancies as extensively reported in the context of a two-dimensional electron gas (2DEG) at the surface of insulating d^0 transition metal oxides.

9.1 Introduction

Among the most emblematic achievements of DMFT is the prediction of a Hubbard satellite, which splits off of the conduction band of a metal. This satellite results from the partial localization of conduction electrons due to their mutual Coulomb repulsion. Early DMFT studies also showed that it is the precursor of the localized electronic states of a Mott insulator [196]. Since then, these predictions promoted a large number of studies using photoemission spectroscopy, which is a technique to directly probe the presence of Hubbard bands. In this context, the transition metal oxide (TMO) SrVO₃ has emerged as the *drosophila* model system to test the predictions of strongly correlated electron theories. In fact, SrVO₃ is arguably the simplest correlated metal. It is a cubic perovskite, with nominally one electron per vanadium site, which occupies a 3 fold degenerate t_{2g} conduction band. While the presence of a satellite in the photoemission spectra of Ni metal was

already well known, in the context of correlated TMOs, the Hubbard band was originally reported in a systematic investigation of Ca_{1-x}Sr_xVO₃ [197], which was followed by many subsequent studies, including ARPES [54, 55, 198] and comparison with theoretical predictions (see for instance Refs. [36, 51, 57, 123, 126, 199–204] among others).

One of the most salient features in SrVO₃ is the observation of a broad peak at an energy of about -1.5 eV in angle integrated photoemission spectra, (see upper black curve in Fig. 9.1 (a)), which is interpreted as a Hubbard satellite linked to the V t_{2g} electrons. This feature is also seen in a large range of $3d^1$ materials [205, 206]. The ratio of spectral strength between the quasiparticle state and the incoherent satellite in SrVO₃ is an important indicator of the magnitude of electron correlations [80, 207]. However, photoemission experiments using different photon energies or light brilliance have reported very dissimilar values for such ratio [51], making the quantitative benchmarking of realistic *ab initio* theories for correlated-electron systems difficult [51, 52, 197, 203, 208]. Moreover, as shown in Fig. 9.1 (a), a broad peak at about the same energy is also observed in several d^0 TMO cubic perovskites, such as SrTiO₃, KTaO₃, or anatase TiO₂. Nevertheless, in all these cases the feature has been clearly linked to the presence of oxygen defects [209–216]. Interestingly, recent *ab initio* calculations show that spectral weight at -1.3 eV in SrTiO₃ most likely is not of Ti t_{2g} orbital character, but should be understood as an in-gap defect state with Ti e_g character [217–220]. Thus, we are confronted with the fact that at about 1.5 eV below the Fermi level, we find the lower Hubbard bands of d^1 systems as well as the in-gap states of oxygen-deficient d^0 systems. In view of these observations one may unavoidably wonder (and worry), despite the great success of LDA+DMFT methods, whether the putative Hubbard satellite of SrVO₃ might also originate from oxygen vacancies states. Moreover, one should also worry about the possibility of these extrinsic states affecting the features of the conduction band dispersion. These are the questions that motivated us to take a closer look at the presumably simplest correlated system of SrVO₃.

In order to provide context for our theoretical investigations, we present the results of the systematic photoemission study of SrVO₃ by the group of Santander-Syro *et al.*, to demonstrate dramatic consequences in the spectra due to production of oxygen vacancies. The ARPES experiments will show that the UV/X rays used for measurements can produce a large enhancement, of almost an order of magnitude, of the peak at -1.5 eV, similar to the effect observed in d^0 oxide insulators [210–212, 215, 221]. Despite these significant effects on the energy states around the Mott-Hubbard band, the experiments are able to determine the bulk SrVO₃ photoemission spectrum *in the zero-vacancy limit*, where a clear signal of the correlated Hubbard band remains. We support the interpretation of the experimental data by means of our LDA+DMFT calculations on SrVO₃ *with oxygen vacancies*. Consistent with the experimental data, our calculations show that oxygen vacancies produce states (of e_g symmetry) at energies near the Hubbard satellite. While our study provides definite evidence of a correlated Hubbard band in SrVO₃ as predicted by LDA+DMFT, it also underlines the significant effects due to oxygen vacancies, which may also affect photoemission data in other TMOs.

9.2 Computational and experimental details

For the DFT calculations in the local density approximation (LDA) and LDA+DMFT calculations we consider a $2 \times 2 \times 3$ supercell where two adjacent oxygen atoms to a vanadium have been removed. This leads to a stripe-like configuration of vacancies with a concentration of $2/36 \approx 5.56\%$. The internal atomic positions of this structure has been relaxed using the GPAW code [222]. For the LDA+DMFT calculations we used the WIEN2K [161] implementation in the local density approximation in combination with a continuous-time quantum Monte Carlo (CTQMC) impurity solver in the hybridization expansion [8] from the ALPS [9, 164] project. We projected the Bloch wave functions onto localized V $3d$ orbitals [36, 163] (see Chapter 6.2) in the unit cell, leading to a set of 6 inequivalent impurities for the two vacancy structure. Within the DMFT approximation we assume that (i) the multiple impurity atoms only hybridize with an effective bath that is determined self-consistently and (ii) the intersite hybridization to be small. This allows us to solve the impurity problems separately and obtain the local Selfenergy for all 6 vanadium atoms, as described in Chap-

ter 6.5. The projection comprises the V t_{2g} and e_g orbitals in the energy window $[-1.5, 6.0]$ eV. The calculations were performed for the inverse temperature $\beta = 40 \text{ eV}^{-1}$ (290 K) with the interaction parameters used in the definition of the Slater integrals [85] with average $U = 2.5 \text{ eV}$ and $J_H = 0.6 \text{ eV}$ (see Chapter 6.6). For the double counting correction we used the FLL [82, 167] scheme and we checked that different values of the double counting only lead to small quantitative changes in the spectral function. We performed analytic continuation directly on the impurity Self-energies $\Sigma_a(i\omega_n)$ by stochastic analytic continuation [93] to obtain $\Sigma_a(\omega)$ on the real axis. In the following we always show the atom- and orbital resolved spectral function of the t_{2g} and e_g states summed over all atoms.

In this chapter we also included the effects of bandwidth renormalization due to dynamically screened Coulomb interactions using a low-energy effective model with an effective Hamiltonian

$$H_{eff} = - \sum_{ij\sigma} Z_B t_{ij} d_{i\sigma}^\dagger d_{j\sigma} + U \sum_i d_{i\uparrow}^\dagger d_{i\uparrow} d_{i\downarrow}^\dagger d_{i\downarrow}, \quad (9.2.1)$$

with the screened Hubbard interaction U , where the renormalization parameter Z_B mimics the effective bandwidth renormalization introduced by a frequency dependent screened Coulomb interaction. This approach has been suggested in Ref. [56], and proved to be a good approximation to the full treatment of the dynamically screened Coulomb interaction. For the bandwidth renormalization factor we used $Z_B = 0.7$ [56].

The bulk crystalline (001) oriented SrVO_3 thin films were grown by pulsed laser deposition (PLD) either at the GEMaC laboratory, then measured at the CASSIOPEE beamline of Synchrotron SOLEIL, or in a PLD chamber directly connected to the ARPES setup at beamline 2A of KEK-Photon Factory (KEK-PF) [55, 223] by the group of Santander-Syro *et al.* Directions and planes are defined in the cubic unit cell of SrVO_3 . We note $[hkl]$ the crystallographic directions in real space, $\langle hkl \rangle$ the corresponding directions in reciprocal space, and (hkl) the planes orthogonal to those directions. The indices h , k , and l of Γ_{hkl} correspond to the reciprocal lattice vectors of the cubic unit cell of SrVO_3 . Further details about the experimental setup, sample growth and measurements can be found in the original publication [224].

9.3 Results

9.3.1 Experimental results

Figure 9.1(b) shows the integrated photoemission spectra of SrVO_3 as a function of the UV dose, measured at SOLEIL under the same conditions of light brilliance of any standard ARPES experiment at a third-generation synchrotron. The measurements were done by continuously irradiating the sample with $h\nu = 33 \text{ eV}$ photons while recording the spectra as a function of irradiation time, with an accumulation time of about 2 minutes per spectrum. The blue and black curves show spectra for the lowest and highest measured doses, obtained respectively after ~ 2 minutes and ~ 2 hours of irradiation. These data clearly demonstrate that the very UV/X rays used for photoemission experiments can effect radical changes in the measured spectra of SrVO_3 . Note in fact that a similar effect has been observed for VO_2 [225]. In particular, from Fig. 9.1(b) it can be observed that the amplitude of the in-gap state at -1.5 eV , and more significantly, the ratio of in-gap to quasiparticle (QP) amplitudes, strongly increase with increasing UV dose, going from about 1 : 3 in a pristine sample to more than 2 : 1 in a heavily irradiated sample. Importantly, note that the QP peak position remains basically dose-independent, implying that the carriers created by the UV/X irradiation do not significantly dope the conduction band, and form dominantly localized states. This is confirmed in Fig. 9.1(c), which shows that the Fermi momenta of the QP band, given by the peaks' positions in the momentum distribution curves (MDCs) at E_F , are also dose-independent. Thus, the observed increase in intensity of the in-gap state upon UV irradiation *cannot* be ascribed to a change in filling of the conduction band, which could have affected the electron correlations. Instead, this unambiguously shows the light-assisted formation of localized defect states at essentially the same energy

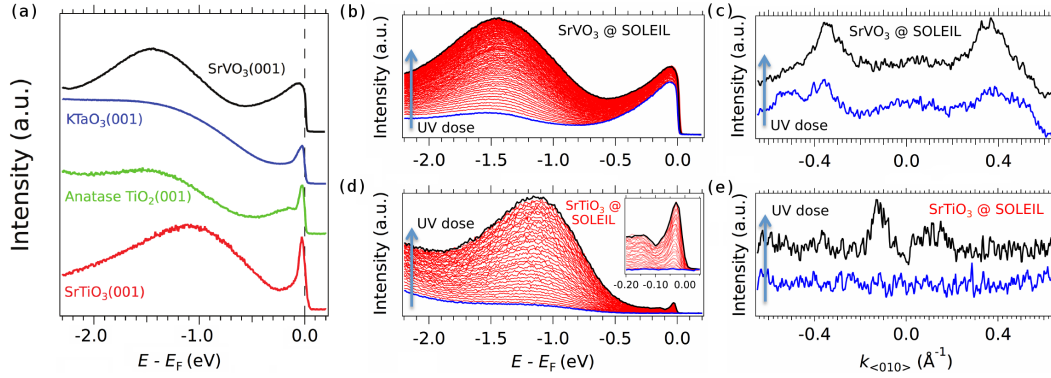


Figure 9.1: (a) Integrated UV photoemission spectra for various perovskite oxides, showing a quasi-particle peak (QP) at E_F and an in-gap state at energies between -1 eV and -1.5 eV. For SrVO₃ (upper black curve), a correlated-electron metal, the QP peak corresponds to the bulk conduction band, and as will be shown further, the in-gap state is a superposition of the lower Hubbard band and localized electronic states associated to oxygen vacancies. For the other d^0 oxides, such as KTaO₃ (blue curve), anatase TiO₂ (green curve), or SrTiO₃ (red curve), the QP peak and in-gap state correspond respectively to a confined quasi-2D electron gas at the sample surface and to localized states, all formed by oxygen vacancies. The crystal orientation (normal to the samples' surface) is indicated in all cases.

(b) Photoemission spectra of SrVO₃ as a function of UV dose, measured at Synchrotron SOLEIL. The energy distribution curves (EDCs) were extracted from raw ARPES data around the Γ_{002} point integrated along the $k = \langle 010 \rangle$ direction, obtained by the group of Santander-Syro et al.. (c) Corresponding momentum distribution curves (MDCs) integrated over 50 meV below E_F . Peaks in the MDCs indicate the Fermi momenta. (d, e) Same as (b, c) for SrTiO₃. The filling of a 2DEG upon UV irradiation is evidenced by the formation of QP peaks in the EDCs and MDCs at E_F (inset of (c) and panel (d), respectively). All data were taken at 20 K.

as that of the expected intrinsic lower Hubbard band, which should then resemble the in-gap peak observed at the lowest UV doses.

In fact, as mentioned previously, it is well established that strong doses of UV/X rays create a large concentration of oxygen vacancies in several d^0 perovskites [209–216, 226]. As illustrated in Figs. 9.1(d, e) for the case of SrTiO₃, the progressive doping of the surface region with oxygen vacancies, due to synchrotron UV irradiation, has two effects: formation of a very intense in-gap state at about -1.3 eV, and, in contrast to SrVO₃, simultaneous creation of a sharp QP peak at E_F corresponding to a confined quasi-2D electron gas (2DEG) at the samples' surface. The effective mass of such 2DEG, precisely determined by ARPES, matches the mass expected from density functional theory calculations [210, 211, 227, 228]. Thus, as in SrVO₃, the increase in intensity of the in-gap state observed in SrTiO₃ upon UV/X irradiation cannot be due to an onset or increase of electron correlations, and should be ascribed to an extrinsic effect.

This leads to the conclusion that in SrVO₃ exposure to synchrotron UV/X rays creates oxygen vacancies, which are in turn responsible for the extrinsic increase in intensity of the in-gap state evidenced by our measurements. This effect, never discussed or taken into account in the literature before our investigation, can seriously obscure the determination of the spectral function of this model system, thus hampering the advancement of valid theories for correlated-electron systems.

All the previous findings imply that the correct experimental determination of the vacancy-free photoemission spectrum of SrVO₃ should (i) use samples that from the beginning have the lowest possible concentration of oxygen vacancies, and (ii) use doses of UV or X-ray light low enough to avoid light-induced changes in the measured spectra. To this end, we show the results of the measurement of SrVO₃ thin-films grown directly *in-situ* at beamline 2A of KEK-PF by our experimental collaborators. As mentioned before, the growth protocol of such thin films minimizes the forma-

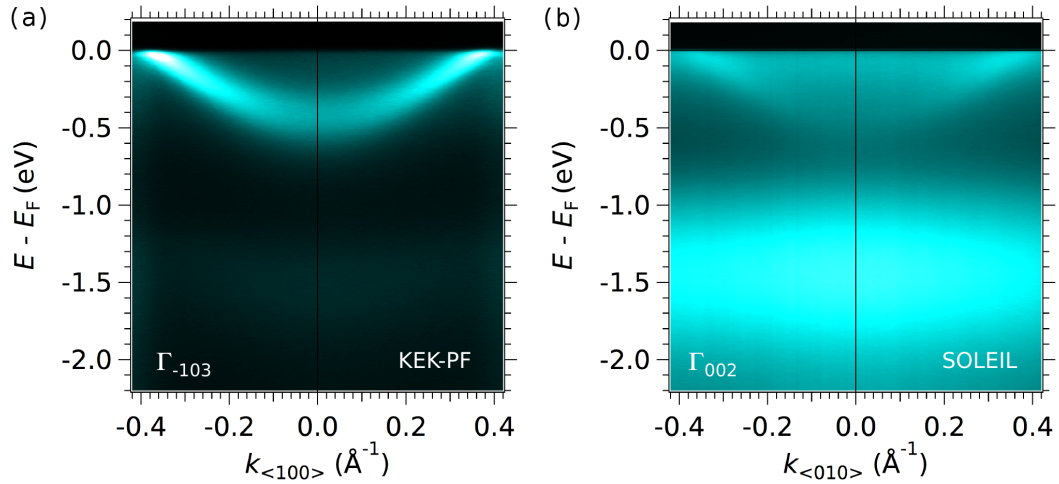


Figure 9.2: (a) Energy-momentum ARPES intensity map measured at KEK-PF with a low UV dose on an SrVO_3 sample prepared in-situ, using a well-established protocol to minimize the formation of oxygen vacancies (see main text). Note that due to the choice of light polarization, the heavy bands along (100) are not observed and only the contribution of the light d_{xy} band is detected. (b) Same as (a) after a strong UV irradiation dose, measured at SOLEIL, and typical of modern third-generation synchrotrons. All data were taken at 20 K.

tion of vacancies, while the UV light brilliance at KEK-PF is ~ 100 times smaller than the one in Figs. 9.1(b, c) from measurements at SOLEIL. Under these conditions the spectra did not change with time, even after several hours of measurements.

The resulting energy-momentum ARPES map is shown in Fig. 9.2 (a). One clearly observes the dispersing QP band along with the weaker intensity in-gap state, corresponding to the intrinsic lower Hubbard band, as reported in previous works [54]. By contrast, Fig. 9.2 (b) shows the momentum-resolved electronic structure of a sample, measured at SOLEIL, that was intensively irradiated. There, the peak at -1.5 eV becomes broader, more intense, and non-dispersive – all characteristic signatures of a high random concentration of oxygen vacancies.

9.3.2 Theoretical results

To rationalize from a microscopic point of view the influence of oxygen vacancies on the electronic structure of SrVO_3 , we performed charge self-consistent LDA+DMFT calculations for bulk SrVO_3 and various relaxed oxygen-deficient SrVO_3 supercells. The latter are computationally demanding calculations. We shall focus here on the case of a $2 \times 2 \times 3$ supercell with two oxygen vacancies located at opposite apical sites of one vanadium atom, as shown in the inset of Fig. 9.3 (b). We use such vacancy arrangement as it is the prototypical one for d^0 compounds [227].

For our LDA+DMFT calculations we chose values of $U = 2.5$ eV and $J = 0.6$ eV for vanadium and included the effects of bandwidth renormalization due to dynamically screened Coulomb interactions as described in the previous section. The unrenormalized data LDA+DMFT are shown in the next section.

In Figs. 9.3(a) and (c) we show, respectively, the results of the k -integrated and k -resolved spectral functions for bulk SrVO_3 without oxygen vacancies. We find the expected features of a t_{2g} quasiparticle peak at the Fermi level and a lower Hubbard band at negative energies of the same t_{2g} nature, in agreement with the photoemission spectra in Figs. 9.1(b) and 9.2 (a). The light band at E_F along $k_{<100>}$ (see Fig. 9.3(c)), consists of two degenerate bands of d_{xy} and d_{xz} characters, while the heavy band along the same direction has d_{yz} character. While comparing with the measured k -resolved spectral function, Fig. 9.2(a), one should bear in mind that along Γ -X (or Γ -Y) the heavy d_{yz} (or d_{xz}) bands are silenced by dipole-transition selection rules in the experiment [210]. Inclu-

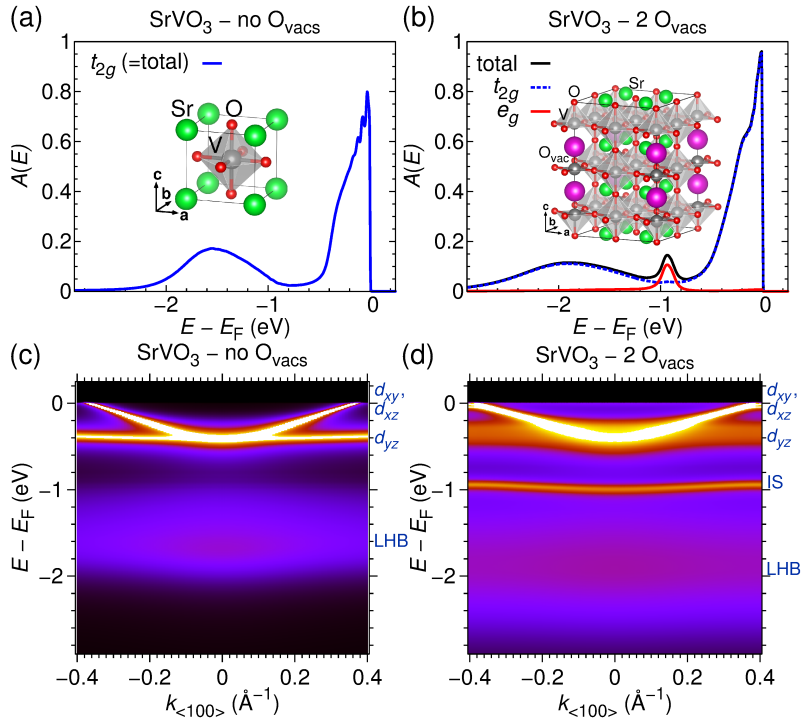


Figure 9.3: LDA+DMFT results for SrVO₃ including bandwidth renormalization effects [56]. (a) k -integrated spectral function for bulk SrVO₃. The V t_{2g} orbitals show a quasiparticle peak at E_F and a lower Hubbard band at -1.6 eV. (b) Spectral function for the $2 \times 2 \times 3$ supercell of SrVO₃ with two oxygen vacancies. An additional non-dispersive V e_g vacancy state originating from the V atom neighboring the oxygen vacancies lead to a sharp peak below the Fermi level at -1.1 eV. The V t_{2g} orbitals show a quasiparticle peak at E_F and a lower Hubbard band at -1.8 eV. (c) and (d) show the corresponding spectral functions (multiplied by a Fermi-Dirac function at 20 K) along the X- Γ -X path.

sion of bandwidth renormalization [56] renders the lower Hubbard band at an energy (-1.6 eV) in reasonable agreement with experiment (-1.5 eV). Please note the difference in position of the lower Hubbard band compared to Fig. 6.2 in Chapter 6.3 which was obtained without the inclusion of the effective bandwidth renormalization. We adopted typical values for U and J_H from the literature. We did not attempt to further optimize the values to get a better quantitative agreement with the experimental data, due to two reasons. Firstly, the heavy numerical cost, and secondly, as we show next in the calculations with oxygen vacancies, the adopted values facilitate the distinct visualization of the contributions from the Hubbard and localized states to the incoherent peak at ~ -1.5 eV.

The removal of oxygen atoms in the system leads to the donation of two electrons per oxygen to its surrounding. Already at the level of density functional theory in the local density approximation (see Fig. 9.4), we find that most of the charge coming from the additional electrons is transferred to the $3d_{z^2}$ orbitals of the neighbouring V atom, developing into a sharp peak of e_g symmetry located around -1.1 eV, *i.e.* at an energy close to the position of the experimentally observed oxygen vacancy states. In analogy to the experimental average over many lattice sites, note that averaging among various supercells with different oxygen vacancy locations and concentrations (what is beyond the scope of this work) would result in a wider in-gap e_g band, as demonstrated for the case of SrTiO₃ (see Fig. 3 of Ref. [218]) and for some cases in SrVO₃ (see Fig. 9.5). By including electronic correlations within (bandwidth renormalized) LDA+DMFT we then see that all the experimental observations qualitatively emerge. In fact, the conducting t_{2g} orbitals develop a lower Hubbard band peaked at energies about -1.8 eV (Figs. 9.3(b) and (d)) similar to the bulk case without oxygen

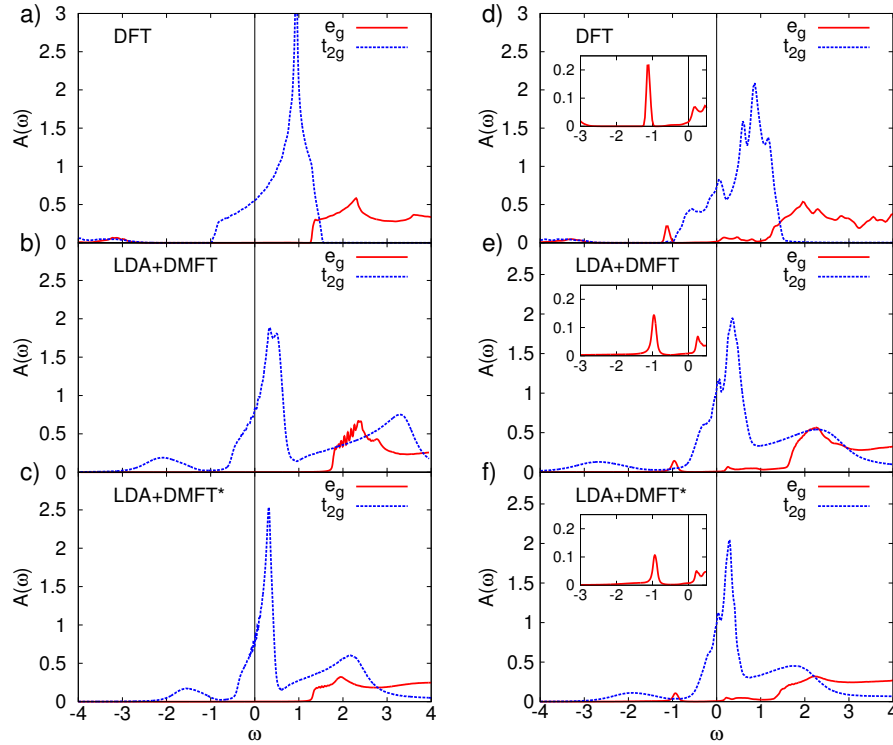


Figure 9.4: Comparison for bulk SrVO_3 between (a) the DFT result, (b) the LDA+DMFT result, and (c) the LDA+DMFT including an effective treatment of the dynamical Coulomb interacting screening indicated by a *. (d-f): Same comparison for the 2 vacancy structure of SrVO_3 . The main effect of the renormalization factor is a shift of the upper and lower t_{2g} Hubbard bands towards the Fermi level, yielding a better agreement with experiment.

vacancies. Most notably, this lower Hubbard satellite does not increase in amplitude with the introduction of vacancies, but rather broadens. In addition, the oxygen-vacancy defect states situated at about -1 eV remain qualitatively unchanged by the correlation effects, but experience a broadening with respect to the pure LDA case. This is in agreement with the photoemission data measured by our experimental collaborators, evidencing that the increase in intensity of the in-gap state in the oxygen-deficient SrVO_3 is not to be attributed to an increase in population of the lower Hubbard satellite, but instead to the manifestation of vacancy states of e_g character.

9.3.3 Standard LDA+DMFT vs. LDA+DMFT including dynamical screening

In Fig. 9.4 we show a comparison between standard DFT, “standard” LDA+DMFT and the LDA+DMFT approach including the effective screening of the Coulomb interaction for a)-c) bulk SrVO_3 and d)-f) the two vacancy structure of SrVO_3 . The main effect of including the Coulomb interaction screening via this approach is a shift of the upper and lower t_{2g} Hubbard bands towards the Fermi level, originating from the effective reduction of bandwidth. Compared to experiment, “standard” LDA+DMFT consistently locates the lower Hubbard band at higher binding energies, in both the bulk and vacancy structure, whereas the effective model yields a much better agreement. Especially in the bulk system the position of the lower Hubbard band is brought to a good agreement.

Finally, the calculations with oxygen vacancies produce a ladder of heavy bands near E_F , that originate from the non-equivalence in all the vanadium atoms of the super-cell contributing t_{2g} bands near the Fermi level. This V non-equivalence is due to the presence of oxygen vacancies that lower the symmetry. In the more realistic case with larger cells, only the in-gap e_g states of the V near the

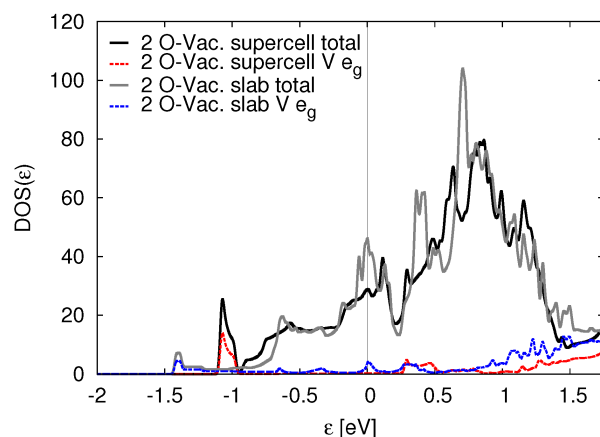


Figure 9.5: GGA Total and Vanadium e_g resolved density of states (DOS) for $2 \times 2 \times 3$ bulk and the $2 \times 2 \times 4$ slab structures with two oxygen vacancies. See text for details.

vacancy/vacancies would produce a significant spectral feature, while essentially all the vanadium atoms of the cell would be equivalent, and the effects of the t_{2g} states coming from the few non-equivalent vanadium atoms around the vacancy would be negligible. At present, such a calculation is however computationally infeasible in the framework of LDA+DMFT.

9.3.4 Comparison of DFT results between different oxygen vacancy configurations

In order to strengthen the claim regarding the position of the in-gap states, we have also constructed a stoichiometric $2 \times 2 \times 4$ slab of SrVO₃ with 20Å of vacuum and two oxygen vacancies in the VO₂ surface. We have relaxed this structure with the Vienna Ab initio simulation package (VASP) [229]. Both for the $2 \times 2 \times 3$ bulk and the $2 \times 2 \times 4$ slab structures with two oxygen vacancies we have performed GGA calculations with the full potential local orbital (FPLO) method [190]. The calculations have been converged with $12 \times 12 \times 12$ k points in the bulk and $8 \times 8 \times 8$ k points in the slab case. As shown in Fig. 9.5, we find that the in-gap state for the slab appears around -1.5 eV, and shows a weak dispersion due to the finite size of the slab considered, while the in-gap state for the supercell is at -1 eV. Additionally, we also checked the effects of correlations on that in-gap state via GGA+U calculations (see Chapter 2.5), which showed no significant effect on its position. Therefore, we conclude that also LDA+DMFT will not change the position of the in-gap state, as we have already found to be the case in all other calculations we performed. So the lower Hubbard band will indeed fall in the same position as the in-gap state of vanadium e_g character when considering an average over various spatial distributions of vacancies.

9.4 Conclusion

In conclusion we have found that oxygen vacancy states, which are created by UV/X-ray irradiation of the sample, emerge at energies close to the Hubbard satellite in this material and contribute with significant weight to the total spectral function. This dramatically affects the measured line-shape of the Mott-Hubbard band and the ratio of intensities between the quasi-particle and the Mott-Hubbard peaks.

In the experimental investigations performed by the group of Santander-Syro *et al.* it was possible to extract the photoemission spectrum of the bulk SrVO₃ system in the zero-vacancy limit, confirming the presence of a lower Hubbard band also in the bulk system. This is a satisfactory result since it showed the validity of previous LDA+DMFT investigations of this material that so far

had never considered oxygen vacancies in the calculation. Furthermore, we could show that within a multi-vacancy supercell calculation LDA+DMFT is able to capture both the contributions of the incoherent spectral weight arising from the lower Hubbard band and as well as the coherent states induced by oxygen vacancies.

These results will have important implications for the interpretation of spectral properties also in other correlated materials that are prone to the formation of vacancies. Furthermore, LDA+DMFT has proven to be a valuable tool for the explanation of experimental observations also for the study of intricate structural configurations with multiple non-equivalent atoms, where both effects of strong and weak electronic correlations are present.

Chapter 10

Summary and Outlook

In this thesis we have introduced the LDA+DMFT method to obtain insight into the electronic properties of strongly correlated systems and applied this method to the rather new type of iron-pnictide superconductors.

In Chapter 2 we started with an introduction into density functional theory (DFT), today's state-of-the-art method for electronic structure calculations and discussed the most common approximations that are applied to the Coulomb interaction. In this context we have seen that DFT has certain weaknesses regarding the correct description of strongly correlated systems, which mainly stem from the approximation of the exchange-correlation functional that is derived from a homogeneous electron gas and, therefore, underestimates electronic correlations.

In preparation for an improved treatment of electronic correlations we introduced the Green's function formalism in Chapter 3. Green's functions proved to be a very useful tool to clearly identify the difference between a non-interacting and an interacting system in the form of a Selfenergy and the relation between them. We discussed the peculiarity of the imaginary time formalism and how it can simplify the calculation of interacting Green's functions.

Connected to that, we dedicated Chapter 4 to the problem of analytic continuation that arises when we extract observable properties from Green's functions defined on the imaginary time or frequency axis. Since this problem is very ill-conditioned, even small numerical noise in the input can lead to unphysical results in the observable properties. Therefore, sophisticated probabilistic or stochastic approaches are needed, from which we discussed the most common, the maximum entropy method and the more general approach of the stochastic analytic continuation method.

With the Green's function formalism as a background, we were able to introduce the dynamical mean-field theory (DMFT) in Chapter 5 as an approach to solve strongly correlated lattice models. We saw that in the DMFT limit of infinite dimensions or infinite number of nearest-neighbours the Selfenergy becomes momentum-independent and the lattice model can be mapped onto an effective Anderson impurity model which leads to a tremendous simplification of the problem. Being non-perturbative in both the kinetic energy and Coulomb interaction, the DMFT turned out to be well suited for the investigation of strongly correlated systems.

In Chapter 6 we then discussed how DMFT can be applied to investigate realistic systems within the LDA+DMFT method. This method combines density functional theory for obtaining an effective lattice model with parameters that describes the real system with high accuracy and DMFT for solving this effective model and properly accounting for electronic correlations. We further discussed the difficulties that arise in the actual implementation, like obtaining a local basis from the Kohn-Sham wave functions in DFT, the choice of the energy window of states taken into account, the double counting problem and how to obtain observables like the Fermi surface from the converged Green's function.

We then studied the hole-doped iron-pnictide superconductor KFe_2As_2 within LDA+DMFT and presented our results in Chapter 7. We found that KFe_2As_2 is a rather strongly correlated metal, where DFT is incapable of explaining the electronic structure found in photoemission experiments. The treatment of electronic correlations within DMFT improved the agreement with experiment con-

siderably and allowed us to obtain the correct Fermi surface topology in this system. The modified shape of the Fermi surface cylinders also resulted in an improved description of the de Haas-van Alphen frequencies.

We then continued the study of the hole-doped 122 family of iron-pnictide superconductors based on the isovalent series (K,Rb,Cs)Fe₂As₂ in Chapter 8, which allowed for a unique investigation of the effect of pressure and lattice expansion on electronic correlations. While the starting point system KFe₂As₂ already shows significant effects of correlation, the strength of correlations and especially the incoherence properties increased dramatically as the system was substituted with atoms of increasing radius. We attribute these changes to an increase of the localization of the iron 3*d* orbitals caused by the lattice expansion, confirmed by the reduced hopping amplitudes between the iron atoms. We showed that these systems are so-called Hund's metals, where the Hund's coupling J_H is responsible for a suppression of orbital fluctuations that lead to a highly incoherent bad metal behaviour in these systems which are still not in direct proximity of a Mott transition.

Finally, in Chapter 9 we return to one of the best studied system within LDA+DMFT, the cubic perovskite SrVO₃, which was known so far to show effects of strong electronic correlations in form of an upper and lower Hubbard band. Since related systems are known for oxygen vacancies being responsible for the emergence of an additional state at lower energies, we considered the question of whether the low energy feature in SrVO₃ might actually also be caused by oxygen vacancies rather than strong electronic correlations. To answer this question, we employed sophisticated LDA+DMFT calculations including oxygen vacancies in collaboration with an experimental group performing photoemission experiments. LDA+DMFT turned out to be well suited for this problem since, being non-perturbative in both the kinetic energy and Coulomb interaction, it can describe weakly as well as strongly correlated systems on equal footing. From our results we were able to conclude that in the vacancy-free case there indeed does exist a lower Hubbard band, while in the realistic case of a low vacancy concentration a superposition of a lower Hubbard band and an additional in-gap state introduced by oxygen vacancies at the same energy are present.

As we have seen, LDA+DMFT can provide an important contribution to an improved understanding of strongly correlated systems. This was made possible by going to the limit of infinite dimensions, which resulted in a momentum-dependent Selfenergy, simplifying the problem significantly. Therefore, non-local fluctuations are completely neglected. While this approximation is not severe for many realistic systems with high coordination number, spatial fluctuations, *e.g.* in the vicinity of a phase transition, are important and are necessary for a correct description of the physical properties. Especially in low-dimensional systems this neglect of spatial fluctuations can lead to significant deficits, like in the two-dimensional Hubbard model where standard DMFT drastically underestimates the critical interaction strength of the Mott transition [230–234].

There are a number of possible extensions to include spatial fluctuations and thus reintroduce the momentum dependence of the Selfenergy. Most of them restrict the range of these fluctuations or treat them perturbatively around the local limit, since the computational cost usually scales exponentially with higher orders.

Cluster DMFT approaches divide the lattice system into separate cells that consist of several sites, where non-local correlations are considered only inside each cell but not between cells [116, 235, 236]. Another similar approach which works in momentum space is the dynamical cluster approximation [237, 238]. It divides the Brillouin zone into patches, where inside each patch the Selfenergy is constant but can be different for each patch due to the different parts of the Brillouin zone included.

For perturbative expansions around the local limit, the most direct approach is to add all diagrams to next order in $1/d$, as proposed in [239]. Another diagrammatic expansion is the dual fermion approach [240], or the dynamical vertex approximation (D Γ A) [241, 242].

Apart from the local approximation, LDA+DMFT still faces some fundamental problems by construction, like that of the double counting discussed in Chapter 6.4. A possible alternative that replaces the LDA part in LDA+DMFT by a purely diagrammatic approach is the GW+DMFT method [243, 244] based on Hedin's GW approximation [245]. It has the advantage of being able to

identify the correlations accounted for in both GW and DMFT, thus in principle removing the double counting problem, as well as treating the non-local parts of the Coulomb interaction.

Another aspect is the screening of the Coulomb interaction by all states that are not treated as correlated. This is in principle a dynamical process, since the screening is for example less efficient at high frequencies, so already the local U term picks up a frequency dependence [127, 130]. Inclusion of frequency dependent interactions in the DMFT impurity model is possible and often combined with GW+DMFT [56, 128, 129].

While all these issues and difficulties are very important and decisive for the reliability of LDA+DMFT, it has already proven to be quite a robust and promising method that lead to a significant improvement of our understanding of correlated electronic systems. Still, it is important that further work is done on resolving the issues states above to secure the future success of the LDA+DMFT method. Compared to the well established DFT method, it is still a young and evolving field and will for sure mature over time as its popularity grows.

Appendix

In order to evaluate the high frequency correction terms analytically, we use the result from Cvijović and Klinowski [246]

$$\frac{\pi^{2k}}{(-1)^k 4(2k-1)!} E_{2k-1}(x) = \sum_{n=0}^{\infty} \frac{\cos((2n+1)\pi x)}{(2n+1)^{2k}} \quad (10.1)$$

$$\frac{\pi^{2k+1}}{(-1)^k 4(2k)!} E_{2k}(x) = \sum_{n=0}^{\infty} \frac{\sin((2n+1)\pi x)}{(2n+1)^{2k+1}}, \quad (10.2)$$

where $x \in (0, 1)$ and $E_k(x)$ are the Euler polynomials, with the first given as

$$E_0(x) = 1 \quad (10.3)$$

$$E_1(x) = x - \frac{1}{2} \quad (10.4)$$

$$E_2(x) = x(x-1) \quad (10.5)$$

$$E_3(x) = \frac{1}{4}(2x-1)(2x^2-2x-1). \quad (10.6)$$

For $\tau \in (0, \beta)$ we evaluate the summations from above as

$$\frac{1}{\beta} \sum_{n=-\infty}^{\infty} e^{-i\omega_n \tau} \frac{c_1}{i\omega_n} = \frac{c_1}{\beta} \sum_{n=0}^{\infty} \frac{e^{-i\omega_n \tau}}{i\omega_n} + \frac{e^{i\omega_n \tau}}{-i\omega_n} \quad (10.7)$$

$$= \frac{c_1}{\beta} \sum_{n=0}^{\infty} \frac{e^{-i\omega_n \tau} - e^{+i\omega_n \tau}}{i\omega_n} \quad (10.8)$$

$$= \frac{c_1}{\beta} \sum_{n=0}^{\infty} \frac{-2i \sin(\omega_n \tau)}{i\omega_n} \quad (10.9)$$

$$= -\frac{2c_1}{\beta} \sum_{n=0}^{\infty} \frac{\sin(\omega_n \tau)}{\omega_n} \quad (10.10)$$

$$= -\frac{2c_1}{\pi} \sum_{n=0}^{\infty} \frac{\sin((2n+1)\pi \frac{\tau}{\beta})}{(2n+1)^1} \quad (10.11)$$

$$= -\frac{2c_1}{\pi} \frac{\pi^{2 \cdot 0 + 1}}{(-1)^0 4(0)!} E_0\left(\frac{\tau}{\beta}\right) \quad (10.12)$$

$$= -\frac{c_1}{2} \quad (10.13)$$

$$\frac{1}{\beta} \sum_{n=-\infty}^{\infty} e^{-i\omega_n \tau} \frac{c_2}{(i\omega_n)^2} = \frac{2c_2}{\beta} \sum_{n=0}^{\infty} \frac{\cos(\omega_n \tau)}{(i\omega_n)^2} \quad (10.14)$$

$$= -\frac{2c_2}{\beta} \frac{\beta^2}{\pi^2} \sum_{n=0}^{\infty} \frac{\cos((2n+1)\pi\frac{\tau}{\beta})}{(2n+1)^2} \quad (10.15)$$

$$= -\frac{2c_2\beta}{\pi^2} \frac{\pi^2}{(-1)^{14}(2-1)!} E_{2-1}\left(\frac{\tau}{\beta}\right) \quad (10.16)$$

$$= \frac{c_2\beta}{2} \left(\frac{\tau}{\beta} - \frac{1}{2}\right) \quad (10.17)$$

$$= \frac{c_2}{4} (2\tau - \beta) \quad (10.18)$$

$$\frac{1}{\beta} \sum_{n=-\infty}^{\infty} e^{-i\omega_n \tau} \frac{c_3}{(i\omega_n)^3} = \frac{c_3}{\beta} \sum_{n=0}^{\infty} \frac{-2i \sin(\omega_n \tau)}{(i\omega_n)^3} \quad (10.19)$$

$$= \frac{2c_3}{\beta} \sum_{n=0}^{\infty} \frac{\sin(\omega_n \tau)}{\omega_n^3} \quad (10.20)$$

$$= \frac{2c_3\beta^2}{\pi^3} \sum_{n=0}^{\infty} \frac{\sin((2n+1)\frac{\tau}{\beta})}{(2n+1)^3} \quad (10.21)$$

$$= \frac{2c_3\beta^2}{\pi^3} \frac{\pi^{2+1}}{(-1)^{14}(2)!} E_2\left(\frac{\tau}{\beta}\right) \quad (10.22)$$

$$= -\frac{c_3\beta^2}{4} \frac{\tau}{\beta} \left(\frac{\tau}{\beta} - 1\right) \quad (10.23)$$

$$= \frac{c_3}{4} \tau (\beta - \tau) \quad (10.24)$$

$$\frac{1}{\beta} \sum_{n=-\infty}^{\infty} e^{-i\omega_n \tau} \frac{c_4}{(i\omega_n)^4} = \frac{2c_4}{\beta} \sum_{n=0}^{\infty} \frac{\cos(\omega_n \tau)}{(i\omega_n)^4} \quad (10.25)$$

$$= \frac{2c_4}{\beta} \frac{\beta^4}{\pi^4} \sum_{n=0}^{\infty} \frac{\cos((2n+1)\pi\frac{\tau}{\beta})}{(2n+1)^4} \quad (10.26)$$

$$= \frac{2c_4\beta^3}{\pi^4} \frac{\pi^{2 \cdot 2}}{(-1)^{24}(2 \cdot 2 - 1)!} E_{2 \cdot 2 - 1}\left(\frac{\tau}{\beta}\right) \quad (10.27)$$

$$= \frac{c_4\beta^3}{12} \left(\frac{1}{4}(2\frac{\tau}{\beta} - 1)(2\frac{\tau^2}{\beta^2} - 2\frac{\tau}{\beta} - 1)\right) \quad (10.28)$$

$$= \frac{c_4}{48} (2\tau - \beta)(2\tau^2 - 2\tau\beta - \beta^2) \quad (10.29)$$

For $\tau \in (-\beta, 0)$ we can reuse the above equations and get

$$\frac{1}{\beta} \sum_{n=-\infty}^{\infty} e^{-i\omega_n(-|\tau|)} \frac{c_1}{i\omega_n} = - \left(\frac{1}{\beta} \sum_{n=-\infty}^{\infty} e^{-i\omega_n|\tau|} \frac{c_1}{i\omega_n} \right)^* \quad (10.30)$$

$$= - \left(-\frac{c_1}{2} \right) \quad (10.31)$$

$$= \frac{c_1}{2} \quad (10.32)$$

$$\frac{1}{\beta} \sum_{n=-\infty}^{\infty} e^{-i\omega_n(-|\tau|)} \frac{c_2}{(i\omega_n)^2} = \left(\frac{1}{\beta} \sum_{n=-\infty}^{\infty} e^{-i\omega_n|\tau|} \frac{c_2}{(i\omega_n)^2} \right)^* \quad (10.33)$$

$$= \frac{c_2}{4} (2\tau - \beta) \quad (10.34)$$

$$\frac{1}{\beta} \sum_{n=-\infty}^{\infty} e^{-i\omega_n(-|\tau|)} \frac{c_3}{(i\omega_n)^3} = - \left(\frac{1}{\beta} \sum_{n=-\infty}^{\infty} e^{-i\omega_n|\tau|} \frac{c_3}{(i\omega_n)^3} \right)^* \quad (10.35)$$

$$= -\frac{c_3}{4} \tau (\beta - \tau) \quad (10.36)$$

$$\frac{1}{\beta} \sum_{n=-\infty}^{\infty} e^{-i\omega_n(-|\tau|)} \frac{c_4}{(i\omega_n)^4} = \left(\frac{1}{\beta} \sum_{n=-\infty}^{\infty} e^{-i\omega_n|\tau|} \frac{c_4}{(i\omega_n)^4} \right)^* \quad (10.37)$$

$$= \frac{c_4}{48} (2\tau - \beta)(2\tau^2 - 2\tau\beta - \beta^2) \quad (10.38)$$

This result could also be obtained by using the property of the imaginary time Green's function $F(-\tau) = -F(\beta - \tau)$ and evaluating the results from above at $\beta - \tau$ with an overall sign change.

References

- [1] P. Hohenberg and W. Kohn. Inhomogeneous electron gas. *Physical Review*, 136, 1964.
- [2] Martin C. Gutzwiller. Effect of correlation on the ferromagnetism of transition metals. *Phys. Rev. Lett.*, 10:159–162, Mar 1963.
- [3] J. Hubbard. Electron correlations in narrow energy bands. *Proceedings of the Royal Society of London A: Mathematical, Physical and Engineering Sciences*, 276(1365):238–257, 1963.
- [4] Junjiro Kanamori. Electron correlation and ferromagnetism of transition metals. *Progress of Theoretical Physics*, 30(3):275–289, 1963.
- [5] Elliott H. Lieb and F. Y. Wu. Absence of mott transition in an exact solution of the short-range, one-band model in one dimension. *Phys. Rev. Lett.*, 20:1445–1448, Jun 1968.
- [6] Walter Metzner and Dieter Vollhardt. Correlated lattice fermions in $d = \infty$ dimensions. *Phys. Rev. Lett.*, 62:324–327, Jan 1989.
- [7] Antoine Georges and Gabriel Kotliar. Hubbard model in infinite dimensions. *Phys. Rev. B*, 45:6479–6483, Mar 1992.
- [8] Philipp Werner, Armin Comanac, Luca de’ Medici, Matthias Troyer, and Andrew J. Millis. Continuous-time solver for quantum impurity models. *Phys. Rev. Lett.*, 97:076405, Aug 2006.
- [9] Emanuel Gull, Andrew J. Millis, Alexander I. Lichtenstein, Alexey N. Rubtsov, Matthias Troyer, and Philipp Werner. Continuous-time monte carlo methods for quantum impurity models. *Rev. Mod. Phys.*, 83:349–404, May 2011.
- [10] Patrick Sémon, Kristjan Haule, and Gabriel Kotliar. Validity of the local approximation in iron-pnictides and chalcogenides. *arXiv:1606.03660 (unpublished)*, 2016.
- [11] Yoichi Kamihara, Hidenori Hiramatsu, Masahiro Hirano, Ryuto Kawamura, Hiroshi Yanagi, Toshio Kamiya, and Hideo Hosono. Iron-based layered superconductor: LaFePO. *J. Am. Chem. Soc.*, 128, 2006.
- [12] Yoichi Kamihara, Takumi Watanabe, Masahiro Hirano, and Hideo Hosono. Iron-based layered superconductor La[O_{1-x}F_x]FeAs ($x = 0.05 - 0.12$) with $T_c = 26$ K. *J. Am. Chem. Soc.*, 130, 2008.
- [13] L.H. Greene and B.G. Bagley. *Physical properties of high temperature superconductors II*. World Scientific Publishing Co. Pty. Ltd., 1990.
- [14] G. Wu, Y. L. Xie, H. Chen, M. Zhong, R. H. Liu, B. C. Shi, Q. J. Li, X. F. Wang, T. Wu, Y. J. Yan, J. J. Ying, and X. H. Chen. Fast track communication: Superconductivity at 56 K in samarium-doped SrFeAsF. *Journal of Physics Condensed Matter*, 21, 2009.
- [15] Jian-Feng Ge, Zhi-Long Liu, Canhua Liu, Chun-Lei Gao, Dong Qian, Qi-Kun Xue, Ying Liu, and Jin-Feng Jia. Superconductivity above 100 K in single-layer FeSe films on doped SrTiO₃. *Nature Materials*, 14, 2015.

- [16] K. Momma and F. Izumi. Vesta: a three-dimensional visualization system for electronic and structural analysis. *J. Appl. Crystallogr.*, 41:653–658, 2008.
- [17] I. I. Mazin and M. D. Johannes. A key role for unusual spin dynamics in ferropnictides. *Nature Physics*, 5, 2009.
- [18] M. M. Qazilbash, J. J. Hamlin, R. E. Baumbach, Lijun Zhang, D. J. Singh, M. B. Maple, and D. N. Basov. Electronic correlations in the iron pnictides. *Nature Physics*, 5, 2009.
- [19] T. Sato, K. Nakayama, Y. Sekiba, P. Richard, Y. M. Xu, S. Souma, T. Takahashi, G. F. Chen, J. L. Luo, N. L. Wang, and H. Ding. Band structure and fermi surface of an extremely overdoped iron-based superconductor KFe_2As_2 . *Physical Review Letters*, 103, 2009.
- [20] T. Yoshida, I. Nishi, A. Fujimori, M. Yi, R. G. Moore, D. H. Lu, Z. X. Shen, K. Kihou, P. M. Shirage, H. Kito, C. H. Lee, A. Iyo, H. Eisaki, and H. Harima. Fermi surfaces and quasi-particle band dispersions of the iron pnictides superconductor KFe_2As_2 observed by angle-resolved photoemission spectroscopy. *Journal of Physics and Chemistry of Solids*, 72, 2011.
- [21] Teppei Yoshida, Shin-Ichiro Ideta, Ichiro Nishi, Atsushi Fujimori, Ming Yi, Rob G. Moore, Sung-Kwan Mo, Donghui Lu, Zhi-Xun Shen, Zahid Hussain, Kunihiro Kihou, Parasharam M. Shirage, Hijiri Kito, Chul-Ho Lee, Akira Iyo, Hiroshi Eisaki, and Hisatomo Harima. Orbital character and electron correlation effects on two- and three-dimensional fermi surfaces in KFe_2As_2 revealed by angle-resolved photoemission spectroscopy. *Frontiers in Physics*, 2, 2014.
- [22] A. I. Coldea, J. D. Fletcher, A. Carrington, J. G. Analytis, A. F. Bangura, J. H. Chu, A. S. Erickson, I. R. Fisher, N. E. Hussey, and R. D. McDonald. Fermi surface of superconducting LaFePO determined from quantum oscillations. *Physical Review Letters*, 101, 2008.
- [23] Taichi Terashima, Motoi Kimata, Nobuyuki Kurita, Hidetaka Satsukawa, Atsushi Harada, Kaori Hazama, Motoharu Imai, Akira Sato, Kunihiro Kihou, Chul-Ho Lee, Hijiri Kito, Hiroshi Eisaki, Akira Iyo, Taku Saito, Hideto Fukazawa, Yoh Kohori, Hisatomo Harima, and Shinya Uji. Fermi surface and mass enhancement in KFe_2As_2 from de haas-van alphen effect measurements. *Journal of the Physical Society of Japan*, 79, 2010.
- [24] A Carrington. Quantum oscillation studies of the fermi surface of iron-pnictide superconductors. *Reports on Progress in Physics*, 74(12):124507, 2011.
- [25] C. Putzke, A. I. Coldea, I. Guillaumón, D. Vignolles, A. McCollam, D. Leboeuf, M. D. Watson, I. I. Mazin, S. Kasahara, T. Terashima, T. Shibauchi, Y. Matsuda, and A. Carrington. de haas-van alphen study of the fermi surfaces of superconducting LiFeP and LiFeAs . *Physical Review Letters*, 108, 2012.
- [26] Taichi Terashima, Nobuyuki Kurita, Motoi Kimata, Megumi Tomita, Satoshi Tsuchiya, Motoharu Imai, Akira Sato, Kunihiro Kihou, Chul-Ho Lee, Hijiri Kito, Hiroshi Eisaki, Akira Iyo, Taku Saito, Hideto Fukazawa, Yoh Kohori, Hisatomo Harima, and Shinya Uji. Fermi surface in KFe_2As_2 determined via de haas-van alphen oscillation measurements. *Physical Review B*, 87, 2013.
- [27] Johannes Ferber, Harald O. Jeschke, and Roser Valentí. Fermi surface topology of LaFePO and LiFeP . *Physical Review Letters*, 109, 2012.
- [28] Z. P. Yin, K. Haule, and G. Kotliar. Kinetic frustration and the nature of the magnetic and paramagnetic states in iron pnictides and iron chalcogenides. *Nature Materials*, 10, 2011.
- [29] Markus Aichhorn, Silke Biermann, Takashi Miyake, Antoine Georges, and Masatoshi Imada. Theoretical evidence for strong correlations and incoherent metallic state in FeSe . *Physical Review B*, 82, 2010.

- [30] P. Hansmann, R. Arita, A. Toschi, S. Sakai, G. Sangiovanni, and K. Held. Dichotomy between large local and small ordered magnetic moments in iron-based superconductors. *Physical Review Letters*, 104, 2010.
- [31] Markus Aichhorn, Leonid Pourovskii, and Antoine Georges. Importance of electronic correlations for structural and magnetic properties of the iron pnictide superconductor LaFeAsO. *Physical Review B*, 84, 2011.
- [32] Johannes Ferber, Kateryna Foyevtsova, Roser Valentí, and Harald O. Jeschke. LDA+DMFT study of the effects of correlation in LiFeAs. *Physical Review B*, 85, 2012.
- [33] G Haule, K and Kotliar. Coherence-incoherence crossover in the normal state of iron oxypnictides and importance of hund's rule coupling. *New Journal of Physics*, 11, 2009.
- [34] Luca de' Medici, Jernej Mravlje, and Antoine Georges. Janus-faced influence of hund's rule coupling in strongly correlated materials. *Physical Review Letters*, 107, 2011.
- [35] Rong Yu and Qimiao Si. Mott transition in multiorbital models for iron pnictides. *Physical Review B*, 84, 2011.
- [36] Markus Aichhorn, Leonid Pourovskii, Veronica Vildosola, Michel Ferrero, Olivier Parcollet, Takashi Miyake, Antoine Georges, and Silke Biermann. Dynamical mean-field theory within an augmented plane-wave framework: Assessing electronic correlations in the iron pnictide LaFeAsO. *Phys. Rev. B*, 80:085101, Aug 2009.
- [37] Ansgar Liebsch. High-energy pseudogap induced by hund coupling in a degenerate hubbard model. *Physical Review B*, 84, 2011.
- [38] Antoine Georges, Luca de Medici, and Jernej Mravlje. Strong correlations from hund's coupling. *Annual Review of Condensed Matter Physics*, 4, 2013.
- [39] Rong Yu and Qimiao Si. Orbital-selective mott phase in multiorbital models for alkaline iron selenides $K_{1-x}Fe_{2-y}Se_2$. *Physical Review Letters*, 110, 2013.
- [40] Luca de' Medici, Gianluca Giovannetti, and Massimo Capone. Selective mott physics as a key to iron superconductors. *Physical Review Letters*, 112, 2014.
- [41] L. Fanfarillo and E. Bascones. Electronic correlations in hund metals. *Physical Review B*, 92, 2015.
- [42] F. Hardy, A. E. Böhmer, D. Aoki, P. Burger, T. Wolf, P. Schweiss, R. Heid, P. Adelman, Y. X. Yao, G. Kotliar, J. Schmalian, and C. Meingast. Evidence of strong correlations and coherence-incoherence crossover in the iron pnictide superconductor KFe_2As_2 . *Physical Review Letters*, 111, 2013.
- [43] Yong Liu and Thomas A. Lograsso. Crossover in the magnetic response of single-crystalline $Ba_{1-x}K_xFe_2As_2$ and lifshitz critical point evidenced by hall effect measurements. *Physical Review B*, 90, 2014.
- [44] J. G. Storey, J. W. Loram, J. R. Cooper, Z. Bukowski, and J. Karpinski. Electronic specific heat of $Ba_{1-x}K_xFe_2As_2$ from 2 to 380 k. *Physical Review B*, 88, 2013.
- [45] A. E. Böhmer. Competing phases in iron-based superconductors studied by high-resolution thermal-expansion and shear-modulus measurements. *Ph.D. thesis, Karlsruhe*, 2014.
- [46] F. Eilers. Superconductivity and electronic structure of KFe_2As_2 , $RbFe_2As_2$, and $CsFe_2As_2$ probed by thermal expansion and magnetostriction at very low temperatures. *Ph.D. thesis, Karlsruhe*, 2014.

- [47] Z. Shermadini, J. Kanter, C. Baines, M. Bendele, Z. Bukowski, R. Khasanov, H. H. Klauss, H. Luetkens, H. Maeter, G. Pascua, B. Batlogg, and A. Amato. Microscopic study of the superconducting state of the iron pnictide RbFe_2As_2 via muon spin rotation. *Physical Review B*, 82, 2010.
- [48] Z. Zhang, A. F. Wang, X. C. Hong, J. Zhang, B. Y. Pan, J. Pan, Y. Xu, X. G. Luo, X. H. Chen, and S. Y. Li. Heat transport in RbFe_2As_2 single crystals: Evidence for nodal superconducting gap. *Physical Review B*, 91, 2015.
- [49] S. L. Skornyakov, V. I. Anisimov, and D. Vollhardt. Effect of correlations and doping on the spin susceptibility of iron pnictides: the case of KFe_2As_2 . *Soviet Journal of Experimental and Theoretical Physics Letters*, 100, 2014.
- [50] K. Morikawa, T. Mizokawa, K. Kobayashi, A. Fujimori, H. Eisaki, S. Uchida, F. Iga, and Y. Nishihara. Spectral weight transfer and mass renormalization in mott-hubbard systems SrVO_3 and CaVO_3 : Influence of long-range coulomb interaction. *Phys. Rev. B*, 52:13711–13714, Nov 1995.
- [51] A. Sekiyama, H. Fujiwara, S. Imada, S. Suga, H. Eisaki, S. I. Uchida, K. Takegahara, H. Harima, Y. Saitoh, I. A. Nekrasov, G. Keller, D. E. Kondakov, A. V. Kozhevnikov, Th. Pruschke, K. Held, D. Vollhardt, and V. I. Anisimov. Mutual experimental and theoretical validation of bulk photoemission spectra of $\text{Sr}_{1-x}\text{Ca}_x\text{VO}_3$. *Phys. Rev. Lett.*, 93:156402, Oct 2004.
- [52] R. Eguchi, T. Kiss, S. Tsuda, T. Shimojima, T. Mizokami, T. Yokoya, A. Chainani, S. Shin, I. H. Inoue, T. Togashi, S. Watanabe, C. Q. Zhang, C. T. Chen, M. Arita, K. Shimada, H. Namatame, and M. Taniguchi. Bulk- and surface-sensitive high-resolution photoemission study of two mott-hubbard systems: SrVO_3 and CaVO_3 . *Phys. Rev. Lett.*, 96:076402, Feb 2006.
- [53] F. Lechermann, A. Georges, A. Poteryaev, S. Biermann, M. Posternak, A. Yamasaki, and O. K. Andersen. Dynamical mean-field theory using wannier functions: A flexible route to electronic structure calculations of strongly correlated materials. *Phys. Rev. B*, 74:125120, Sep 2006.
- [54] M. Takizawa, M. Minohara, H. Kumigashira, D. Toyota, M. Oshima, H. Wadati, T. Yoshida, A. Fujimori, M. Lippmaa, M. Kawasaki, H. Koinuma, G. Sordi, and M. Rozenberg. Coherent and incoherent d band dispersions in SrVO_3 . *Phys. Rev. B*, 80:235104, Dec 2009.
- [55] S. Aizaki, T. Yoshida, K. Yoshimatsu, M. Takizawa, M. Minohara, S. Ideta, A. Fujimori, K. Gupta, P. Mahadevan, K. Horiba, H. Kumigashira, and M. Oshima. Self-energy on the low-to high-energy electronic structure of correlated metal SrVO_3 . *Phys. Rev. Lett.*, 109:056401, Jul 2012.
- [56] M. Casula, Ph. Werner, L. Vaugier, F. Aryasetiawan, T. Miyake, A. J. Millis, and S. Biermann. Low-energy models for correlated materials: Bandwidth renormalization from coulombic screening. *Phys. Rev. Lett.*, 109:126408, Sep 2012.
- [57] Ambroise van Roekeghem and Silke Biermann. Screened exchange dynamical mean-field theory and its relation to density functional theory: SrVO_3 and SrTiO_3 . *EPL (Europhysics Letters)*, 108(5):57003, 2014.
- [58] S. Cottenier. *Density Functional Theory and the family of (L)APW-methods: a step-by-step introduction*. 2 edition, 2002-2013. freely available at http://www.wien2k.at/reg_user/textbooks.
- [59] W. Kohn and L. J. Sham. Self-consistent equations including exchange and correlation effects. *Phys. Rev.*, 140:A1133–A1138, Nov 1965.

- [60] John P. Perdew, Robert G. Parr, Mel Levy, and Jose L. Balduz. Density-functional theory for fractional particle number: Derivative discontinuities of the energy. *Phys. Rev. Lett.*, 49:1691–1694, Dec 1982.
- [61] Ulrike Salzner and Roi Baer. Koopmans’ springs to life. *The Journal of Chemical Physics*, 131(23), 2009.
- [62] Weitao Parr, Robert G; Yang. *Density-Functional Theory of Atoms and Molecules*. Oxford: Oxford University Press, 1994.
- [63] Vladimir I. Anisimov, Jan Zaanen, and Ole K. Andersen. Band theory and mott insulators: Hubbard U instead of stoner I . *Phys. Rev. B*, 44:943–954, Jul 1991.
- [64] J. P. Perdew, K. Burke, and M. Ernzerhof. Generalized gradient approximation made simple. *Phys. Rev. Lett.*, 77, 1996.
- [65] E. I. Proynov, E. Ruiz, A. Vela, and D. R. Salahub. Determining and extending the domain of exchange and correlation functionals. *International Journal of Quantum Chemistry*, 56(S29):61–78, 1995.
- [66] Troy Van Voorhis and Gustavo E. Scuseria. A novel form for the exchange-correlation energy functional. *The Journal of Chemical Physics*, 109(2):400–410, 1998.
- [67] Axel D. Becke. A new inhomogeneity parameter in density-functional theory. *The Journal of Chemical Physics*, 109(6):2092–2098, 1998.
- [68] Jianmin Tao, John P. Perdew, Viktor N. Staroverov, and Gustavo E. Scuseria. Climbing the density functional ladder: Nonempirical meta-generalized gradient approximation designed for molecules and solids. *Phys. Rev. Lett.*, 91:146401, Sep 2003.
- [69] Axel D. Becke. A new mixing of hartree-fock and local density-functional theories. *The Journal of Chemical Physics*, 98(2):1372–1377, 1993.
- [70] Axel D. Becke. Density-functional thermochemistry. iii. the role of exact exchange. *The Journal of Chemical Physics*, 98(7):5648–5652, 1993.
- [71] J. Harris and R. O. Jones. The surface energy of a bounded electron gas. *J. Phys. F: Metal Phys.*, 4, 1974.
- [72] O. Gunnarsson and B. I. Lundqvist. Exchange and correlation in atoms, molecules, and solids by the spin-density-functional formalism. *Phys. Rev. B*, 13:4274–4298, May 1976.
- [73] John P. Perdew, Matthias Ernzerhof, and Kieron Burke. Rationale for mixing exact exchange with density functional approximations. *The Journal of Chemical Physics*, 105(22):9982–9985, 1996.
- [74] P. J. Stephens, F. J. Devlin, C. F. Chabalowski, and M. J. Frisch. Ab initio calculation of vibrational absorption and circular dichroism spectra using density functional force fields. *J. Phys. Chem.*, 98, 1994.
- [75] Jochen Heyd, Gustavo E. Scuseria, and Matthias Ernzerhof. Hybrid functionals based on a screened coulomb potential. *The Journal of Chemical Physics*, 118(18):8207–8215, 2003.
- [76] Aliaksandr V. Krukau, Oleg A. Vydrov, Artur F. Izmaylov, and Gustavo E. Scuseria. Influence of the exchange screening parameter on the performance of screened hybrid functionals. *The Journal of Chemical Physics*, 125(22), 2006.
- [77] Eberhard Engel and Reiner M. Dreizler. *Density Functional Theory: An Advanced Course*. Springer Science, 2011.

- [78] I. G. Austin and N. F. Mott. Metallic and nonmetallic behavior in transition metal oxides. *Science*, 168(3927):71–77, 1970.
- [79] R. B. Laughlin. Perspectives a critique of two metals. *Advances in Physics*, 47(6):943–958, 1998.
- [80] Masatoshi Imada, Atsushi Fujimori, and Yoshinori Tokura. Metal-insulator transitions. *Rev. Mod. Phys.*, 70:1039–1263, Oct 1998.
- [81] Tudor D. Stanescu, Philip Phillips, and Ting-Pong Choy. Theory of the luttinger surface in doped mott insulators. *Phys. Rev. B*, 75:104503, Mar 2007.
- [82] V. I. Anisimov, I. V. Solovyev, M. A. Korotin, M. T. Czyżyk, and G. A. Sawatzky. Density-functional theory and NiO photoemission spectra. *Phys. Rev. B*, 48:16929–16934, Dec 1993.
- [83] I. V. Solovyev, P. H. Dederichs, and V. I. Anisimov. Corrected atomic limit in the local-density approximation and the electronic structure of d impurities in Rb. *Phys. Rev. B*, 50:16861–16871, Dec 1994.
- [84] Vladimir I Anisimov, F Aryasetiawan, and A I Lichtenstein. First-principles calculations of the electronic structure and spectra of strongly correlated systems: the LDA+U method. *Journal of Physics: Condensed Matter*, 9(4):767, 1997.
- [85] A. I. Liechtenstein, V. I. Anisimov, and J. Zaanen. Density-functional theory and strong interactions: Orbital ordering in mott-hubbard insulators. *Physical Review B*, 52, 1995.
- [86] André-Marie Tremblay. Phy-892 problème à n-corps (notes de cours).
- [87] C. Itzykson and J.-M. Drouffe. Statistical field theory. *Cambridge University Press, Cambridge*, 1989.
- [88] Gordon Baym and N. David Mermin. Determination of thermodynamic green’s functions. *J. Math. Phys.*, 2, 1961.
- [89] Georg Frobenius. über relationen zwischen den Näherungsbrüchen von Potenzreihen. *Journal für die reine und angewandte Mathematik (Crelle’s Journal)*, 1881 (90), 1881.
- [90] Henri Padé. Sur la représentation approchée d’une fonction par des fractions rationnelles. *Ann. Sci. École Norm. Sup. Suppl. (3)*, 9, 1892.
- [91] Mark Jarrell and J.E. Gubernatis. Bayesian inference and the analytic continuation of imaginary-time quantum monte carlo data. *Physics Reports*, 269, 1996.
- [92] R. K. Bryan. Maximum entropy analysis of oversampled data problems. *European Biophysics Journal*, 18(3):165–174, 1990.
- [93] K. S. D. Beach. Identifying the maximum entropy method as a special limit of stochastic analytic continuation. *arXiv:cond-mat/0403055*, 2004.
- [94] Ryan Levy, J.P.F. LeBlanc, and Emanuel Gull. Implementation of the maximum entropy method for analytic continuation. *arXiv:1606.00368*, <https://github.com/CQMP/Maxent>, 2016.
- [95] A. S. Mishchenko, N. V. Prokof’ev, A. Sakamoto, and B. V. Svistunov. Diagrammatic quantum monte carlo study of the fröhlich polaron. *Phys. Rev. B*, 62, 2000.
- [96] Anders W. Sandvik. Stochastic method for analytic continuation of quantum monte carlo data. *Phys. Rev. B*, 57, 1998.
- [97] Enzo Marinari. Optimized monte carlo methods. *arXiv:cond-mat/9612010*, 1996.

- [98] <http://www.wordreference.com/>. 2016.
- [99] R. J. Baxter. Exactly solved models in statistical mechanics. *Academic Press, London*, 1982.
- [100] R. Brout. Statistical mechanical theory of ferromagnetism. high density behavior. *Phys. Rev.*, 118:1009–1019, May 1960.
- [101] Colin J. Thompson. Ising model in the high density limit. *Comm. Math. Phys.*, 36(4):255–262, 1974.
- [102] Dieter Vollhardt. Dynamical mean-field theory of electronic correlations in models and materials. *AIP Conference Proceedings*, 1297(1):339–403, 2010.
- [103] Krzysztof Byczuk and Dieter Vollhardt. Correlated bosons on a lattice: Dynamical mean-field theory for bose-einstein condensed and normal phases. *Phys. Rev. B*, 77:235106, Jun 2008.
- [104] Walter Metzner. Variational theory for correlated lattice fermions in high dimensions. *Zeitschrift für Physik B Condensed Matter*, 77(2):253–266, 1989.
- [105] P. G. J. van Dongen, F. Gebhard, and D. Vollhardt. Variational evaluation of correlation functions for lattice electrons in high dimensions. *Zeitschrift für Physik B Condensed Matter*, 76(2):199–210, 1989.
- [106] E. Müller-Hartmann. Correlated fermions on a lattice in high dimensions. *Zeitschrift für Physik B Condensed Matter*, 74(4):507–512, 1989.
- [107] Fusayoshi J. Ohkawa. Electron correlation in the hubbard model in $d = \infty$ dimension. *Journal of the Physical Society of Japan*, 60(10):3218–3221, 1991.
- [108] Alexander Cyril Hewson. *The Kondo Problem to Heavy Fermions*. Cambridge University Press, 1993. Cambridge Books Online.
- [109] J. E. Hirsch and R. M. Fye. Monte carlo method for magnetic impurities in metals. *Phys. Rev. Lett.*, 56:2521–2524, Jun 1986.
- [110] M. Jarrell. Hubbard model in infinite dimensions: A quantum monte carlo study. *Phys. Rev. Lett.*, 69:168–171, Jul 1992.
- [111] Michel Caffarel and Werner Krauth. Exact diagonalization approach to correlated fermions in infinite dimensions: Mott transition and superconductivity. *Phys. Rev. Lett.*, 72:1545–1548, Mar 1994.
- [112] Qimiao Si, M. J. Rozenberg, G. Kotliar, and A. E. Ruckenstein. Correlation induced insulator to metal transitions. *Phys. Rev. Lett.*, 72:2761–2764, Apr 1994.
- [113] O. Sakai and Y. Kuramoto. Application of the numerical renormalization group method to the hubbard model in infinite dimensions. *Solid State Communications*, 89(4):307 – 311, 1994.
- [114] V. Janiš. A new construction of thermodynamic mean-field theories of itinerant fermions: application to the falicov-kimball model. *Zeitschrift für Physik B Condensed Matter*, 83(2):227–235, 1991.
- [115] Janiš. and D. Vollhardt. Comprehensive mean field theory for the hubbard model. *International Journal of Modern Physics B*, 06(05n06):731–747, 1992.
- [116] Antoine Georges, Gabriel Kotliar, Werner Krauth, and Marcelo J. Rozenberg. Dynamical mean-field theory of strongly correlated fermion systems and the limit of infinite dimensions. *Rev. Mod. Phys.*, 68:13–125, Jan 1996.
- [117] Daniel V. Peskin, Michael E.; Schroeder. An introduction to quantum field theory. *Addison-Wesley*, 1995.

- [118] V I Anisimov, A I Poteryaev, M A Korotin, A O Anokhin, and G Kotliar. First-principles calculations of the electronic structure and spectra of strongly correlated systems: dynamical mean-field theory. *Journal of Physics: Condensed Matter*, 9(35):7359, 1997.
- [119] A. I. Lichtenstein and M. I. Katsnelson. Ab initio calculations of quasiparticle band structure in correlated systems: LDA++ approach. *Phys. Rev. B*, 57:6884–6895, Mar 1998.
- [120] A. I. Lichtenstein, M. I. Katsnelson, and G. Kotliar. Finite-temperature magnetism of transition metals: An *ab initio* dynamical mean-field theory. *Phys. Rev. Lett.*, 87:067205, Jul 2001.
- [121] G. Kotliar, S. Y. Savrasov, K. Haule, V. S. Oudovenko, O. Parcollet, and C. A. Marianetti. Electronic structure calculations with dynamical mean-field theory. *Rev. Mod. Phys.*, 78:865–951, Aug 2006.
- [122] S. Y. Savrasov, G. Kotliar, and E. Abrahams. Correlated electrons in δ -plutonium within a dynamical mean-field picture. *Nature*, 410:793–795, 2001.
- [123] E. Pavarini, S. Biermann, A. Poteryaev, A. I. Lichtenstein, A. Georges, and O. K. Andersen. Mott transition and suppression of orbital fluctuations in orthorhombic $3d^1$ perovskites. *Phys. Rev. Lett.*, 92:176403, Apr 2004.
- [124] V. I. Anisimov, D. E. Kondakov, A. V. Kozhevnikov, I. A. Nekrasov, Z. V. Pchelkina, J. W. Allen, S.-K. Mo, H.-D. Kim, P. Metcalf, S. Suga, A. Sekiyama, G. Keller, I. Leonov, X. Ren, and D. Vollhardt. Full orbital calculation scheme for materials with strongly correlated electrons. *Phys. Rev. B*, 71:125119, Mar 2005.
- [125] Wei Ku, H. Rosner, W. E. Pickett, and R. T. Scalettar. Insulating ferromagnetism in $\text{La}_4\text{Ba}_2\text{Cu}_2\text{O}_{10}$: An *Ab Initio* wannier function analysis. *Phys. Rev. Lett.*, 89:167204, Sep 2002.
- [126] B. Amadon, F. Lechermann, A. Georges, F. Jollet, T. O. Wehling, and A. I. Lichtenstein. Plane-wave based electronic structure calculations for correlated materials using dynamical mean-field theory and projected local orbitals. *Phys. Rev. B*, 77:205112, May 2008.
- [127] F. Aryasetiawan, M. Imada, A. Georges, G. Kotliar, S. Biermann, and A. I. Lichtenstein. Frequency-dependent local interactions and low-energy effective models from electronic structure calculations. *Phys. Rev. B*, 70:195104, Nov 2004.
- [128] Michele Casula, Alexey Rubtsov, and Silke Biermann. Dynamical screening effects in correlated materials: Plasmon satellites and spectral weight transfers from a green’s function ansatz to extended dynamical mean field theory. *Phys. Rev. B*, 85:035115, Jan 2012.
- [129] Silke Biermann. Dynamical screening effects in correlated electron materials - a progress report on combined many-body perturbation and dynamical mean field theory: GW+DMFT. *Journal of Physics: Condensed Matter*, 26(17):173202, 2014.
- [130] F. Aryasetiawan, K. Karlsson, O. Jepsen, and U. Schönberger. Calculations of Hubbard U from first-principles. *Phys. Rev. B*, 74:125106, Sep 2006.
- [131] Takashi Miyake, Kazuma Nakamura, Ryotaro Arita, and Masatoshi Imada. Comparison of ab initio low-energy models for LaFePO , LaFeAsO , BaFe_2As_2 , LiFeAs , FeSe , and FeTe : Electron correlation and covalency. *Journal of the Physical Society of Japan*, 79(4):044705, 2010.
- [132] D. M. Bylander and Leonard Kleinman. Good semiconductor band gaps with a modified local-density approximation. *Phys. Rev. B*, 41:7868–7871, Apr 1990.
- [133] J. Paier, M. Marsman, K. Hummer, G. Kresse, I. C. Gerber, and J. G. Ángyán. Screened hybrid density functionals applied to solids. *The Journal of Chemical Physics*, 124(15), 2006.

- [134] M. T. Czyżyk and G. A. Sawatzky. Local-density functional and on-site correlations: The electronic structure of La_2 , CuO_4 and LaCuO_3 . *Phys. Rev. B*, 49:14211–14228, May 1994.
- [135] M. Karolak, G. Ulm, T. Wehling, V. Mazurenko, A. Poteryaev, and A. Lichtenstein. Double counting in LDA + DMFT: The example of NiO. *Journal of Electron Spectroscopy and Related Phenomena*, 181(1):11 – 15, 2010. Proceedings of International Workshop on Strong Correlations and Angle-Resolved Photoemission Spectroscopy 2009.
- [136] Hyowon Park, Andrew J. Millis, and Chris A. Marianetti. Total energy calculations using DFT+DMFT: Computing the pressure phase diagram of the rare earth nickelates. *Phys. Rev. B*, 89:245133, Jun 2014.
- [137] Kristjan Haule, Chuck-Hou Yee, and Kyo Kim. Dynamical mean-field theory within the full-potential methods: Electronic structure of CeIrIn_5 , CeCoIn_5 , and CeRhIn_5 . *Phys. Rev. B*, 81:195107, May 2010.
- [138] Kristjan Haule, Turan Birol, and Gabriel Kotliar. Covalency in transition-metal oxides within all-electron dynamical mean-field theory. *Phys. Rev. B*, 90:075136, Aug 2014.
- [139] Kristjan Haule. Exact double counting in combining the dynamical mean field theory and the density functional theory. *Phys. Rev. Lett.*, 115:196403, Nov 2015.
- [140] Eva Pavarini, Erik Koch, Dieter Vollhardt, , and Alexander Lichtenstein. *The LDA+DMFT approach to strongly correlated materials*. Verlag des Forschungszentrum Jülich, 2011.
- [141] John C. Slater. Quantum theory of atomic structure. *McGraw-Hill (New York)*, 1, 1960.
- [142] D. van der Marel and G. A. Sawatzky. Electron-electron interaction and localization in d and f transition metals. *Phys. Rev. B*, 37:10674–10684, Jun 1988.
- [143] S. Y. Savrasov and G. Kotliar. Spectral density functionals for electronic structure calculations. *Phys. Rev. B*, 69:245101, Jun 2004.
- [144] L. V. Pourovskii, B. Amadon, S. Biermann, and A. Georges. Self-consistency over the charge density in dynamical mean-field theory: A linear muffin-tin implementation and some physical implications. *Phys. Rev. B*, 76:235101, Dec 2007.
- [145] B. Amadon, S. Biermann, A. Georges, and F. Aryasetiawan. The α - γ transition of cerium is entropy driven. *Phys. Rev. Lett.*, 96:066402, Feb 2006.
- [146] Marianne Rotter, Marcus Tegel, Dirk Johrendt, Inga Schellenberg, Wilfried Hermes, and Rainer Pöttgen. Spin-density-wave anomaly at 140 K in the ternary iron arsenide BaFe_2As_2 . *Physical Review B*, 78, 2008.
- [147] Kunihiro Kihou, Taku Saito, Shigeyuki Ishida, Masamichi Nakajima, Yasuhide Tomioka, Hideto Fukazawa, Yoh Kohori, Toshimitsu Ito, Shin-ichi Uchida, Akira Iyo, Chul-Ho Lee, and Hiroshi Eisaki. Single crystal growth and characterization of the iron-based superconductor KFe_2As_2 synthesized by kas flux method. *Journal of the Physical Society of Japan*, 79, 2010.
- [148] Fa Wang and Dung-Hai Lee. The electron-pairing mechanism of iron-based superconductors. *Science*, 332, 2011.
- [149] P. J. Hirschfeld, M. M. Korshunov, and I. I. Mazin. Gap symmetry and structure of Fe-based superconductors. *Reports on Progress in Physics*, 74, 2011.
- [150] Andrey Chubukov. Pairing mechanism in Fe-based superconductors. *Annu. Rev. Condens. Matter Phys.*, 3, 2012.

- [151] K. Okazaki, Y. Ota, Y. Kotani, W. Malaeb, Y. Ishida, T. Shimojima, T. Kiss, S. Watanabe, C. T. Chen, K. Kihou, C. H. Lee, A. Iyo, H. Eisaki, T. Saito, H. Fukazawa, Y. Kohori, K. Hashimoto, T. Shibauchi, Y. Matsuda, H. Ikeda, H. Miyahara, R. Arita, A. Chainani, and S. Shin. Octet-line node structure of superconducting order parameter in KFe_2As_2 . *Science*, 337, 2012.
- [152] Ronny Thomale, Christian Platt, Werner Hanke, and B. Andrei Bernevig. Mechanism for explaining differences in the order parameters of fea-based and fep-based pnictide superconductors. *Physical Review Letters*, 106, 2011.
- [153] J. Ph. Reid, M. A. Tanatar, A. Juneau-Fecteau, R. T. Gordon, S. René de Cotret, N. Doiron-Leyraud, T. Saito, H. Fukazawa, Y. Kohori, K. Kihou, C. H. Lee, A. Iyo, H. Eisaki, R. Prozorov, and Louis Taillefer. Universal heat conduction in the iron arsenide superconductor KFe_2As_2 : Evidence of a d-wave state. *Physical Review Letters*, 109, 2012.
- [154] S. Maiti, M. M. Korshunov, T. A. Maier, P. J. Hirschfeld, and A. V. Chubukov. Evolution of the superconducting state of Fe-based compounds with doping. *Physical Review Letters*, 107, 2011.
- [155] Katsuhiko Suzuki, Hidetomo Usui, and Kazuhiko Kuroki. Spin fluctuations and unconventional pairing in KFe_2As_2 . *Physical Review B*, 84, 2011.
- [156] F. F. Tafti, A. Juneau-Fecteau, M. È. Delage, S. René de Cotret, J. Ph. Reid, A. F. Wang, X. G. Luo, X. H. Chen, N. Doiron-Leyraud, and Louis Taillefer. Sudden reversal in the pressure dependence of t_c in the iron-based superconductor KFe_2As_2 . *Nature Physics*, 9, 2013.
- [157] Motoi Kimata, Taichi Terashima, Nobuyuki Kurita, Hidetaka Satsukawa, Atsushi Harada, Kouta Kodama, Kanji Takehana, Yasutaka Imanaka, Tadashi Takamasu, Kunihiko Kihou, Chul-Ho Lee, Hijiri Kito, Hiroshi Eisaki, Akira Iyo, Hideto Fukazawa, Yoh Kohori, Hisatomo Harima, and Shinya Uji. Cyclotron resonance and mass enhancement by electron correlation in KFe_2As_2 . *Physical Review Letters*, 107, 2011.
- [158] Taichi Terashima, Kunihiko Kihou, Megumi Tomita, Satoshi Tsuchiya, Naoki Kikugawa, Shigeyuki Ishida, Chul-Ho Lee, Akira Iyo, Hiroshi Eisaki, and Shinya Uji. Hysteretic superconducting resistive transition in $\text{Ba}_{0.07}\text{K}_{0.93}\text{Fe}_2\text{As}_2$. *Physical Review B*, 87, 2013.
- [159] F. F. Tafti, J. P. Clancy, M. Lapointe-Major, C. Collignon, S. Faucher, J. A. Sears, A. Juneau-Fecteau, N. Doiron-Leyraud, A. F. Wang, X. G. Luo, X. H. Chen, S. Desgreniers, Young-June Kim, and Louis Taillefer. Sudden reversal in the pressure dependence of t_c in the iron-based superconductor CsFe_2As_2 : A possible link between inelastic scattering and pairing symmetry. *Physical Review B*, 89, 2014.
- [160] Rosza S. and Schuster H. U. Zur struktur von KFe_2As_2 , KCo_2As_2 , KRh_2As / crystal structure of KFe_2As_2 , KCo_2 , KRh_2As_2 and KRh_2P_2 . *Z. Naturforsch. B*, 36, 1981.
- [161] Blaha P, Schwarz K and Madsen G K H, Kvasnicka D, and Luit J. Wien2k: An augmented planewave+localorbitals program for calculating crystal properties. *Karlheinz Schwarz, Techn. Universität Wien, Austria*, 2001.
- [162] John P. Perdew, Kieron Burke, and Matthias Ernzerhof. Generalized gradient approximation made simple. *Physical Review Letters*, 77, 1996.
- [163] Johannes Ferber, Kateryna Foyevtsova, Harald O. Jeschke, and Roser Valentí. Unveiling the microscopic nature of correlated organic conductors: The case of κ -(ET)₂Cu[N(CN)₂]Br_xCl_{1-x}. *Phys. Rev. B*, 89:205106, May 2014.

- [164] B. Bauer, L. D. Carr, H. G. Evertz, A. Feiguin, J. Freire, S. Fuchs, L. Gamper, J. Gukelberger, E. Gull, S. Guertler, A. Hehn, R. Igarashi, S. V. Isakov, D. Koop, P. N. Ma, P. Mates, H. Matsuo, O. Parcollet, G. Pawłowski, J. D. Picon, L. Pollet, E. Santos, V. W. Scarola, U. Schollwöck, C. Silva, B. Surer, S. Todo, S. Trebst, M. Troyer, M. L. Wall, P. Werner, and S. Wessel. The alps project release 2.0: open source software for strongly correlated systems. *Journal of Statistical Mechanics: Theory and Experiment*, 2011, 2011.
- [165] Lewin Boehnke, Hartmut Hafermann, Michel Ferrero, Frank Lechermann, and Olivier Parcollet. Orthogonal polynomial representation of imaginary-time green's functions. *Physical Review B*, 84, 2011.
- [166] Hartmut Hafermann, Kelly R. Patton, and Philipp Werner. Improved estimators for the self-energy and vertex function in hybridization-expansion continuous-time quantum monte carlo simulations. *Physical Review B*, 85, 2012.
- [167] S. L. Dudarev, G. A. Botton, S. Y. Savrasov, C. J. Humphreys, and A. P. Sutton. Electron-energy-loss spectra and the structural stability of nickel oxide: An LSDA+U study. *Phys. Rev. B*, 57:1505–1509, Jan 1998.
- [168] P. M. C. Rourke and S. R. Julian. Numerical extraction of de haas-van alphen frequencies from calculated band energies. *Computer Physics Communications*, 183, 2012.
- [169] L. Ortenzi, E. Cappelluti, L. Benfatto, and L. Pietronero. Fermi-surface shrinking and inter-band coupling in iron-based pnictides. *Physical Review Letters*, 103, 2009.
- [170] Kyu Won Lee and Cheol Eui Lee. Intrinsic impurity-band stoner ferromagnetism in $C_{60}H_n$. *Physical Review Letters*, 106, 2011.
- [171] Masanori Hirano, Yuji Yamada, Taku Saito, Ryo Nagashima, Takehisa Konishi, Tatsuya Toriyama, Yukinori Ohta, Hideto Fukazawa, Yoh Kohori, Yuji Furukawa, Kunihiro Kihou, Chul-Ho Lee, Akira Iyo, and Hiroshi Eisaki. Potential antiferromagnetic fluctuations in hole-doped iron-pnictide superconductor $Ba_{1-x}K_xFe_2As_2$ studied by 75as nuclear magnetic resonance measurement. *Journal of the Physical Society of Japan*, 81, 2012.
- [172] Yu-Zhong Zhang, Ingo Opahle, Harald O. Jeschke, and Roser Valentí. Pressure-driven phase transitions in tiocl and the family $(Ca, Sr, Ba)Fe_2As_2$. *Journal of Physics Condensed Matter*, 22, 2010.
- [173] Diego A. Zocco, Kai Grube, Felix Eilers, Thomas Wolf, and Hilbert v. Löhneysen. Fermi surface of KFe_2As_2 from quantum oscillations in magnetostriction. *Proceedings of the International Conference on Strongly Correlated Electron Systems (SCES2013)*, 2014.
- [174] Y. X. Yao, J. Schmalian, C. Z. Wang, K. M. Ho, and G. Kotliar. Comparative study of the electronic and magnetic properties of $BaFe_2As_2$ and $BaMn_2As_2$ using the gutzwiller approximation. *Physical Review B*, 84, 2011.
- [175] Johnpierre Paglione and Richard L. Greene. High-temperature superconductivity in iron-based materials. *Nature Physics*, 6, 2010.
- [176] A. E. Böhmer, F. Hardy, L. Wang, T. Wolf, P. Schweiss, and C. Meingast. Superconductivity-induced re-entrance of the orthorhombic distortion in $Ba_{1-x}K_xFe_2As_2$. *Nature Communications*, 6, 2015.
- [177] J. K. Dong, S. Y. Zhou, T. Y. Guan, H. Zhang, Y. F. Dai, X. Qiu, X. F. Wang, Y. He, X. H. Chen, and S. Y. Li. Quantum criticality and nodal superconductivity in the feas-based superconductor KFe_2As_2 . *Physical Review Letters*, 104, 2010.

- [178] X. C. Hong, X. L. Li, B. Y. Pan, L. P. He, A. F. Wang, X. G. Luo, X. H. Chen, and S. Y. Li. Nodal gap in iron-based superconductor CsFe_2As_2 probed by quasiparticle heat transport. *Physical Review B*, 87, 2013.
- [179] A. F. Wang, B. Y. Pan, X. G. Luo, F. Chen, Y. J. Yan, J. J. Ying, G. J. Ye, P. Cheng, X. C. Hong, S. Y. Li, and X. H. Chen. Calorimetric study of single-crystal CsFe_2As_2 . *Physical Review B*, 87, 2013.
- [180] H. Ding, P. Richard, K. Nakayama, K. Sugawara, T. Arakane, Y. Sekiba, A. Takayama, S. Souma, T. Sato, T. Takahashi, Z. Wang, X. Dai, Z. Fang, G. F. Chen, J. L. Luo, and N. L. Wang. Observation of fermi-surface dependent nodeless superconducting gaps in $\text{Ba}_{0.6}\text{K}_{0.4}\text{Fe}_2\text{As}_2$. *EPL (Europhysics Letters)*, 83, 2008.
- [181] K. Terashima, Y. Sekiba, J. H. Bowen, K. Nakayama, T. Kawahara, T. Sato, P. Richard, Y. M. Xu, L. J. Li, G. H. Cao, Z. A. Xu, H. Ding, and T. Takahashi. Fermi surface nesting induced strong pairing in iron-based superconductors. *Proceedings of the National Academy of Science*, 106, 2009.
- [182] X. G. Luo, M. A. Tanatar, J. Ph. Reid, H. Shakeripour, N. Doiron-Leyraud, N. Ni, S. L. Bud'Ko, P. C. Canfield, Huiqian Luo, Zhaosheng Wang, Hai-Hu Wen, R. Prozorov, and Louis Taillefer. Quasiparticle heat transport in single-crystalline $\text{Ba}_{1-x}\text{K}_x\text{Fe}_2\text{As}_2$: Evidence for a k -dependent superconducting gap without nodes. *Physical Review B*, 80, 2009.
- [183] Philipp Werner, Michele Casula, Takashi Miyake, Ferdi Aryasetiawan, Andrew J. Millis, and Silke Biermann. Satellites and large doping and temperature dependence of electronic properties in hole-doped BaFe_2As_2 . *Nature Physics*, 8, 2012.
- [184] P. Popovich, A. V. Boris, O. V. Dolgov, A. A. Golubov, D. L. Sun, C. T. Lin, R. K. Kremer, and B. Keimer. Specific heat measurements of $\text{Ba}_{0.68}\text{K}_{0.32}\text{Fe}_2\text{As}_2$ single crystals: Evidence for a multiband strong-coupling superconducting state. *Physical Review Letters*, 105, 2010.
- [185] Gang Mu, Huiqian Luo, Zhaosheng Wang, Lei Shan, Cong Ren, and Hai-Hu Wen. Low temperature specific heat of the hole-doped $\text{Ba}_{0.6}\text{K}_{0.4}\text{Fe}_2\text{As}_2$ single crystals. *Physical Review B*, 79, 2009.
- [186] Jean Diehl, Steffen Backes, Daniel Guterding, Harald O. Jeschke, and Roser Valentí. Correlation effects in the tetragonal and collapsed-tetragonal phase of CaFe_2As_2 . *Physical Review B*, 90, 2014.
- [187] Subhasish Mandal, R. E. Cohen, and K. Haule. Pressure suppression of electron correlation in the collapsed tetragonal phase of CaFe_2As_2 : A DFT-DMFT investigation. *Physical Review B*, 90, 2014.
- [188] Daniel Guterding, Harald O. Jeschke, P. J. Hirschfeld, and Roser Valentí. Unified picture of the doping dependence of superconducting transition temperatures in alkali metal/ammonia intercalated FeSe . *Physical Review B*, 91, 2015.
- [189] Helmut Eschrig and Klaus Koepnik. Tight-binding models for the iron-based superconductors. *Physical Review B*, 80, 2009.
- [190] Klaus Koepnik and Helmut Eschrig. Full-potential nonorthogonal local-orbital minimum-basis band-structure scheme. *Physical Review B*, 59, 1999.
- [191] B. Valenzuela M. J. Calderón and E. Bascones. Tight-binding model for iron pnictides. *Physical Review B*, 80, 2009.
- [192] Hung T. Dang, Jernej Mravlje, Antoine Georges, and Andrew J. Millis. Electronic correlations, magnetism, and Hund's rule coupling in the ruthenium perovskites SrRuO_3 and CaRuO_3 . *Physical Review B*, 91, 2015.

- [193] S. Biermann, L. de' Medici, and A. Georges. Non-fermi-liquid behavior and double-exchange physics in orbital-selective mott systems. *Physical Review Letters*, 95, 2005.
- [194] Th. Pruschke and R. Bulla. Hund's coupling and the metal-insulator transition in the two-band hubbard model. *European Physical Journal B*, 44, 2005.
- [195] A. E. Antipov, I. S. Krivenko, V. I. Anisimov, A. I. Lichtenstein, and A. N. Rubtsov. Role of rotational symmetry in the magnetism of a multiorbital model. *Physical Review B*, 86, 2012.
- [196] X. Y. Zhang, M. J. Rozenberg, and G. Kotliar. Mott transition in the $d = \infty$ Hubbard model at zero temperature. *Phys. Rev. Lett.*, 70:1666–1669, Mar 1993.
- [197] I. H. Inoue, I. Hase, Y. Aiura, A. Fujimori, Y. Haruyama, T. Maruyama, and Y. Nishihara. Systematic development of the spectral function in the $3d^1$ mott-hubbard system $\text{Ca}_{1-x}\text{Sr}_x\text{VO}_3$. *Phys. Rev. Lett.*, 74:2539–2542, Mar 1995.
- [198] T. Yoshida, M. Hashimoto, T. Takizawa, A. Fujimori, M. Kubota, K. Ono, and H. Eisaki. Mass renormalization in the bandwidth-controlled mott-hubbard systems SrVO_3 and CaVO_3 studied by angle-resolved photoemission spectroscopy. *Phys. Rev. B*, 82:085119, Aug 2010.
- [199] M. J. Rozenberg, I. H. Inoue, H. Makino, F. Iga, and Y. Nishihara. Low frequency spectroscopy of the correlated metallic system $\text{Ca}_x\text{Sr}_{1-x}\text{VO}_3$. *Phys. Rev. Lett.*, 76:4781–4784, Jun 1996.
- [200] M Karolak, T O Wehling, F Lechermann, and A I Lichtenstein. General dft++ method implemented with projector augmented waves: electronic structure of SrVO_3 and the mott transition in $\text{Ca}_{2-x}\text{Sr}_x\text{RuO}_4$. *Journal of Physics: Condensed Matter*, 23(8):085601, 2011.
- [201] Hunpyo Lee, Kateryna Foyevtsova, Johannes Ferber, Markus Aichhorn, Harald O. Jeschke, and Roser Valentí. Dynamical cluster approximation within an augmented plane wave framework: Spectral properties of SrVO_3 . *Phys. Rev. B*, 85:165103, Apr 2012.
- [202] Jan M. Tomczak, Michele Casula, Takashi Miyake, Ferdi Aryasetiawan, and Silke Biermann. Combined GW and dynamical mean-field theory: Dynamical screening effects in transition metal oxides. *EPL (Europhysics Letters)*, 100(6):67001, 2012.
- [203] C. Taranto, M. Kaltak, N. Parragh, G. Sangiovanni, G. Kresse, A. Toschi, and K. Held. Comparing quasiparticle $\text{GW}+\text{DMFT}$ and $\text{LDA}+\text{DMFT}$ for the test bed material SrVO_3 . *Phys. Rev. B*, 88:165119, Oct 2013.
- [204] Jan M. Tomczak, M. Casula, T. Miyake, and S. Biermann. Asymmetry in band widening and quasiparticle lifetimes in SrVO_3 : Competition between screened exchange and local correlations from combined GW and dynamical mean-field theory $\text{GW}+\text{DMFT}$. *Phys. Rev. B*, 90:165138, Oct 2014.
- [205] A. Fujimori, I. Hase, H. Namatame, Y. Fujishima, Y. Tokura, H. Eisaki, S. Uchida, K. Takegahara, and F. M. F. de Groot. Evolution of the spectral function in mott-hubbard systems with d^1 configuration. *Phys. Rev. Lett.*, 69:1796–1799, Sep 1992.
- [206] K. Morikawa, T. Mizokawa, A. Fujimori, Y. Taguchi, and Y. Tokura. Photoemission spectral weight distribution in $\text{Y}_{1-x}\text{Ca}_x\text{TiO}_3$. *Phys. Rev. B*, 54:8446–8451, Sep 1996.
- [207] Antoine Georges, Gabriel Kotliar, Werner Krauth, and Marcelo J. Rozenberg. Dynamical mean-field theory of strongly correlated fermion systems and the limit of infinite dimensions. *Reviews of Modern Physics*, 68, 1996.
- [208] I. A. Nekrasov, G. Keller, D. E. Kondakov, A. V. Kozhevnikov, Th. Pruschke, K. Held, D. Vollhardt, and V. I. Anisimov. Comparative study of correlation effects in CaVO_3 and SrVO_3 . *Phys. Rev. B*, 72:155106, Oct 2005.

- [209] Y. Aiur, I. Hase, H. Bando, T. Yasue, T. Saitoh, and D.S. Dessau. Photoemission study of the metallic state of lightly electron-doped SrTiO₃. *Surf. Sci.*, 515, 2002.
- [210] A. F. Santander-Syro, O. Copie, T. Kondo, F. Fortuna, S. Pailhès, R. Weht, X. G. Qiu, F. Bertran, A. Nicolaou, A. Taleb-Ibrahimi, P. Le Fèvre, G. Herranz, M. Bibes, N. Reyren, Y. Apertet, P. Lecoeur, A. Barthélémy, and M. J. Rozenberg. Two-dimensional electron gas with universal subbands at the surface of SrTiO₃. *Nature*, 469, 2011.
- [211] W. Meevasana, P. D. C. King, R. H. He, S.-K. Mo, M. Hashimoto, A. Tamai, P. Songsiriritthigul, F. Baumberger, and Z.-X. Shen. Creation and control of a two-dimensional electron liquid at the bare SrTiO₃ surface. *Nature Mater.*, 10, 2011.
- [212] P. D. C. King, R. H. He, T. Eknapakul, P. Buaphet, S.-K. Mo, Y. Kaneko, S. Harashima, Y. Hikita, M. S. Bahramy, C. Bell, Z. Hussain, Y. Tokura, Z.-X. Shen, H. Y. Hwang, F. Baumberger, and W. Meevasana. Subband structure of a two-dimensional electron gas formed at the polar surface of the strong spin-orbit perovskite KTaO₃. *Phys. Rev. Lett.*, 108:117602, Mar 2012.
- [213] S. Moser, L. Moreschini, J. Jaćimović, O. S. Barišić, H. Berger, A. Magrez, Y. J. Chang, K. S. Kim, A. Bostwick, E. Rotenberg, L. Forró, and M. Grioni. Tunable polaronic conduction in anatase TiO₂. *Phys. Rev. Lett.*, 110:196403, May 2013.
- [214] McKeown Walker, S., de la Torre, A., Bruno, F. Y., Tamai, A., Kim, T. K., Hoesch, M., Shi, M., Bahramy, M. S., King, P. D. C., and F. Baumberger. Control of a two-dimensional electron gas on SrTiO₃(111) by atomic oxygen. *Phys. Rev. Lett.*, 113:177601, Oct 2014.
- [215] T. C. Rödel, F. Fortuna, F. Bertran, M. Gabay, M. J. Rozenberg, A. F. Santander-Syro, and P. Le Fèvre. Engineering two-dimensional electron gases at the (001) and (101) surfaces of TiO₂ anatase using light. *Phys. Rev. B*, 92:041106, Jul 2015.
- [216] S. McKeown Walker, F. Y. Bruno, Z. Wang, A. de la Torre, S. Riccò, A. Tamai, T. K. Kim, M. Hoesch, M. Shi, M. S. Bahramy, P. D. C. King, , and F. Baumberger. Carrier-density control of the SrTiO₃ (001) surface 2d electron gas studied by ARPES. *Adv. Mater.*, 27, 2015.
- [217] Chungwei Lin, Chandrima Mitra, and Alexander A. Demkov. Orbital ordering under reduced symmetry in transition metal perovskites: Oxygen vacancy in SrTiO₃. *Phys. Rev. B*, 86:161102, Oct 2012.
- [218] H. O. Jeschke, J. Shen, and R. Valentí. Localized versus itinerant states created by multiple oxygen vacancies in SrTiO₃. *New J. Phys.*, 17, 2015.
- [219] Michaela Altmeyer, Harald O. Jeschke, Oliver Hijano-Cubelos, Cyril Martins, Frank Lechermann, Klaus Koepernik, Andrés F. Santander-Syro, Marcelo J. Rozenberg, Roser Valentí, and Marc Gabay. Magnetism, spin texture, and in-gap states: Atomic specialization at the surface of oxygen-deficient SrTiO₃. *Phys. Rev. Lett.*, 116:157203, Apr 2016.
- [220] Frank Lechermann, Lewin Boehnke, Daniel Grieger, and Christoph Piefke. Electron correlation and magnetism at the LaAlO₃/SrTiO₃ interface: A DFT+DMFT investigation. *Phys. Rev. B*, 90:085125, Aug 2014.
- [221] A. F. Santander-Syro, C. Bareille, F. Fortuna, O. Copie, M. Gabay, F. Bertran, A. Taleb-Ibrahimi, P. Le Fèvre, G. Herranz, N. Reyren, M. Bibes, A. Barthélémy, P. Lecoeur, J. Guevara, and M. J. Rozenberg. Orbital symmetry reconstruction and strong mass renormalization in the two-dimensional electron gas at the surface of KTaO₃. *Phys. Rev. B*, 86:121107, Sep 2012.

- [222] J. Enkovaara, C. Rostgaard, J. J. Mortensen, J. Chen, M. Dułk, L. Ferrighi, J. Gavnholt, C. Glinsvad, V. Haikola, H. A. Hansen, H. H. Kristoffersen, M. Kuisma, A. H. Larsen, L. Lehtovaara, M. Ljungberg, O. Lopez-Acevedo, P. G. Moses, J. Ojanen, T. Olsen, V. Petzold, N. A. Romero, J. Stausholm-Møller, M. Strange, G. A. Tritsarlis, M. Vanin, M. Walter, B. Hammer, H. Häkkinen, G. K. H. Madsen, R. M. Nieminen, J. K. Nørskov, M. Puska, T. T. Rantala, J. Schiøtz, K. S. Thygesen, and K. W. Jacobsen. Electronic structure calculations with gpaw: a real-space implementation of the projector augmented-wave method. *Journal of Physics Condensed Matter*, 22, 2010.
- [223] K. Yoshimatsu, T. Okabe, H. Kumigashira, S. Okamoto, S. Aizaki, A. Fujimori, and M. Oshima. Dimensional-crossover-driven metal-insulator transition in SrVO₃ ultrathin films. *Phys. Rev. Lett.*, 104:147601, Apr 2010.
- [224] S. Backes, T. C. Rödel, F. Fortuna, E. Frantzeskakis, P. Le Fèvre, F. Bertran, M. Kobayashi, R. Yukawa, T. Mitsuhashi, M. Kitamura, K. Horiba, H. Kumigashira, R. Saint-Martin, A. Fouchet, B. Berini, Y. Dumont, A. J. Kim, F. Lechermann, H. O. Jeschke, M. J. Rozenberg, R. Valentí, and A. F. Santander-Syro. Hubbard band or oxygen vacancy states in the correlated electron metal SrVO₃? *arXiv:1602.06909 (unpublished)*, 2016.
- [225] Yuji Muraoka, Hiroki Nagao, Shinsuke Katayama, Takanori Wakita, Masaaki Hirai, Takayoshi Yokoya, Hiroshi Kumigashira, and Masaharu Oshima. Persistent insulator-to-metal transition of a VO₂ thin film induced by soft x-ray irradiation. *Japanese Journal of Applied Physics*, 53, 2014.
- [226] T. C. Rödel, C. Bareille, F. Fortuna, C. Baumier, F. Bertran, P. Le Fèvre, M. Gabay, O. Hijano Cubelos, M. J. Rozenberg, T. Maroutian, P. Lecoeur, and A. F. Santander-Syro. Orientational tuning of the fermi sea of confined electrons at the SrTiO₃ (110) and (111) surfaces. *Phys. Rev. Applied*, 1:051002, Jun 2014.
- [227] Juan Shen, Hunpyo Lee, Roser Valentí, and Harald O. Jeschke. *Ab initio* study of the two-dimensional metallic state at the surface of SrTiO₃: Importance of oxygen vacancies. *Phys. Rev. B*, 86:195119, Nov 2012.
- [228] N. C. Plumb, M. Salluzzo, E. Razzoli, M. Månsson, M. Falub, J. Krempasky, C. E. Matt, J. Chang, M. Schulte, J. Braun, H. Ebert, J. Minár, B. Delley, K.-J. Zhou, T. Schmitt, M. Shi, J. Mesot, L. Patthey, and M. Radović. Mixed dimensionality of confined conducting electrons in the surface region of SrTiO₃. *Phys. Rev. Lett.*, 113:086801, Aug 2014.
- [229] G. Kresse and J. Furthmüller. Efficiency of ab-initio total energy calculations for metals and semiconductors using a plane-wave basis set. *Computational Materials Science*, 6, 1996.
- [230] H. Park, K. Haule, and G. Kotliar. Cluster dynamical mean field theory of the mott transition. *Phys. Rev. Lett.*, 101:186403, Oct 2008.
- [231] D. Rost, E. V. Gorelik, F. Assaad, and N. Blümer. Momentum-dependent pseudogaps in the half-filled two-dimensional hubbard model. *Phys. Rev. B*, 86:155109, Oct 2012.
- [232] Emanuel Gull, Olivier Parcollet, and Andrew J. Millis. Superconductivity and the pseudogap in the two-dimensional hubbard model. *Phys. Rev. Lett.*, 110:216405, May 2013.
- [233] J. Merino and O. Gunnarsson. Pseudogap and singlet formation in organic and cuprate superconductors. *Phys. Rev. B*, 89:245130, Jun 2014.
- [234] T. Schäfer, F. Geles, D. Rost, G. Rohringer, E. Arrigoni, K. Held, N. Blümer, M. Aichhorn, and A. Toschi. Fate of the false mott-hubbard transition in two dimensions. *Phys. Rev. B*, 91:125109, Mar 2015.
- [235] Giulio Biroli and Gabriel Kotliar. Cluster methods for strongly correlated electron systems. *Phys. Rev. B*, 65:155112, Apr 2002.

- [236] A. I. Lichtenstein and M. I. Katsnelson. Antiferromagnetism and d -wave superconductivity in cuprates: A cluster dynamical mean-field theory. *Phys. Rev. B*, 62:R9283–R9286, Oct 2000.
- [237] M. H. Hettler, A. N. Tahvildar-Zadeh, M. Jarrell, T. Pruschke, and H. R. Krishnamurthy. Non-local dynamical correlations of strongly interacting electron systems. *Phys. Rev. B*, 58:R7475–R7479, Sep 1998.
- [238] Thomas Maier, Mark Jarrell, Thomas Pruschke, and Matthias H. Hettler. Quantum cluster theories. *Rev. Mod. Phys.*, 77:1027–1080, Oct 2005.
- [239] Avraham Schiller and Kevin Ingersent. Systematic $1/d$ corrections to the infinite-dimensional limit of correlated lattice electron models. *Phys. Rev. Lett.*, 75:113–116, Jul 1995.
- [240] A. N. Rubtsov, M. I. Katsnelson, and A. I. Lichtenstein. Dual fermion approach to nonlocal correlations in the hubbard model. *Phys. Rev. B*, 77:033101, Jan 2008.
- [241] A. Toschi, A. A. Katanin, and K. Held. Dynamical vertex approximation: A step beyond dynamical mean-field theory. *Phys. Rev. B*, 75:045118, Jan 2007.
- [242] G. Rohringer, A. Toschi, A. Katanin, and K. Held. Critical properties of the half-filled hubbard model in three dimensions. *Phys. Rev. Lett.*, 107:256402, Dec 2011.
- [243] Ping Sun and Gabriel Kotliar. Extended dynamical mean-field theory and GW method. *Phys. Rev. B*, 66:085120, Aug 2002.
- [244] S. Biermann, F. Aryasetiawan, and A. Georges. First-principles approach to the electronic structure of strongly correlated systems: Combining the GW approximation and dynamical mean-field theory. *Phys. Rev. Lett.*, 90:086402, Feb 2003.
- [245] Lars Hedin. New method for calculating the one-particle green's function with application to the electron-gas problem. *Phys. Rev.*, 139:A796–A823, Aug 1965.
- [246] Djurdje Cvijović and Jacek Klinowski. New formulae for the bernoulli and euler polynomials at rational arguments. *Proc. Amer. Math. Soc.*, 123, 1995.

Acknowledgements

This thesis is the result of my Ph.D. studies of almost four years in Prof. Dr. Roser Valentí's group at the University Frankfurt, Germany. How much this time has influenced me and my way of thinking, as well as my gratitude for the people I met, the friends I made and for the discussions we had cannot be put properly into words.

First of all, I would like to thank my supervisor Roser Valentí for giving me the opportunity to be a part of her amazing group and being able to work on and write my Ph.D. thesis. Her helpful guidance and the knowledge I gained from our multiple discussions are unmatched, as well as the trust and respect in our collaboration that allowed me to pursue also my own personal scientific interests in this work.

I also want to thank Harald Jeschke, for his invaluable guidance and helpful discussions that expanded my scientific understanding more than I could have ever imagined.

I am very thankful to Eberhard Engel for being the second referee of my thesis and the very friendly and fruitful discussions we had.

My sincere gratitude goes to all my colleagues, group members and friends that I have made. Your immeasurable support and friendship are next to none and allowed me to retain my sanity. I especially would like to thank my office mate Kira Riedl for careful proofreading, Michaela Altmeyer, Karim Zantout, Laura Martin, Philipp Lange, Steve Winter, Rodrigo Echeveste, Bulcsú Sándor, Hendrik Wernecke, Mirco Parschau, Mario Bijelic, Julian Stobbe, Daniel Guterding, Benjamin Linnik, Robert Rüger and Jean Diehl for their constant support, help and friendship.

I am really grateful for the people I had the opportunity to discuss with and that helped me to continue every time I was stuck. They include Markus Aichhorn, Peter Blöchl, Peter Hirschfeld, Emanuel Gull, Silke Biermann, Hartmut Hafermann, Igor Mazin, Johannes Ferber, Frédéric Hardy, Christoph Meingast, Frank Lechermann, and many more.

I acknowledge the financial support from the Deutsche Forschungsgemeinschaft through SPP1458.

- PUBLICATIONS M. D. Watson, **S. Backes**, A. A. Haghighirad, M. Hoesch, T. K. Kim, A. I. Coldea, R. Valentí,
Formation of Hubbard-like bands as a fingerprint of strong electron-electron interactions in FeSe,
Phys. Rev. B 95, 081106(R) (2017)
- S. Backes**, T. C. Roedel, F. Fortuna, E. Frantzeskakis, P. Le Fevre, F. Bertran, M. Kobayashi, R. Yukawa, T. Mitsuhashi, M. Kitamura, K. Horiba, H. Kumigashira, R. Saint-Martin, A. Fouchet, B. Berini, Y. Dumont, A. J. Kim, F. Lechermann, H. O. Jeschke, M. J. Rozenberg, R. Valentí, A. F. Santander-Syro,
Hubbard band or oxygen vacancy states in the correlated electron metal SrVO₃?,
Phys. Rev. B 94, 241110(R) (2016)
- A. Chernenkaya, **S. Backes**, H.-J. Elmers, G. Schönhense, H. O. Jeschke, R. Valentí *et al.*,
Microscopic origin of the charge transfer in single crystals based on thiophene derivatives: A combined NEXAFS and density functional theory approach,
J. of Chem. Phys. 145, 3, 10.1063/1.4958659 (2016)
- F. Lechermann, H. O. Jeschke, A. J. Kim, **S. Backes**, and R. Valentí,
Electron dichotomy on the SrTiO₃ defect surface augmented by many-body effects,
Phys. Rev. B 93, 121103(R) (2016)
- S. Backes**, H. O. Jeschke, R. Valentí,
Microscopic nature of correlations in multi-orbital AFe₂As₂ (A=K, Rb, Cs): Hund's coupling versus Coulomb repulsion,
Phys. Rev. B 92, 195128 (2015)
- D. Guterding, **S. Backes**, H. O. Jeschke, R. Valentí,
Origin of the superconducting state in the collapsed tetragonal phase of KFe₂As₂,
Phys. Rev. B 91, 140503(R) (2015)
- J. Diehl, **S. Backes**, D. Guterding, H. O. Jeschke, R. Valentí,
Correlation effects in the tetragonal and collapsed tetragonal phase of CaFe₂As₂,
Phys. Rev. B 90, 085110 (2014)
- S. Backes**, D. Guterding, H. O. Jeschke, R. Valentí,
Electronic structure and de Haas-van Alphen frequencies in KFe₂As₂ within LDA+DMFT,
New J. Phys. 16, 083025 (2014)
- S. Backes**, H. O. Jeschke,
Finite temperature and pressure molecular dynamics for BaFe₂As₂,
Phys. Rev. B 88, 075111 (2013)
- S. Backes**, I. Titvinidze, A. Privitera, and W. Hofstetter,
Monte Carlo study of fermionic trions in a square lattice with harmonic confinement,
Phys. Rev. A 86, 013633 (2012)